



## 저작자표시-비영리-동일조건변경허락 2.0 대한민국

이용자는 아래의 조건을 따르는 경우에 한하여 자유롭게

- 이 저작물을 복제, 배포, 전송, 전시, 공연 및 방송할 수 있습니다.
- 이차적 저작물을 작성할 수 있습니다.

다음과 같은 조건을 따라야 합니다:



저작자표시. 귀하는 원저작자를 표시하여야 합니다.



비영리. 귀하는 이 저작물을 영리 목적으로 이용할 수 없습니다.



동일조건변경허락. 귀하가 이 저작물을 개작, 변형 또는 가공했을 경우에는, 이 저작물과 동일한 이용허락조건하에서만 배포할 수 있습니다.

- 귀하는, 이 저작물의 재이용이나 배포의 경우, 이 저작물에 적용된 이용허락조건을 명확하게 나타내어야 합니다.
- 저작권자로부터 별도의 허가를 받으면 이러한 조건들은 적용되지 않습니다.

저작권법에 따른 이용자의 권리는 위의 내용에 의하여 영향을 받지 않습니다.

이것은 [이용허락규약\(Legal Code\)](#)을 이해하기 쉽게 요약한 것입니다.

[Disclaimer](#)

공학박사 학위논문

**Performance Based Earthquake  
Design/Analysis Methods for  
Reinforced Concrete Beam-Column  
Connections**

철근콘크리트 보-기둥 접합부의 성능 기반  
내진설계 및 해석 방법

2014 년 2 월

서울대학교 대학원

건축학과

황 현 중

# **Performance Based Earthquake Design/Analysis Methods for Reinforced Concrete Beam-Column Connections**

지도 교수 박 홍 근

이 논문을 공학박사 학위논문으로 제출함  
2014 년 2 월

서울대학교 대학원  
건축학과  
황 현 중

황현중의 공학박사 학위논문을 인준함  
2014 년 2 월

위 원 장 \_\_\_\_\_ (인)

부위원장 \_\_\_\_\_ (인)

위 원 \_\_\_\_\_ (인)

위 원 \_\_\_\_\_ (인)

위 원 \_\_\_\_\_ (인)

## **Abstract**

# **Performance Based Earthquake Design/Analysis Methods for Reinforced Concrete Beam-Column Connections**

Hwang, Hyeon-Jong  
Department of Architecture and Architectural Engineering  
College of Engineering  
Seoul National University

In reinforced concrete moment-resisting frames subjected to cyclic loading, the cyclic response, including stiffness degradation, strength degradation, and energy dissipation, is significantly affected by the behavior of the beam-column joints. In the present study, for performance based earthquake design methods of reinforced concrete structures, analytical and experimental studies were performed to evaluate the earthquake response and seismic performance of the beam-column connections.

The cyclic behavior of the beam-column connections is significantly affected by bar bond-slip and joint shear deformations. An experimental study was performed to evaluate the seismic performance of beam-column connections using grade 600 MPa bars for beam flexural reinforcement. Full

scale four interior connections and three exterior connections were tested under cyclic lateral loading. The specimens were designed according to the special seismic provisions in ACI 318-11. The structural performance of the specimens with 600 MPa D22 and D25 bars was directly compared with that of the specimen with 400 MPa D25 bars. In the case of the interior connections, the load-carrying capacity and maximum deformation were close to those of the specimen with 400 MPa bars. On the other hand, the energy dissipation capacity of the specimens with 600 MPa bars decreased by a maximum of 25% due to the increased bond-slip at the joints. In the case of the exterior connections, significant bond-slip occurred at the beam bottom bars due to insufficient development length, which decreased the deformation capacity and energy dissipation capacity of the specimens.

To predict the bond-slip of beam flexural bars in the joint, a bond-slip model was developed. The proposed model estimated the bond-slip relationship using simplified bond strength and bar strain distribution in the beam-column joint. The bond strength was defined from the existing test results of beam-column connections that showed complete bond failure. For verification, the prediction of the proposed model was compared with existing test results of concrete block specimens for bond-slip and beam-column connection specimens. The result showed that the proposed model predicted well the bond strength degradation and bond-slip in the beam-column joints.

On the basis of the bond-slip model, a joint shear strength model addressing the effect of bond-slip of beam re-bars was developed. The

proposed model consists of truss mechanism and diagonal strut mechanism. The developed bond-slip model of beam re-bars was implemented in the proposed model. For verification, the predictions of joint shear capacity and deformation capacity were compared with existing test results of 64 interior beam-column connections. The result showed that the proposed model predicted the joint shear strength degradation and deformation capacity with reasonable precision.

Using existing test results of 69 interior and 63 exterior connections, the variation of energy dissipation (per load cycle) according to the bond-slip and joint shear strength was statistically investigated. The results showed that the energy dissipation correlated with the parameters of the bar bond-slip, better than with the joint shear strength. On the basis of the result, the energy dissipation of beam-column connections was defined as the function of the bond parameters. By using the energy function and the Pinching 4 model of OpenSees, an energy-based hysteresis model was developed, such that the area enclosed by the cyclic curve is the same as the predicted energy dissipation. The proposed model was applied to existing test specimens. The predictions were compared with the test results, and showed good agreement.

On the basis of the developed energy-based model with various energy dissipation capacities ( $\kappa = 0.2, 0.4, 0.6$ , and elasto-perfectly plastic for beam-column connections; and  $\kappa = 0.4$  and elasto-perfectly plastic for columns on ground), nonlinear dynamic analysis was performed for three types of low-rise moment frame structures. The results showed that the energy dissipation

capacity degradation in the joint increases the lateral drift and ductility demand of moment frame structures. Furthermore, in the moment frame structures with shorter natural period, the lateral drift was increased. For larger yield strength reduction factor, structure performance was greatly affected by the energy dissipation capacity of the structure

Finally, to restrain the bond-slip and improve the structural performance of beam-column connections, relocated plastic hinge methods were proposed. Cyclic load tests were performed for beam-column connections strengthened with 45° bent bars and 90° hooked bars to confirm the effects of plastic hinge relocation. The test results showed that despite small  $h_c/d_b$  values less than 20, by using the strengthening methods, the bar bond- and shear strength-degradations in the joints were substantially decreased. To address the enhanced performance, the bond resistance of the beam flexural bars and the joint shear strength were redefined considering the details of the strengthening methods so that engineers can design the strengthening methods according to current design codes for conventional beam-column connections. On the basis of existing test results, the seismic design and detailing of beam-column joints with strengthening bars were recommended.

**Keywords :** Performance based earthquake design; RC beam-column connection; Nonlinear time history analysis; Bond-slip; Joint shear strength; High-strength bars; Strengthening method

**Student Number :** 2010-30175

# Contents

<b>Abstract .....</b>	<b>i</b>
<b>Contents.....</b>	<b>v</b>
<b>List of Tables .....</b>	<b>x</b>
<b>List of Figures .....</b>	<b>xi</b>
<b>List of Symbols .....</b>	<b>xvii</b>
<b>Chapter 1. Introduction .....</b>	<b>1</b>
1.1 General.....	1
1.2 Scope and Objectives.....	11
1.3 Outline of Dissertation .....	13
<b>Chapter 2. Behavior of Beam-Column Connections Using Grade 600 MPa Bars.....</b>	<b>16</b>
2.1 Introduction .....	16
2.2 Test Plan.....	20
2.3 Test Results.....	32
2.3.1 Lateral Load-Story Drift Relationship.....	32
2.3.2 Failure Modes .....	37
2.3.3 Strain of Flexural Re-bar in the Connection.....	40
2.3.4 Strain of Ties.....	47
2.3.5 Joint Shear Deformation.....	48
2.3.6 Hysteretic Energy Dissipation .....	50



2.4 Evaluation According to ACI 374.1-05 .....	53
2.5 Discussion.....	57

### **Chapter 3. Bond-Slip Relationship of Beam Flexural Bars in Interior Joint ..... 60**

3.1 Introduction .....	60
3.2 Re-bar Bond Model at Beam-Column Joint .....	65
3.3 Bond Stress .....	75
3.4 Verification of the Proposed Bond Model .....	87
3.5 Bond Performance Requirement .....	98
3.6 Discussion.....	103

### **Chapter 4. Joint Shear Strength and Deformation Capacity..... 105**

4.1 Introduction .....	105
4.2 Shear Force Transferred to Joint.....	110
4.3 Joint Shear Resistance Capacity .....	114
4.3.1 Resistance by Truss Mechanism $V_T$ .....	115
4.3.2 Resistance by Diagonal Strut $V_C$ .....	116
4.4 Joint Shear Deformation and Effective Concrete Strength .....	119
4.5 Relationship Between Joint and Beam-Column Connection ...	129
4.6 Flexural Deformation Capacity of Beam Section.....	134
4.7 Evaluation and Verification of Joint Deformation Capacity ....	136
4.7.1 Calculation of Joint Deformation and Shear Strength.....	136
4.7.2 Comparison of Predictions and Test Results .....	137
4.8 Discussion.....	152

### **Chapter 5. Relationship between Energy Dissipation and Bond Resistance..... 154**

5.1 Introduction .....	154
5.2 Evaluation of Energy Dissipation Capacity.....	158
5.3 Discussion.....	173
<b>Chapter 6. Energy-Based Hysteresis Model .....</b>	<b>174</b>
6.1 Introduction .....	174
6.2 Energy-Based Hysteresis Model .....	178
6.3 Applications .....	190
6.4 Discussion.....	202
<b>Chapter 7. Nonlinear Time History Analysis Using Energy-Based Model .....</b>	<b>204</b>
7.1 Introduction .....	204
7.2 Analysis Model Using OpenSees .....	207
7.2.1 Moment Frame Structure.....	207
7.2.2 Nonlinear Analysis Algorithm.....	213
7.3 Earthquake Response According to Energy Dissipation Capacity on El-Centro Earthquake Loading.....	219
7.3.1 3 Stories-1 Bay Structure.....	219
7.3.2 3 Stories-3 Bay Structure.....	226
7.3.3 5 Stories-3 Bay Structure.....	230
7.3.4 Plastic Hinge Distributions .....	235
7.4 Earthquake Response According to Energy Dissipation Capacity on Northridge and Kobe Earthquake Loadings .....	242
7.4.1 3 Stories-1 Bay Structure.....	242
7.4.2 3 Stories-3 Bay Structure.....	247
7.4.3 5 Stories-3 Bay Structure.....	251
7.5 Influence Parameters of Earthquake Response .....	257
7.5.1 Relationship between Energy Dissipation of Structures and Earthquake Response.....	257

7.5.2 Relationship between Energy Dissipation Ratio of Beam-Column Connections and Earthquake Response .....	262
7.5.3 Relationship between Natural Period of Structures and Earthquake Response.....	263
7.6 Discussion.....	266

## **Chapter 8. Plastic Hinge Relocation Method Using Strengthening Bars..... 267**

8.1 Introduction .....	267
8.2 Relocation of Beam Plastic Hinge Zone .....	271
8.3 Test Program.....	277
8.4 Test Results .....	285
8.4.1 Lateral Load-Drift Ratio Relationship and Failure Mode .....	285
8.4.2 Load-carrying Capacity and Deformation Capacity .....	291
8.4.3 Shear Strength of Beam-Column Joints .....	293
8.4.4 Secant Stiffness and Energy Dissipation Capacity .....	295
8.5 Deformations at Beam-Column Joints .....	302
8.5.1 Re-bar Strain.....	302
8.5.2 Shear Deformation.....	306
8.6 Design Recommendations .....	308
8.7 Discussion.....	311

## **Chapter 9. Summary and Conclusions..... 314**

9.1 Summary.....	314
9.2 Conclusions .....	318
9.2.1 Behavior of Beam-Column Connections.....	318
9.2.2 Joint Shear Strength Depending on Bar Bond-Slip .....	321
9.2.3 Dynamic Response of Structures Using Energy-Based Model ..	323
9.2.4 Design Recommendations for Strengthening Methods .....	325
9.2.5 Performance Based Earthquake Design.....	327

<b>References .....</b>	<b>328</b>
<b>Appendix A: Joint Shear Strength and Deformation Capacity Matlab Code .....</b>	<b>345</b>
<b>Appendix B: Nonlinear Time History Analysis OpenSees Code .....</b>	<b>356</b>

## List of Tables

Table 2-1. Summary of test program .....	24
Table 2-2. Design of beam-column joints .....	25
Table 2-3. Evaluation of seismic performance of test specimens (ACI 374.1-05, see Fig. 2-14).....	56
Table 3-1. Test parameters of existing test specimens.....	81
Table 4-1. Test parameters of existing test specimens.....	139
Table 5-1. Summary of interior beam-column connection tests.....	163
Table 5-2. Summary of exterior beam-column connection tests .....	165
Table 6-1. Modeling parameters for existing test specimens .....	191
Table 8-1. Properties of test specimens (mm, %, MPa, kN, and kN-m) .....	280
Table 8-2. Test results (kN, kN/mm, and %) .....	288
Table 8-3. Summary on existing test results .....	300

## List of Figures

Fig. 1-1. Building structures damaged by earthquake load .....	1
Fig. 1-2. Forces of beams and columns framed into the joint .....	2
Fig. 1-3. Hysteretic response of RC beam-column joint according to $h_c/d_b$ .....	4
Fig. 1-4. Relationship between earthquake hazard and earthquake performance level for performance based earthquake design.....	5
Fig. 1-5. Composition of performance based earthquake design .....	10
Fig. 2-1. Details of test specimens (unit: mm) .....	22
Fig. 2-2. Stress-strain relationships of re-bar .....	23
Fig. 2-3. Calculation of load-carrying capacity of beam-column joints .....	30
Fig. 2-4. Test setup.....	31
Fig. 2-5. Lateral load-story drift ratio relationships of specimens .....	35
Fig. 2-6. Failure modes of test specimens at the end of test.....	38
Fig. 2-7. Strain of beam re-bars at interface of interior joints .....	42
Fig. 2-8. Strain distributions of beam top and bottom bars in interior connections .....	44
Fig. 2-9. Strain of beam re-bars at the center of interior and exterior joints .....	46
Fig. 2-10. Strain of beam re-bars at interface of exterior joint S7.....	47
Fig. 2-11. Strain of tie bars at the interior and exterior joints .....	48
Fig. 2-12. Joint shear distortion .....	49
Fig. 2-13. Energy dissipation capacities of test specimens .....	51
Fig. 2-14. Acceptance criteria by ACI 374.1-05.....	55
Fig. 3-1. Load transfer of beam-column joint in interior connection ...	61
Fig. 3-2. Mechanism of bond resistance of beam flexural bars (Eligeha-	

usen et al., 1983).....	66
Fig. 3-3. Re-bar stress variation by bond stress.....	68
Fig. 3-4. Stress and strain distribution of beam re-bars due to bond-slip in beam-column joint under cyclic loading .....	72
Fig. 3-5. Evaluation of residual bond stress from existing test results of beam-column connections .....	77
Fig. 3-6. Variation of residual bond stress according to design paramet- ers .....	80
Fig. 3-7. Comparison between cyclic test and bond stress model.....	89
Fig. 3-8. Strain distribution of re-bars for No.14 .....	91
Fig. 3-9. Comparison of strain distribution for No.14 (Elmorsi et al., 2000).....	93
Fig. 3-10. Comparison of strain distribution after yielding of re-bars .	94
Fig. 3-11. Comparison of elongation of beam re-bars.....	96
Fig. 3-12. Comparison of design requirement $h_c/d_b$ for interior beam- column joint.....	101
Fig. 4-1. Failure modes of interior beam-column connection depending on bar-bond and shear resistance.....	106
Fig. 4-2. Load-transfer mechanisms at beam-column joints .....	111
Fig. 4-3. Truss mechanism in joint panel .....	115
Fig. 4-4. Diagonal strut strength.....	117
Fig. 4-5. Simplified deformation model for beam-column joint after bond-slip of beam longitudinal bars .....	120
Fig. 4-6. Comparison of shear distortion and bond displacement.....	125
Fig. 4-7. Interior beam-column connection .....	129
Fig. 4-8. Load-deformation relationship.....	138
Fig. 4-9. Comparisons between hysteresis curves and predictions ....	143
Fig. 5-1. Typical cyclic response and joint load-transfer mechanism of beam-column connections .....	155
Fig. 5-2. Definition of energy dissipation ratio (ACI 374.01-5) .....	159

Fig. 5-3. Variation of energy dissipation ratio according to bond parameters: interior connections.....	167
Fig. 5-4. Variation of energy dissipation ratio according to bond parameters: exterior connections.....	168
Fig. 5-5. Variation of energy dissipation ratio according to joint shear parameters.....	170
Fig. 5-6. Variations of energy dissipation according to beam rebar ratio .....	171
Fig. 6-1. Energy-based hysteresis model for beam-column connections .....	180
Fig. 6-2. Comparison of predicted energy dissipation ratios with test results.....	187
Fig. 6-3. Predicted cyclic responses vs. test results for interior connections (Brooke et al., 2006; Dai and Park, 1987; Durrani and Wight, 1982; Xian et al., 1992; Hwang et al., 2011).....	193
Fig. 6-4. Predicted cyclic responses vs. test results for exterior connections (Ehsani et al., 1987; Kaku and Asakusa, 1991; Chutarat and Aboutaha, 2003; Tsonos et al., 1992; Shiohara, 2010).....	194
Fig. 6-5. Interior connection Dai and Park U1 (Dai and Park, 1987). 197	
Fig. 6-6. Exterior connection: Ehsani 2 (Ehsani et al., 1987).....	199
Fig. 7-1. Structure modeling for dynamic analysis of OpenSees .....	208
Fig. 7-2. Hysteretic behaviors of interior and exterior joint and column .....	211
Fig. 7-3. Ground acceleration .....	211
Fig. 7-4. Load-displacement relationship for nonlinear system .....	213
Fig. 7-5. Displacements at 3 <sup>rd</sup> floor in 3 stories-1 bay structure (R= 2) .....	220
Fig. 7-6. Displacements at 3 <sup>rd</sup> floor in 3 stories-1 bay structure (R= 4) .....	222
Fig. 7-7. Comparison of displacement according to energy dissipation ratio of 3 stories-1 bay structure .....	224
Fig. 7-8. Comparison of ductility according to energy dissipation ratio	



of 3 stories-1 bay structure .....	224
Fig. 7-9. Moment-rotation relationship according to energy dissipation ratio for $R=2$ .....	225
Fig. 7-10. Moment-rotation relationship according to energy dissipation ratio for $R=4$ .....	226
Fig. 7-11. Displacements at 3 <sup>rd</sup> floor in 3 stories-3 bay structure ( $R= 2$ ) .....	227
Fig. 7-12. Displacements at 3 <sup>rd</sup> floor in 3 stories-3 bay structure ( $R= 4$ ) .....	228
Fig. 7-13. Comparison of displacement according to energy dissipation ratio of 3 stories-3 bay structure .....	229
Fig. 7-14. Comparison of displacement according to energy dissipation ratio of 3 stories-3 bay structure .....	230
Fig. 7-15. Displacements at 5 <sup>th</sup> floor in 5 stories-3 bay structure ( $R= 2$ ) .....	232
Fig. 7-16. Displacements at 5 <sup>th</sup> floor in 5 stories-3 bay structure ( $R= 4$ ) .....	233
Fig. 7-17. Comparison of displacement according to energy dissipation ratio of 5 stories-3 bay structure .....	234
Fig. 7-18. Comparison of ductility according to energy dissipation ratio of 5 stories-3 bay structure .....	234
Fig. 7-19. Plastic hinge distribution at positive direction for $R= 4$ in 3 stories-1 bay structure.....	236
Fig. 7-20. Plastic hinge distribution at negative direction for $R= 4$ in 3 stories-3 bay structure.....	237
Fig. 7-21. Plastic hinge distribution at positive direction for $R= 4$ in 3 stories-3 bay structure.....	238
Fig. 7-22. Plastic hinge distribution at negative direction for $R= 4$ in 3 stories-3 bay structure.....	239
Fig. 7-23. Plastic hinge distribution at positive direction for $R= 4$ in 5 stories-3 bay structure.....	240
Fig. 7-24. Plastic hinge distribution at negative direction for $R= 4$ in 5	

stories-3 bay structure.....	241
Fig. 7-25. Comparison of displacement according to energy dissipation ratio of 3 stories-1 bay structure subjected to Northridge earthquake load .....	243
Fig. 7-26. Comparison of ductility according to energy dissipation ratio of 3 stories-1 bay structure subjected to Northridge earthquake load	244
Fig. 7-27. Comparison of displacement according to energy dissipation ratio of 3 stories-1 bay structure subjected to Kobe earthquake load.	245
Fig. 7-28. Comparison of ductility according to energy dissipation ratio of 3 stories-1 bay structure subjected to Kobe earthquake load .....	246
Fig. 7-29. Comparison of displacement according to energy dissipation ratio of 3 stories-3 bay structure subjected to Northridge earthquake load .....	248
Fig. 7-30. Comparison of ductility according to energy dissipation ratio of 3 stories-3 bay structure subjected to Northridge earthquake load	249
Fig. 7-31. Comparison of displacement according to energy dissipation ratio of 3 stories-3 bay structure subjected to Kobe earthquake load.	250
Fig. 7-32. Comparison of ductility according to energy dissipation ratio of 3 stories-3 bay structure subjected to Kobe earthquake load .....	251
Fig. 7-33. Comparison of displacement according to energy dissipation ratio of 5 stories-3 bay structure subjected to Northridge earthquake load .....	253
Fig. 7-34. Comparison of ductility according to energy dissipation ratio of 5 stories-3 bay structure subjected to Northridge earthquake load	253
Fig. 7-35. Comparison of displacement according to energy dissipation ratio of 5 stories-3 bay structure subjected to Kobe earthquake load.	255
Fig. 7-36. Comparison of ductility according to energy dissipation ratio of 5 stories-3 bay structure subjected to Kobe earthquake load .....	256
Fig. 7-37. Energy dissipation in 3 stories-1 bay structures .....	258
Fig. 7-38. Energy dissipation in 3 stories-3 bay structures .....	259
Fig. 7-39. Energy dissipation in 5 stories-3 bay structures .....	260
Fig. 7-40. Relationship between energy dissipation and plastic rotation	

.....	261
Fig. 7-41. Earthquake responses according to energy dissipation ratio .....	263
Fig. 7-42. Earthquake responses according to natural period.....	264
Fig. 8-1. Load transfer of interior beam-column joint.....	267
Fig. 8-2. Strengthening methods for beam-column joint.....	272
Fig. 8-3. Shear demand of beam-column joint with strengthening bars .....	274
Fig. 8-4. Dimensions and re-bar details of connection specimens .....	279
Fig. 8-5. Test setup.....	284
Fig. 8-6. Lateral load-drift ratio relationship of connection specimens .....	287
Fig. 8-7. Failure modes of specimens at the end of the test .....	290
Fig. 8-8. Calculation of load-carrying capacity .....	292
Fig. 8-9. Shear strength of beam-column joints with strengthening bars .....	295
Fig. 8-10. Energy dissipation ratio of specimens .....	298
Fig. 8-11. Strains of beam flexural bars .....	304
Fig. 8-12. Strains of strengthening bars.....	305
Fig. 8-13. Shear deformation at beam-column joints .....	307

## List of Symbols

$A_s$	Section area of re-bar ( $\text{mm}^2$ )
$A_s'$	Section area of top flexural bars ( $\text{mm}^2$ )
$A_h$	Section area of transverse bar ( $\text{mm}^2$ )
$A_j$	Effective joint area ( $\text{mm}^2$ )
$C$	Viscous damping coefficient matrix
$C_{bl}$	Compression re-bar strength (kN)
$C_0$	Parameter of joint bond strength
$E_c$	Modulus of concrete (MPa)
$E_c I_b$	Effective flexural stiffness of beam ( $\text{N} \cdot \text{mm}^2$ )
$E_c I_c$	Effective flexural stiffness of column ( $\text{N} \cdot \text{mm}^2$ )
$E_{ep}$	Idealized elastic-perfectly plastic energy dissipation ( $\text{kN} \cdot \text{m}$ )
$E_s$	Elastic stiffness of re-bar (MPa)
$E_{sh}$	Hardening stiffness of re-bar (MPa)
$E_{II}$	Actual energy dissipation per load cycle ( $\text{kN} \cdot \text{m}$ )
$F_b$	Bond strength of bottom bars (kN)
$F_b'$	Bond strength of top bars (kN)
$F_{bt}$	Bond strength applied to truss mechanism region (kN)
$H$	Net column height (mm)
$I_g$	Second-order moment of inertia of the gross cross-section ( $\text{mm}^4$ )
$K$	Stiffness matrix
$L_p$	Beam plastic hinge length (mm)

$M$	Mass matrix
$\sum M_b$	Sum of beam flexural capacities (kN·m)
$M_{bn}$	Moment by the yield of the top re-bar of beam (kN·m)
$M_{bp}$	Moment by the yield of the bottom re-bar of beam (kN·m)
$M_{cr}$	Cracking moment at the critical section of beam (kN·m)
$\sum M_c$	Sum of column flexural capacities (kN·m)
$M_l$	Beam flexural moment developed by $\tau_u$ (kN·m)
$M_n$	Nominal flexural capacity (kN·m)
$M_{nj}$	Nominal flexural capacity at the column face (kN·m)
$M_{ny}$	Yield moment at the critical section of beam (kN·m)
$M_r$	Residual flexural capacity (kN·m)
$N_c$	Compression load at column (kN)
$P_n$	Load carrying capacity (kN)
$P_0$	Constant loading without stiffness variation (kN)
$R$	Yield strength reduction factor
$R^2$	Correlation coefficient
$T_{b2}$	Tension re-bar strength (kN)
$T_n$	Natural period (second)
$V_C$	Diagonal strut resistance (kN)
$V_c$	Shear force applied to column (kN)
$V_{cf}$	Diagonal compression field strength (kN)
$V_{jn}$	Nominal shear strength of joint concrete panel (kN)
$V_n$	Joint shear capacity (kN)
$V_T$	Diagonal compression field resistance (kN)
$V_u$	Joint shear demand (kN)

$a$	Horizontal distance between the ends of diagonal linear potentiometers (mm)
$a_0$	Mass proportional damping coefficient
$a_1$	Stiffness proportional damping coefficient
$b$	Vertical distance between the ends of diagonal linear potentiometers (mm)
$b_b$	Beam width (mm)
$b_c$	Column width (mm)
$c$	Neutral axis depth at the beam section (mm)
$c'$	Neutral axis depth at the beam section under negative moment (mm)
$c_{b1}$ and $c_{b2}$	Compression zone depth of the beam (mm)
$c_{c1}$ and $c_{c2}$	Compression zone depth of the column (mm)
$d$	Effective beam depth (mm)
$d'$	Distance from beam bottom face to bottom re-bars (mm)
$d_b$	Re-bar diameter of a beam (mm)
$d_j$	Distance from the column face to the beam critical section (mm)
$d_n$	Effective beam depth under negative moment (mm)
$e_b$	Elongation of beam flexural bar (mm)
$f_c'$	Concrete strength (MPa)
$f_{ce}$	Effective compression strength of diagonal strut (MPa)
$f_{cef}$	Effective compression strength of diagonal compression field (MPa)
$f_{ctm}$	Concrete tensile strength (MPa)

## List of Symbols

---

$f_y$	Yield strength of re-bar (MPa)
$f_{yt}$	Yield strength of transverse bar (MPa)
$f_u$	Ultimate strength of re-bar (MPa)
$h$	Net column height (mm)
$h_b$	Beam depth (mm)
$h_c$	Column depth (mm)
$h_s$	Distance between top and bottom flexural bars (mm)
$i$	Load cycle number
$j_d$	Moment lever arm length of a beam (mm)
$k_D$	Coefficient related to the ductility
$k_i$	Initial stiffness (kN/mm)
$k_s$	Secant stiffness (kN/mm)
$k_{un}$	Negative unloading stiffness (kN/mm)
$k_{up}$	Positive unloading stiffness (kN/mm)
$k_{yn}$	Secant stiffness connecting point O and the negative yield point (kN/mm)
$k_{yp}$	Secant stiffness connecting point O and the positive yield point (kN/mm)
$l$	Beam length between the vertical supports (mm)
$l_c$	Compressive bond length (mm)
$l_{db}$	Compression development length (mm)
$l_{dh}$	Development length of hooked bars (mm)
$l_{dj}$	Modified development length (mm)
$l_e$	Tensile bond length (mm)
$l_s$	Distance from the column face to the location of zero

	moment in beam (mm)
$l_u$	Friction bond length (mm)
$l_x$	Distance contributed to bond-slip (mm)
$n_b$	the number of bottom flexural bars of beam cross-section
$n_t$	the number of top flexural bars of beam cross-section
$s$	Anchorage bond-slip (mm)
$t$	Diagonal strut depth (mm)
$u$	Displacement matrix
$\dot{u}$	Velocity matrix
$\ddot{u}$	Acceleration matrix
$\ddot{u}_g$	Earthquake acceleration
$w$	Width of concrete strut (mm)
$x$	Smaller perpendicular distance from the longitudinal axis of beam to the column side (mm)
$y_t$	Distance between the neutral axis and the tension end (mm)
$\alpha$	Stress multiplier for longitudinal re-bar
$\alpha_1$	Coefficient related to the details of hook anchorage
$\alpha_2$	Coefficient related to the joint confinement by transverse hoops
$\alpha_0$	Coefficient related to the location of the plastic hinge of beams
$\alpha_d$	Coefficient related to the ductility of the plastic hinge of beams
$\alpha_f$	Coefficient related to the direction of the beam re-bars
$\beta$	Coefficient related to the ultimate flexural capacity



$\beta_l$	Coefficient between neutral axis and compression zone of equivalent stress block
$\beta_r$	Coefficient related to the residual flexural capacity
$\gamma$	Coefficient related to inter-storey drift
$\gamma_j$	Joint shear distortion (rad.)
$\gamma_k$	Coefficient related to the degradation of the unloading stiffness
$\gamma_{Rd}$	Overstrength factor of the beam flexural bars
$\gamma_s$	Coefficient related to the cyclic strength degradation
$\delta$	Story drift ratio (%)
$\delta_T$	Total story drift ratio of beam-column connection (%)
$\delta_c$	Drift by column deformation (%)
$\delta_{b,p}$	Drift by plastic hinge deformation of beam (%)
$\delta_{b,r}$	Drift by anchorage slip at joint interface (%)
$\delta_{b,y}$	Drift by elastic deformation of beam (%)
$\delta_j$	Drift by joint shear deformation (%)
$\delta_j'$	Diagonal deformation measured by the two linear potentiometers (mm)
$\delta_u$	Ultimate story drift (mm)
$\delta_y$	Yield story drift (mm)
$\varepsilon$	Strain of re-bar (mm/mm)
$\varepsilon_1$	Principal tension strain of joint diagonal strut (mm/mm)
$\varepsilon_2$	Principal compression strain (mm/mm)
$\varepsilon_c$	Compression strain of re-bar (mm/mm)
$\varepsilon_{cb}$	Concrete compression at beam bottom bars (mm/mm)

$\varepsilon_t$	Given tension strain of re-bar (mm/mm)
$\varepsilon_{xx}$	Horizontal uniform tensile strain at the joint concrete (mm/mm)
$\varepsilon_y$	Yield strain of re-bar (mm/mm)
$\varepsilon_{yy}$	Vertical uniform tensile strain at the joint concrete (mm/mm)
$\zeta$	Damping ratio
$\theta$	Concrete strut angle (degree)
$\theta_{bu}$	Maximum plastic rotation angle of the beam (rad.)
$\theta_{ju}$	Maximum plastic rotation angle of the joint (rad.)
$\theta_c$	Plastic deformation angle at cracking state (rad.)
$\theta_y$	Plastic deformation angle at yield state (rad.)
$\theta_r$	Plastic deformation angle at residual state (rad.)
$\theta_u$	Plastic deformation angle at ultimate state (rad.)
$\kappa$	Energy dissipation ratio ( $\kappa = E_{II} / E_{ep}$ )
$\lambda_M$	Coefficient related to the flexural moment and energy function
$\lambda_\theta$	Coefficient related to the plastic deformation angle and energy function
$\mu$	Ductility ( $\mu = \delta_u / \delta_y$ )
$\mu_\phi$	Curvature ductility ( $\mu_\phi = \phi_t / \phi_y$ )
$\nu_d$	Column axial load ratio
$\rho'$	Compression bar ratio of the beam section
$\rho_{max}$	The maximum tension bar ratio of the beam section
$\sigma$	Re-bar stress (MPa)

## List of Symbols

---

$\tau_e$	Bearing bond stress (MPa)
$\tau_u$	Friction bond stress (MPa)
$\varphi_t$	Curvature of beam cross-section (1/m)
$\varphi_y$	yield curvature of beam cross-section (1/m)
$\omega_i$	Natural frequencies of i <sup>th</sup> mode
$\omega_j$	Natural frequencies of j <sup>th</sup> mode

# Chapter 1. Introduction

## 1.1 General

Recently, human life and property damages are occurred by strong earthquake load in the world. In Korea, earthquake has increased in frequency over recent years. As a result, to secure safety for earthquake in building structures, seismic design requirement was strengthened in Korean Building Code (KBC, 2009). Fig. 1-1 shows the building structures damaged by earthquake load. Most of reinforcement concrete (RC) building structures are damaged in beam-column connection by earthquake. This is because stress is concentrated in the joint that connects between beams and columns. Therefore, earthquake resisting structural performance of building structures are significantly affected by joint cyclic behaviors.



Fig. 1-1. Building structures damaged by earthquake load

Fig. 1-2 shows earthquake load transfer mechanism in RC beam-column connection. In beam-column connection subjected to cyclic loading, joint diagonal cracking is developed by bond failure between beam re-bars and concrete, bond-slip of beam re-bars, and joint shear deformation. According to Kitayama et al. (1987), the joint behavior is significantly affected by the ratio of column depth  $h_c$  to beam re-bar diameter  $d_b$ . When the beam re-bars are not sufficiently anchored at the joint with low  $h_c/d_b$ , re-bars bond-failure and -slip are significantly occurred by cyclic loading. As a result, energy dissipation capacity and stiffness decrease in the joint. Furthermore, joint shear deformation and diagonal cracking are increased, and diagonal concrete crushing can be occurred in the joint by large joint shear demand.

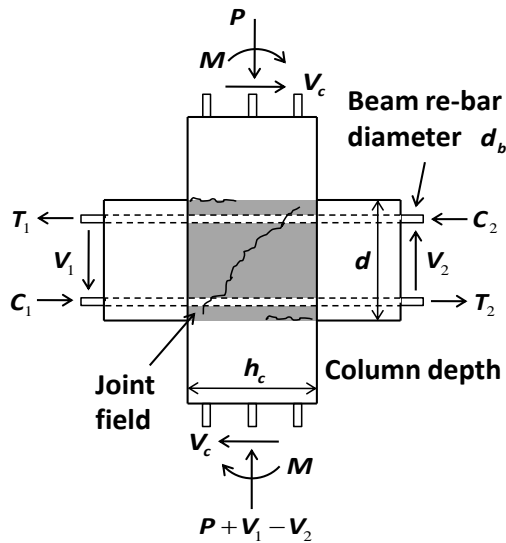


Fig. 1-2. Forces of beams and columns framed into the joint

Fig. 1-3 shows hysteretic behavior of interior beam-column connections according to  $h_c/d_b$ . In the beam-column connection with low  $h_c/d_b$ , diagonal cracking was increased and concrete crushing occurred in the joint by cyclic loading. This joint concrete failure decreases compression resistant capacity of column, and induces the joint brittle failure by diagonal cracking. Furthermore, as shown in Fig. 1-3(a), re-bar bond-failure and bond-slip increased pinching in the joint under cyclic loading. As a result, earthquake resisting performance of the joint was degraded by decreased stiffness and energy dissipation capacity. On the other hand, as shown in Fig. 1-3(b), in beam-column joint with  $h_c/d_b = 30$ , joint concrete damage was decreased because of sufficient bond resistance of beam re-bars. Furthermore, re-bar bond-failure and bond-slip were not occurred, and great energy dissipation was developed.

As aforementioned, the joint behavior including energy dissipation capacity, deformation capacity, failure mode, and stiffness is dependent on re-bar development performance  $h_c/d_b$  in RC beam-column connection. To secure the safety for earthquake on building structures, large re-bar diameter ratio  $h_c/d_b$  is required. To increase the ratio  $h_c/d_b$ , column depth  $h_c$  should be increased or beam re-bar diameter  $d_b$  should be decreased. Particularly, in low rise building structures, large column restricts architecture design and reduces the economics. On the other hand, small beam re-bar diameter increases the re-bar amount, and drops the constructability.

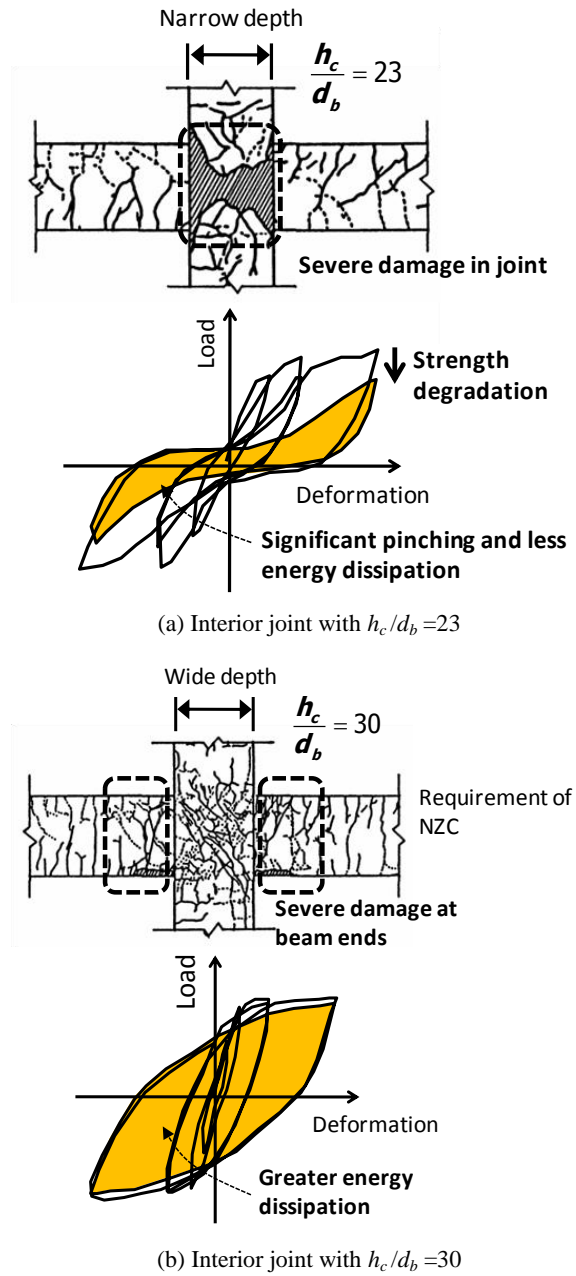


Fig. 1-3. Hysteretic response of RC beam-column joint according to  $h_c/d_b$

Recently, as a post earthquake design code, performance based earthquake design has been discussed. In performance based earthquake design, structural performance of building and beam-column connection should satisfy the performance level, such as immediate occupancy, life safety, and collapse prevention, determined from external environment and natural property of each building structure. Considering the earthquake design cost and uncertainty of earthquake, from the performance based design concept, beam-column joints in all of building structures need not to satisfy the earthquake resisting performance. For unimportant building structures with low performance requirement, it is rational to apply little low earthquake performance but economical to the joint. To implement the performance based earthquake design, earthquake response of building structures including strength, deformation capacity, energy dissipation, and stiffness depending on joint details should be accurately evaluated.

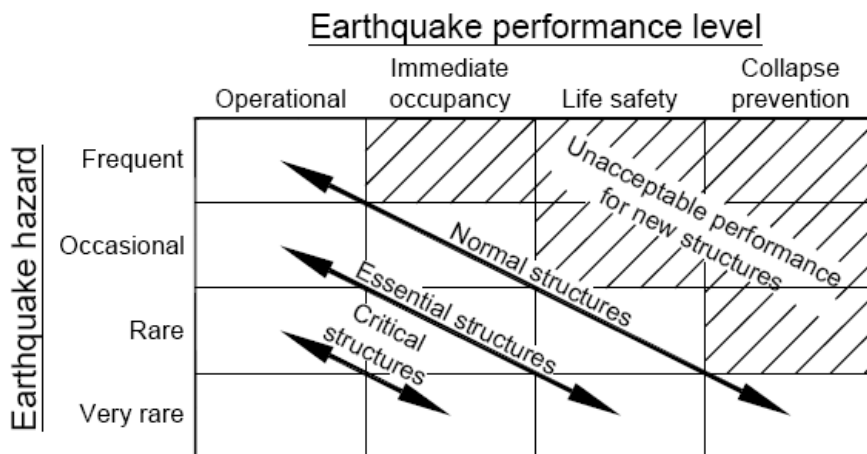


Fig. 1-4. Relationship between earthquake hazard and earthquake performance level for performance based earthquake design



Under cyclic loading, when yielding of the beam flexural bars penetrates into the joint panel and X-type diagonal cracking occurs in the joint panel, significant bond slip and shear strength degradation occur in the joint. It makes difficult to predict the accurate structural performance of beam-column connections. Particularly, when high-strength re-bars are used to save cost and to enhance constructability by reducing the number of re-bars, the critical issue that should be addressed in the design is the increase of the splice length and anchorage length. As a result, the use of high strength re-bars may significantly degrade the structural performance of beam-column connections by increasing bond-slip in the joint. To improve the structural performance and the economics of earthquake resisting beam-column connections, structural performance of the beam-column connections using high strength re-bars should be verified.

To mitigate the bond-slip of a re-bar and prevent joint shear failure, current earthquake design codes (ACI 318-11, 2011; ACI 352R-02, 2002; NZS 3101:2006, 2006; Eurocode 8, 2004) specify the minimum requirement of bond resistance and joint shear strength. However, existing cyclic loading test of beam-column connections have shown that even when the minimum requirement was satisfied, joint is failed principally by strength degradation due to increasing deformation at the joint (Lee et al., 2009; Priestley, 2000; Hwang et al., 2013). Particularly, when the column depth  $h_c$  is short, premature failure can be occurred in the joint by the significant bond-slip of the beam flexural bars. Furthermore, because the design requirements were empirically developed on the basis of the beam-column joint tests, it is very

difficult to accurately evaluate the bar bond-slip and joint shear strength. For performance based earthquake design, however, the bar bond-slip and joint shear strength need to be determined from joint ductility demand.

Until a recent date, a lot of researches have been studied for shear strength and deformation capacity of beam-column connections on the basis of failure mechanism of a joint panel (Lee et al., 2009; Lee and Lin, 2011; Hong et al., 2011; FEMA 356, 2000; Hwang and Lee, 2000; Murakami et al., 2000; Park et al., 2012). However, various failure mechanisms including gap at the joint interface due to bond-slip of beam flexural bars and flexural failure of beam cross-section due to increasing anchorage strength of re-bars as well as joint shear failure affects to the shear strength and deformation capacity of the beam-column connections. Thus, the bond-slip of beam flexural bars should be considered to determine load-carrying capacity and deformation capacity of beam-column connection.

In current earthquake design codes, design earthquake load is decreased using response modification factors defined by deformation capacity. According to Kitayama et al. (1987), Leon (1989), Hakuto et al. (1999), Song and Pincheira (2000), Sucuoğlu and Erberik (2004), Ibarra et al. (2005), FEMA 440 (2005), and Brooke et al. (2006), however, the earthquake response of the structures is significantly affected by the inelastic hysteretic response and energy dissipation of beam-column connection as well as the deformation capacity.

In order to address the effects of the inelastic hysteretic response including the bond-slip and joint shear deformation in the earthquake response of the structures, various elaborate component models have been developed (Lowes and Altoontash, 2003; Elmorsi et al., 2000; Fleury et al., 2000; Altoontash and Deierlein, 2003; Mitra and Lowes, 2007; Uma and Prasad, 2004). Although addressing all components affecting the connection behavior, these models require great time and effort in modeling and computations, particularly when numerical analysis of the entire moment frame structures is required. More importantly, in actual design of new structures without test results, it is not feasible to accurately define the unloading/reloading stiffness considering the complicated joint behavior such as the bar bond-slip and diagonal shear cracking. Therefore, the joint hysteretic behavior such as bond-slip, deformation capacity, and energy dissipation capacity which can be conveniently used for practical design/analysis of reinforced concrete moment frames need to be developed. Furthermore, to predict earthquake response of building structures accurately for performance based earthquake design, nonlinear time history analysis of the structures depending on the joint cyclic behaviors should be performed.

When the beam-column connection does not satisfy the earthquake requirement due to architectural design, the structural performance of the beam-column connection can be improved by using strengthening methods. Existing test results showed that the strengthening methods efficiently enhanced the bond-resistance and shear strength in the beam-column joints (Galunic et al., 1977; Park and Milburn, 1983; Adbel-Fattah and Wight, 1987;

Joh et al., 1991; Fenwick and Irvine, 1997; Yamamoto et al., 2008). Even with an identical strengthening method, the performance of beam-column connections significantly varies according to the design parameters. Thus, the effects of the design parameters on the performance need to be quantified in order to apply the strengthening method to the performance-based design of beam-column connections.

Fig. 1-5 shows the composition of performance based earthquake design. For performance based earthquake design, earthquake response of moment frame structures depending on beam-column joint behavior and earthquake resisting capacity of beam-column joint should be accurately estimated. In current earthquake design codes, however, the requirements of bar bond-slip and joint shear strength that influences on the joint behavior are defined as constant values, and the earthquake response of building structures is not affected by beam-column joint behavior. In this dissertation, bar bond-slip requirement and joint shear strength were proposed on the basis of deformation capacity of beam-column connection. Furthermore, prediction method for earthquake response of moment frame structures with various beam-column joint behaviors was proposed by using energy based joint hysteresis model. As a result, earthquake performance of moment frame structure can be accurately estimated. Finally, to improve the structural performance of beam-column connections, the enhancement methods using strengthening bars were proposed.

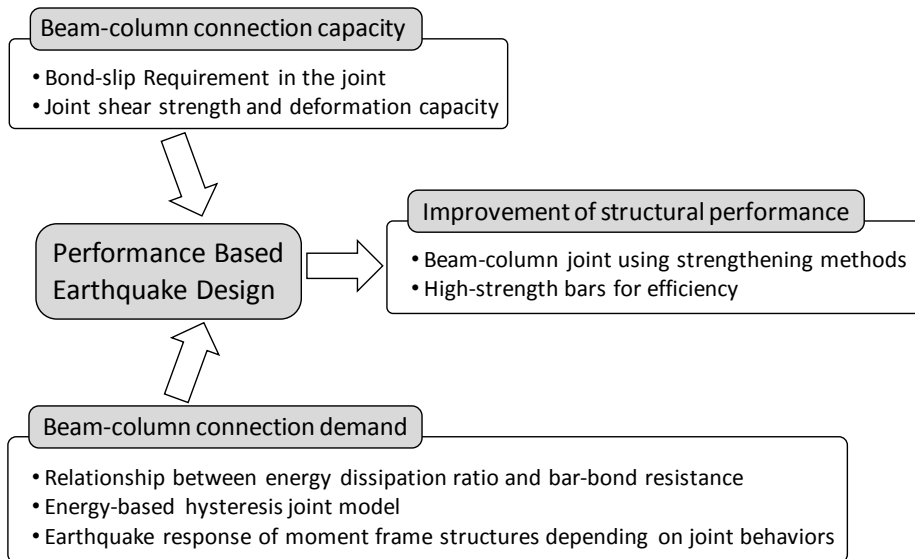


Fig. 1-5. Composition of performance based earthquake design

## 1.2 Scope and Objectives

The primary objective of this dissertation is to study the evaluation of earthquake response of reinforce concrete moment frame structure for performance based earthquake design. To achieve this objective, cyclic tests for beam-column connections were performed, and various analysis/design models were developed. First, to investigate the validity of high strength re-bars on the structural performance under earthquake loading, interior and exterior beam-column connections with Grade 600 MPa bars were tested. On the basis of the test results and existing test results, energy dissipation capacity of beam-column connections was estimated considering the design parameters. Then, the energy-based hysteresis model was defined using the predicted energy dissipation. To evaluate the seismic response of moment frame structure, nonlinear dynamic analysis was performed using the developed energy-based hysteresis model. From the nonlinear dynamic analysis, earthquake performance demand of building structures according to cyclic behavior of beam-column connection can be estimated.

Another objective of this dissertation is to predict the structure performance of reinforce concrete beam-column connections. To achieve this objective, joint deformation based shear strength evaluation model was developed. Because the joint shear strength and deformation are significantly affected by bond-slip of beam flexural bars, simplified bond model was also developed to predict the re-bar bond-slip in beam-column joint subjected to

cyclic loading. As a result, earthquake performance capacity of building structures can be estimated. Considering the earthquake performance demand and capacity, building structures can be designed to satisfy the earthquake performance level.

A final objective of this dissertation was to propose design recommendations for the bar bond- and joint shear-design of beam-column connections with the strengthening methods, which is used to enhance the bond resistance and shear strength at the joint. To achieve this objective, cyclic loading tests for beam-column connections intentionally designed with small  $h_c/d_b$  ratios less than 20 were performed to examine the effects and details of the strengthening methods.

### 1.3 Outline of Dissertation

In Chapter 2, an experimental study was performed to evaluate the seismic performance of interior and exterior beam-column connections using grade 600 MPa bars for beam flexural reinforcement. The bond-slip and shear strength requirement specified on the current earthquake design code was verified for beam-column connections using grade 600 MPa bars. The structural performance of the specimens including load-carrying capacity, maximum deformation, and hysteretic energy dissipation were evaluated and compared with the requirements of ACI 374.1-05.

In Chapter 3, a bond-slip model was developed to evaluate the relationship between bond-slip and bond-strength of beam re-bars in beam-column joints. The proposed model estimated the bond-slip relationship using simplified bond strength and bar strain distribution in the beam-column joint. The prediction of the proposed model was compared with existing test results of concrete block specimens for bond-slip and beam-column connection specimens. On the basis of the proposed model, bond-slip requirement of interior beam-column connection was evaluated, and compared with the requirement specified on the current earthquake design codes.

In Chapter 4, a joint shear strength model addressing the effect of bond-slip of beam re-bars was developed to evaluate the load-deformation relationship of beam-column connections. Bar bond-slip model was



considered to estimate the joint shear deformation and joint shear capacity. The proposed model consists of truss mechanism due to bar bond-strength and diagonal strut mechanism due to bearing force. The predictions of joint shear capacity and deformation capacity were compared with existing test results of 64 interior beam-column connections.

In Chapter 5, using existing test results of 69 interior and 63 exterior connections subjected to cyclic loading, the variation of energy dissipation (per load cycle) according to the bar bond-slip parameters, re-bar ratio, and joint shear strength was statistically investigated. On the basis of the result, the energy dissipation of beam-column connections was defined as the function of the bond parameters.

In Chapter 6, by using the energy function and the existing backbone curve of FEMA 356, an energy-based hysteresis model was developed. The proposed model consists of elastic beam-column elements and plastic rotational spring elements, which describe the energy dissipation capacity of the joint and the plastic deformation of the beam and the joint. As the plastic rotational spring elements, Pinching 4 model of OpenSees was modified such that the area enclosed by the cyclic curve is the same as the predicted energy dissipation. The proposed model was applied to existing test specimens, and the results were compared with the test results.

In Chapter 7, for low-rise moment-resisting frame structures, nonlinear time history analysis was performed by using energy-based hysteresis model

and OpenSees program. Various energy-based models were applied to beam-column connections and columns. El-Centro earthquake acceleration was applied for dynamic analysis. Earthquake responses of the structure were evaluated according to energy dissipation capacity and natural period of the structure.

In Chapter 8, to improve the structural performance of beam-column connections with insufficient bond resistance, strengthening method that relocated the plastic hinge zone from the joint interface towards the beams was proposed. Cyclic load tests were performed for beam-column connections strengthened with  $45^\circ$  bent bars and  $90^\circ$  hooked bars. On the basis of existing test results, recommendations were given for the seismic design and detailing of beam-column joints with strengthening bars.

Finally, summary and conclusions were presented in Chapter 9.

## **Chapter 2. Behavior of Beam-Column Connections Using Grade 600 MPa Bars**

### **2.1 Introduction**

Recently, the use of high strength reinforcing bars (re-bars) has increased to save cost and to enhance constructability by reducing the number of re-bars. However, current design codes limit the maximum yield strength of re-bars. ACI 318-11 (2011) specifies 550 MPa for the maximum yield strength of flexural re-bars. The special seismic provisions in ACI 318-11 (2011) limit the yield strength to 420 MPa for special moment frames. On the other hand, ACI-ASCE 352R-02 (2002) does not specifically limit the yield strength of re-bars. Eurocode 2 (2004) allows the use of grade 600 MPa bars. NZS 3101:2006 (2006) limits the yield strength to 500 MPa.

When high-strength re-bars are used, the critical issue that should be addressed in the design is the increase of the splice length and anchorage length. Particularly in beam-column connections under earthquake loading, bond-slip increases at the joint, which decreases the hysteretic energy dissipation and shear strength of the connections. To prevent excessive bond-slip, current design codes limit the column depth to beam re-bar diameter ratio ( $h_c/d_b$ ).

$$\frac{h_c}{d_b} \geq 20 \quad \text{in Chapter 21, ACI 318-11} \quad (2-1a)$$

$$\frac{h_c}{d_b} \geq 20 \frac{f_y}{420} \quad \text{in ACI 352R-02 (MPa)} \quad (2-1b)$$

$$\frac{h_c}{d_b} \geq \frac{\alpha_0 f_y}{3.3 \alpha_f \sqrt{f'_c}} \quad \text{in NZS 3101:1995 (MPa)} \quad (2-1c)$$

$$\frac{h_c}{d_b} \geq \frac{1.25 f_y}{3.3 \alpha_f \alpha_d \gamma \sqrt{f'_c}} \quad \text{in NZS 3101:2006 (MPa)} \quad (2-1d)$$

where  $\alpha_0$  is the coefficient related to the location of the plastic hinge of beams (= 1.0 - 1.25);  $\alpha_f$  is the coefficient related to the direction of the beam re-bars; (= 0.85 - 1.0);  $\alpha_{fd}$  is the coefficient related to the ductility of the plastic hinge of beams (= 1.0 - 1.2);  $\gamma$  is the coefficient related to inter-storey drift when the yield strength of beam re-bars is greater than 300 MPa ( $\gamma = 1.53 - 0.29\delta_c \leq 1.0$ ); and  $\delta_c$  is the inter-storey drift ratio expressed as a percentage.

Megget et al. (2003) tested four two-thirds scale cruciform beam-column connections with Grade 500 MPa bars (actual yield strength = 588 MPa). The specimens were designed with  $h_c/d_b = 32.5$ , according to the previous New Zealand design provisions (NZS 3101:1995, 1995). The test result showed that significant bond-slip occurred in the beam-column joint even with the relatively large  $h_c/d_b$  ratio. On the basis of the test results, the coefficient  $\gamma$

was introduced in NZS for the limitation of  $h_c/d_b$ . Brooke et al. (2006) performed four two-thirds scale cruciform beam-column connections with Grade 500 bars. The  $h_c/d_b$  ratios ranged from 27 to 32. Although the  $h_c/d_b$  ratio was 13 - 24 percent less than the requirement of NZS 3101:1995 (1995), the specimens showed good performance. On the basis of the result, Brooke reported that the revised provision of NZS 3101:1995 (1995) is excessively conservative. Sugano et al. (1991) tested eight half scale cruciform beam-column connections with re-bar yield strength of 392 - 588 MPa and concrete strength of 39 - 78 MPa. The  $h_c/d_b$  ratio was 20. On the basis of the test results, they proposed that to prevent bond-slip of re-bars in the joint,  $h_c/d_b$  ratios be greater than  $f_y/11\sqrt{f'_c}$ . Xian et al. (1992) tested six two-third scale cruciform beam-column connections with re-bar yield strength of 445 - 492 MPa and concrete strength of 31 - 61 MPa. The  $h_c/d_b$  ratios ranged from 16 - 38. They reported that excessive bond-slip of high strength re-bars was prevented by the use of high strength concrete.

As such, the majority of previous studies have been performed for interior beam-column connections with re-bar yield strengths of Grade 500 or less (actual yield strength = 588 MPa or less). Thus, to use higher strength bars such as Grade 550 and 600 bars for seismic design, relevant experimental evidences are required. Furthermore, as presented in Eq. (2-1), the  $h_c/d_b$  requirements of ACI 318-11 (2011) and ACI 352R-02 (2002) are significantly less than that of the New Zealand code (1995, 2006) (see Eq. (2-1)). For example, when  $f'_c = 30$  MPa and  $f_y = 600$  MPa, ACI 318-11 (2011) and ACI 352R-02 (2002) require  $h_c/d_b = 20$  and 29, respectively, assuming that the

ACI provisions are applicable to 600 MPa bars. On the other hand, NZS 3101:1995 (1995) and NZS 3101:2006 (2006) require greater values of  $h_c/d_b = 41$  and  $44$ , assuming  $\alpha_o = 1.25$ ,  $\alpha_f = 1.0$ ,  $\alpha_d = 1.0$ , and  $\gamma = 0.95$ . The difference in the code requirements increases as the re-bar yield strength increases. Thus, when high strength bars are used, the applicability of the current design codes should be verified on the basis of the relevant test results.

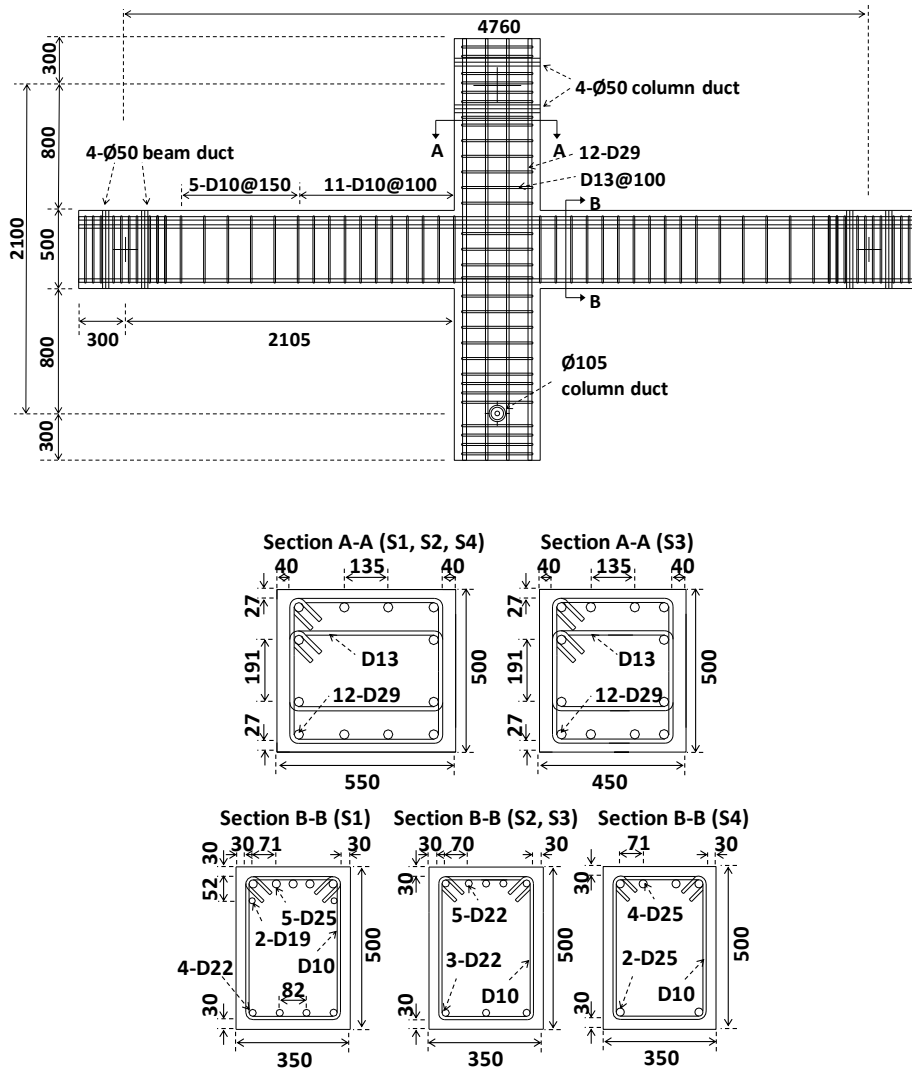
In the present study, beam-column connections with Grade 600 MPa bars were tested to investigate the effects of high strength re-bars on the structural performance under earthquake loading. For this purpose, the following studies were performed.

- 1) According to ACI 318-11 (2011), the beams of the test specimens were designed with Grade 400 MPa or 600 MPa bars.
- 2) Four full-scale cruciform connections (interior connections,  $h_c/d_b = 20 - 25$ ) and three full-scale T-shaped connections (exterior connections,  $l_{dh}/d_b = 19.6 - 22.6$ ) were tested under cyclic loading.
- 3) The structural performance of the specimens (load-carrying capacity, maximum deformation, and hysteretic energy dissipation) were evaluated and compared with the requirements of ACI 374.1-05 (2005).

## 2.2 Test Plan

Four cruciform specimens, S1, S2, S3, and S4, and three T-shaped specimens, S5, S6, and S7 were prepared for testing (Table 2-1 and Fig. 2-1). The specimens were designed according to the requirements of strong column-weak beam concept in ACI 318-11 (2011) (see (4) in Table 2-2).

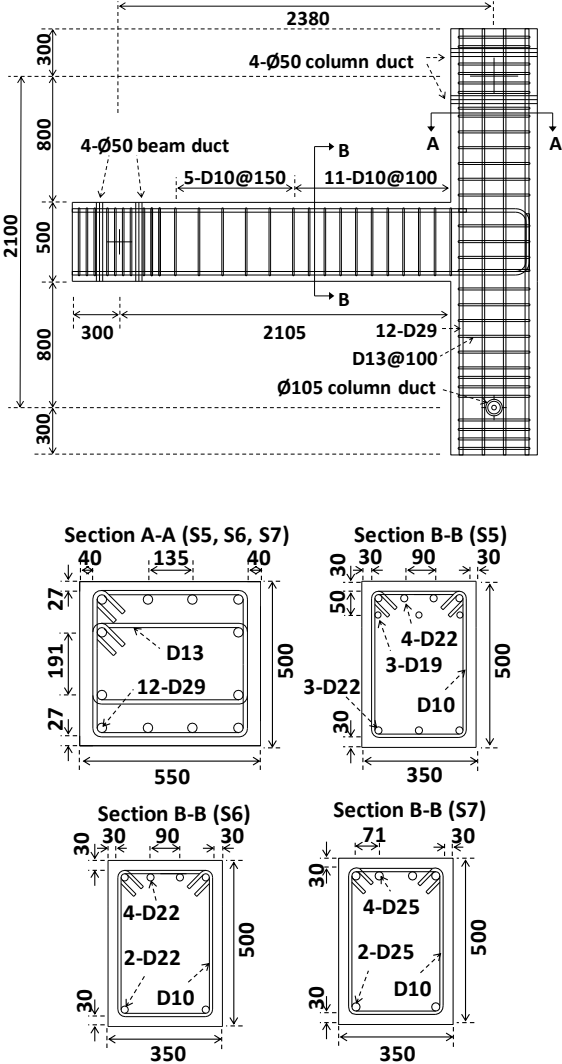
The properties of the specimens are listed in Tables 2-1 and 2-2. The compressive strength of the concrete was 29.6 - 32.0 MPa. The Grade 400 bars (specified yield strength = 400 MPa) and Grade 600 (specified yield strength = 600 MPa) bars are specified in the Korean Industrial Standard (KS B 0802, 2008). The reinforcing bars were tested under uniaxial tension. The actual yield strengths of Grade 400 bars were 446 MPa (D13, deformed bar, nominal diameter = 13mm), 440 MPa (D19), 520 MPa (D22), 465 MPa (D25), and 510 MPa (D29). The actual yield strengths of Grade 600 bars were 710 MPa (D22) and 635 MPa (D25). The yield strengths of re-bars are the average values of three re-bar test results. The ratios of the ultimate strength to yield strength of Grade 400 bars were  $f_u/f_y = 1.39$  for D13, 1.46 for D19, 1.17 for D22, 1.32 for D25, and 1.22 for D29. The  $f_u/f_y$  ratio of Grade 600 bars were 1.26 for D22 and 1.30 for D25 (see Fig. 2-2).



(a) Interior specimens (S1, S2, S3, S4)

Fig. 2-1. Details of test specimens (unit: mm) (Continued)





(b) Exterior specimens (S5, S6, S7)

Fig. 2-1. Details of test specimens (unit: mm)

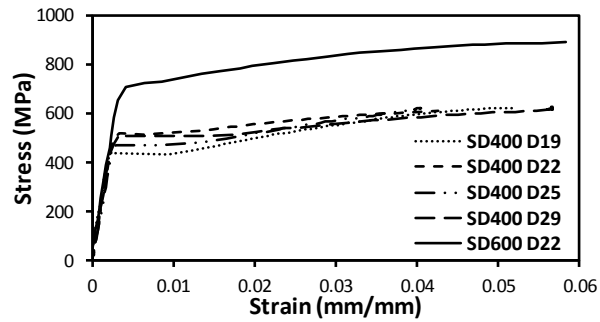


Fig. 2-2. Stress-strain relationships of re-bar

The primary test parameters for the cruciform specimens were the yield strengths of the beam longitudinal bars (Grade 400 bars in S1 and Grade 600 bars in S2, S3, and S4), diameter of Grade 600 bars (D22 in S2 and D25 in S4), and joint shear strength (S2:  $V_n/V_u = 1.05$ , S3:  $V_n/V_u = 0.86$ , and S4:  $V_n/V_u = 1.02$ ). The test parameters for the exterior connections were the yield strength of the beam longitudinal re-bars (Grade 400 bars in S5 and Grade 600 bars in S6 and S7) and the diameter of Grade 600 bars (D22 in S6 and D25 in S7).

Table 2-1. Summary of test program

Specimens	Cruciform				T-shape		
	S1	S2	S3	S4	S5	S6	S7
(1) Dimensions ( $b \times h$ ) (mm $\times$ mm)				350 $\times$ 500			
(2) Concrete strength (MPa)	32.0	32.0	32.0	29.6	32.0	32.0	29.6
(3) Top re-bars ( $\rho^1$ , %)	5-D25 + 2-D19 (1.98)	5-D22 (1.23)	5-D22 (1.23)	4-D25 (1.30)	4-D22 + 3-D19 (1.53)	4-D22 (0.99)	4-D25 (1.30)
(4) Bottom re-bars (%)	4-D22 (0.99)	3-D22 (0.74)	3-D22 (0.74)	2-D25 (0.65)	3-D22 (0.74)	2-D22 (0.50)	2-D25 (0.65)
Beam (5) Type of re-bar grade <sup>2)</sup>	Grade 400	Grade 600	Grade 600	Grade 600	Grade 400	Grade 600	Grade 600
(6) Stirrup (Type of re-bars)	D10 (Grade 400)						
(7) Nominal positive moment capacity <sup>3)</sup> $M_n^+$ (kN·m)	327.5	334.5	334.5	265.7	252.0	230.9	265.7
(8) Nominal negative moment capacity <sup>3)</sup> $M_n^-$ (kN·m)	533.3	517.8	517.8	483.8	438.1	430.1	483.8
(9) Dimensions ( $b \times h$ ) (mm $\times$ mm)	500 $\times$ 550	500 $\times$ 550	500 $\times$ 450	500 $\times$ 550	500 $\times$ 550	500 $\times$ 550	500 $\times$ 550
(10) Concrete strength (MPa)	32.0	32.0	32.0	29.6	32.0	32.0	29.6
(11) Re-bar ratio ( $\rho^1$ , %)	2.23	2.23	2.72	2.23	2.23	2.23	2.23
Column (12) Type of reinforcement <sup>2)</sup>	Grade 400						
(13) Tie (Type of re-bars)	D13 (Grade 400)						
(14) Nominal flexural moment capacity <sup>3)</sup> (kN·m)	717.9	717.9	520.5	706.3	717.9	717.9	706.3

<sup>1)</sup>  $\rho = A_s/bd$  for beam,  $\rho = A_s/bh$  for column

<sup>2)</sup> Yield strength: (Grade 400 D13 -  $f_y = 446$  MPa), (Grade 400 D19 -  $f_y = 440$  MPa), (Grade 400 D22 -  $f_y = 520$  MPa), (Grade 400 D25 -  $f_y = 465$  MPa), (Grade 400 D29 -  $f_y = 510$  MPa), (Grade 600 D22 -  $f_y = 710$  MPa), (Grade 600 D25 -  $f_y = 635$  MPa)

<sup>3)</sup> Capacity of cross-section based on the results of material tests

Table 2-2. Design of beam-column joints

Specimens	Cruciform					T-shape	
	S1	S2	S3	S4	S5	S6	S7
(1) Development length – Design (mm) ( $h_c/d_b$ )	550 (22.0)	550 (25.0)	450 (20.5)	550 (22.0)	497	497	497
(2) Development length required – ACI 318 (mm)	500 <sup>1)</sup>	440 <sup>1)</sup>	440 <sup>1)</sup>	500 <sup>1)</sup>	288 <sup>3)</sup> 389 <sup>4)</sup>	432 <sup>3)</sup> 583 <sup>4)</sup>	511 <sup>3)</sup> 689 <sup>4)</sup>
(3) Development length required – ACI 352 (mm)	476 <sup>2)</sup>	629 <sup>2)</sup>	629 <sup>2)</sup>	714 <sup>2)</sup>	314 <sup>5)</sup>	470 <sup>5)</sup>	556 <sup>5)</sup>
(4) Ratio of column moment capacity to beam moment capacity ( $\lambda$ )	1.67	1.68	1.22	1.88	3.28	3.34	2.92
(5) Ratio of joint shear capacity to shear demand	$\frac{1937\text{kN}}{1860\text{kN}}$ =1.04	$\frac{1937\text{kN}}{1842\text{kN}}$ =1.05	$\frac{1585\text{kN}}{1853\text{kN}}$ =0.86	$\frac{1863\text{kN}}{1832\text{kN}}$ =1.02	$\frac{1549\text{kN}}{999\text{kN}}$ =1.60	$\frac{1549\text{kN}}{919\text{kN}}$ =1.69	$\frac{1490\text{kN}}{1233\text{kN}}$ =1.21

<sup>1)</sup>  $h_c = 20d_b = 20 \times 25 = 500$  for S1 and S4,  $h_c = 20 \times 22 = 440$  for S2 and S3

<sup>2)</sup>  $h_c = 20d_b (f_y/420) = 20 \times 25 \times (400/420) = 476$  for S1,  $h_c = 20 \times 22 \times (600/420) = 629$  for S2 and S3,  $h_c = 20 \times 25 \times (600/420) = 714$  for S4

<sup>3)</sup>  $l_{dh} = f_y d_b / (5.4 \sqrt{f'_c}) = 400 \times 22 / (5.4 \sqrt{32}) = 288$  for S5,  $l_{dh} = 600 \times 22 / (5.4 \sqrt{32}) = 432$  for S6,  $l_{dh} = 600 \times 25 / (5.4 \sqrt{29.6}) = 511$  for S7

<sup>4)</sup>  $l_{db} = f_y d_b / (4 \sqrt{f'_c}) = 400 \times 22 / (4 \sqrt{32}) = 389$  for S5,  $l_{db} = 600 \times 22 / (4 \sqrt{32}) = 583$  for S6,  $l_{db} = 600 \times 25 / (4 \sqrt{29.6}) = 689$  for S7

<sup>5)</sup>  $l_{dh} = \alpha f_y d_b / (6.2 \sqrt{f'_c}) = 1.25 \times 400 \times 22 / (6.2 \sqrt{32}) = 314$  for S5,  $l_{dh} = 1.25 \times 600 \times 22 / (6.2 \sqrt{32}) = 470$  for S6,  $l_{dh} = 1.25 \times 600 \times 25 / (6.2 \sqrt{29.6}) = 556$  for S7

In specimen S1 (Grade 400 re-bar), the re-bar ratios at the top and bottom of the beam section were determined as 1.98% and 0.99%, respectively, considering the range of re-bar ratios that are generally used in actual design of RC beams. In specimens S2 and S3 with Grade 600 bars (D22), the top and bottom re-bar ratios decreased to 1.23% and 0.74%, respectively. However, because of the higher yield strength, the load-carrying capacities of S2 and S3 were equivalent to that of S1 with Grade 400 bars (Table 2-1 (7), (8)). In specimen S4 with Grade 600 bars, the bar diameter was increased to D25, but the ratio of beam longitudinal bars (1.30% and 0.65%) was equivalent to that of S2 and S3. In the exterior connection S5 with Grade 400 bars, the top and bottom bar ratios were 1.53% and 0.74%, respectively. In S6 using Grade 600 bars (D22), the re-bar ratios decreased to 0.99% and 0.50%. In S7 using greater diameter bars (Grade 600, D25) the re-bar ratios were 1.30% and 0.65%.

In all specimens, to satisfy the requirement of strong column-weak beam, the flexural strength (longitudinal re-bar ratio = 2.2%) of the columns was greater than that of the beams. D10 (Grade 400) and D13 (Grade 400) bars were used for the stirrups and ties, respectively. The column depths of the interior specimens were 550 mm [21.7 in] for S1, S2, and S4 and 450 mm [17.7 in] for S3. The column depths of S2, S3, and S4 using Grade 600 bars satisfied the  $h_c/d_b$  requirement of ACI 318-11 (2011) in Eq. (2-1a), but did not satisfy the requirement of ACI 352R-02 (2002) in Eq. (2-1b) (see Table 2-2 (1) - (3)).

For the exterior connections S5, S6, and S7, 90° standard hook bars were used. ACI 318-11 (2011) and ACI 352R-02 (2002) specifies the development length  $l_{dh}$  of a 90° hook bar as follows.

$$l_{dh} \geq f_y d_b / 5.4 \sqrt{f_c'} \quad \text{in ACI 318-11 (MPa)} \quad (2-2a)$$

$$l_{dh} \geq \alpha f_y d_b / 6.2 \sqrt{f_c'} \quad \text{in ACI 352R-02 (MPa)} \quad (2-2b)$$

where  $\alpha = 1.25$ . In the exterior specimens S5 and S6, the development length of the hook bars was 497 mm, which satisfied both Eqs. (2-2a) and (2-2b) (see Table 2-2 (1) - (3)). On the other hand, in the exterior specimen S7 using a greater bar diameter (D25), the development length of the hook bars (497 mm) did not satisfy Eqs. (2-2a) and (2-2b) (see Table 2-2 (1) - (3)).

In exterior connections under reversed cyclic loading, beam re-bars are subjected to compressive yield force as well as tension yield force, because of the presence of the plastic tensile strain of the beam longitudinal bars. Thus, theoretically, compressive development length is required for the beam longitudinal bars. Since the 90° hook is not valid for the compression development length, the straight bar length of the hook bar should satisfy the following requirement of ACI 318-11 (2011).

$$l_{db} \geq \frac{f_y d_b}{4 \sqrt{f_c'}} \quad \text{in ACI 318-11 (MPa)} \quad (2-3)$$

The required compressive development lengths  $l_{db}$  of the beam bottom bars were 389 mm for S5 (Grade 400 D22 bars), 583 mm for S6 (Grade 600 D22 bars), and 689 mm for S7 (Grade 600 D25 bars). In the specimens, the actual development length was 497 mm. Thus, specimens S6 and S7 did not satisfy the requirement of ACI 318-11 (2011).

It should be noted that from Eqs. (2-2a) and (2-3), the compression development length is always greater than the tension development length of 90° hook bar. Thus, if the compression development length should be satisfied for the seismic design of exterior connections, the requirement of the development length of 90° hook bar in Eq. (2-2a) is inadequate. Further, to satisfy the requirement of the compression development length, the dimension of the column section should be at least 650mm for S6 (Grade 600 D22 bars), and 750 mm for S7 (Grade 600 D25 bars), which may be too large to be used for low-rise buildings. For this reason, in the present study, we investigated whether the requirement of the compression development length should be satisfied for exterior connections with 600MPa bars.

In ACI 318-11 (2011), joint shear capacity  $V_n$  is defined as follows.

$$V_n = 1.25\sqrt{f'_c}A_j \quad \text{for joint confined on two opposite faces (MPa)} \quad (2-4a)$$

$$V_n = 1.0\sqrt{f'_c}A_j \quad \text{for unconfined joint (MPa)} \quad (2-4b)$$

where  $A_j$  is the effective area parallel to the beam longitudinal re-bar in the

joint. The joint shear capacities of the cruciform specimens (S1, S2, S3, and S4) and the T-shaped specimens (S5, S6, and S7) were calculated using Eqs. (2-4a) and (2-4b), respectively. The joint shear capacity  $V_n$  should be greater than the joint shear demand  $V_u$ .  $V_u$  is calculated as follows.

$$V_u = C_{b1} + T_{b2} - V_c \quad (2-5)$$

where  $C_{b1} = A_{s1} \alpha f_y$ ;  $T_{b2} = A_{s2} \alpha f_y$ ; and  $V_c$  is the shear force applied to the column, which is the same as the lateral load  $P_n$  (Fig. 2-3). In the specimens designed according to the concept of strong column-weak beam, the lateral load-carrying capacity  $P_n (= V_c)$  can be calculated assuming yielding of the beam longitudinal re-bars at the joint. In Fig. 2-3, the load-carrying capacity of the specimen is calculated from the force-equilibrium, as follows.

$$P_n = \frac{(V_{bp} + V_{bn})l}{2h} = \frac{(M_{bp} + M_{bn})l}{h(l - h_c)} \quad (2-6)$$

where  $V_{bp}$  and  $M_{bp}$  are the shear force and moment developed by yielding of the beam bottom bars;  $V_{bn}$  and  $M_{bn}$  are the shear force and moment developed by yielding of the beam top bars;  $l$  is the beam length between the vertical supports;  $h$  is the net column height; and  $h_c$  is the column depth.



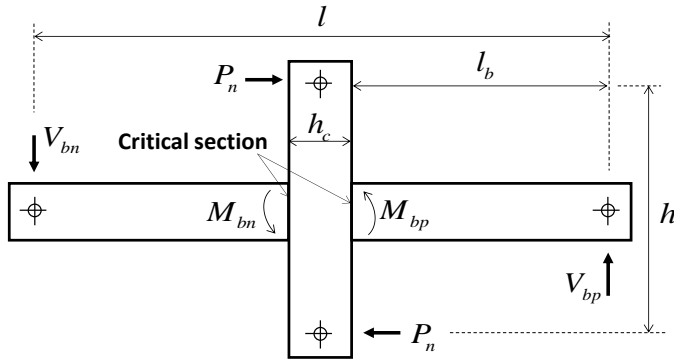
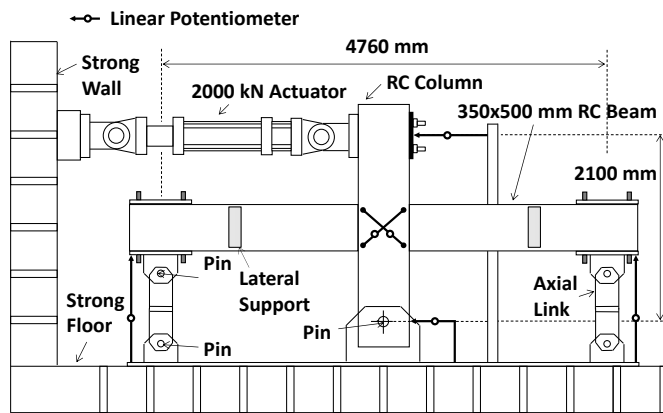


Fig. 2-3. Calculation of load-carrying capacity of beam-column joints

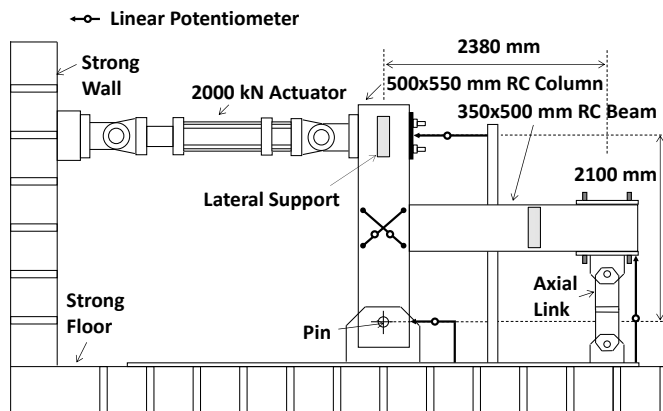
Table 2-2 (5) presents the ratios of the joint shear capacity to joint shear demand for the specimens: 1.04, 1.05, 0.86, 1.02, 1.60, 1.69, and 1.21, for S1 - S7. Thus, all the specimens except S3 satisfied the requirement of joint shear force. S3 was tested to verify the accuracy of Eq. (2-4) by comparing the test results of S2 and S3. As shown in Fig. 2-1(a), four layers of 4-D13 tie bars were placed in the joint. Thus, the area of a layer of 4-D13 was  $516 \text{ mm}^2$ , which is greater than the requirement of ACI 318-11 (2011) ( $420 \text{ mm}^2$  at 100mm spacing for S1, S2, S5, and S6;  $481 \text{ mm}^2$  at 100mm spacing for S3;  $388 \text{ mm}^2$  at 100mm spacing for S4 and S7). Thus, the requirement of tie bars was satisfied.

Fig. 2-4 shows the test set-up. In the cruciform specimen, the beam ends were vertically supported allowing lateral movement. The beam length between the vertical supports was 4760 mm. The column height from the bottom hinge to the lateral loading point was 2100 mm. A cyclic lateral load was applied to the top of the column. The cyclic loading was planned by

modifying the specification of ACI 374.1-05 (2005). At 0.25%, 0.5%, 0.75%, and 1.0% story drift ratio, three load cycles were applied. After the inter-story drift ratio exceeded 1.0%, three load cycles were applied at every 0.5% increase. No axial force was applied to the column. The story drift, joint shear deformation, and support movements were measured using the linear potentiometers.



(a) Interior specimens



(b) Exterior specimens

Fig. 2-4. Test setup

## 2.3 Test Results

### 2.3.1 Lateral Load-Story Drift Relationship

Fig. 2-5 shows the lateral load - story drift relationships of the specimens. The story drift indicates the net horizontal displacement at the loading point of the column, and the story drift ratio was calculated by dividing the net lateral story drift by the net column height (2,100 mm). The yield story drifts  $\delta_y^+$  and  $\delta_y^-$ , were defined as the lateral drift ratio of the equivalent elastic-plastic envelop curve defined by the secant stiffness at 75% of the maximum strength (see Fig. 2-5(h); Park, 1988). The secant stiffness was defined as the yield stiffness. The ultimate (or maximum) story drifts  $\delta_u^+$  and  $\delta_u^-$  are defined as the post-peak lateral drift corresponding to 75% of the maximum strength (see Fig. 2-5(h); ACI 374.1-05, 2005; Park, 1988). The theoretical lateral load-carrying capacities  $P_n^+$  and  $P_n^-$  were calculated by Eq. (2-6) using the ultimate flexural strengths of the beams determined from the ACI stress-block method (ACI 318-11, 2011).

In the cruciform specimens (Fig. 2-5(a) - (d)), the yield stiffnesses of S2 (14.1 kN/mm), S3 (11.5 kN/mm), and S4 (15.8 kN/mm) using Grade 600 bars were less than that of S1 (16.5 kN/mm) using Grade 400 bars because of the lower re-bar ratio of Grade 600 bars. For the same reason, the yield drift ratios of S2 (1.62 %), and S3 (1.94 %) using Grade 600 bars were greater than that of S1 (1.41%) using Grade 400 bars. In specimen S4, the yield drift ratio (1.22%) was less than that of S1, because of the lower yield strength of the

specimen. In all specimens, the maximum strengths occurred at about 2% story drift ratio. After the maximum strength, the load-carrying capacity gradually decreased. The maximum deformation corresponding to 0.75 times the peak strength exceeded 3.5% story drift ratio, regardless of the re-bar grade. Under cyclic loading, bond-slip of the beam longitudinal re-bars occurred at the joint, which decreased the unloading/reloading stiffness, showing pinching in the load-story drift relationship. Pinching was severe in S4 using greater diameter bars D25.

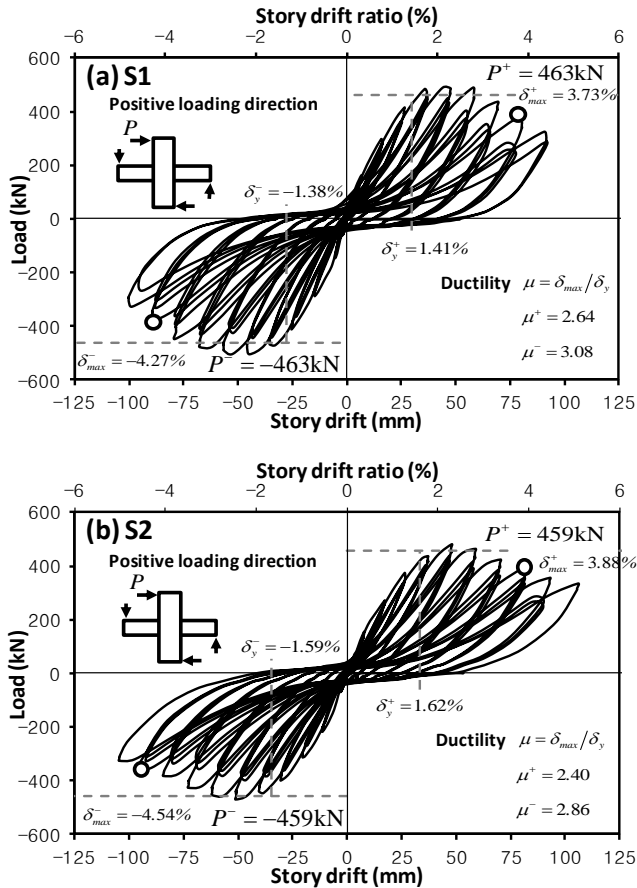


Fig. 2-5. Lateral load-story drift ratio relationships of specimens (Continued)

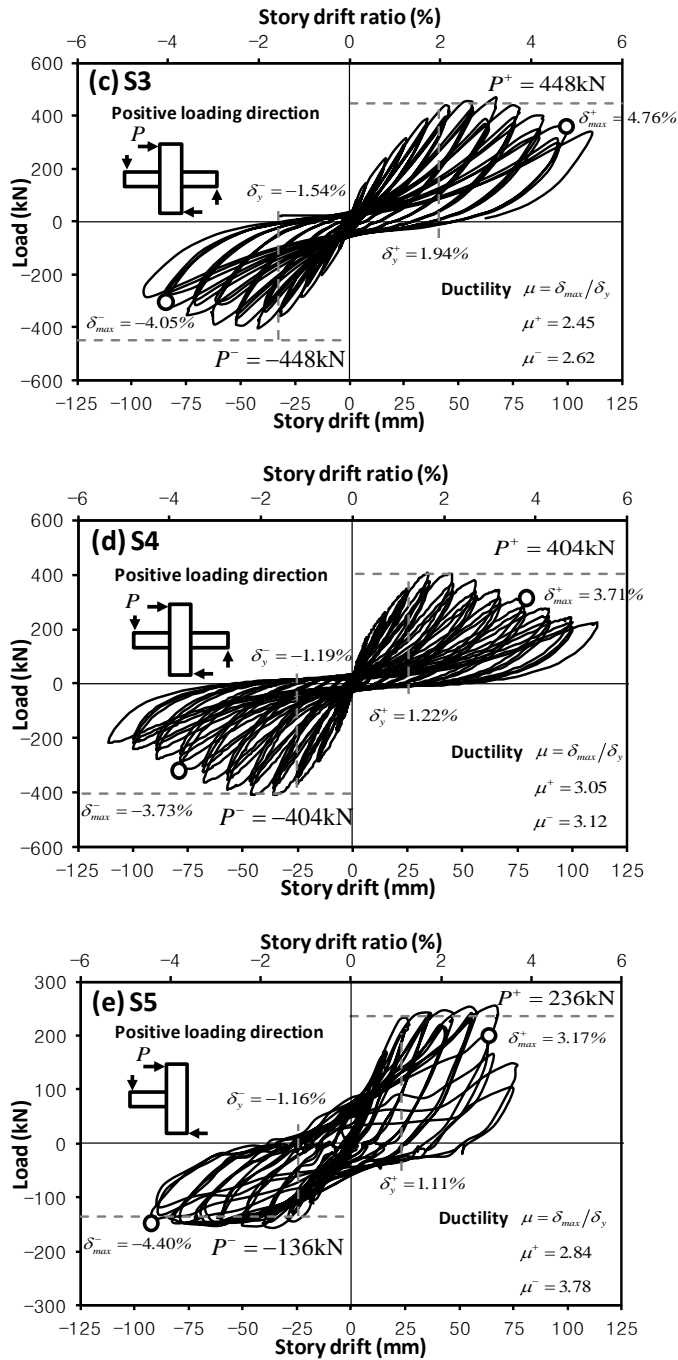


Fig. 2-5. Lateral load-story drift ratio relationships of specimens (Continued)

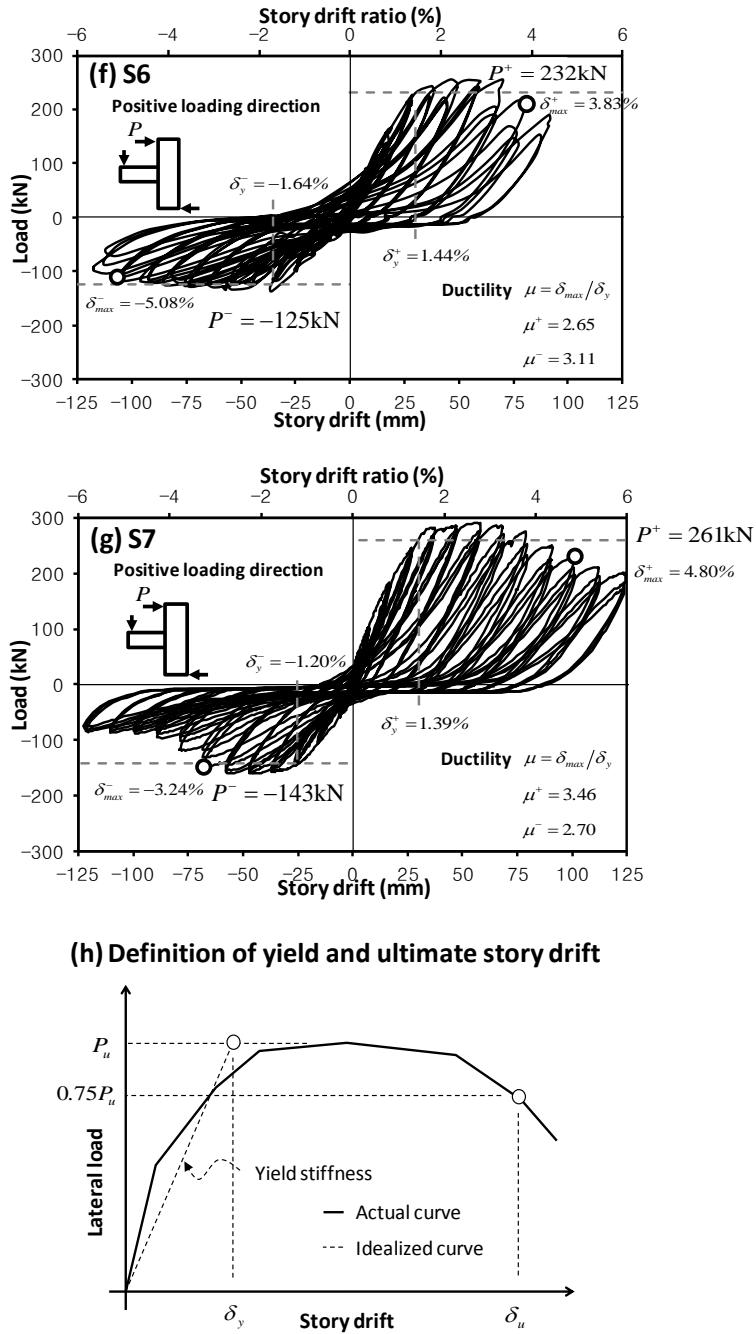


Fig. 2-5. Lateral load-story drift ratio relationships of specimens

In the T-shaped specimens shown S5 - S7 in Fig. 2-5(e) - (g), the load-carrying capacities under the positive loading were greater than those under the negative loading. This is because in the beam cross-section, the number of top bars was greater than that of bottom bars. The yield stiffnesses of S6 was 8.43 kN/mm and 3.95 kN/mm for the positive and negative loadings, respectively. The yield stiffness of S7 using Grade 600 bars was 10.0 kN/mm and 6.39 kN/mm. The yield stiffness of S5 using Grade 400 bars was 11.0 kN/mm and 6.36 kN/mm, which was greater than those of S6 and S7. The yield drift ratios of S6 (1.44% and -1.64%) and S7 (1.39% and -1.20%) using Grade 600 bars were greater than that of S5 (1.11% and -1.16%) using Grade 400 bars.

Under the positive loading (negative moment at the beam end), the maximum deformations of S6 and S7 with Grade 600 bars were 3.83% and 4.80% story drift ratios, respectively, which was greater than the 3.17% story drift ratio of S5 using Grade 400 bars. On the other hand, under the negative loading (positive moment at the beam end), the maximum deformation of S7 was -3.24% story drift ratio, which was less than the -4.40% story drift ratio of S5 because of significant bond-slip. This result indicates that under cyclic inelastic deformations, the tensile force of the beam bottom bars decreased due to significant bond-slip (The bond resistance was deteriorated in both tension and compression due to the insufficient development length), and on the other hand, the effect of bond-slip was limited in the beam top bars. Due to the effect of bond-slip, the unloading/reloading stiffness of specimen S7 was significantly degraded.

In the cruciform specimens S1, S2, and S4, the ratio of the load-carrying capacities to the predictions  $P_n^+$  and  $P_n^-$  (Eq. (2-6)) were 1.00 - 1.06, which indicates that the load-carrying capacity of the connections with Grade 600 bars was accurately predicted. However, in the case of S3 with insufficient joint shear capacity, the load-story drift ratio relationship was unsymmetrical, and the load-carrying capacity under the negative loading was 90% of the prediction  $P_n^-$ . The strength ratio was close to the ratio of the joint shear capacity to shear demand, 0.87 (see Table 2-2 (5)). In the T-shaped specimens S5, S6, and S7, the load-carrying capacities were 1.08 - 1.14 times the predictions, which indicates that the predictions agree with the test results.

### 2.3.2 Failure Modes

Fig. 2-6 shows the failure modes of the test specimens at the end of the test. In the cases of S1, S2, and S4, the damage mode was diagonal cracking at the joint - flexural yielding of beams - bond-slip of beam flexural bars. Ultimately, concrete crushing occurred at the interface between the beam end and the joint panel. Particularly, concrete crushing was concentrated at the bottom of the beam end. This is because at the bottom of the beam end, relatively large compressive stresses developed due to the force-equilibrium of greater area of the top bars in the beam cross-section. Furthermore, due to the bond-slip at the joint, the beam flexural bars at the opposite side of the joint were anchored to the beam end. The anchorage force aggravated the damage of the beam bottom end.



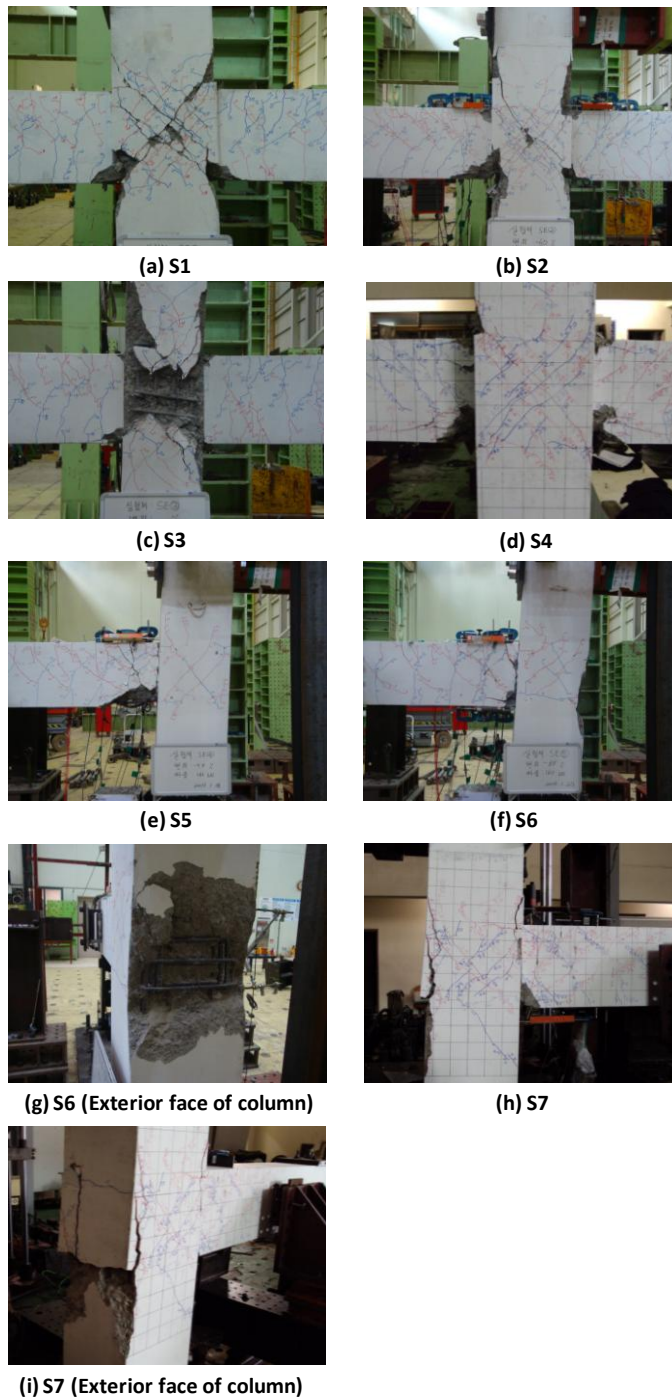


Fig. 2-6. Failure modes of test specimens at the end of test

In the case of S3, the damage mode was similar to that of the other cruciform specimens: diagonal cracking at the joint - flexural yielding of beams - bond-slip of beam flexural bars. However, since the joint shear capacity did not satisfy the requirement (Eqs. (2-4a) and (2-5)), ultimately the specimen failed due to joint shear after the concrete cover was completely delaminated.

In the case of the exterior connection S5 with grade 400 bars, diagonal cracking decreased due to the reduced joint shear force. Ultimately, similar to the interior connections, concrete crushing failure occurred at the bottom of the beam end. The failure modes of S6 and S7 using Grade 600 bars were similar to that of S5. However, in S6 and S7, as the cyclic loading progressed, a gap occurred at the column-beam interface (particularly at the location of the beam bottom re-bars) and continued to increase, which indicates that bond-slip gradually increased in the beam-column joint. As shown in Figs. 2-6 (g) and (i), at 3.8% story drift ratio, concrete cover spalling and punching occurred at the location of the beam bottom bars in the exterior face of the column. Under cyclic loading, compressive yield stress develops in the beam bottom bars showing large tensile plastic strains. However, specimens S6 and S7 did not satisfy the requirement of compressive development length in Eq. (2-3) (ACI 318-11, 2011) (the required length = 583 mm for S6 and 689 mm for S7, and the actual development length = 497 mm). The insufficient compressive development length resulted in concrete cover spalling and punching at the exterior face of the column. Thus, in the exterior connections, the hook bar development length should be satisfied in compression as well as

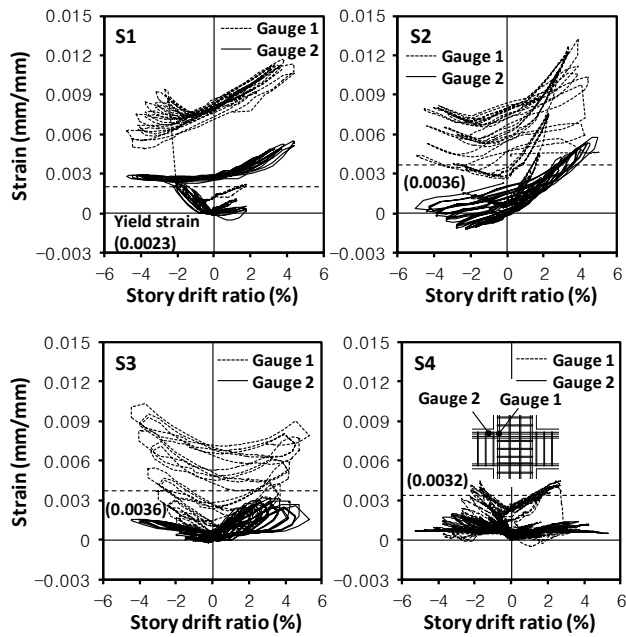
tension, particularly for the beam bottom bars.

As shown in Fig. 2-1, as a test parameter, cross-ties were not used for the interior longitudinal bars in beams. The test results showed that despite the absence of cross-ties, buckling did not occur in the beam longitudinal bars, and concrete spalling was not severe. This result indicates that cross-ties for the interior bars do not significantly affect the behavior of the beam plastic hinge zones. However, in the specimens tested in the present study, the majority of inelastic deformation of the beam-column connection was caused by the bond-slip of the beam longitudinal bars, and the flexural plastic deformation of the beam longitudinal bars was limited. On the other hand, if the majority of inelastic deformation is caused by flexural action of the beam plastic hinge zone, a large plastic deformation occurs in the beam longitudinal bars, which may accelerate buckling of the beam longitudinal bars. Thus, further study is required to confirm the need of cross-ties for interior longitudinal bars in beam plastic hinge zones.

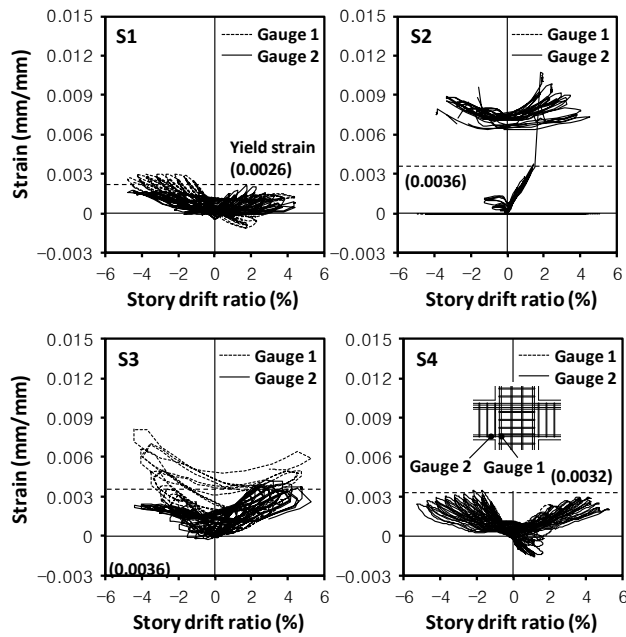
### **2.3.3 Strain of Flexural Re-bar in the Connection**

Fig. 2-7 shows the strains of the beam top (Grade 400 D25 for S1, Grade 600 D22 for S2 and S3, and Grade 600 D25 for S4) and bottom bars (Grade 400 D22 for S1, Grade 600 D22 for S2 and S3, and Grade 600 D25 for S4) within the joint region (Gauge 1) and at the outside (Gauge 2) of the interior joints (S1, S2, S3, and S4). In specimens S1 and S2, initial yielding occurred at the outside of the joint (i.e. the beam end), and after flexural yielding, the

strain within the joint region exceeded the strain at the beam end. This is because re-bar yield penetration occurred in the joint region due to the bond failure. On the other hand, in specimens S3 and S4, the strain within the joint region started to increase before yielding of the re-bars, due to significant yield penetration. However, in S4 with Grade 600 D25 bars (large diameter bars (D25)), the strain within the joint region (Gauge 1) did not significantly increase because of bond-slip. Generally in the specimens, due to the yield penetration, the strain within the joint region (Gauge 1) exceeded the strain at the beam end (Gauge 2). In Fig. 2-7(b), the strains of the beam bottom bars were less than those of the beam top bars shown in Fig. 2-7(a). This result indicates that significant bond-slip occurred at the beam bottom bars. The strain distributions of the beam top and bottom bars along the bar locations were compared in Fig. 2-8. In S2 of Fig. 2-7(b), a sudden increase of strain occurred in Gauge 2, which might be caused by bond-slip. However, accurate reason for such behavior was not found. Gauge 1 was malfunctioned.



(a) Beam top re-bars



(b) Beam bottom re-bars

Fig. 2-7. Strain of beam re-bars at interface of interior joints

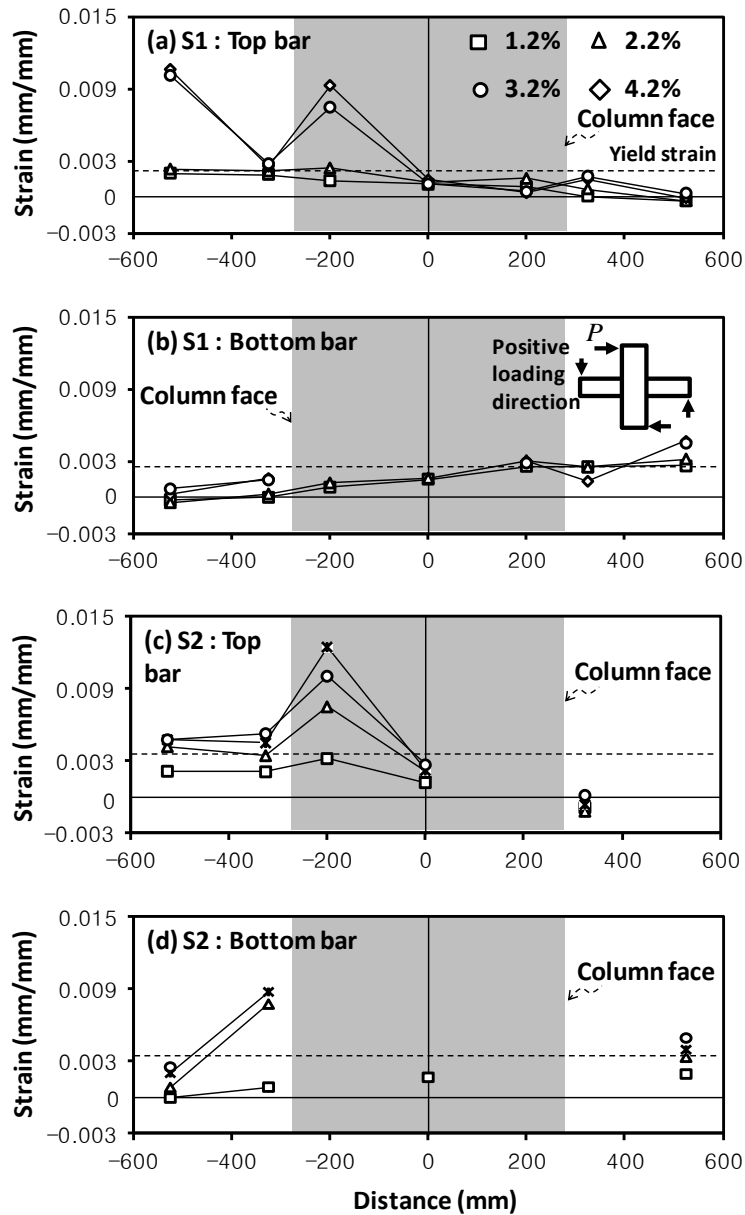


Fig. 2-8. Strain distributions of beam top and bottom bars in interior connections (Continued)

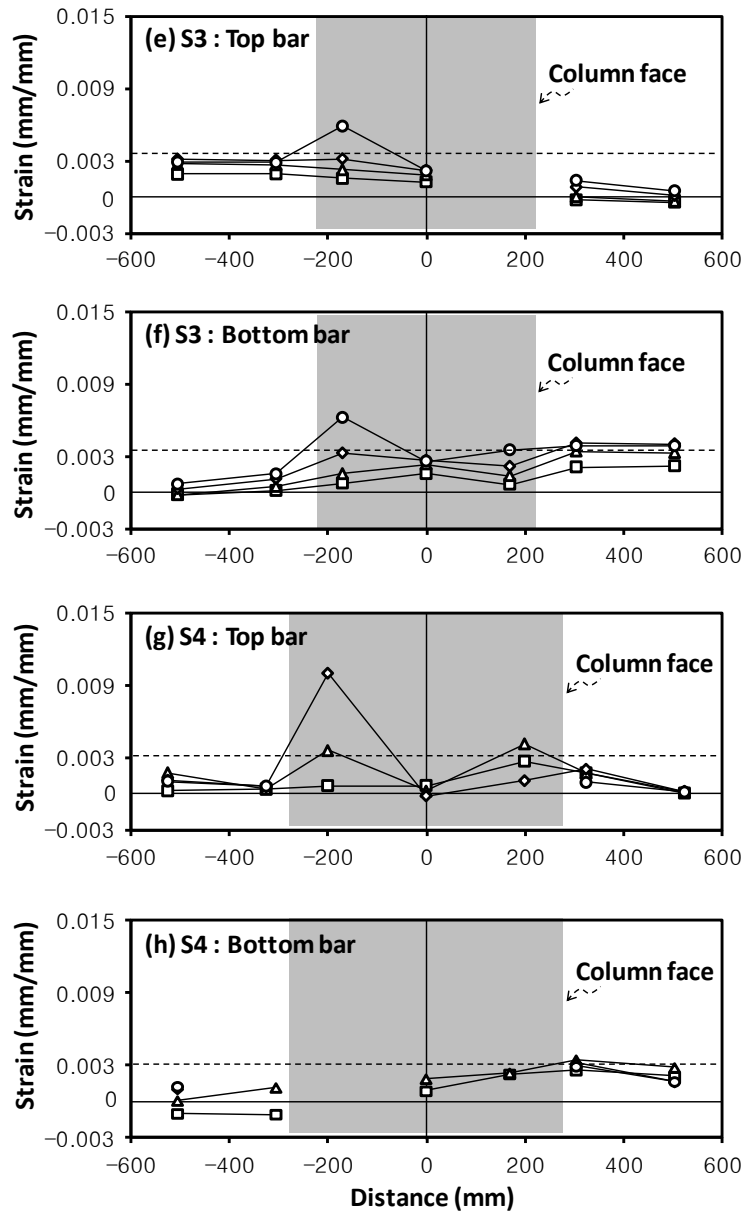
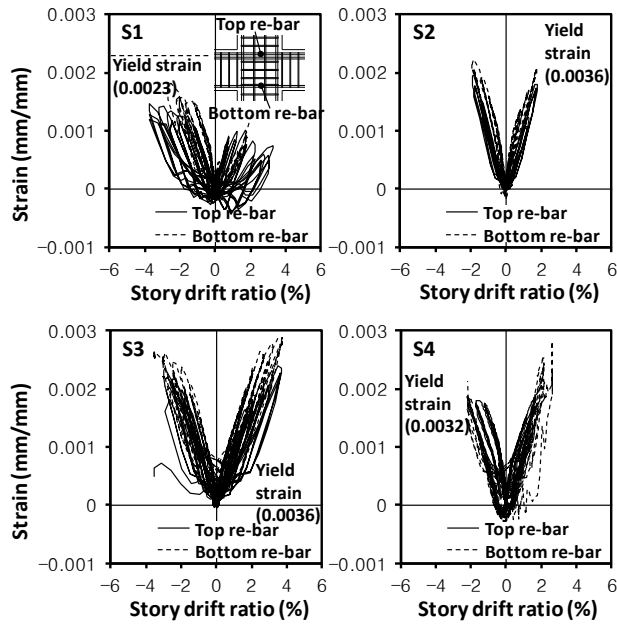


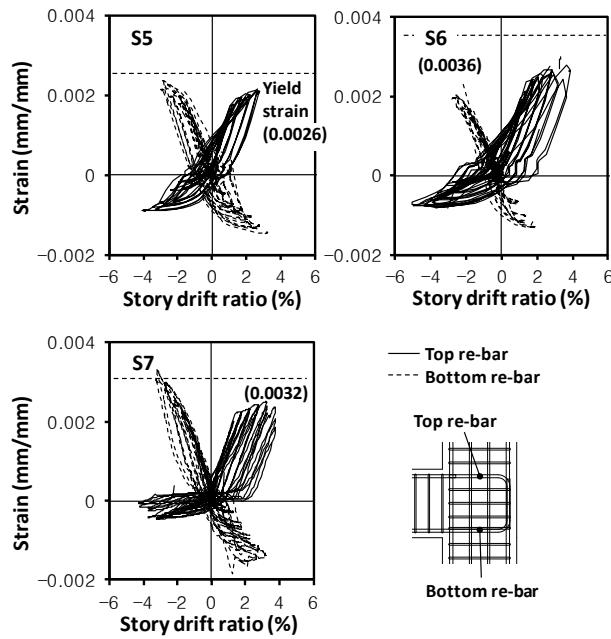
Fig. 2-8. Strain distributions of beam top and bottom bars in interior connections

Fig. 2-9(a) shows the beam re-bar strains measured at the center of the interior beam-column joints S1, S2, S3, and S4. The solid and dotted lines indicate the top re-bar strains and the bottom re-bar strains, respectively. The bottom bar strain of S1 using Grade 400 D22 bars was the least. The strain reached 0.0018 which was close to the yield strain ( $=0.0026$ ). The strains of S2, S3, and S4 using Grade 600 bars were greater, and the strain of S3 with the least column depth was the greatest. However, the strains of the Grade 600 bars were less than the yield strain (0.0036 for D22 and 0.0032 for D25). Fig. 2-9(b) shows the strains of the top and bottom bars (D22 and D25) at the center of the exterior joints S5, S6, and S7. Unlike the interior connections shown in Fig. 2-9(a), the bars showed compressive strains as well as tensile strains. Particularly, as the story drift ratio increased, the compressive strain of the bottom bars was greater than that of the top bars. This result indicates that sufficient compressive development length should be provided for the bottom bars. As mentioned, in the joints of S6 and S7 with Grade 600 bars, the insufficient compressive development length caused concrete cover spalling in the exterior face of the column.





(a) Interior joints



(b) Exterior joints

Fig. 2-9. Strain of beam re-bars at the center of interior and exterior joints

Fig. 2-10 shows the strains of the top and bottom bars (D25) at the beam end in the exterior connection S7. The bottom bars with the smaller area showed greater strains due to the force-equilibrium in the cross-section. Further, the figure shows that the strains did not vary after punching at the exterior face of the column, which indicates the occurrence of bond failure.

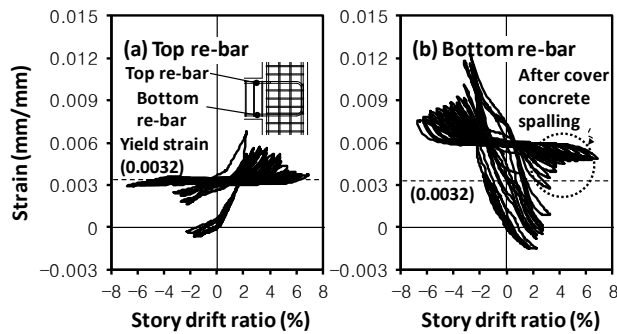


Fig. 2-10. Strain of beam re-bars at interface of exterior joint S7

### 2.3.4 Strain of Ties

Fig. 2-11 shows the strains of the tie bars at the top (Gauge 1) and center (Gauge 2) of the joint in S4 and S7. In interior specimen S4, the maximum strain was 0.0021, which was close to the yield strain ( $=0.0022$ ). On the other hand, in the exterior specimen S7, the maximum strain ( $=0.001$ ) was less than the yield strain, because of the lower joint shear demand.

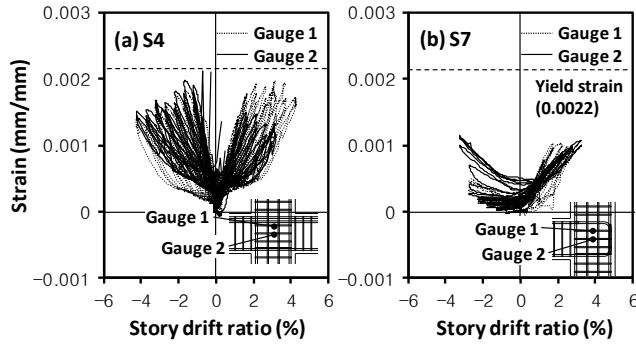


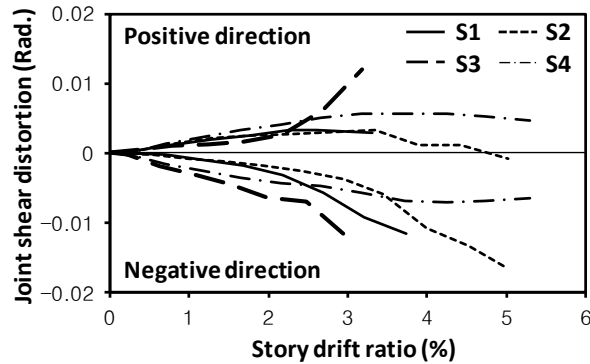
Fig. 2-11. Strain of tie bars at the interior and exterior joints

### 2.3.5 Joint Shear Deformation

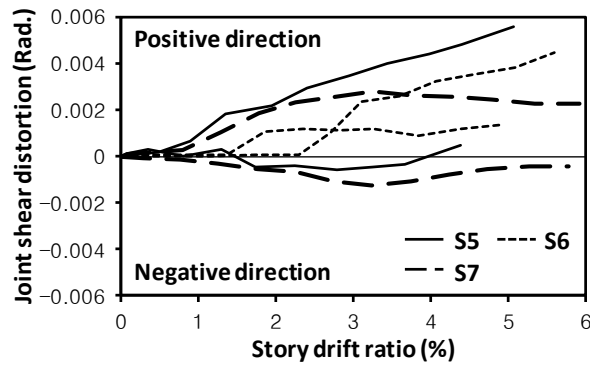
Fig. 2-12 shows the variation of joint shear distortion ( $\gamma_j$ ) according to the story drift ratio. The joint shear distortion was estimated from the test measurement.

$$\gamma_j = (\delta_j - \delta'_j) \sqrt{a^2 + b^2} / 2ab \quad (2-7)$$

where  $\delta_j$  and  $\delta'_j$  are the diagonal deformations measured by the two diagonal linear potentiometers at the joint (Fig. 2-3); and  $a$  and  $b$  are the horizontal and vertical distances, respectively, between the ends of the diagonal linear potentiometers.



(a) Interior joint S1, S2, S3, and S4



(b) Exterior joint S5, S6, and S7

Fig. 2-12. Joint shear distortion

In the interior connection S1 with Grade 400 bars and S2 with Grade 600 bars, the joint shear distortion was relatively small. The shear distortions of S3 with a smaller column depth and S4 with Grade 600 D25 bars were greater than that of S2 with Grade 600 D22 bars. Particularly, in S3 which did not satisfy the joint shear requirement, the joint shear distortion significantly increased. In the exterior connections, under the positive loading which develops negative moment at the beam end, the joint shear distortion was

greater because of the greater shear force. The joint shear distortions of S6 and S7 with Grade 600 bars were equivalent to that of S5 with Grade 400 bars.

### **2.3.6 Hysteretic Energy Dissipation**

Fig. 2-13 shows hysteretic energy dissipation per load cycle of interior specimens S1, S2, S3, and S4 and exterior specimens S5, S6, and S7. The hysteretic energy dissipation per load cycle is defined as the area enclosed by a cyclic curve in Fig. 2-5. As shown in Fig. 2-13, in all specimens, the hysteretic energy dissipation at the second load cycle was significantly less than that at the first load cycle; the hysteretic energy dissipation of the second cycle was 0.51 - 0.90 times that of the first cycle. The hysteretic energy dissipation capacity at the third cycle was close to that of the second cycle.

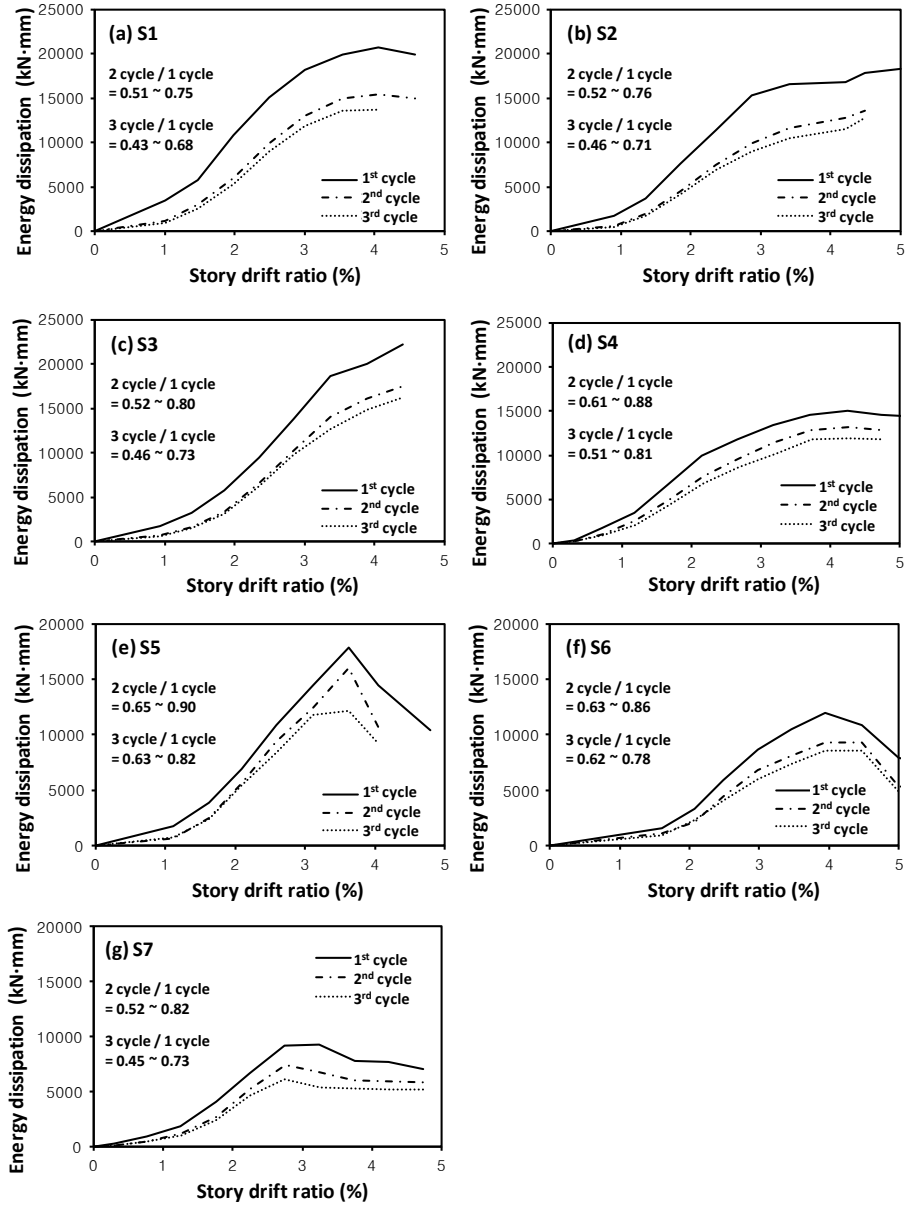


Fig. 2-13. Energy dissipation capacities of test specimens

At the third load cycle of the 3.5% story drift angle, the hysteretic energy dissipation of the interior connections S2, S3, and S4 was 7 - 25% less than that of S1 with Grade 400 bars (see Table 2-3 (9)). This is because bar bond-slip was increased by using Grade 600 bars. In the exterior connections, the hysteretic energy dissipations of S6 and S7 were 42 - 58% less than that of S5 with Grade 400 bars (see Table 2-3 (9)). In the exterior connections with Grade 600 bars, the energy dissipation was significantly decreased by the bond-slip caused by the insufficient bar development length.

The hysteretic energy dissipation (per load cycle) of exterior connection S5 was less than those of S1 - S3, but was greater than S4, particularly at the ultimate state. This is because in S4 using high strength larger diameter bars (600MPa D25), significant bond-slip occurred, while in S5, bond-slip was restrained by using less yield strength smaller diameter bars (400MPa D22) and the hook anchorages.

## 2.4 Evaluation According to ACI 374.1-05

For the seismic performance of the beam-column connections, ACI 374.1-05 (2005) specifies the following evaluation criteria regarding the deformation capacity, secant stiffness, and energy dissipation at the third load cycle of the 3.5% story drift angle.

- 1) At the third load cycle of the 3.5% story drift angle, the load-carrying capacity should be greater than  $0.75P_{\max}$ .
- 2) The secant stiffness between the story drift ratio of -0.35% - +0.35% should not be less than 0.05 times the initial stiffness.
- 3) The hysteretic energy dissipation ratio should not be less than 0.125.

The properties of the test specimens regarding the performance criteria are given in Table 2-3. Table 2-3 (3) presents the values for the requirement (a): the ratios of  $(P / 0.75P_{\max})$  at the third load cycle of the 3.5% story drift angle. In all specimens including the specimens with Grade 400 bars, the requirement (a) was not satisfied, but the ratios were close to 1.0.

Table 2-3 (7) presents the values for requirement (b): the ratio of the secant stiffness to 0.05 times the initial stiffness. The cruciform specimens S1 and S2 did not satisfy the performance criterion. On the other hand, S3 and S4



satisfied the criterion despite the short development length. The T-shaped specimens, S5 and S6, satisfied the requirement. S7 did not satisfy the requirement because of bond-slip.

In requirement (c), the hysteretic energy dissipation ratio is defined as the ratio of the energy dissipation at the third load cycle to the energy dissipation calculated from an idealized elasto-perfectly plastic behavior (see Fig. 2-14). The elasto-perfectly plastic energy dissipation  $A_E$  can be estimated as follows.

$$A_E = (M_1 + M_2) \times (\theta_1 + \theta_2) \quad (2-8a)$$

$$\theta_1 = 3.5\% - M_1 / K \quad (2-8b)$$

$$\theta_2 = -3.5\% - M_2 / K' \quad (2-8c)$$

where  $M_1$ ,  $M_2$ ,  $\theta_1$ , and  $\theta_2$  are defined in Fig. 2-14. Table 2-3 (10) presents the energy dissipation ratio. All the specimens satisfied requirement (c), showing the ratios greater than 0.125.

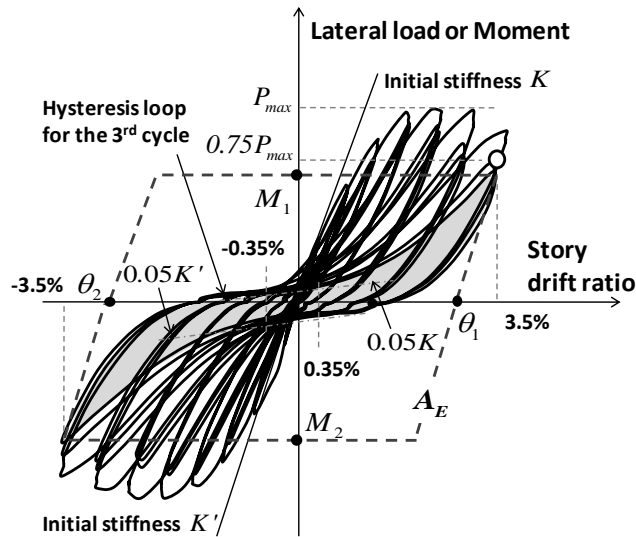


Fig. 2-14. Acceptance criteria by ACI 374.1-05

In the evaluation by ACI 374.1-05 (2005), neither the specimens with Grade 600 bars or Grade 400 bars satisfied the secant stiffness criteria at 3.5% story drift ratio. However, the requirements of deformation capacity and energy dissipation were satisfied.

Table 2-3. Evaluation of seismic performance of test specimens (ACI 374.1-05, see Fig. 2-14)

Specimens		S1		S2		S3		S4		S5		S6		S7	
		+ dir.	- dir.	+ dir.	- dir.	+ dir.	- dir.	+ dir.	- dir.	+ dir.	- dir.	+ dir.	- dir.	+ dir.	- dir.
Lateral force at 3.5 % drift ratio (kN)	(1) $0.75P_{max}$	367	-378	361	-354	351	-302	305	-308	192	-117	191	-102	219	-121
	(2) $P$ at 3.5%	333	-359	363	-337	372	-293	295	-303	165	-146	184	-118	258	-118
	(3) Ratio= (2)/(1)	0.91	0.95	1.01	0.95	1.06	0.97	0.97	0.98	0.86	1.25	0.96	1.15	1.18	0.98
Stiffness (kN/mm)	(4) Initial $K$	18.7	19.7	19.1	19.5	17.7	16.0	18.4	18.6	11.6	6.49	9.48	4.24	11.2	6.81
	(5) 5% of initial $K$	0.94	0.94	0.96	0.96	0.89	0.80	0.92	0.93	0.58	0.32	0.47	0.21	0.56	0.34
	(6) $K$ at 3.5%	1.23	0.84	0.66	0.60	1.42	2.07	1.08	1.03	1.23	1.04	1.54	0.71	0.47	0.45
	(7) Ratio= (6)/(5)	1.31	0.89	0.69	0.63	1.60	2.59	1.17	1.11	2.12	3.25	3.28	3.38	0.84	1.32
Energy dissipation (kN-mm)	(8) Elastic plastic Energy dissipation	75042		71011		65237		61685		33307		30845		35950	
	(9) Actual Energy dissipation	13672		10507		12665		10191		12788		7446		5369	
	(10) Ratio= (9)/(8)	0.18		0.15		0.19		0.17		0.38		0.24		0.15	

## 2.5 Discussion

A study was carried out on the seismic performance of the beam-column connections using Grade 600 (the specified yield strength = 600 MPa) bars for the beam longitudinal bars. To evaluate the structural performance, four cruciform interior connections and three T-shaped exterior connections using Grade 400 or 600 bars were designed as part of the special moment frame and were tested under cyclic lateral loading.

The primary test results are summarized as follows:

- 1) In the interior connections, S2 and S4 ( $h_c/d_b = 25$  and  $22$ ), the damage mode was diagonal cracking at the joint – yielding of beam flexural bars - bond-slip of beam flexural bars. Ultimately, concrete crushing occurred at the bottom of the beam end. This is because a large compressive force developed at the bottom of the beam end due to the asymmetric re-bar layout and significant bond-slip. The damage and failure modes were the same as those of specimen S1 ( $h_c/d_b = 22$ ) with Grade 400 bars.
- 2) In specimen S3 which had smaller column depth than that of S2, joint shear failure occurred after concrete delamination, because of the unsatisfactory joint shear strength. This result demonstrates the adequacy of the joint shear strength specified in ACI 318-11 (2011).

- 3) In the exterior connection S5 ( $l_{dh}/d_b = 22.6$ ), the specimen failed due to concrete crushing at the bottom of the beam end. In specimens S6 and S7 ( $l_{dh}/d_b = 22.6$  and  $19.6$ ), in addition to the concrete crushing at the beam bottom, concrete cover spalling and punching occurred at the location of the beam bottom bars in the exterior face of the column, due to the insufficient bar development length in compression. However, such negative effect of bond-slip was not observed in the beam top bars. Thus, the development length for beam bottom bars should be satisfied in compression as well as tension. In this case, the development length of  $90^\circ$  hook bars in ACI 318-11 (2011) needs to be revised.
- 4) The load-carrying capacities of the interior and exterior connections with Grade 600 bars (except S3 with unsatisfactory joint shear strength) agree with the predicted nominal strengths.
- 5) The maximum story drift ratios of S2 and S4 were 3.71% to 4.76% and -3.73% to -4.54%, which were comparable to those of S1 (3.73% and -4.27%).
- 6) The maximum story drift ratios of S6 which satisfied the bar development length in tension were 3.83% and -5.08%, which were comparable to those of S5 (3.17% and -4.40%). However, in S7, which did not satisfy the bar development length in both tension and compression, the deformation capacity in negative loading was decreased by bond-slip. In exterior connections, the bar development length in both tension and

compression of Grade 600 bars can be satisfied by extending 90° hook bars to stub beam installed in the opposite side of the joint.

- 7) At the 3.5% story drift angle, the hysteretic energy dissipation of S2 – S4 was 7% - 25% less than that of S1, due to the increased bond-slip. The hysteretic energy dissipation of S6 and S7 was only 42% - 58% of S5, due to the insufficient bar development length.
- 8) In the evaluation by ACI 374.1-05 (2005), all specimens satisfied the requirements of deformation capacity and energy dissipation at 3.5% story drift ratio. However, neither the specimens with Grade 600 bars or Grade 400 bars satisfied the secant stiffness criteria.
- 9) In the test specimens, despite the absence of cross-ties, buckling did not occur in the beam longitudinal bars, and concrete spalling was not severe. However, the majority of inelastic deformation was caused by the bond-slip of the beam longitudinal bars, without significant flexural deformation of the beams. Thus, further study is required to confirm the need of cross-ties.

The test results herein are valid for the following design parameters: Grade 600 MPa bars for beam longitudinal re-bars; bar diameters less than 25 mm; beam re-bar ratios less than 1.30 %; and the column depth to bar diameter ratio  $h_c/d_b \geq 22$ . However, to confirm the test results, further studies are required.

## **Chapter 3. Bond-Slip Relationship of Beam Flexural Bars in Interior Joint**

### **3.1 Introduction**

In reinforced concrete moment-resisting frame structures subjected to earthquake load, the earthquake resistance of the beam-column joint is significantly affected by the concrete diagonal cracking and bond-slip of a beam flexural bar at the joint (Kitayama et al., 1987; Leon, 1989; Hakuto et al., 1999; Meinheit and Jirsa, 1977; Bonacci and Pantazopoulou, 1993; Lee et al., 2009; Lee and Lin, 2011; Hong et al., 2011). Particularly, in the interior beam-column joint that inelastic deformation significantly occurs, the bond-slip of the beam flexural bar contributes to 35% of total deformation of the beam-column joint (Soleimani et al., 1979).

Fig. 3-1 shows the load transfer mechanism in interior beam-column joint subjected to earthquake load. Under cyclic loading, bond-stress is developed at the beam-column joint for compression force as well as tension force by the tensile residual deformation of beam flexural bar. Thus, compared with monotonic loading, two times bond strength ( $T_1+C_2$  or  $T_2+C_1$  in Fig. 3-1) is required in the beam flexural bar at the beam-column joint under cyclic loading. On the other hand, because the maximum development length of the beam flexural bar is limited by column depth  $h_c$ , it is difficult to secure a sufficient development performance of the re-bar. Thus, in the beam-

column joint with small  $h_c/d_b$  ( $d_b$  = diameter of a beam flexural bar), bond failure between the beam flexural bar and concrete increases the bond-slip of the re-bar (Hakuto et al., 1999).

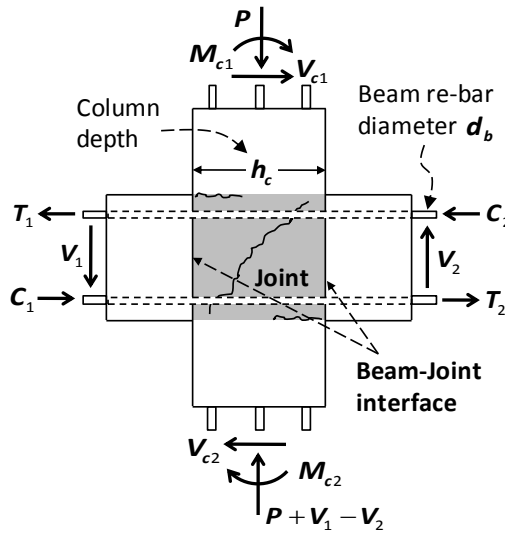


Fig. 3-1. Load transfer of beam-column joint in interior connection

To mitigate the bond-slip of a re-bar, current earthquake design codes (ACI 318-11, 2011; ACI 352R-02, 2002; NZS 3101:2006, 2006; Eurocode 8, 2004) specify the minimum requirement of column depth-to-bar diameter ratio  $h_c/d_b$ . In ACI 352R-02 (2002),  $h_c/d_b$  is simply required as the yield strength ratio of the re-bar. In NZS 3101:2006 (2006) and Eurocode 8 (2004), the additional design parameters including concrete tensile strength, column axial load, and structural performance demand are required. The design requirements were empirically developed on the basis of the beam-column



joint tests.

As an analytical and experimental study, Eligehausen et al. (1983) studied the bond performance of non-yielded re-bars in the specimens simulating beam-column joint under monotonic and cyclic loading, and proposed the bond strength-slip relationship of the re-bar. Ciampi et al. (1982) and Elmsori et al. (2000) developed the bond model for finite element analysis of reinforced concrete by modifying the bond model of Eligehausen et al. (1983). Viathanatepa et al. (1979) studied the bond strength-slip relationship for the yielded re-bar under cyclic loading. Alsiwat and Saatcioglu (1992) and Marti et al. (1998) proposed the strain based bond model dividing into before re-bar yielding and after. Hong et al. (2011) and Lowes and Altoontash (2003) applied the strain based bond model to interior beam-column joint, and predicted the strain variation and anchorage slip of the beam flexural bar.

The existing test results and bond models showed the great achievement to predict the bond-slip in the beam-column joint. However, the following studies are required to improve the prediction in the beam-column joint.

- 1) In the existing tests, concrete block tests were performed to evaluate the bond-slip of a re-bar. Compared to actual beam-column joint, concrete block test shows the different load and deformation conditions. In the concrete block test, re-bar is anchored by the bond stress inside the concrete block. In elastic strain range of the re-bar, the bond stress can be

accurately evaluated from the concrete block test. However, when the bond stress is decreased by bond failure inside the concrete block, strain of the re-bar is no more increased and yield strength are decreased because the strain and stress of the re-bar are governed by the bond-slip and bond-stress in the concrete block. In the actual beam-column joint, even with the complete bond-slip, inelastic strain of the re-bar is significantly increased and yield strength occurs because the re-bar is anchored at the opposite beam. Thus, the bond behaviors of the re-bar including strain distribution, bond-stress, and bond strength in the actual beam-column joint can be different from those of the concrete block test.

- 2) In concrete block test, bond stress-slip relationship of a re-bar is clearly affected by bond damage inside the concrete block. On the other hand, in actual beam-column joint, concrete diagonal cracking increases the bond damage and affects the bond stress. Furthermore, cracking confinement effect by hoop bars at the joint affects the bond strength.
- 3) Current design codes specify the bond requirement of beam flexural bars regardless of deformation capacity of beam-column joint. However, for performance based design, the bond requirement is need to be defined depending on the ductility demand of the beam.

In the present study, simplified bond model was developed to predict the re-bar bond-slip in beam-column joint subjected to cyclic loading. On the basis of existing beam-column joint tests, bond stress and bond failure were

redefined, and the bond model was improved. The proposed bond model was compared with the existing test results for verification. Furthermore, for performance based seismic design, beam ductility based bond requirement was proposed, and compared with current earthquake design codes.

### **3.2 Re-bar Bond Model at Beam-Column Joint**

When anchorage failure of a deformed bar occurs in concrete, bond resistance is provided by bearing stress of ribs and surface friction of the re-bar (Eligehausen et al., 1983). Fig. 3-2 shows the bond stress variation of re-bar and concrete damage in the vicinity of the re-bar by bond-slip. Fig. 3-2(a) indicates the initial stage of bond-slip where stress of the re-bar is transferred to concrete by bearing mechanism of ribs. As shown in Fig. 3-2(b), after concrete crushing by bearing mechanism, the bond resistance by the bearing force is significantly decreased, and the bond resistance is developed by friction mechanism. Fig. 3-2(c) shows the bond stress-slip relationship of the re-bar by load reversal (i.e. cyclic loading). After bond failure of the re-bar at the 1<sup>st</sup> loading (see Fig. 3-2(b)), the bond stress at load reversal cannot be recovered by the damaged concrete, and only residual bond stress is provided by friction mechanism.

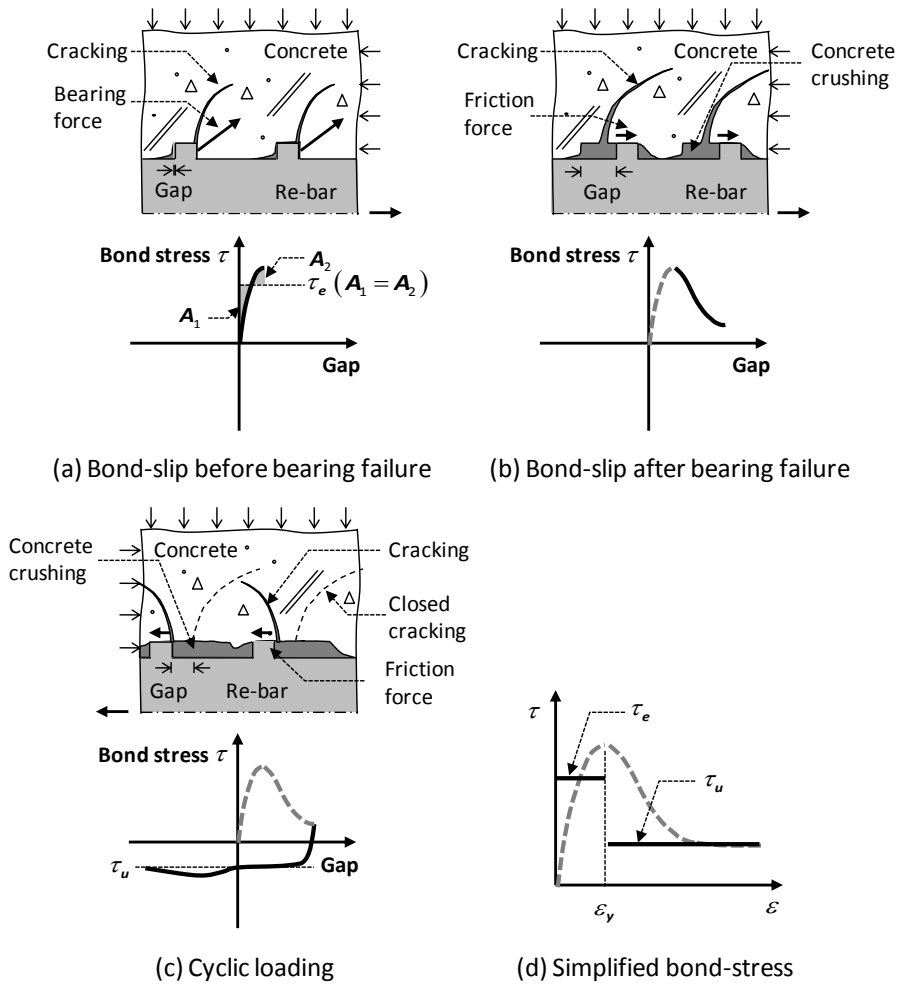


Fig. 3-2. Mechanism of bond resistance of beam flexural bars (Eligehausen et al., 1983)

As shown in Fig. 3-2, before concrete bearing failure by bond-slip, bond stress is increased proportionally to bar-slip. On the other hand, after the concrete bearing failure, the bond stress by surface friction remains almost constant regardless of bar-slip and loading direction. Therefore, the bond stress can be divided by the concrete bearing failure in principle.

Concrete bearing failure is significantly associated with re-bar yielding. Before re-bar yielding, deformation between the re-bar and concrete is very small because of large elastic stiffness of the re-bar. Thus, concrete damage by bearing mechanism is not almost occurred. After re-bar yielding, on the other hand, the deformation is significantly increased. It results in the concrete cracking and bearing failure. That is, bond stress can be defined as a concrete bearing bond stress before re-bar yielding and a friction bond stress after re-bar yielding.

In the present study, as shown in Fig. 3-2(d), the average bond stress before re-bar yielding (= elastic range) and after (= plastic range) were defined as bearing bond stress  $\tau_e$  and friction bond stress  $\tau_u$ , respectively (Hong et al., 2011; Lowes and Altoontash, 2003). Bearing bond stress  $\tau_e$  is defined such that the area due to  $\tau_e$ -slip relationship is same to the area calculated by actual bond stress-slip relationship in the elastic range before re-bar yielding (see Fig. 3-2(a)). Friction bond stress  $\tau_u$  is defined as the average value of the almost uniform residual bond stress after bond stress degradation in Fig. 3-2(c). Bearing bond stress and friction bond stress are determined in Chapter “3.3 BOND STRESS”.

Fig. 3-3 shows the stress variation depending on a development length. Re-bar stress and bond-stress relationship is determined by equilibrium condition as follows.

$$d\sigma \left( \pi \frac{d_b^2}{4} \right) = \tau_e (\pi d_b dx) \quad \text{or} \quad \frac{d\sigma}{dx} = \frac{4\tau_e}{d_b} \quad (3-1a)$$

$$d\sigma \left( \pi \frac{d_b^2}{4} \right) = \tau_u (\pi d_b dx) \quad \text{or} \quad \frac{d\sigma}{dx} = \frac{4\tau_u}{d_b} \quad (3-1b)$$

where  $d_b$  = re-bar diameter;  $\tau_e$  = bearing bond stress of re-bar; and  $\tau_u$  = friction bond stress of re-bar. Eqs. 3-1(a) and (b) are applied to  $\sigma \leq f_y$  and  $\sigma > f_y$  ( $f_y$  = re-bar yield strength), respectively.

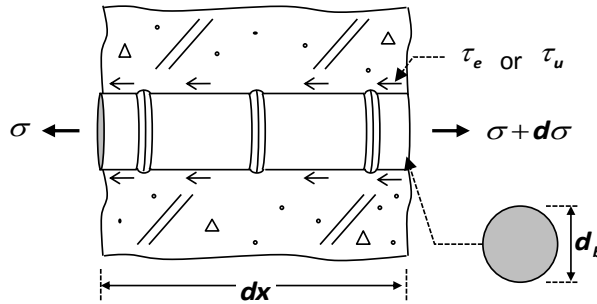


Fig. 3-3. Re-bar stress variation by bond stress

When stress-strain relationship of a re-bar is defined as bilinear relationship that consists of elastic stiffness  $E_s$  and hardening stiffness  $E_{sh}$ , stress increment of the re-bar before yielding and after can be defined as  $d\sigma = E_s d\varepsilon$  and  $E_{sh} d\varepsilon$ , respectively. Therefore, the strain variation rate of the re-bar according to length is as follows from Eqs. 3-2(a) and (b).

$$\frac{d\varepsilon}{dx} = \frac{4\tau_e}{E_s d_b} \quad \text{for} \quad |\varepsilon| \leq \varepsilon_y \quad (3-2a)$$

$$\frac{d\varepsilon}{dx} = \frac{4\tau_u}{E_{sh} d_b} \quad \text{for} \quad |\varepsilon| > \varepsilon_y \quad (3-2b)$$

where  $\varepsilon_y$  = yield strain of re-bar.

Fig. 3-4 shows bond-stress-, re-bar strain-, and re-bar stress-distribution depending on bond-slip of beam flexural bars in interior beam-column joint. Fig. 3-4(a) presents the limited stage of bond-slip. Due to sufficient bond strength in the joint, compressive and tensile stress are applied to the beam flexural bars. Compressive and tensile friction bond stress  $\tau_u$  are applied to the yielding length of re-bar at the joint interface. Bearing bond stress  $\tau_e$  is applied to the elastic length of re-bar inside the joint. Fig. 3-4(b) presents the partial bond-slip stage that only tensile stress is applied to the beam flexural bars in the joint. That is, insufficient bond strength caused the tensile bond strength at total joint length. Plastic bond stress is defined at the both of the joint interface by cyclic loading, and elastic bond strength is defined at the center of the joint. In this case, tension forces of the re-bars are anchored at the compression zone of an opposite beam. Fig. 3-4(c) presents the complete bond-slip stage that the only plastic bond strength is applied to the total joint length.



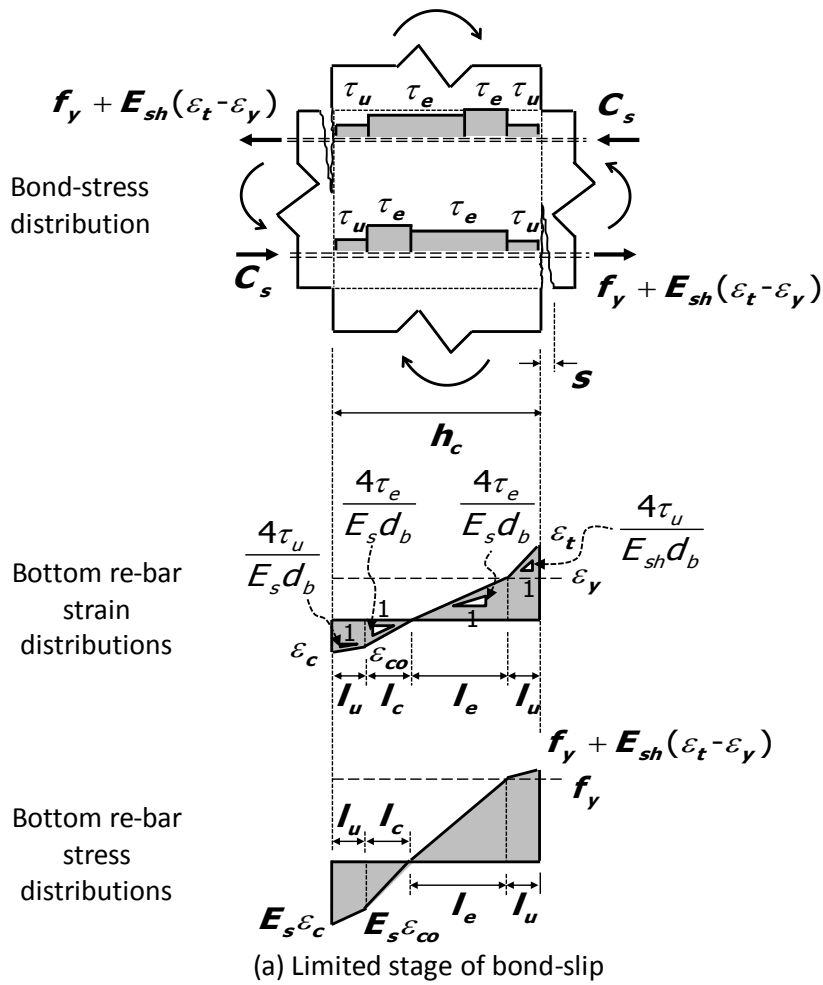


Fig. 3-4. Stress and strain distribution of beam re-bars due to bond-slip in beam-column joint under cyclic loading (Continued)

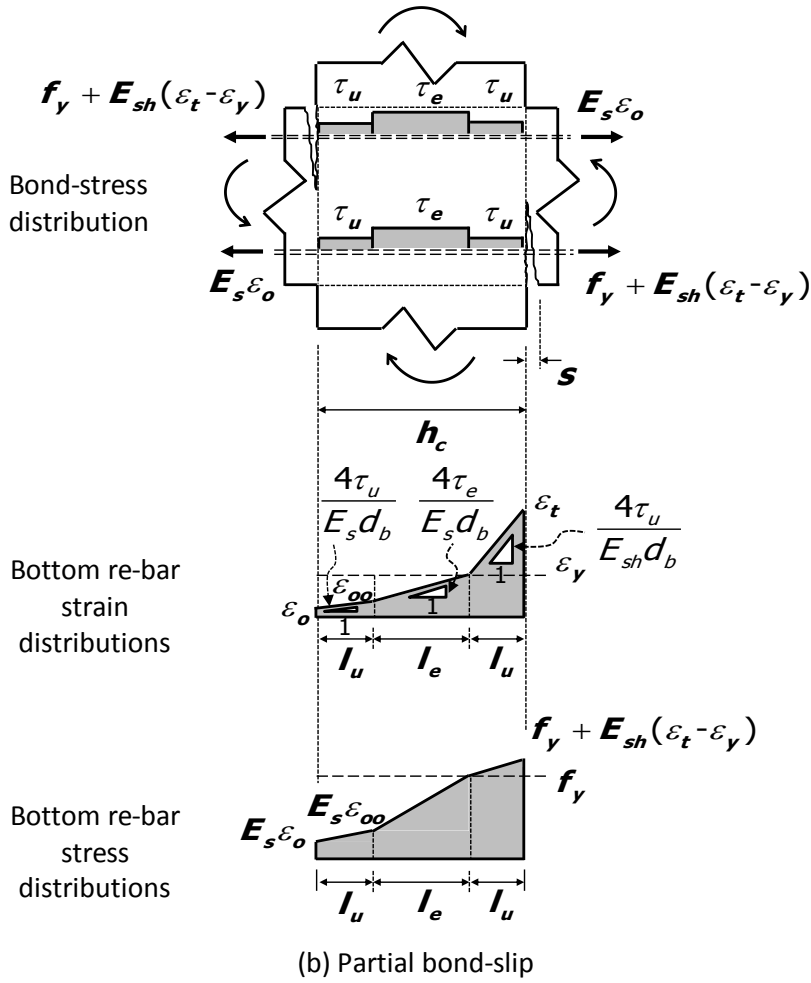


Fig. 3-4. Stress and strain distribution of beam re-bars due to bond-slip in beam-column joint under cyclic loading (Continued)

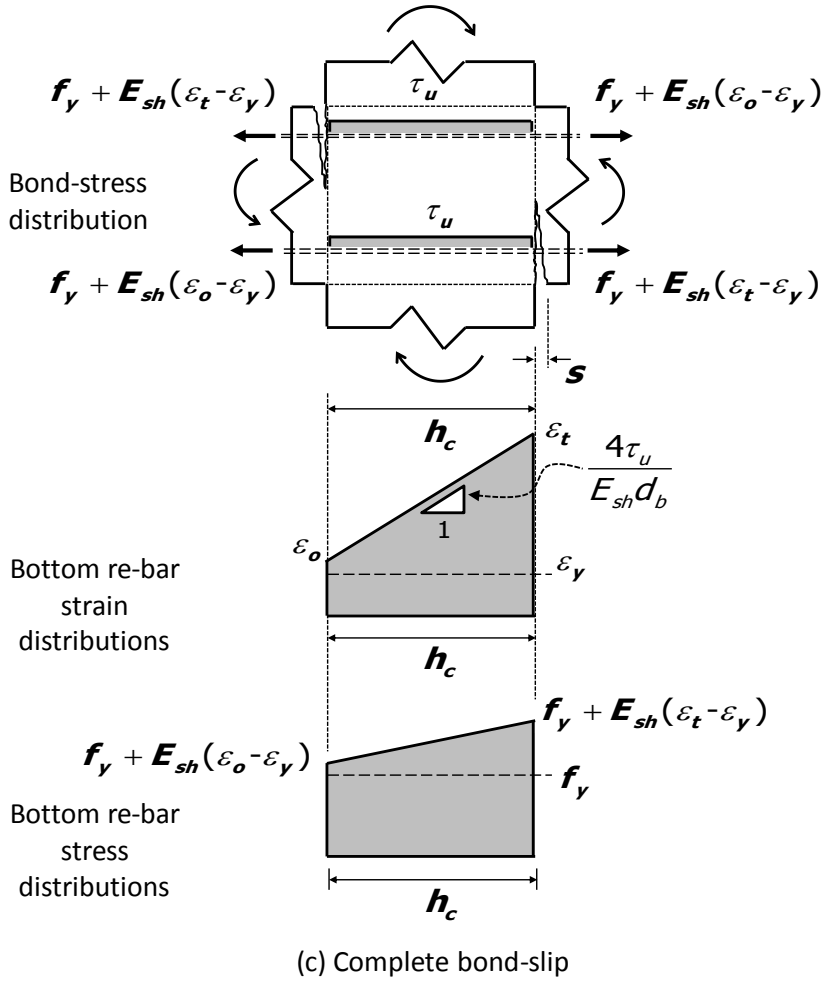


Fig. 3-4. Stress and strain distribution of beam re-bars due to bond-slip in beam-column joint under cyclic loading

In Fig. 3-4(a), when a re-bar strain  $\varepsilon_t$  is less than yield strain  $\varepsilon_y$ , bearing bond stress  $\tau_e$  is applied to bearing bond length. The other portion is defined as friction bond length  $l_u$ . Here, compressive bearing bond stress  $\tau_e$  is greater than tensile bearing bond stress (see “3.3 BOND STRESS”). Therefore, tensile bond length  $l_e$  is longer than compressive bond length  $l_c$ . Under cyclic

loading, because a yield penetration of re-bar occurs almost symmetrically, bond stress of beam flexural bars decreases at left and right joint interface. Furthermore, because the once degraded bond stress is not recovered, regardless of the beam flexural bars strength and direction, bond stress degraded length  $l_u$  is same at the left and right interface, and same friction bond stress  $\tau_u$  is applied.

In Fig. 3-4(b), the friction bond length  $l_u$  is determined as the portion that a tensile strain of re-bar  $\varepsilon_t$  is greater than yield strain  $\varepsilon_y$ . Due to cyclic loading in beam-column joint, equal friction bond length  $l_u$  is developed at the both of the joint interface. Tensile bearing bond length at the center of the joint is determined from  $l_e = h_c - 2l_u$ , and uniform tensile bearing bond stress  $\tau_e$  is applied to the re-bar.

As shown in Fig. 3-4(c), when friction bond length  $l_u$  is longer than half joint length  $h_c/2$ , the total joint length is defined as the friction bond length addressing cyclic loading, and uniform friction bond stress  $\tau_u$  is applied.

Stress and strain distributions of a re-bar in joint can be determined by using bond stress  $\tau_e$ ,  $\tau_u$ , and Eq. (3-2). As shown in Fig. 3-4, for the arbitrary maximum tensile strain at the joint interface, strain distribution of the re-bar can be determined using bond stress  $\tau_e$ ,  $\tau_u$ , and Eq. (3-2). On the basis of the result, bearing bond length ( $l_e$  and  $l_c$ ) and friction bond length ( $l_u$ ) can be calculated. An elongation  $e_b$  of the beam flexural bar at the joint interface can be calculated by integration of the strain at each portion.

$$e_b = \int_0^{h_c} \varepsilon \, dx \quad \text{for} \quad \varepsilon \geq 0 \quad (3-3)$$

Furthermore, integrating bond stress at each portion, tension (or compression) of re-bars by bond strength can be calculated.

The aforementioned re-bar bond model was developed on the basis of the methods by Hong et al. (2011) and Lowes and Altoontash (2003). In the proposed model, unlike the existing models, cyclic loading effect was more accurately considered. That is, in the proposed model, friction bond stress  $\tau_u$  is determined from the test results of existing beam-column joint. Furthermore, as shown in Fig. 3-4, to consider the bond damage behavior under cyclic loading, bond damage was defined symmetrically at the both of the joint interface.

### 3.3 Bond Stress

Even under cyclic loading, the discrepancy of bond properties between cyclic loading and monotonic loading is not critical before re-bar yielding (Eligehausen et al., 1983; Viwathanatepa et al., 1979). Thus, bearing bond stress  $\tau_e$  between a beam flexural bar penetrating into joint and concrete was used as a concrete strength function defined by Lowes and Altoontash (2003) from the test result of Eligehausen et al. (1983).

$$\tau_e = 1.8\sqrt{f'_c} \quad \text{in tension (in MPa)} \quad (3-4)$$

$$= 2.2\sqrt{f'_c} \quad \text{in compression (in MPa)} \quad (3-5)$$

This is similar to the proposed values from test result by Viwathanatepa et al. (1979).

To define friction bond stress  $\tau_u$  after re-bar yielding, Lowes and Altoontash (2003) proposed the range of  $\tau_u$  as follows on the basis of the re-bar bond test results using concrete block under cyclic loading performed by Eligehausen et al. (1983) and Shima et al. (1987). From the similar bond test result, Viwathanatepa et al. (1979) proposed  $\tau_u$  as Eq. (3-6b), and Marti et al. (1998) proposed the  $\tau_u$  as Eq. (3-6c) for monotonic loading condition.

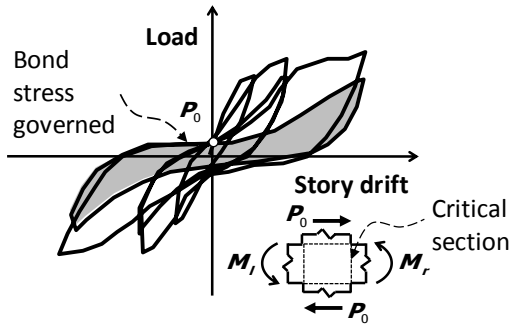
$$0.05\sqrt{f'_c} \leq \tau_u \leq 0.4\sqrt{f'_c} \quad (\text{in MPa}) \quad (3-6a)$$

$$\tau_u = 0.06\sqrt{f'_c} \quad (\text{in MPa}) \quad (3-6b)$$

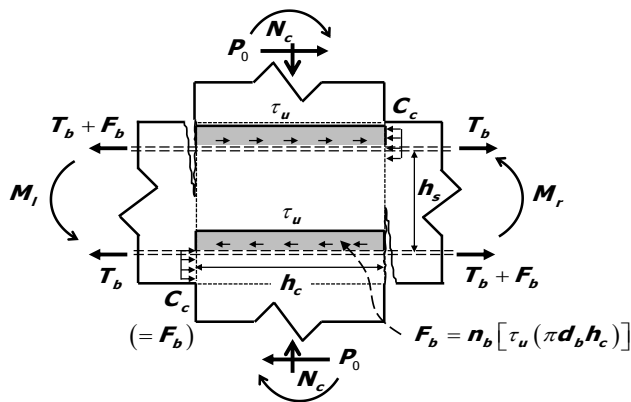
$$\tau_u \leq 0.3\sqrt[3]{f'^2_c} \quad (\text{in MPa}) \quad (3-6c)$$

As mentioned above, because the loading and boundary conditions in actual beam-column joint differ from those in component test using concrete block, it is difficult to accurately evaluate the friction bond stress (residual bond stress)  $\tau_u$ . In the present study, friction bond stress  $\tau_u$  of a beam flexural bar was proposed on the basis of existing beam-column joint tests.

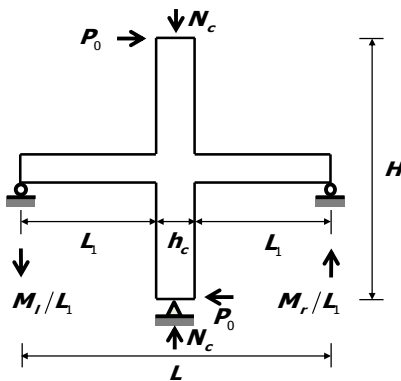
Fig 3-5(a) shows the load-drift relationship in beam-column joint with significant pinching under cyclic loading. In the beam-column joint with significant bond-slip, constant loading  $P_0$  without stiffness variation is applied to pinching region where lateral drift is reversed. As shown in Fig. 3-2(c), after complete bond failure under cyclic loading, bond stress remains constant as residual bond stress  $\tau_u$ . Furthermore, flexural tensile cracking of a beam is opened at the both of the joint interface. Therefore, load transfer between beam and column is developed by the friction bond stress  $\tau_u$  at the joint. That is, load-carrying capacity  $P_0$  at the joint is governed by the re-bar bond stress  $\tau_u$ , and the bond stress of the beam flexural bar  $\tau_u$  can be determined from the loading of specimen  $P_0$ .



(a) Joint behavior with bond-slip



(b) Relationship between bond-stress and re-bar stress



(c) Configuration of interior beam-column joint

Fig. 3-5. Evaluation of residual bond stress from existing test results of beam-column connections



During bond-slip of beam flexural bar, as shown in Fig. 3-5(b), bond stress  $\tau_u$  results in the difference of tension force of the beam flexural bar at the left and right joint interface. Beam flexural moments  $M_l$  and  $M_r$  are developed by tension due to  $\tau_u$  and compression zone of a beam cross-section.  $M_l$  and  $M_r$  are approximately as follows.

$$M_l = \tau_u \left( \sum_{i=1}^{n_t} \pi d_{bi} h_c \right) h_s \quad (3-7a)$$

$$M_r = \tau_u \left( \sum_{i=1}^{n_b} \pi d_{bi} h_c \right) h_s \quad (3-7b)$$

where  $n_t$  and  $n_b$  = the number of top and bottom flexural bars of a beam cross-section;  $d_{bi}$  = re-bar diameter; and  $h_s$  = distance between top and bottom flexural bars.

Load-carrying capacity  $P_0$  by flexural beam moments  $M_l$  and  $M_r$  at left and right joint interface can be determined by the moment equilibrium condition for support reactions as follows (see Fig. 3-5(c)).

$$P_0 = \frac{(M_l + M_r)(h_c/L_1 + 2)}{2H} \quad (3-8)$$

where  $L_1$  = shear span of the both beams; and  $H$  = net column height. As shown in Fig. 3-5(c), Eq. (3-8) is applied to the symmetric interior beam-

column joint.

Substituting Eq. (3-7) into Eq. (3-8), residual bond stress  $\tau_u$  at the joint is as follows.

$$\tau_u = \frac{2P_0H}{h_s \left( \sum_{i=1}^{n_t} \pi d_{bi} h_c + \sum_{i=1}^{n_b} \pi d_{bi} h_c \right) (h_c/L_1 + 2)} \quad (3-9)$$

Fig. 3-6 shows the principal test parameters and friction bond stress  $\tau_u$  calculated from Eq. (3-8) for 67 exiting beam-column joint with bond-slip of beam flexural bars penetrating into the joint (Lee et al., 2009; Hwang et al., 2013; Hwang et al., 2013; Teraoka et al., 1994; Susanto and Hua, 2003; Durrani and Wight, 1982; Hayashi et al., 1993; Sugano et al., 1991; Oda et al., 1997; Joh et al., 1991; Otani et al., 1984; Wong et al., 1990; Walker, 2001; Xian et al., 1992; Shiohara et al., 2001; Shiohara, 2010; Kawai et al., 1997; Kaku et al., 1993; Kitayama et al., 1989; Yoshino et al., 1997; Kawasazaki et al., 1992; Tateishi and Ishibashi, 1998; Asou et al., 1993; Leon, 1990; Leon, 1984). To clearly consider the plastic bond stress distribution such as Fig. 3-4(c), the beam-column joints with significant pinching under cyclic loading were analyzed, as shown in Figs. 3-6(a) - (c). Pinching specimens was defined as the beam-column joint that the secant stiffness from -0.35 to 0.35 % drift ratio is less than 0.05 times the initial stiffness according to ACI 374.1-05 (2005). The principal test parameters are  $f'_c = 20.8 - 84.4$  MPa,  $f_y = 300 - 858$  MPa,  $d_b = 9.5 - 31.8$  mm, and  $h_c = 240 - 550$  mm. Specific test parameters are listed in Table 3-1.  $P_0$  of pinching region for analysis was determined as an

average value of positive and negative loadings in hysteresis curve of the beam-column joint (see Figs. 3-6(a) - (c)).

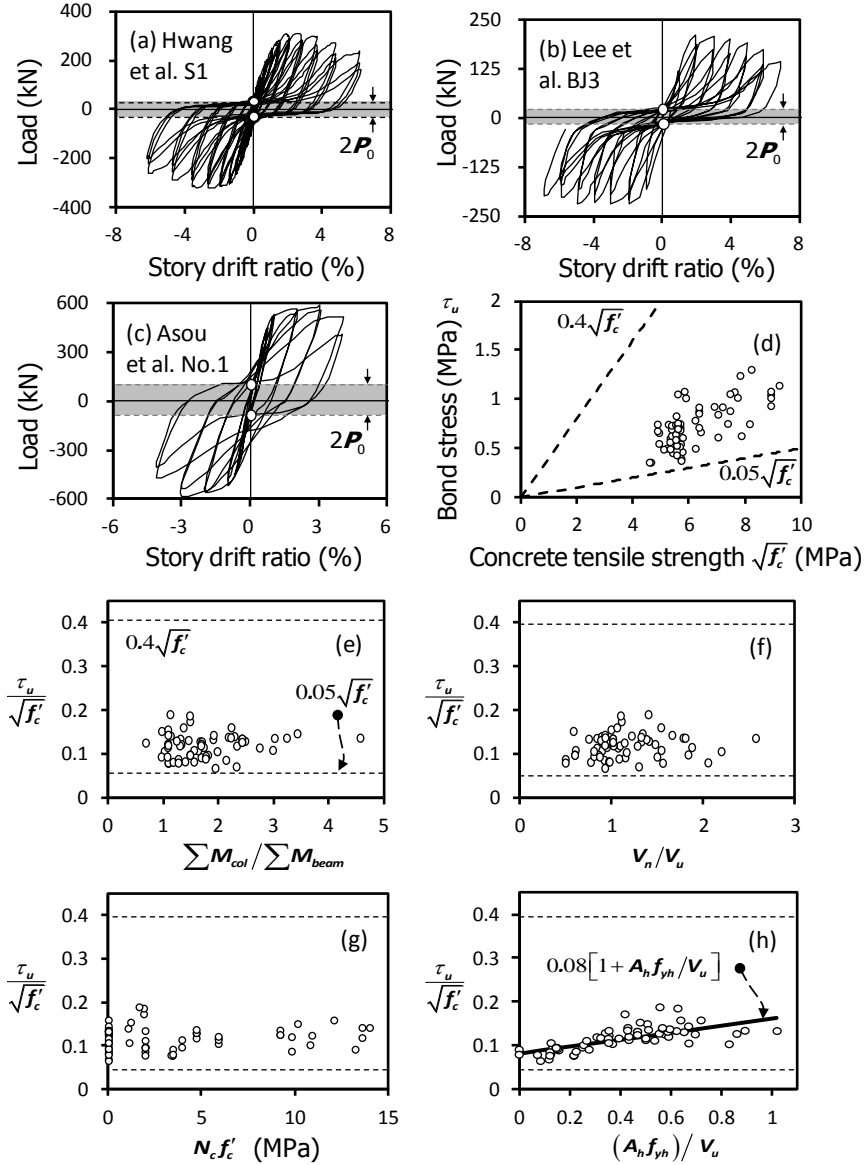


Fig. 3-6. Variation of residual bond stress according to design parameters

Table 3-1. Test parameters of existing test specimens (Continued)

Specimens		Geometric properties <sup>a</sup>						Top re-bar of beam <sup>b</sup>				Bottom re-bar of beam <sup>b</sup>					Joint hoop <sup>c</sup>		Concrete strength	Axial load	Lateral load	Bond strength
		$L$	$H$	$h_b$	$b_b$	$h_c$	$b_c$	$A_s$	$f_y$	$d_b$	$n$	$A_s$	$f_y$	$d_b$	$n$	$h_s$	$A_h$	$f_{yh}$	$f'_c$ (MPa)	$N_c / (f'_c b_c h_c)$	$P_0$ (MPa)	$\tau_u$ (MPa)
Lee et al. (2009)	BJ1	2500	1560	400	300	350	350	1194	510	15.9	6	1194	510	15.9	6	270	1136	510	40.0	0.00	37.4	0.88
	BJ2	2500	1560	400	300	350	350	995	510	15.9	5	995	510	15.9	5	270	852	510	40.0	0.00	25.3	0.72
	BJ3	2500	1560	400	300	350	350	796	510	15.9	4	796	510	15.9	4	270	852	510	40.0	0.00	26.1	0.92
	B1	2500	1560	400	300	350	350	597	510	15.9	3	597	510	15.9	3	270	852	510	40.0	0.00	18.2	0.86
Hwang et al. (2013)	S1	5760	2100	500	350	460	500	2040	452	25.4	4	1020	452	25.4	2	394	1548	496	38.3	0.00	35.7	0.79
Hwang et al. (2013)	S1	4760	2100	500	350	550	500	3110	465	25.4	6	1524	520	22.2	4	387	2064	496	32.0	0.00	63.0	0.72
	S2	4760	2100	500	350	550	500	1935	710	22.2	5	1161	710	22.2	3	396	2064	496	32.0	0.00	45.2	0.69
	S3	4760	2100	500	350	450	500	1935	710	22.2	5	1161	710	22.2	3	396	2064	496	32.0	0.00	39.6	0.76
Teraoka et al. (1994)	NO47	3000	2000	400	300	400	400	1701	382	19.1	6	1701	382	19.1	6	310	785	347	54.0	0.20	38.6	0.76
Susanto and Hua (2003)	S1	4000	2626	400	200	300	400	995	510	15.9	5	597	510	15.9	3	326	1065	440	33.0	0.00	10.4	0.61
Durrani and Wight (1982)	X1	2496	2248	419	279	362	362	1548	331	22.2	4	1136	345	19.1	4	350	864	352	34.3	0.06	34.7	1.02
	X2	2496	2248	419	279	362	362	1548	331	22.2	4	1136	345	19.1	4	350	1297	352	33.7	0.06	37.0	1.09
	X3	2496	2248	419	279	362	362	1163	331	22.2	3	855	345	19.1	3	350	864	352	31.0	0.05	27.1	1.06
Hayashi et al. (1993)	NO46	3000	2000	400	300	400	400	568	858	19.1	2	568	858	19.1	2	310	710	347	49.1	0.20	14.5	0.85
	NO47	3000	2000	400	300	400	400	1704	383	19.1	6	1704	383	19.1	6	280	710	347	49.1	0.20	28.5	0.62
Sugano et al. (1991)	J4-0	2780	1400	400	300	440	440	3096	386	22.2	8	3096	386	22.2	8	260	1024	923	30.4	0.33	90.4	0.83
Oda et al. (1997)	BN1	2800	1500	475	300	450	450	2322	502	22.2	6	2322	502	22.2	6	365	1016	817	79.0	0.07	114.7	1.05
	BN2	2800	1500	475	300	450	450	3096	502	22.2	8	3096	502	22.2	8	350	1016	817	79.0	0.07	131.0	0.94
	BN3	2800	1500	475	300	450	450	2550	535	25.4	5	2550	535	25.4	5	377	1016	817	79.0	0.07	110.3	1.02
	BN4	2800	1500	475	300	450	450	2550	535	25.4	5	2550	535	25.4	5	377	1016	817	79.0	0.07	117.6	1.09
	BN5	2800	1500	475	300	450	450	2040	535	25.4	4	2040	535	25.4	4	395	1016	817	51.3	0.09	84.1	0.93

Table 3-1. Test parameters of existing test specimens (Continued)

Specimens		Geometric properties <sup>a</sup>						Top re-bar of beam <sup>b</sup>				Bottom re-bar of beam <sup>b</sup>					Joint hoop <sup>c</sup>		Concrete strength	Axial load	Lateral load	Bond strength
		<i>L</i>	<i>H</i>	<i>h<sub>b</sub></i>	<i>b<sub>b</sub></i>	<i>h<sub>c</sub></i>	<i>b<sub>c</sub></i>	<i>A<sub>s</sub></i>	<i>f<sub>y</sub></i>	<i>d<sub>b</sub></i>	<i>n</i>	<i>A<sub>s</sub></i>	<i>f<sub>y</sub></i>	<i>d<sub>b</sub></i>	<i>n</i>	<i>h<sub>s</sub></i>	<i>A<sub>h</sub></i>	<i>f<sub>yh</sub></i>	<i>f<sub>c</sub>'</i> (MPa)	<i>N<sub>c</sub>'</i> / ( <i>f<sub>c</sub>'</i> <i>b<sub>c</sub>h<sub>c</sub></i> )	<i>P<sub>0</sub></i> (MPa)	<i>τ<sub>u</sub></i> (MPa)
Joh et al. (1991)	B1	3000	1750	350	150	300	300	398	371	12.7	3	398	371	12.7	3	290	170	307	21.3	0.16	5.0	0.36
	B2	3000	1750	350	300	300	300	398	371	12.7	3	398	371	12.7	3	290	170	307	20.8	0.16	5.0	0.36
	LH	3000	1750	350	200	300	300	387	404	12.7	3	387	404	12.7	3	290	170	377	26.9	0.15	6.8	0.51
	MH	3000	1750	350	200	300	300	387	404	12.7	3	387	404	12.7	3	290	339	377	28.1	0.14	8.2	0.61
Otani et al. (1984)	J1	2700	1470	300	200	300	300	1061	401	13.0	8	531	401	13.0	4	225	192	368	25.7	0.08	12.5	0.49
	J2	2700	1470	300	200	300	300	1061	401	13.0	8	531	401	13.0	4	225	384	368	24.0	0.08	14.0	0.55
	J3	2700	1470	300	200	300	300	1061	401	13.0	8	531	401	13.0	4	225	896	368	24.0	0.08	16.8	0.66
Wong et al. (1990)	U1	4238	2575	457	229	406	305	1592	300	15.9	8	1592	300	15.9	8	220	384	339	32.2	0.00	16.9	0.55
	U2	2602	2575	457	229	406	305	1592	300	15.9	8	1592	300	15.9	8	220	384	339	28.1	0.00	16.4	0.50
Walker (2001)	Peer14	3658	2134	508	406	457	406	1571	423	22.2	4	787	504	15.9	4	384	0	0	31.8	0.11	23.7	0.52
	Peer22	3658	2134	508	406	457	406	2002	528	20.6	6	1335	528	20.6	4	360	0	0	38.4	0.09	28.8	0.50
Xian et al. (1992)	U1	3500	2470	500	250	450	300	791	453	12.0	7	791	453	12.0	7	383	1459	348	30.9	0.00	30.3	0.72
	U2	3500	2470	500	250	450	300	804	445	15.9	4	402	445	15.9	2	416	1029	350	40.8	0.00	17.7	0.67
	U4	3500	2470	500	250	450	300	628	492	20.0	2	402	445	15.9	2	398	1167	348	47.2	0.00	17.6	0.93
	U5	3500	2470	500	250	450	300	942	492	20.0	3	942	492	20.0	3	400	1648	330	60.7	0.00	39.3	1.25
	U6	3500	2470	500	250	450	300	1232	463	28.0	2	942	492	20.0	3	420	1648	330	59.3	0.00	32.7	1.02
Shiohara et al. (2001)	S3	2700	1470	300	200	300	300	995	470	15.9	5	995	470	15.9	5	202	256	390	28.0	0.04	13.2	0.57
Shiohara (2010)	B04	1400	1400	240	240	240	240	516	378	12.7	4	516	378	12.7	4	192	128	399	29.0	0.00	5.2	0.40
	B06	1400	1400	240	240	240	240	645	378	12.7	5	645	378	12.7	5	192	128	399	29.0	0.00	6.9	0.43
	D03	1400	1400	170	240	340	240	645	378	12.7	5	645	378	12.7	5	122	128	399	32.4	0.00	5.9	0.37
	D07	1400	1400	170	240	340	240	903	378	12.7	7	903	378	12.7	7	122	128	399	32.4	0.00	8.4	0.38
	D11	1400	1400	240	240	240	240	903	378	12.7	7	387	378	12.7	3	182	128	399	32.9	0.00	6.3	0.41
	E03	1400	1400	240	240	240	240	995	425	15.9	5	995	425	15.9	5	192	128	399	61.4	0.00	12.2	0.61

Table 3-1. Test parameters of existing test specimens (Continued)

Specimens		Geometric properties <sup>a</sup>						Top re-bar of beam <sup>b</sup>				Bottom re-bar of beam <sup>b</sup>					Joint hoop <sup>c</sup>		Concrete strength	Axial load	Lateral load	Bond strength
		$L$	$H$	$h_b$	$b_b$	$h_c$	$b_c$	$A_s$	$f_y$	$d_b$	$n$	$A_s$	$f_y$	$d_b$	$n$	$h_s$	$A_h$	$f_{yh}$	$f'_c$ (MPa)	$N_c / (f'_c b_c h_c)$	$P_0$ (MPa)	$\tau_u$ (MPa)
Kawai et al. (1997)	I6C	3800	1600	450	325	475	475	2709	522	22.2	7	2709	522	22.2	7	339	640	928	66.1	0.20	84.6	0.75
Kaku et al. (1993)	J11C	2250	1250	350	260	400	300	1136	378	19.1	4	1136	378	19.1	4	290	384	911	57.6	0.24	58.1	1.08
	J31A	2250	1250	350	260	400	300	2040	370	25.4	4	2040	370	25.4	4	290	384	911	55.2	0.25	64.4	0.89
	J32B	2250	1250	350	260	400	300	2040	370	25.4	4	2040	370	25.4	4	290	512	911	55.2	0.25	76.9	1.06
Kitayama et al. (1989)	A1	2700	1470	300	200	300	300	1032	780	12.7	8	516	780	12.7	4	213	384	320	30.6	0.06	11.5	0.48
	A2	2700	1470	300	200	300	300	1032	780	12.7	8	516	780	12.7	4	213	384	320	30.6	0.06	10.4	0.44
	A3	2700	1470	300	200	300	300	774	780	12.7	6	516	780	12.7	4	218	384	320	30.6	0.06	11.0	0.54
	A4	2700	1470	300	200	300	300	774	780	12.7	6	516	780	12.7	4	218	384	320	30.6	0.06	10.9	0.53
Yoshino et al. (1997)	No1	2000	1400	250	180	250	250	516	382	12.7	4	516	382	12.7	4	170	320	420	28.6	0.16	7.1	0.63
	No3	2000	1400	250	180	250	250	603	379	15.9	3	603	379	15.9	3	170	320	420	28.6	0.16	7.4	0.70
	No4	2000	1400	250	180	250	250	402	379	15.9	2	402	379	15.9	2	170	320	420	28.6	0.16	5.2	0.74
Kawasazaki et al. (1992)	MKJ1	2700	1470	300	200	300	300	568	771	19.1	2	568	771	19.1	2	220	384	675	84.4	0.13	13.8	1.15
Tateishi and Ishibashi (1998)	AIJ	3750	1800	400	300	350	350	1005	336	15.9	5	1005	336	15.9	5	314	852	363	23.5	0.04	23.2	0.68
	HBS	3750	1800	400	300	350	350	1032	388	12.7	8	1032	388	12.7	8	270	852	376	23.5	0.05	28.3	0.75
Leon (1990)	BCJ2	2032	2464	305	203	254	254	516	414	12.7	4	284	414	9.5	4	203	256	414	30.2	0.00	4.4	0.65
	BCJ3	2032	2464	305	203	305	254	516	414	12.7	4	284	414	9.5	4	203	256	414	30.2	0.00	5.0	0.59
	BCJ4	2032	2464	305	203	356	254	516	414	12.7	4	284	414	9.5	4	203	256	414	30.2	0.00	7.5	0.75
Leon (1984)	BCJ5	3448	3823	457	330	381	381	1530	414	25.4	3	852	414	19.1	3	304	1016	414	31.1	0.30	10.1	0.70
	BCJ8	3448	3823	457	330	381	381	1530	414	25.4	3	852	414	19.1	3	304	1016	414	31.1	0.00	10.7	0.75
	BCJ9	3448	3823	457	330	381	381	1530	414	25.4	3	852	414	19.1	3	304	1016	414	31.1	0.00	10.7	0.75
	BCJ11	3448	3823	457	330	381	381	1530	414	31.8	2	1020	414	25.4	2	304	1016	414	31.1	0.30	9.3	0.76
	BCJ12	3448	3823	457	330	381	381	1530	414	25.4	3	852	414	19.1	3	304	1016	414	31.1	0.30	10.1	0.70

Table 3-1. Test parameters of existing test specimens (Continued)

Specimens	Geometric properties <sup>a</sup>							Top re-bar of beam <sup>b</sup>				Bottom re-bar of beam <sup>b</sup>					Joint hoop <sup>c</sup>		Concrete strength	Axial load	Lateral load	Bond strength
	<i>L</i>	<i>H</i>	<i>h<sub>b</sub></i>	<i>b<sub>b</sub></i>	<i>h<sub>c</sub></i>	<i>b<sub>c</sub></i>	<i>A<sub>s</sub></i>	<i>f<sub>y</sub></i>	<i>d<sub>b</sub></i>	<i>n</i>	<i>A<sub>s</sub></i>	<i>f<sub>y</sub></i>	<i>d<sub>b</sub></i>	<i>n</i>	<i>h<sub>s</sub></i>	<i>A<sub>h</sub></i>	<i>f<sub>yh</sub></i>	<i>f<sub>c</sub></i>	<i>N<sub>c</sub> / (f<sub>c</sub></i>	<i>P<sub>0</sub></i>	<i>τ<sub>u</sub></i>	
																		(MPa)	<i>b, h<sub>c</sub></i> )	(MPa)	(MPa)	
Asou et al. (1993)	No1	2700	1450	400	300	440	440	1935	520	22.2	5	1935	520	22.2	5	298	1024	949	67.1	0.18	98.6	1.31

<sup>a</sup>)  $L$ = beam length (mm);  $H$ = column height (mm);  $h_b$ = beam depth (mm);  $b_b$ = beam width (mm);  $h_c$ = column depth (mm); and  $b_c$ = column width (mm)

<sup>b</sup>)  $A_s$ = area of re-bar (mm<sup>2</sup>);  $f_y$ = yield strength of re-bar based on material test result (MPa); and  $d_b$ = re-bar diameter (mm)

<sup>c</sup>)  $A_h$ = area of transverse bar (mm<sup>2</sup>); and  $f_{yh}$ = yield strength of transverse bar based on material test result (MPa)

According to Eligehausen et al. (1983), bond stress-slip relationship can be affected by bar diameter, concrete strength, clear spacing between bars, restraining bars, transverse pressure, loading rate, and position of bars during casting. Among these parameters, in beam-column connections, clear spacing between bars is related to joint transverse bars and column flexural bars, restraining bars is related to column flexural moment, and transverse pressure is related to axial force of column and transverse bars strength of joint. Unfortunately, because loading rate and concrete casting condition were not reported, these parameters were not considered. On the basis of the existing test result, various effects of test parameters causing bond stress including concrete tensile strength, axial force of column, column flexural moment-to-beam flexural moment ratio, joint shear strength, and transverse bars strength of joint were verified in analysis of test results.

In Fig. 3-6(d), friction bond stress  $\tau_u$  seems to correlate with concrete tensile strength  $\sqrt{f'_c}$ , but great error occurs. Test results of  $\tau_u$  were in range of Eq. (3-6a) proposed by Lowes and Altoontash (2003). Figs. 3-6(e) - (g) show the variation of  $\tau_u / \sqrt{f'_c}$  depending on flexural moment-to-beam flexural moment ratio, joint shear strength ratio, compressive stress of column, but these parameters were not critical.

Fig. 3-6(h) shows the influence of transverse bar strength to shear demand force  $V_u$  ratio at joint. As shown in this figure, friction bond stress  $\tau_u$  is increased proportionally to the transverse bar strength ratio. On the basis of the result, the friction bond stress was defined as follows.



$$\left(\tau_u / \sqrt{f'_c}\right) = 0.08 \left[ 1 + \left( A_h f_{yh} \right) / V_u \right] \quad (3-10)$$

where  $0 \leq (A_h f_{yh}) / V_u \leq 1.0$ ;  $A_h$  = sum of joint transverse bar area parallel to beam flexural bars;  $f_{yh}$  = yield strength of transverse bar;  $V_u = (\sum A_s f_y) - P_u$ ;  $\sum A_s$  = sum of top and bottom flexural bars of a beam;  $f_y$  = yield strength of beam flexural bar; and  $P_u$  = the maximum column shear force at the yielded joint by lateral load. In Eq. (3-10), the applied range of  $(A_h f_{yh}) / V_u$  is limited by test parameters.

The results of Fig. 3-6(h) and Eq. (3-10) show that bond strength in beam-column joint is correlated with diagonal cracking restraint effect and tension stiffening effect by joint transverse bars.

### 3.4 Verification of the Proposed Bond Model

For a verification of the proposed bond model, bond test results using concrete block performed by Viwathanatepa et al. (1979) were compared. Fig. 3-7 shows a bond test set-up and test results. In this test, to evaluate the bond behavior between a re-bar and concrete under cyclic loading, identical load  $F_b$  at both ends was applied to the re-bar in concrete block as same direction, and the re-bar elongation  $e_b$  was measured. Test parameters are re-bar diameter  $d_b$  ( $= 19.1 - 31.8$  mm) and development length  $h_c$  ( $= 381 - 635$  mm). Figs. 3-7(a) - (e) show the load-elongation ( $F_b$ - $e_b$ ) relationships of the specimens No.4, No.8, No.11, No.14, and No.17, respectively.  $F_b$ - $e_b$  relationships in Fig. 3-7 were measured at one side of the concrete block, and positive and negative load indicate that tension and compression forces  $F_b$  are applied to the re-bar, respectively. Because the tensile and compressive bond stresses are different (see Eqs. (3-4) and (3-5)), negative elongation  $e_b$  by compression force was measured less than the positive by tension force (see Figs. 3-7(c)-(e)).

Using the proposed bond model, the predictions of  $F_b$ - $e_b$  relationship were compared as thick dotted line in Figs. 3-7(a)-(e). The proposed stress in Eqs. (3-4), (3-5), and (3-10) were used as the elastic bond stress  $\tau_e$  and plastic bond stress  $\tau_u$ , respectively. The prediction by the existing bond model by Lowes and Altoontash (2003) was compared as thin dotted line. In the exiting model (Lowes and Altoontash, 2003),  $\tau_u = 0.23\sqrt{f'_c}$  was used as the average plastic bond stress of the model. Because the load and elongation of a re-bar

were measured at one side of concrete block and identical load is applied to the both ends in the test, load  $F_b$  was calculated as half bond strength integrating bearing and friction bond stress along the total development length  $h_c$ . On the other hand, positive and negative elongations  $e_b$  were calculated by integration of tensile and compressive re-bar strain, respectively (see Eq. (3-3)). Elastic modulus and hardening modulus of the re-bar were  $E_s = 200$  GPa, and  $E_{sh} = 0.01E_s$ , respectively.

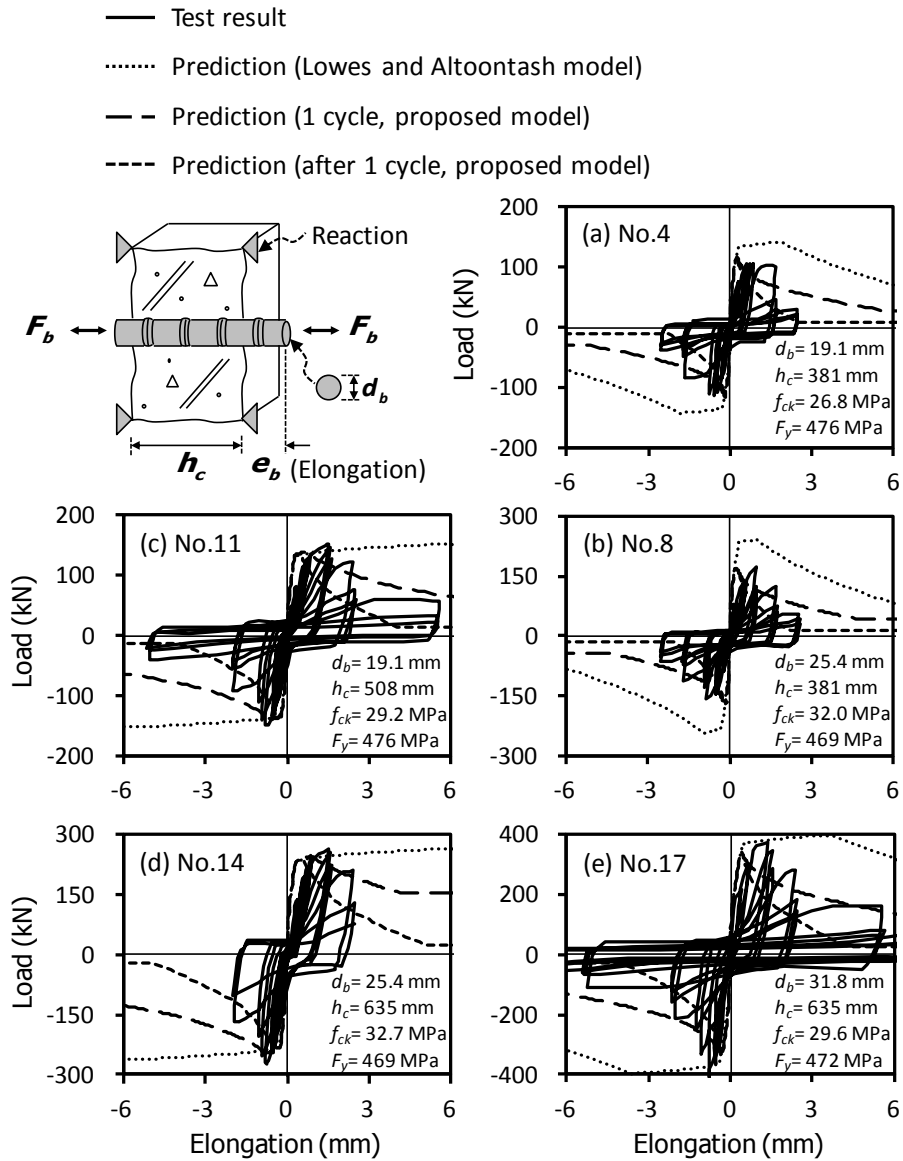


Fig. 3-7. Comparison between cyclic test and bond stress model

For specimen No.14 in Fig. 3-7(d), Specific calculation is as follows.  
 Bond length of concrete block  $h_c = 635$  mm; re-bar diameter  $d_b = 25.4$  mm;  
 concrete strength  $f_c' = 32.7$  MPa; cross-section area of joint hoop bar  $A_h = 1548$  mm<sup>2</sup>; yield strength of joint hoop bar  $f_{yh} = 493$  MPa; cross-section area of bond bar  $A_s = 510$  mm<sup>2</sup>; yield strength of bond bar  $f_y = 469$  MPa; bond stress  $\tau_c (= 2.2\sqrt{f_c'}) = 12.6$  MPa;  $\tau_e (= 1.8\sqrt{f_c'}) = 10.3$  MPa;  $\tau_u (= C_0\sqrt{f_c'}) = 0.92$  MPa ( $V_u = A_s f_y$  for concrete block); re-bar yield strain  $\varepsilon_y = 0.0023$ ; elastic modulus of re-bar  $E_s = 200000$  MPa; and hardening modulus of re-bar  $E_{sh} (= 0.01 E_s) = 2000$  MPa. Elongation of re-bar at bond region is determined from integration of strain  $\varepsilon$  along bond length of concrete block  $h_c$  in Fig. 3-8. For a re-bar strain  $\varepsilon_t = 0.01$ , strain distribution of re-bar in the concrete block is as follows.

$$l_u = (\varepsilon_t - \varepsilon_y) \frac{E_{sh} d_b}{4\tau_u} = 106.0 \text{ mm} \quad (3-11a)$$

$$l_e = \varepsilon_y \frac{E_s d_b}{4\tau_e} \leq (h_c - 2l_u) = 282.3 \text{ mm} \quad (3-11b)$$

$$l_c = h_c - 2l_u - l_e = 140.7 \text{ mm} \quad (3-11c)$$

$$\varepsilon_{oo} = \varepsilon_y - \frac{4\tau_e}{E_s d_b} l_e = 0.0 \quad (3-11d)$$

$$\varepsilon_{co} = -\frac{4\tau_c}{E_s d_b} l_c = -0.0014 \quad (3-11e)$$

$$\varepsilon_c = \varepsilon_{co} - \frac{4\tau_u}{E_s d_b} l_u = -0.0015 \quad (3-11f)$$

When the above tensile strain is integrated, elongation of re-bar  $e_b$  is as follows.

$$e_b = \frac{\varepsilon_y l_e}{2} + \frac{(\varepsilon_t + \varepsilon_y) l_u}{2} = 0.97 \text{ mm} \quad (3-12)$$

Bond strength applied to re-bar  $2F_b$  is determined from the integration of bond stress of the re-bar at the bond length of concrete block  $h_c$ .

$$2F_b = (l_e \tau_e + 2l_u \tau_u + l_c \tau_c)(\pi d_b) = 388.6 \text{ kN} \quad (3-13)$$

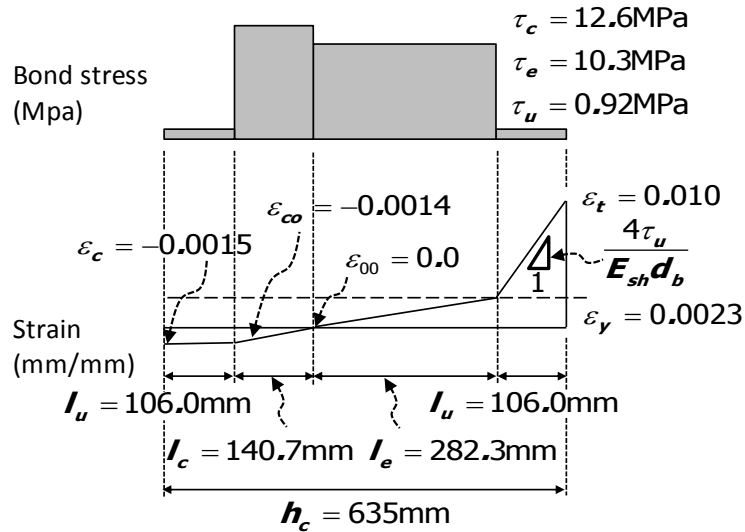


Fig. 3-8. Strain distribution of re-bars for No.14

Using the same method, elongation  $e_b$  and bond strength  $F_b$  of re-bar for any strain can be calculated.

In the bond test, three times cyclic loading was applied to each deformation. As shown in Fig. 3-7, the proposed model underestimated the bond strength for the 1<sup>st</sup> cyclic loading, but agreed well with envelope curves and bond strength for the 2<sup>nd</sup> and 3<sup>rd</sup> cyclic loadings. This is because friction bond stress  $\tau_u$  in the proposed model was evaluated from the large inelastic re-bar subjected to cyclic loading. To predict the bond strength for the 1<sup>st</sup> cyclic loading as shown in Fig. 3-7, the friction bond stress should be defined as approximately  $3\tau_u$ .

On the other hand, the bond model by Lowes and Altoontash (2003) using an average  $\tau_u = 0.23\sqrt{f'_c}$  overestimated the bond strength. Particularly, as shown in Figs. 3-7(a) and (b), test results were overestimated for specimens No.4 and No.8 with insufficient development length. This is because the bond model by Lowes and Altoontash (2003) does not consider the symmetric damage of friction bond stress  $\tau_u$  and bond length  $l_u$  at the left and right side of concrete block subjected to cyclic loading (see Fig. 3-4).

For specimen No.14, strain distribution of a re-bar was compared inside a concrete block. Solid line, dotted line, and dot-and-dash line indicate test result, prediction by the proposed model, and prediction by Lowes and Altoontash (2003), respectively. Figs. 3-9(a) and (b) show strain distribution of the re-bar at the right side of the concrete block when the re-bar yields and

large inelastic strain( $=0.0011$ ) occurs, respectively. When the re-bar yields and inelastic deformation occurs at the right side, most bond damage is occurred at the interface by yield penetration of the re-bar, as shown in Fig. 3-9. The proposed bond model predicted relatively well the bond stress degraded portion and strain distribution of the re-bar inside the joint depending on the increment of the re-bar strain.

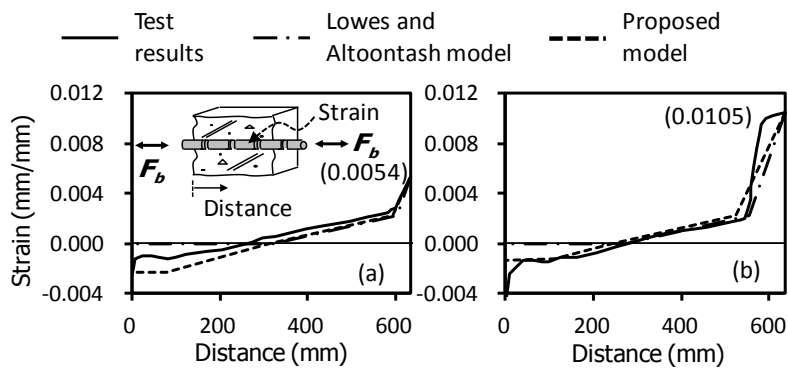


Fig. 3-9. Comparison of strain distribution for No.14 (Elmorsi et al., 2000)

Fig. 3-10 shows the strain distributions of beam bottom flexural bar in beam-column joint subjected to cyclic loading tested by Hwang et al. (2013), Lee et al. (2009), Dai and Park (1987), Asou et al. (1993), and Kawai et al. (1997). For inelastic strain after yielding of the beam flexural bar at the joint interface, prediction was compared with test result. The measured results are indicated by rectangles, and the predictions by Lowes and Altoontash (2003) and the proposed model were indicated by dot-and-dash line and dotted line, respectively. The vertical and horizontal axes indicate the re-bar strains and



the distances from the left interface of the joints.

As shown in Fig. 3-10, after large inelastic deformation of beam flexural bars, tensile strain was occurred at the beam flexural bars in the total joint length by yield penetration. The proposed model predicted relatively well the re-bar strain distribution. On the other hand, the existing model by Lowes and Altoontash (2003) slightly underestimated the re-bar strain distribution. This is because, for the cyclic loading more than twice, the strain was significantly decreased by the overestimated friction bond stress  $\tau_u$ , which increased the strain incline  $4\tau_u/E_{sh}d_b$  at the friction bond length  $l_u$  by Eq. (3-2b).

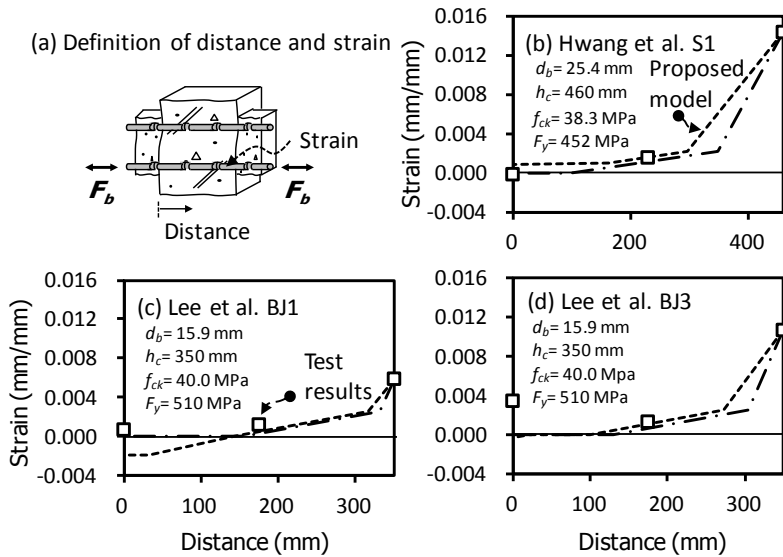


Fig. 3-10. Comparison of strain distribution after yielding of re-bars (Continued)

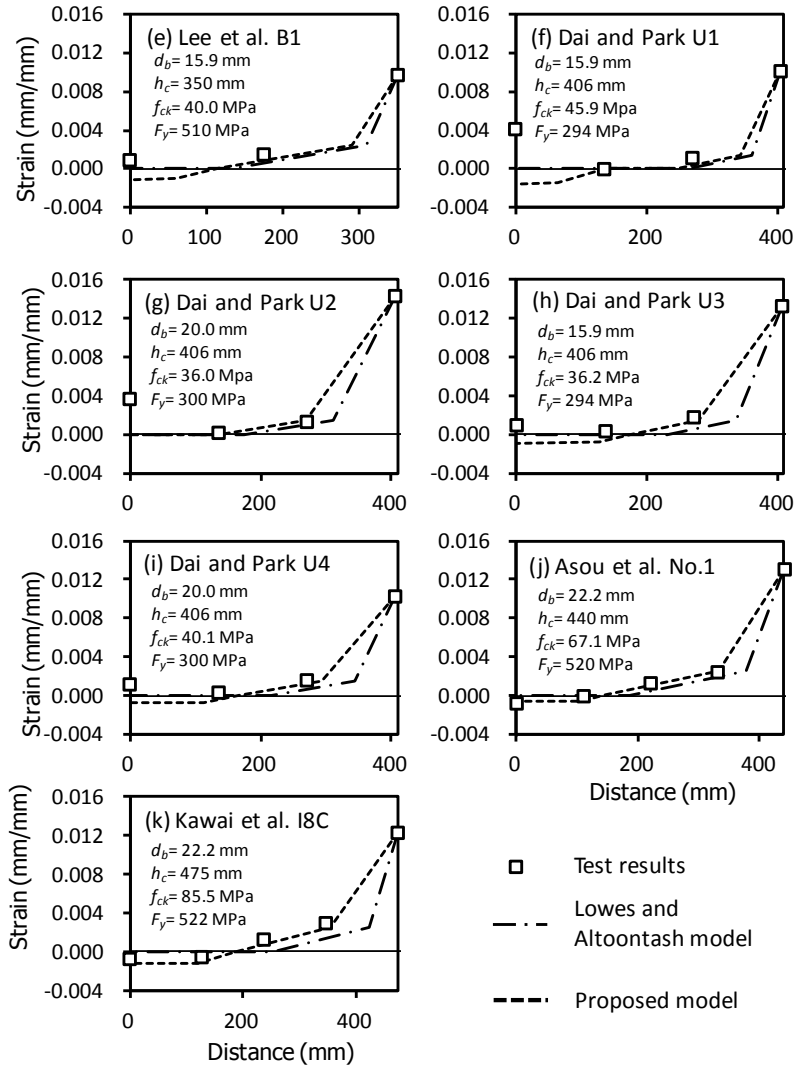


Fig. 3-10. Comparison of strain distribution after yielding of re-bars

Fig. 3-11 shows the elongation  $e_b$  of a beam flexural bar measured at the joint interface in beam-column joint subjected cyclic loading (Kawai et al., 1997; Xian et al., 1992). In this figure, the vertical and horizontal axes indicate the elongation  $e_b$  by Eq. (3-3) and the tensile strain of the re-bar  $\varepsilon_t$  at

the joint interface. Test results are indicated by rectangles, and the  $e_b$  predicted by Lowes and Altoontash (2003) and the proposed model were indicated by dot-and-dash line and dotted line, respectively. As shown in this figure, the prediction  $e_b$  of the proposed model agreed relatively well with the test results. On the other hand, the bond model by Lowes and Altoontash (2003) underestimated the elongation  $e_b$ . The reason why is that, as mentioned above, the inelastic strain portion of the re-bar is short by the overestimated  $\tau_u$  in the bond model of Lowes and Altoontash (2003).

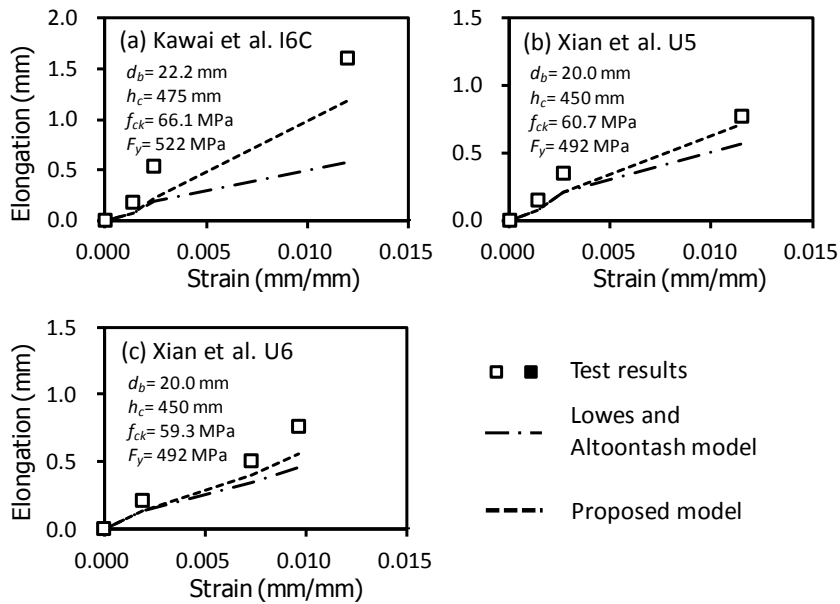


Fig. 3-11. Comparison of elongation of beam re-bars

In Fig. 3-10, the proposed bond model estimated the compressive strain and stress of a beam flexural bar at the left joint interface, but test result was

measured as tension. This is because the beam flexural bar is affected by tensile residual deformation under cyclic loading (Eom and Park, 2009). In the proposed model, the tensile residual deformation was not considered. However, because tensile strain is much greater than compressive strain in prediction, as shown in Fig. 3-11, the residual deformation of the re-bar is not critical to total bond deformation  $e_b$ .

### 3.5 Bond Performance Requirement

To secure seismic performance of beam-column joint, significant bond-slip of a beam flexural bar is restrained, and a sufficient bond resistance should be provided to resist tension force of the beam flexural bar at the joint. When tension force of the flexural bar is anchored at the opposite beam by the re-bar bond-slip, beam flexural moment is decreased by the compression zone increment of the beam section (Hakuto et al., 1999). Thus, the tension of the beam flexural bar should be resisted in the joint. To prevent the bond-slip, the sum of bearing bond length  $l_e$  and friction bond length  $l_u$  to resist the yield strength of the re-bar should be less than the joint length  $h_c$ . That is, as shown in Fig. 3-4(b), the yield strength of the re-bar  $f_y (= E_s \varepsilon_y)$  should be resisted at the center of the joint  $l_e$  (i.e.  $l_e = \varepsilon_y (E_s d_b) / (4\tau_e)$ ), and the bond stress by inelastic deformation of the re-bars should be resisted at bond stress degraded portion  $l_u (= (\varepsilon_t - \varepsilon_y)(E_{sh} d_b) / (4\tau_u))$  in the left and right joint interface. Thus, depth of column section  $h_c$  should be satisfied as follows.

$$h_c \geq l_e + 2l_u = \varepsilon_y \frac{E_s d_b}{4\tau_e} + 2(\varepsilon_t - \varepsilon_y) \frac{E_{sh} d_b}{4\tau_u} \quad (3-14)$$

where  $\varepsilon_t$  = the maximum tensile strain of a beam flexural bar at the joint interface. Substituting  $\tau_e$  in Eq. (3-4),  $\tau_u$  in Eq. (3-10),  $E_{sh} = 0.01E_s$ , yield curvature of a beam section  $\varphi_y = 1.7\varepsilon_y / h_b$  (Priestley, 2000), and curvature of a beam section  $\varphi_t = \varepsilon_t / (d-c)$  (where,  $h_b$  = beam height,  $d$  = effective beam depth,

and  $c$ = neutral axis depth at a beam section) into Eq. (3-14), the requirement of column depth -to- bar diameter ratio ( $h_c/d_b$ ) can be determined.

$$\begin{aligned} \frac{h_c}{d_b} &\geq \frac{f_y}{\sqrt{f'_c}} \left[ \frac{1}{7.2} + \frac{0.01}{2C_0} (\varepsilon_t/\varepsilon_y - 1) \right] \\ &\simeq 0.001 \frac{f_y}{\sqrt{f'_c}} \left[ 140 + [8.5\mu_\phi (d - c)/h_b - 5] / C_0 \right] \end{aligned} \quad (3-15)$$

In Eq. (3-15), the requirement of  $h_c/d_b$  can be defined as a function of re-bar yield strength  $f_y$ , concrete strength  $f'_c$ , curvature ductility demand of a beam  $\mu_\phi = \phi_t / \phi_y$ , tension zone depth ratio of a beam section  $(d - c)/h_b$ , and parameter of joint bond strength  $C_0 = 0.08[1 + (A_h f_{yh})/V_u]$  ( $0 \leq (A_h f_{yh})/V_u \leq 1.0$ ).

In Fig. 3-12, the requirements of  $h_c/d_b$  specified in Eq. (3-15), ACI 318-11 (2011), ACI 352R-02 (2002), NZS 3101:2006 (2006), and Eurocode 8 (2004) were compared according to concrete strength  $f'_c$ , re-bar yield strength  $f_y$ , and curvature ductility  $\mu_\phi$ .

$$\frac{h_c}{d_b} \geq 20 \quad \text{in ACI 318-11} \quad (3-16a)$$

$$\frac{h_c}{d_b} \geq 20 \frac{f_y}{420} \geq 20 \quad \text{in ACI 352R-02} \quad (3-16b)$$

$$\frac{h_c}{d_b} \geq \frac{1.25 f_y}{3.3 \alpha_f \alpha_d \gamma \sqrt{f'_c}} \quad \text{in NZS 3101:2006} \quad (3-16c)$$

$$\frac{h_c}{d_b} \geq \frac{\gamma_{Rd} f_y}{7.5 f_{ctm}} \frac{1 + 0.75 k_D \rho' / \rho_{\max}}{1 + 0.8 v_d} \quad \text{in Eurocode 8} \quad (3-16d)$$

where  $\alpha_f$  = coefficients addressing the direction of the beam flexural bars (= 0.85 - 1.0);  $\alpha_d$  = coefficients addressing the ductility of beam plastic hinges (=1.0 - 1.2); and  $\gamma$  = coefficient addressing the story drift ratio demand  $\delta$  of the joint (= 1.53 - 0.29 $\delta$ ,  $\delta$  in %) in Eq. (3-16c).  $\gamma_{Rd}$  = overstrength factor of the beam flexural bars (= 1.0 - 1.2);  $f_{ctm}$  = concrete tensile strength (=0.3<sup>3</sup> $\sqrt{f_c'}$ <sup>2</sup>);  $k_D$  = coefficients addressing the ductility (= 0.67 - 1.0);  $\rho' / \rho_{\max}$  = compression bar ratio / the maximum tension bar ratio of the beam; and  $v_d$  = column axial load ratio in Eq. (3-16d). In Fig. 3-12,  $\alpha_f = 1.0$ ,  $\alpha_d = 1.0$ ,  $\gamma = 1.0$ ,  $\gamma_{Rd} = 1.2$ ,  $k_D = 1.0$ ,  $\rho' / \rho_{\max} = 1.0$ , and  $v_d = 0$  were applied.

Yield strength of a beam flexural bar  $f_y = 400$  MPa and concrete strength  $f_c' = 40$  MPa were used in Fig. 3-12(a) and (b), respectively. In Fig. 3-12(c), yield strength of a beam flexural bar  $f_y = 400$  MPa and concrete strength  $f_c' = 40$  MPa were used.  $(d-c)/h_b = 0.7$  and  $C_0 = 0.125$ , which is average value in Fig. 3-6(h), were applied to Eq. (3-15). In Fig. 3-12(a), the requirements of  $h_c/d_b$  specified in Eq. (3-15), ACI 318-11 (2011), ACI 352R-02 (2002) were the least among the requirements, and the other requirements decreased as the concrete strength increased. In Fig. 3-12(b), the requirements of  $h_c/d_b$  were increased with the re-bar yield strength. In Fig. 3-12(c), the requirement of  $h_c/d_b$  specified in Eq. (3-15) was increased with the curvature ductility demand of a beam. The requirement of Eq. (3-15) was similar to those of NZS 3101:2006 (2006) and Eurocode 8 (2004) depending on concrete strength and

re-bar yield strength. For the ductility demand of a beam  $\mu_\phi = 6$  and 9, the requirement of Eq. (3-15) agreed well with those of NZS 3101: 2006 (2006) and Eurocode 8 (2004), respectively.

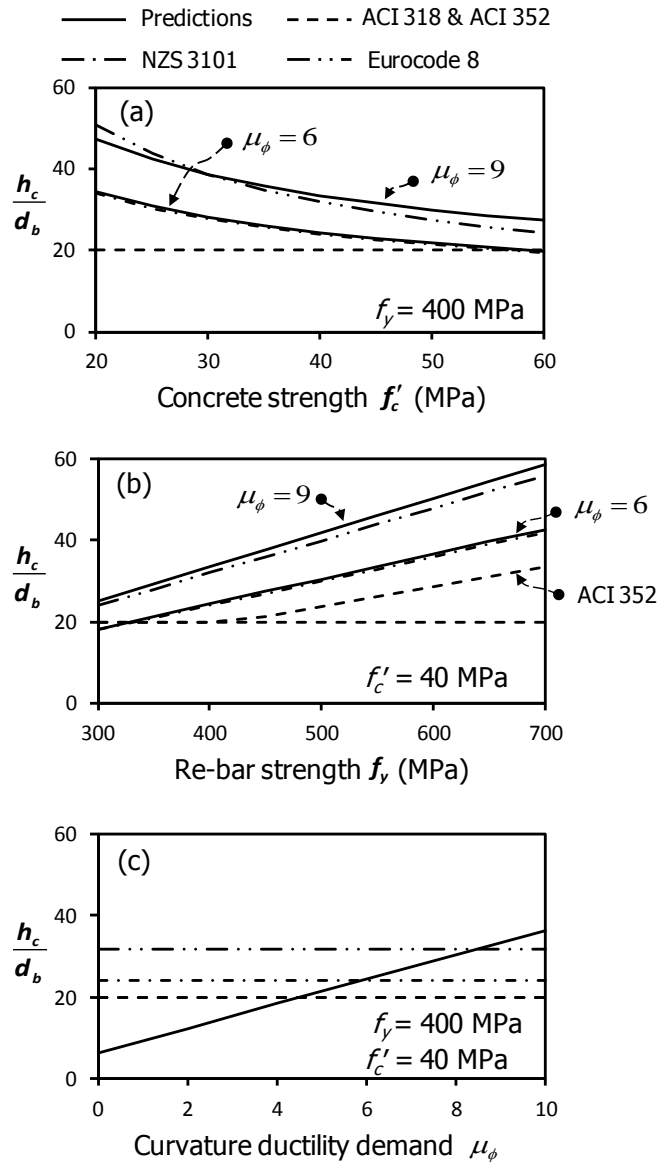


Fig. 3-12. Comparison of design requirement  $h_c/d_b$  for interior beam-column joint



In Eq. (3-15), as the ductility demand of a beam increases, the bond requirement was increased. Thus, the proposed equation can be used at performance based design for beam-column joint. When the top and bottom flexural bars of a beam section are different, Eq. (3-15) should be satisfied for each case.

### 3.6 Discussion

In the present study, simplified bond strength model and bond-slip relationship of re-bar in interior beam-column joint subjected to cyclic loading were studied. The results of this study are summarized as follows.

- 1) To consider bond-slip of beam flexural bars in RC beam-column joint subjected to cyclic loading, strain distribution of re-bar due to yield penetration was proposed. Under cyclic loading, because tensile yielding of re-bar occurs repeatedly at left and right beams of the joint, once degraded bond stress  $\tau_u$  by yield penetration of the re-bar was not recovered. Therefore, in the proposed model, after re-bar yielding, bond stress at the both sides of the joint was decreased equally by cyclic loading.
- 2) For RC beam-column joint with complete bond failure, bond-slip is occurred without the load increment at unloading/reloading behaviors, and constant load is remained by residual friction bond stress  $\tau_u$ .  $\tau_u$  was determined from the hysteresis curves of the RC beam-column joint with complete bond failure to evaluate the bond stress degraded by cyclic loading.  $\tau_u$  was related to joint hoop bar strength and joint shear demand force as well as concrete tensile strength.
- 3) To evaluate the proposed model, the bond-slip relationship and strain

distribution of re-bar predicted by the proposed model was compared with the test results of the component test using concrete block and beam-column joint. The predictions agreed well with bond-slip, bond stress degradation, strain distribution, and elongation of the re-bar under cyclic loading.

- 4) On the basis of the bond stress model, joint depth -to- diameter of beam flexural bar ratio  $h_c/d_b$  was proposed to restrain the bond-slip of re-bar. As concrete strength increases, the requirement of  $h_c/d_b$  was decreased, and as the ductility demand of a beam increases, the requirement of  $h_c/d_b$  was increased. Particularly, the proposed equation at curvature ductility demand 6 and 9 was similar to the requirements specified on NZS 3101:2006 (2006) and Eurocode 8 (2004), respectively.

## Chapter 4. Joint Shear Strength and Deformation Capacity

### 4.1 Introduction

In reinforced concrete moment resisting frames subjected to earthquake load, the beam-column joint is significantly affected by the concrete diagonal cracking, shear deformation, and bond-slip of a beam flexural bar at the joint (Kitayama et al., 1987; Leon, 1989; Hakuto et al., 1999; Meinheit and Jirsa, 1977; Bonacci and Pantazopoulou, 1993; Lee et al., 2009; Lee and Lin, 2011; Hong et al., 2011). To prevent structure damage at the joint, current design codes, such as ACI 318-11 (2011), ACI 352R-02 (2002), and KCI 2012 (2012), specify the requirements of bond resistance of beam flexural bars penetrating into the joint ( $= h_c/d_b$ , where  $h_c$ = column depth;  $d_b$ = diameter of beam flexural bars) and joint shear strength ( $= V_c$ ) for earthquake design.

Fig. 4-1 shows failure modes of interior beam-column connections depending on bar-bond and shear resistance. As Shown in Fig. 4-1(a), as a column depth  $h_c$  is larger, the bond resistance of beam flexural bars and joint shear strength are increased. As a result, structure damage is restrained at the joint, and most of inelastic deformation occurs at the plastic hinge of the beam. On the other hand, as shown in Fig. 4-1(c), when the column depth  $h_c$  is small, early failure can be occurred at the joint because the bond-slip of the beam flexural bars increases and the joint shear resistance decreases.

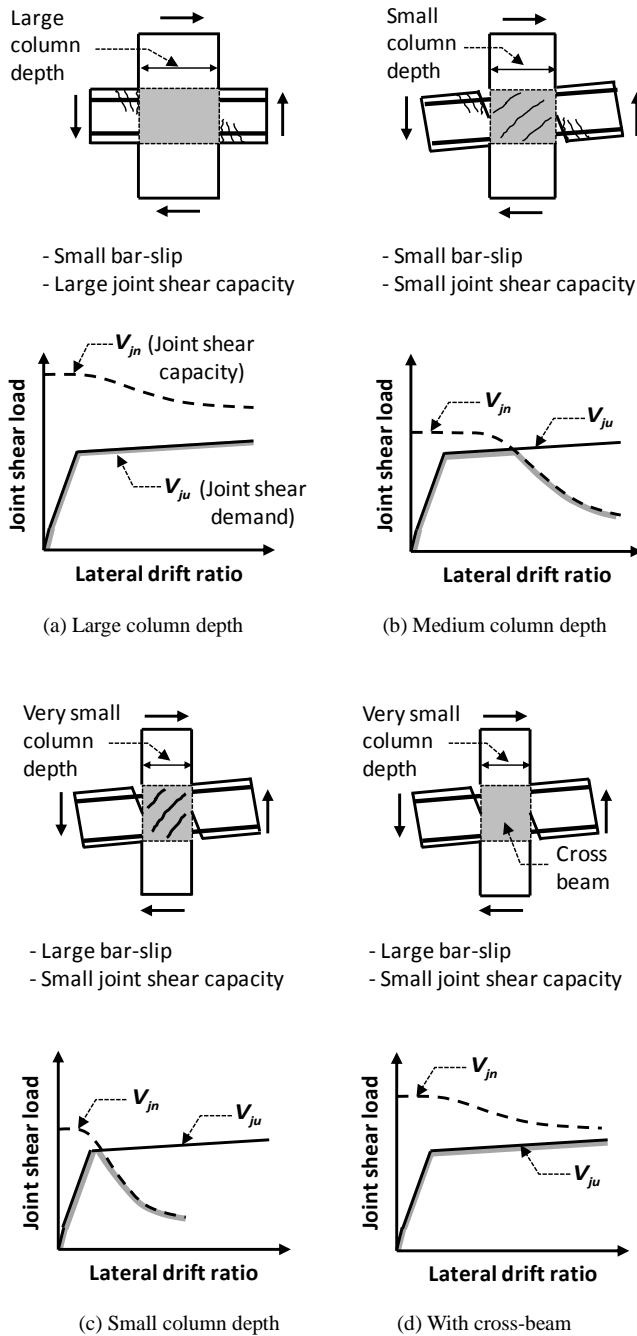


Fig. 4-1. Failure modes of interior beam-column connection depending on bar-bond and shear resistance

According to existing cyclic loading test of beam-column connections (Lee et al., 2009; Priestley, 2000; Hwang et al., 2013), in the beam-column joints satisfying the minimum requirements of bond resistance and joint shear strength specified on current design codes including ACI 318-11 (2011), ACI 352R-02 (2002), and KCI 2012 (2012), plastic deformation occurs at the beam plastic hinge and the joint at the same time as shown in Fig. 4-1(b). In this case, either joint shear failure or plastic hinge failure at the beam is possible. Fig. 4-1(d) shows the joint confined with cross beams. Because the joint shear strength  $V_{jn}$  is significantly increased by the cross beams despite the small column depth, anchorage slip due to bond failure of beam flexural bars is converged to the joint interface. Ultimately, load-carrying capacity is decreased by concrete crushing at the beam cross-section or re-bar fracture due to low-cycle fatigue.

Until a recent date, a lot of researches have been studied for shear strength and deformation capacity of beam-column connections (Lee et al., 2009; Lee and Lin, 2011; Hong et al., 2011; FEMA 356, 2000; Hwang and Lee, 2000; Murakami et al., 2000; Park et al., 2012). FEMA 356 (2000) specified the allowable shear deformation of beam-column joint on the basis of re-bar details. Hwang and Lee (2000) proposed joint shear strength using strut-tie model that considers joint shear deformation. Murakami et al. (2000) evaluated the joint deformation capacity by analyzing parameters including joint shear demand, hoop bar ratio, and yield strength of re-bars from existing joint test results. Lee et al. (2009) evaluated the joint deformation capacity on the basis of the joint shear strength degradation depending on strain

accumulation at the joint subjected cyclic loading. Lee and Lin (2011) studied the load-carrying capacity degradation of the joint with the deformation increment on the basis of bond resistance of beam flexural bars and hoop bar ratio at the joint. Hong et al. (2011) proposed the evaluation model for joint shear strength and deformation capacity based on bond-stress distribution of beam flexural bars. Park et al. (2012) evaluated the deformation capacity considering arch and truss action of the joint according to rotation angle of the beam.

In this chapter, for performance based design of beam-column connection, on the basis of existing theories and test results, joint deformation based shear strength evaluation model was developed. To improve the joint shear strength model, the following was considered.

- 1) Unlike existing studies concentrating into failure mechanism of a joint panel, in the present study, interaction between a beam cross-section and the joint as well as the joint panel were considered. As shown in Fig. 4-1, the proposed model was developed to predict various joint failure mechanisms according to design parameters. That is, the various failure mechanisms including gap at the joint interface due to bond-slip of beam flexural bars and flexural failure of beam cross-section due to increasing anchorage strength of re-bars as well as joint shear failure were considered.
- 2) Shear strength and deformation capacity of joint panel were significantly

affected by bond-slip of beam flexural bars. To predict the bond-slip, bond-strength and –slip model for interior beam-column joint developed in Chapter 3 was applied. The bond model was developed to consider the damage due to cyclic loading by analyzing existing beam-column joint test results.

- 3) Load-carrying capacity and deformation capacity of beam-column connection are affected by the number of cyclic loading. In this study, the damage affected by cyclic loading was considered.



## 4.2 Shear Force Transferred to Joint

Fig. 4-2 shows the joint horizontal shear force  $V_u$  applied to beam-column connection by the top and bottom flexural bars yielding of beams cross-section. For the bottom flexural bars of beam cross-section, joint shear demand  $V_u$  is determined from equilibrium condition of tension force  $T_{s2}$  of bottom bars at the right joint interface, compression force  $C_{s1}$  of the bottom bars at the left interface, bearing force  $C_1$  at beam compression zone, and column lateral load  $P_u$ .

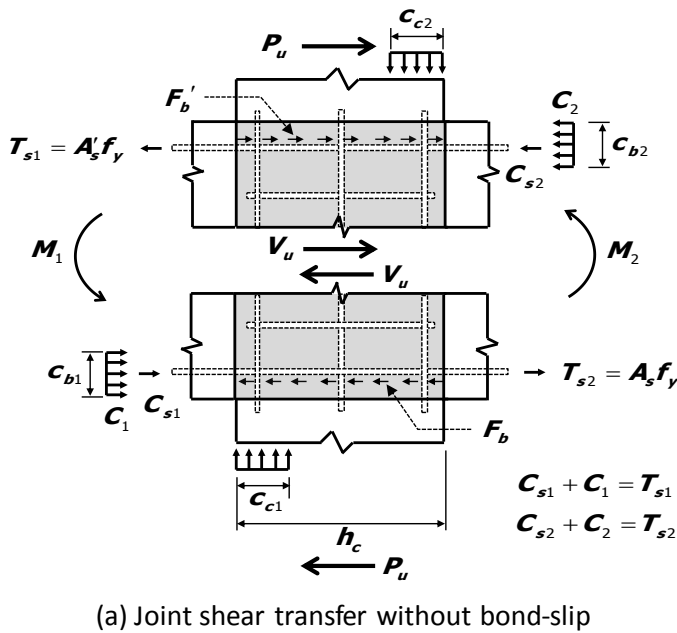


Fig. 4-2. Load-transfer mechanisms at beam-column joints (Continued)

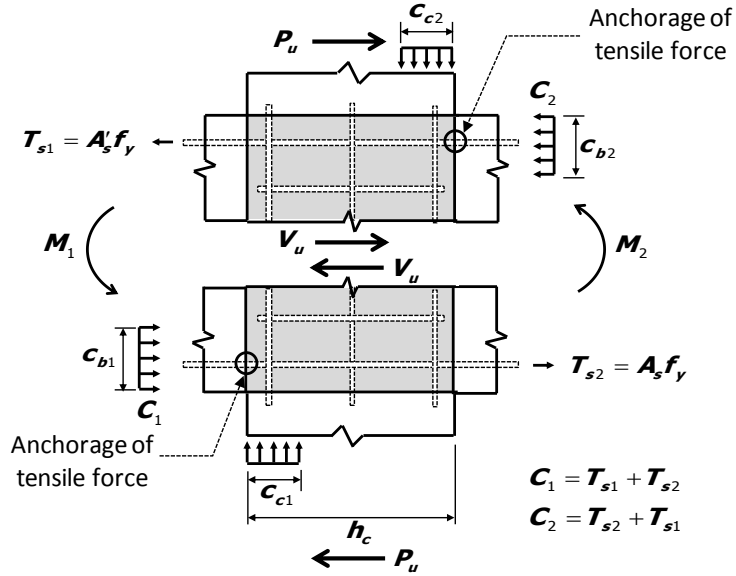


Fig. 4-2. Load-transfer mechanisms at beam-column joints

$$V_u = C_1 + C_{s1} + T_{s2} - P_u = (A_s + A'_s) f_y - P_u \quad (4-1)$$

where sum of beam compression zone and compression force of bottom bars  $C_1 + C_{s1}$  is identical to tension force of top bars  $T_{s1}$  due to equilibrium condition of left beam cross-section;  $A_s$  = sectional area of bottom flexural bars;  $A'_s$  = sectional area of top flexural bars; and  $f_y$  = re-bar yield strength.

When a sufficient bond strength of re-bars is developed at the joint, bearing force of beam compression zone  $C_1$  is applied to the left joint interface, and tension force  $T_{s2}$  and compression force  $C_{s1}$  of beam bottom flexural bars are transferred by the bond strength  $F_b$  into the joint (see Fig. 4-

2(a)). On the other hand, in the joint with the insufficient bond strength of re-bars, bond-slip of re-bars occurs, and tension force and compression force of re-bars are not transferred to the joint. Because tension force  $T_{s2}$  of the beam bottom bars is resisted by anchorage at the opposite beam, the bearing force at the compression zone of the opposite beam transfers the tension force  $T_{s1}$  of top bars and the tension force  $T_{s2}$  of the bottom bars to the joint by the equilibrium condition of the beam cross-section and the anchorage, respectively (see Fig. 4-2(b)). As a result, although joint shear demand  $V_u$  at the joint with bond-slip is same to that of the joint without bond-slip, diagonal cracking is significantly occurred at the joint with bond-slip because the joint shear demand is not distributed by bond strength of re-bars but most of joint shear demand is transferred by bearing force.

In interior beam-column connections, bond strength  $F_b$  can be determined from re-bar diameter, the number of re-bars, and bond stress proposed in Chapter 3. In this study, for strong-column-weak beam connections, it is assumed that the bond strength of column flexural bars is greater than that of beam flexural bars (i.e. beam flexural bars yields at the joint interface). For weak column-strong beam connections, because column flexural bars yields at the joint interface, the bond-slip of the column flexural bars instead of the beam flexural bars should be considered.

After bond failure at the joint, tension re-bars of a beam is anchored to the compression zone of the opposite beam for tension force excluding bond strength. Therefore, the compression zone depth of the beam  $c_{b1}$  and  $c_{b2}$

consist of the compression force by equilibrium condition of the tension re-bars and the compression force by anchorage of the opposite tension re-bars. For ultimate state, the compression zone depth is as follows.

$$c_{b1} = \frac{(A_s + A'_s) f_y - F_b}{0.85 f'_c b_b} \geq \frac{A'_s f_y}{0.85 f'_c b_b} \quad (4-2a)$$

$$c_{b2} = \frac{(A_s + A'_s) f_y - F'_b}{0.85 f'_c b_b} \geq \frac{A_s f_y}{0.85 f'_c b_b} \quad (4-2b)$$

where  $F_b$  and  $F'_b$  = bond strength of bottom and top bars penetrating into the joint ( $F'_b \approx (A'_s/A_s)F_b$ );  $f'_c$  = concrete strength; and  $b_b$  = width of beam section. As the re-bar strain increases, bond strength of re-bar is decreased and compression zone depth is increased.

In strong column-weak beam connections, because the column flexural bars would not be yielded, the column compression zone depth  $c_{c1}$  and  $c_{c2}$  is determined from section analysis, or is approximately as follows.

$$c_{c1} \text{ or } c_{c2} = \left( 0.25 + 0.85 \frac{N_c}{f'_c b_c h_c} \right) h_c \leq h_c \quad (4-3)$$

where  $N_c$  = compression load at column ( $> 0$ ); and  $b_c$  = width of column section.

### 4.3 Joint Shear Resistance Capacity

Figs. 4-3 and 4-4 show joint shear resistance mechanisms of concrete panel after diagonal cracking in interior beam-column connections. According to Hong et al. (2011) and Paulay and Priestley (1992), joint shear resistance consists of truss mechanism by distributed shear stress at a joint panel (Fig. 4-3) and strut mechanism by diagonal strut action connecting the corner of the joint panel (Fig. 4-4).

Basically, after diagonal cracking at the joint, distributed shear stress for truss mechanism is transferred by bond strength of beam flexural bars. Diagonal compression force by diagonal strut action is applied to the joint panel corners as bearing force by compression zones of beam and column. Some of compression field by truss mechanism coincides with diagonal strut by strut mechanism. Thus, in the present study, the shear resistance by diagonal strut is defined as  $V_C$ , and the shear resistance by truss mechanism applying to joint area except diagonal strut is defined as  $V_T$ .

In beam-column joint, nominal shear strength of concrete panel  $V_{jn}$  is sum of the diagonal compression field resistance and the diagonal strut resistance.

$$V_{jn} = V_T + V_C \quad (4-4)$$

### 4.3.1 Resistance by Truss Mechanism $V_T$

Bond strength provided by beam flexural bars was idealized to develop the distributed shear stress at joint panel. The shear stress induces the diagonal compression field of concrete, tension force occurs at joint hoop bars. Therefore, shear resistance by truss mechanism  $V_T$  is determined from the minimum value between the diagonal compression field strength  $V_{cf}$  and the tension strength of the hoop bars  $A_h f_{yh}$ , and should be less than the bond strength  $F_{bt}$  of beam flexural bars applied to truss mechanism region ( $h_c - l_s$ ) (see Fig. 4-3).

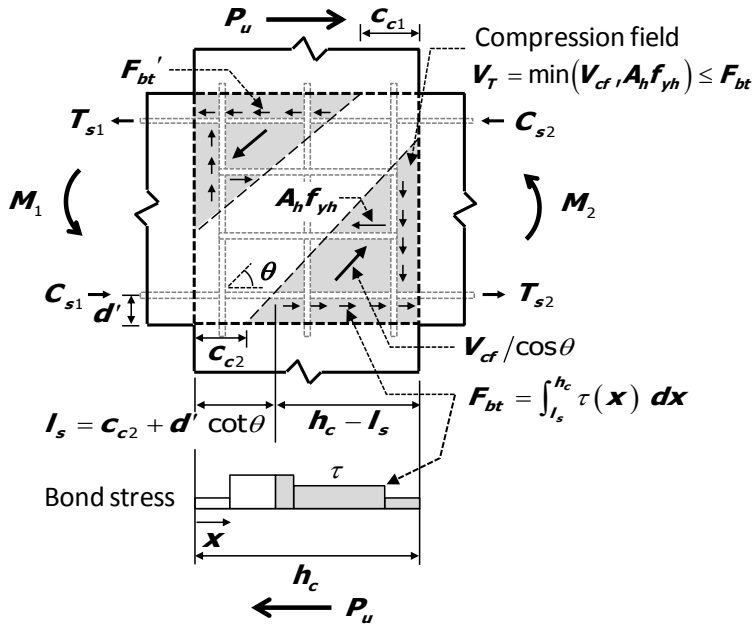


Fig. 4-3. Truss mechanism in joint panel

$$V_T = \min(V_{cf}, A_h f_{yh}) \leq F_{bt} \quad (4-5a)$$

$$F_{bt} = \int_{l_s}^{h_c} \tau(x) dx \quad (4-5b)$$

$$V_{cf} = f_{ce,f} [0.5(h_c - l_s) \sin \theta] t \cos \theta \quad (4-5c)$$

where  $A_h$  = effective sectional area of joint hoop bars;  $f_{yh}$  = yield strength of hoop bars;  $F_{bt}$  = bond strength applied to truss mechanism region ( $h_c - l_s$ );  $l_s$  = length of beam re-bars penetrating into the diagonal strut ( $= c_{c2} + d' \cot \theta$ );  $c_{c2}$  = compression field depth of column cross-section by strut mechanism ( $=$  Eq. (4-3));  $d'$  = distance from beam bottom face to bottom re-bars;  $\theta$  = concrete strut angle ( $=$  Eq. (4-5));  $f_{ce,f}$  = effective compression strength of diagonal compression field in truss mechanism region ( $=$  strength applying  $\varepsilon_{I,f}$  instead of  $\varepsilon_I$  in Eq. (4-14)); and  $t$  = depth of diagonal compression field ( $=$  strut depth in Eq. (4-9)). In Eq. (4-5c), it is assumed that principal stress directions in the diagonal compression field coincide with principal stress directions in the diagonal strut, and the tapered sectional area of the diagonal compression field is equal to average sectional area of the diagonal compression field.

#### 4.3.2 Resistance by Diagonal Strut $V_C$

As shown in Fig. 4-4, joint shear resistance by diagonal strut  $V_C$  is determined from compression resistance of concrete strut connecting C-C-C node developed at joint corner by beam and column flexural moments. Fig. 4-

4 shows the configuration of the diagonal concrete strut at the joint.  $c_{b1}$  and  $c_{b2}$  indicate compression zone depth of beam cross-section at left and right joint interface (see Eq. (4-2)).  $c_{c1}$  and  $c_{c2}$  indicate compression zone depth of column cross-section at top and bottom joint interface (see Eq. (4-3)).

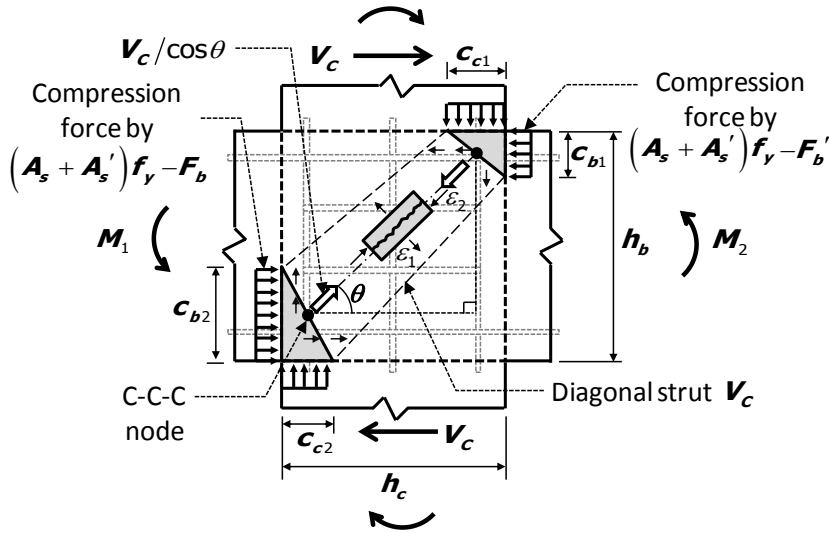


Fig. 4-4. Diagonal strut strength

In beam-column connections, because the sectional area of top flexural bars is not identical to that of bottom flexural bars at beam cross-section ( $A_s' \neq A_s$ ), width of the diagonal strut was not uniform at the joint. Thus, as shown in Fig. 4-4, average values are used in angle  $\theta$  and width  $w$  of concrete strut.

$$\theta = \text{atan} \left( \frac{h_b - (c_{b1} + c_{b2})/2}{h_c - (c_{c1} + c_{c2})/2} \right) \quad (4-6)$$



$$w = \frac{(c_{c1} + c_{c2})\sin\theta + (c_{b1} + c_{b2})\cos\theta}{2} \quad (4-7)$$

Shear resistance of joint concrete panel by diagonal strut  $V_C$  is developed by horizontal compression strength of concrete strut. Thus, when the effective concrete strength applied to diagonal concrete strut shown in Fig. 4-4 is defined as  $f_{ce}$ ,  $V_C$  is as follows.

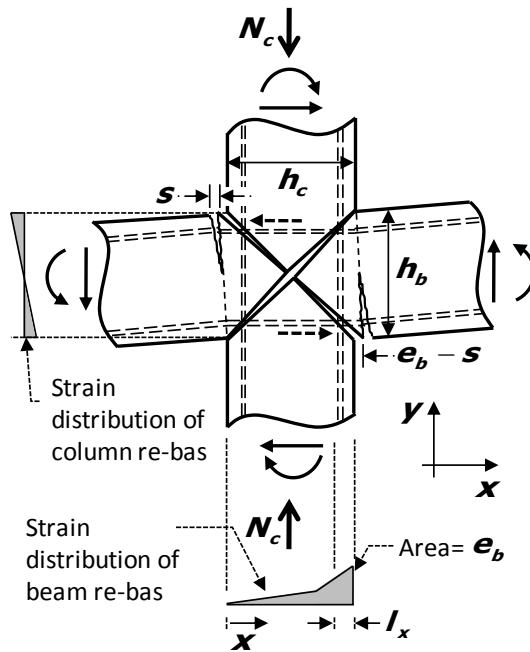
$$V_C = f_{ce} (wt) \cos\theta \quad (4-8)$$

where  $t$  = concrete strut depth, and ACI 352R-02 (2002) defines as follows.

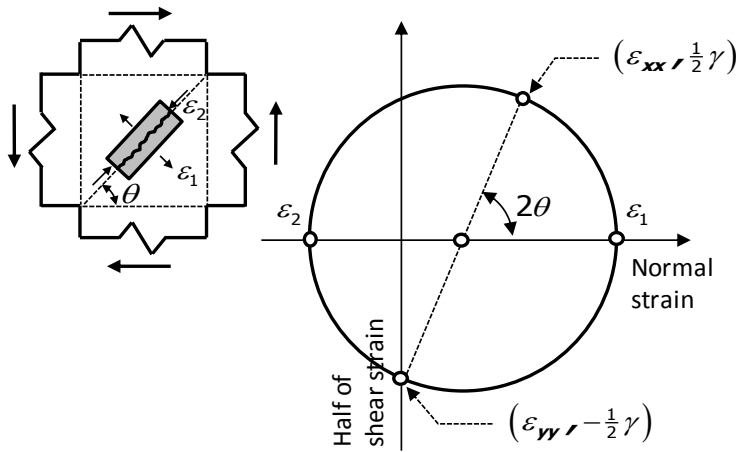
$$t = \min \left\{ \frac{b_b + b_c}{2}, b_b + \frac{h_c}{2} \right\} \quad (4-9)$$

## 4.4 Joint Shear Deformation and Effective Concrete Strength

Fig. 4-5(a) shows the deformed shape of joint concrete panel at the joint region with bond-slip of beam flexural bars. According to Shiohara (2001; 2012), joint shear deformation is occurred by the rotation of the four triangular joint concrete segments and the diagonal cracking. The joint concrete segments are connected by beam and column flexural bars and joint hoop bars to prevent braking into pieces. As a result, before bar bond-slip, the joint shear deformation is uniformly distributed by the fine diagonal cracks in the joint because the force is distributed at the joint panel by re-bar bond strength. On the other hand, the increased bar bond-slip induces the concrete segments rotation and the large diagonal cracking in the joint, and increases the joint deformation. Even though the diagonal cracking direction is not consistent with the diagonal strut direction (Eq. (4-6)), in this chapter, the principal stress directions in the diagonal strut is assumed to coincide with the principal strain directions in the diagonal strut direction for simplicity of model.



(a) Shear strain and bond-slip at joint



(b) Mohr's strain circle for joint concrete

Fig. 4-5. Simplified deformation model for beam-column joint after bond-slip of beam longitudinal bars

Generally, in the beam-column connections of low-rise buildings, it is difficult to secure a sufficient development length of beam flexural bars at the joint due to the limited column depth  $h_c$ . As a result, under cyclic loading, tensile yielding of beam flexural bars by beam flexural yielding is penetrated into the joint, and elongation  $e_b$  is developed by the plastic strain of the beam flexural bars. Before bond failure between concrete and re-bar, the elongation  $e_b$  of the beam flexural bars increases shear deformation  $\gamma_j$  at the joint. However, after bond failure, some of the elongation increases the shear deformation  $\gamma_j$  and the other elongation is cumulated as an anchorage slip  $s$  at the left and right joint interface, which expands the gap between beam and joint interface (see Fig. 4-5(a)).

Because of stiffness variance due to diagonal cracking and ratio variance of bearing force and bond strength applied to the joint, it is difficult to evaluate accurately the quantitative relationship of the beam re-bar elongation  $e_b$ , the joint shear deformation  $\gamma_j$ , and the bond-slip  $s$  cumulated at the joint interface. For simplified estimation, in the present study, it was assumed that the tensile strain of beam flexural bars near the joint interface was cumulated as the anchorage bond-slip  $s$  at the joint interface, and the remained  $e_b - s$  induced the horizontal uniform tensile strain  $\varepsilon_{xx}$  at the joint concrete, which increases the joint shear deformation  $\gamma_j$ . That is,

$$s = \int_{h_c - l_x}^{h_c} \varepsilon dx \quad (4-10)$$

$$\varepsilon_{xx} = \frac{1}{h_c - l_x} \int_0^{h_c - l_x} \varepsilon \, dx = \frac{e_b - s}{h_c - l_x} \quad (4-11)$$

where  $l_x$  = distance contributed to bond-slip of beam flexural bars at the joint interface where tension force is applied to the beam flexural bars. According to Viwathanatepa et al. (1979), anchorage failure of concrete with tensile deformation of re-bar occurs from the joint interface to distance of 3-4 times re-bar diameter. Thus, the bond length contributed to the anchorage slip  $s$  was defined as  $l_x = 3d_b$ .  $\varepsilon$  indicates the strain distribution of the beam flexural bars. Elongation  $e_b$  can be determined from strain distribution of beam flexural bars at the joint proposed in Chapter 3. Horizontal tensile strain  $\varepsilon_{xx}$  was defined as the average strain of the region causing joint shear deformation. The proposed equation was compared with the existing test results for joint shear deformation (Hwang et al., 2013; Hwang et al., 2003; Susanto and Hua, 2003; Brooke et al., 2006; Xian et al., 1992; Li et al., 2002; Lin, 2000).

Fig. 4-6 compares average joint shear distortion according to tensile strain of beam flexural bars or elongation  $e_b$  at the joint. When the tensile strain and the elongation  $e_b$  are not reported, joint shear distortion or anchorage slip  $e_b$ - $s$  according to story drift ratio were compared. Joint shear distortion  $\gamma_j$  is measured by diagonal linear potentiometers, and is coincident with Eq. (4-13). In the proposed model, because the joint deformation beyond tensile yielding of beam flexural bars is considered, the deformation after the re-bar yielding was estimated in Fig. 4-6.

Joint shear distortion  $\gamma_j$  according to tensile strain  $\varepsilon_t$  of beam flexural bars in Fig. 4-6(a) - (c), joint shear distortion  $\gamma_j$  according to elongation  $e_b$  in Fig. 4-6(d) - (k), joint shear distortion  $\gamma_j$  according to story drift ratio in Fig. 4-6(l) - (n), and anchorage slip  $e_b-s$  according to story drift ratio in Fig. 4-6(o) - (p) were compared. Predictions agree well with the test results. This result indicates that Eqs. (4-11) and (4-16) estimate reasonably the joint shear deformation and concrete compressive strain of diagonal strut depending on bond-slip of beam flexural bars.

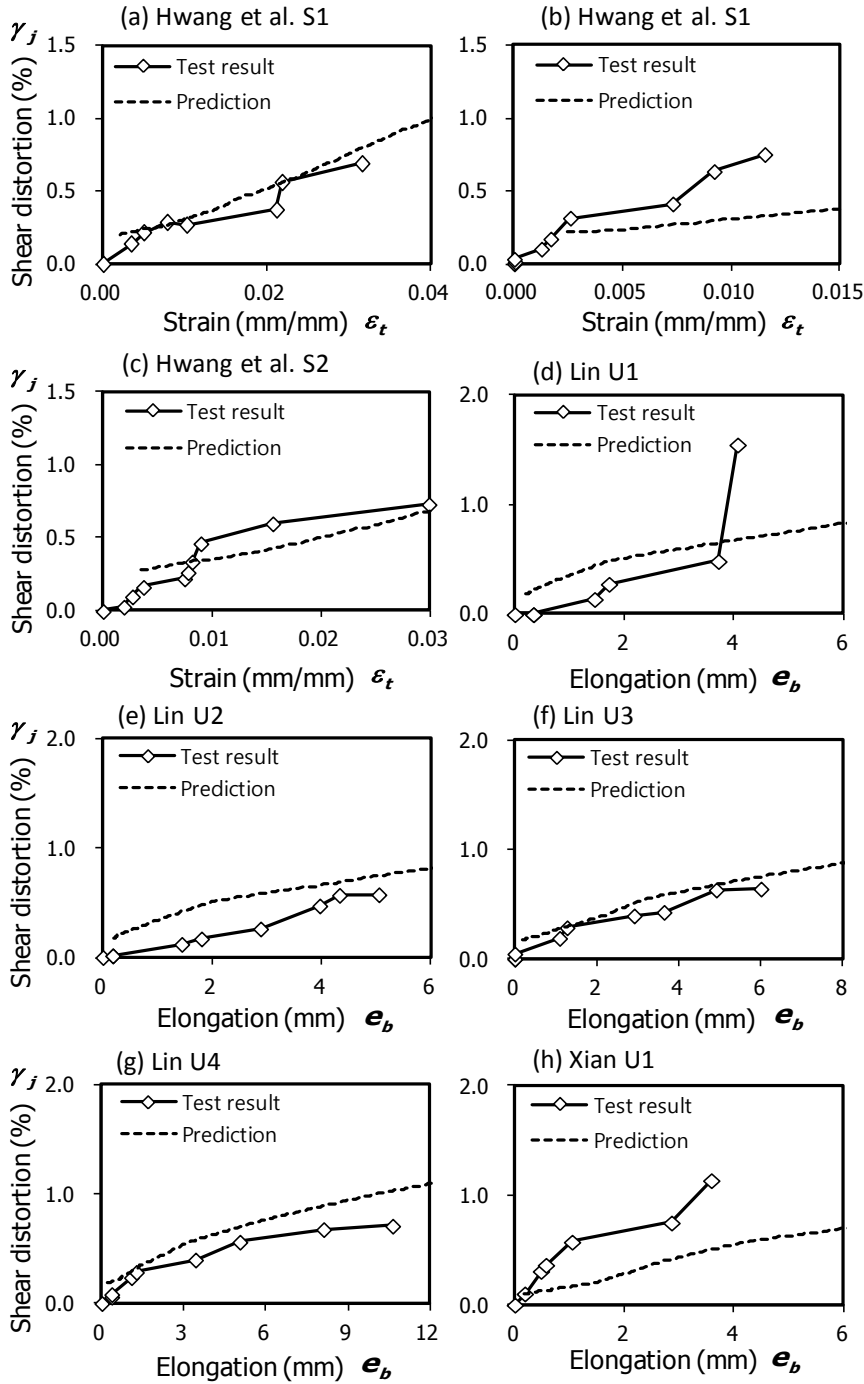


Fig. 4-6. Comparison of shear distortion and bond displacement (Continued)

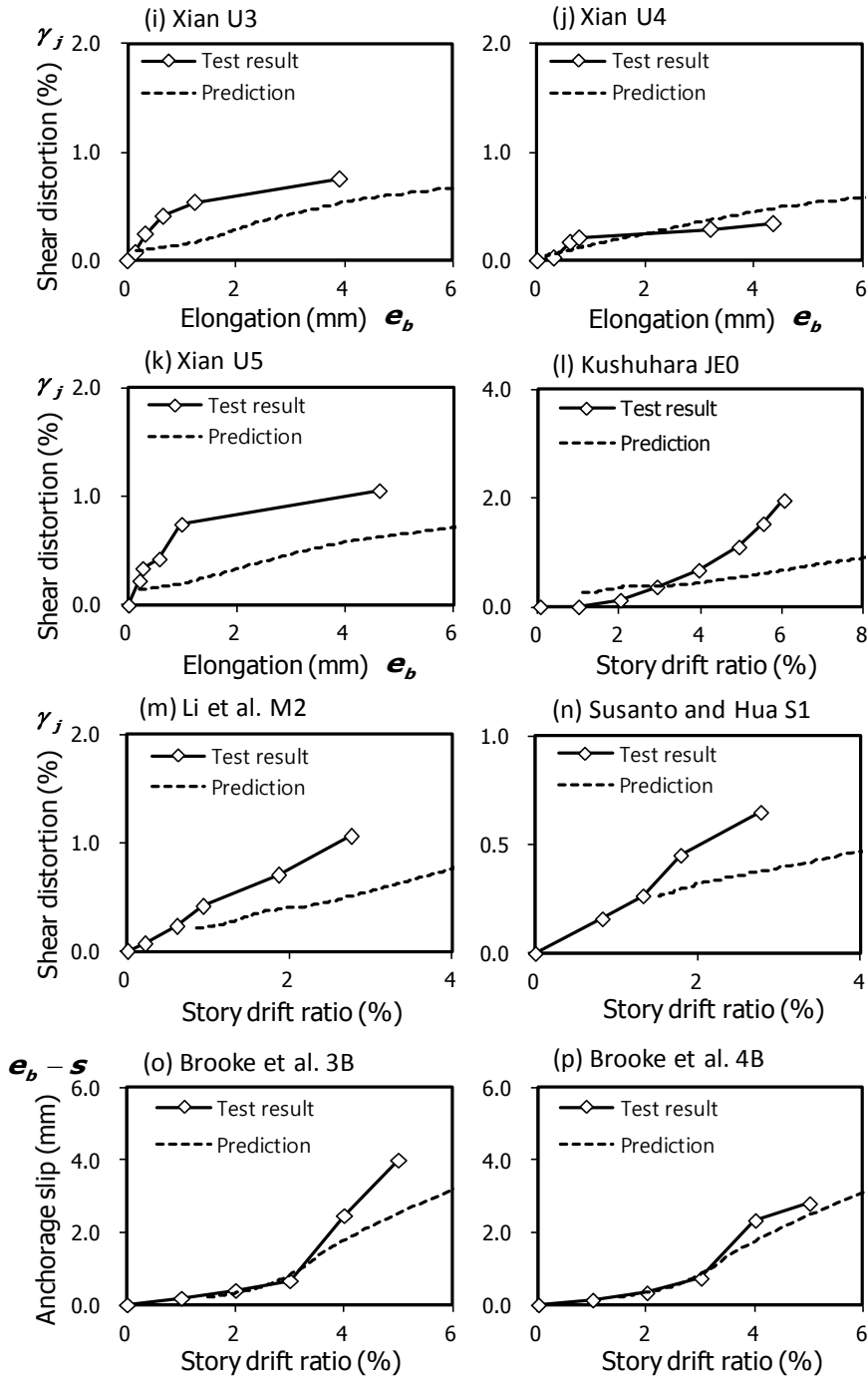


Fig. 4-6. Comparison of shear distortion and bond displacement



Fig. 4-5(b) shows Mohr's strain circle assuming uniform strain field for joint concrete panel (height  $h_c$  and width  $h_c$ ). x (horizontal) and y (vertical) directional strain and shear distortion were defined as  $\varepsilon_{xx}$ ,  $\varepsilon_{yy}$ , and  $\gamma_j$ , respectively. As shown in Eq. (4-11), the average horizontal strain of the joint concrete is approximately  $\varepsilon_{xx} \approx (e_b - s) / (h_c - l_x)$ . For non-yielded column in strong column-weak beam connection,  $\varepsilon_{yy}$  is developed in top and bottom joint interface as shown in strain distribution of column flexural bars shown of Fig. 4-5(a). In the present study, because the strain was close to 0 at the joint center and principal compression strain of diagonal strut was affected by column compression force, average  $\varepsilon_{yy} = 0$  was applied.

For principal compression strain  $\varepsilon_2$  ( $<0$ ) of the diagonal strut in Mohr's strain circle of Fig. 4-5(b), shear distortion  $\gamma_j$  and principal tension strain  $\varepsilon_1$  of the joint concrete panel are as follows.

$$\gamma_j = 2\sqrt{(\varepsilon_{yy} - \varepsilon_2)(\varepsilon_{xx} - \varepsilon_2)} \quad (4-12)$$

$$\varepsilon_1 = \varepsilon_{xx} + \varepsilon_{yy} - \varepsilon_2 \simeq \frac{e_b - s}{h_c - l_x} - \varepsilon_2 \quad (4-13)$$

According to Vecchio and Collins (1986), principal tension strain of joint diagonal strut  $\varepsilon_l$  in Eq. (4-13) decreases the effective compression strength of the strut. Assuming the strut direction in Fig. 4-4 is approximately identical to the principal strain direction of concrete panel in Fig. 4-5(b), the effective concrete strength  $f_{ce}$  in Eqs. (4-5c) and (4-8) is defined as the principal tension

strain  $\varepsilon_l$  by Vecchio and Collins (1986).

$$f_{ce} = \frac{f'_c}{0.8 + 170\varepsilon_l} \leq f'_c \quad (4-14)$$

where because the joint concrete cracking is restrained in beam-column connection with cross-beam, the effective compression strength  $f_{ce} = f'_c$ .

Because load condition and cracking of diagonal compression field in Fig. 4-3 differs from that of diagonal strut in Fig. 4-4, principal compression strain  $\varepsilon_2$  is dissimilar in the diagonal compression field and diagonal strut. Thus, in the diagonal compression field,  $\varepsilon_2$  is applied instead of  $\varepsilon_{2,f}$  and principal tension strain is defined as  $\varepsilon_{1,f}$ . Furthermore, effective compression strength  $f_{ce,f}$  is defined applying  $\varepsilon_{1,f}$  in Eq. (4-14). Principal compression strain of diagonal strut  $\varepsilon_2$  is developed by bearing force of beam and column applied to the strut and re-bar bond strength applied to the strut in Fig. 4-4. Assuming the diagonal strut shape is identical to load direction applied to the diagonal strut, compression force applied to the diagonal strut is approximately  $[(A_s + A'_s)f_y - F_{bt}] / \cos\theta$ . For  $\varepsilon_{2,f}$  of the diagonal compression field, bond strength  $F_{bt}$  in Fig. 4-3 induces compression strain, and is as follows.

$$\varepsilon_2 = -\frac{(A_s + A'_s)f_y - F_{bt}}{(wt)E_c \cos\theta} \quad (4-15a)$$

$$\varepsilon_{2,f} = -\frac{F_{bt}}{\left[(h_c - l_s)\sin\theta\right]tE_c\cos\theta} \quad (4-15b)$$

where  $E_c$  = elastic modulus of joint concrete.

## 4.5 Relationship Between Joint and Beam-Column Connection

To evaluate load-carrying capacity and deformation capacity in beam-column connection, the shear resistance  $V_{jn}$  and the shear distortion  $\gamma_j$  should be converted into lateral load  $P_n$  of beam-column connection (or column lateral load) and lateral drift  $\delta_T$  (or story drift ratio), respectively (see Fig. 4-7).

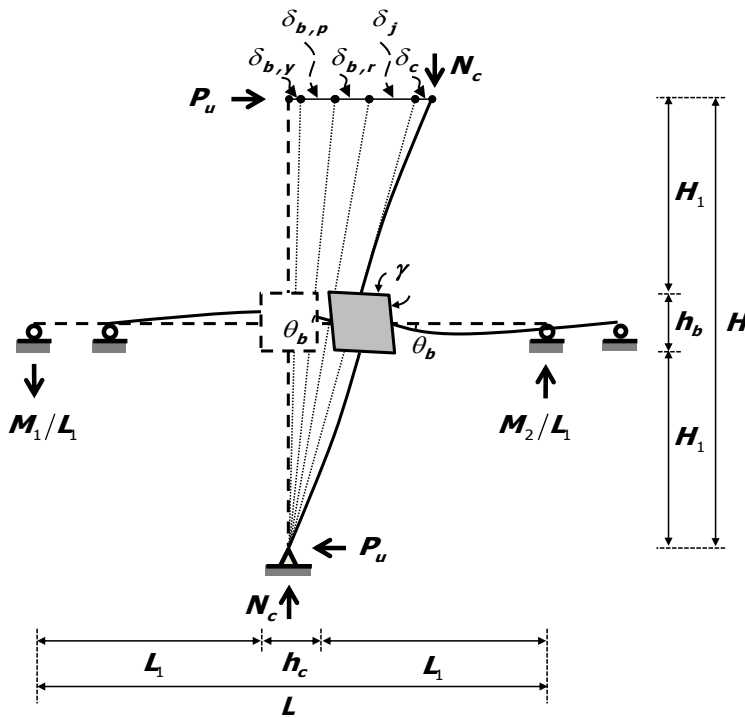


Fig. 4-7. Interior beam-column connection

As shown in Fig. 4-7, total story drift ratio of the beam-column connection  $\delta_T$  consists of drift by elastic deformation of beam  $\delta_{b,y}$ , drift by plastic hinge deformation of beam  $\delta_{b,p}$ , drift by anchorage slip at joint interface  $\delta_{b,r}$ , drift by joint shear deformation  $\delta_j$ , and drift by column deformation  $\delta_c$ .

$$\delta_T = \delta_{b,y} + \delta_{b,p} + \delta_{b,r} + \delta_j + \delta_c \quad (4-16)$$

For strong column-weak beam designed beam-column connection, elastic deformation occurs in the column approximately. Thus, the drift by elastic deformations of beam and column ( $\delta_{b,y} + \delta_c$ ) can be simplified as yield drift ratio of reinforced concrete moment frame structure proposed by Priestley (1998).

$$\delta_{b,y} + \delta_c = 0.5\varepsilon_y \frac{L}{h_b} \quad (4-17)$$

$\delta_{b,p}$  is the story drift ratio by plastic rotation  $\theta_p$  of beam plastic hinge, and defined as follows.

$$\delta_{b,p} = \frac{2}{L} \left( L_1 - \frac{L_p}{2} \right) \theta_p \quad (4-18)$$

where  $\theta_p$  is defined as follows, assuming constant curvature in beam plastic hinge length ( $= L_p$ ).

$$\theta_p \simeq \left( \frac{\varepsilon_t}{d-c} - \phi_y \right) L_p = \left( \frac{\varepsilon_t}{d-c} - \frac{1.7\varepsilon_y}{h_b} \right) L_p \quad (4-19)$$

where  $\varepsilon_t$  = tension strain of beam flexural bars at the joint interface;  $d$  = effective depth of beam cross-section;  $c$  = neutral axis depth of beam cross-section; and  $\phi_y$  = yield curvature of beam cross-section. Yield curvature and plastic hinge length were assumed to be  $\phi_y = 1.7\varepsilon_y/h_b$  (Priestley, 2000) and  $L_p = 0.08L_l + 0.022d_b f_y$  (Paulay and Priestley, 1992), respectively ( $d_b$  = re-bar diameter; and  $f_y$  = yield strength of re-bar).

$\delta_{b,r}$  is the story drift ratio by beam rotation  $\theta_b$  due to anchorage bond-slip  $s$  cumulated at the joint interface, and calculated as follows.

$$\delta_{b,r} = \frac{2}{L} L_1 \theta_b \quad (4-20)$$

where  $\theta_b$  is determined as follows, assuming the rotational center of anchorage slip  $s$  as  $d - c$  (see Eq. (4-10)).

$$\theta_b \simeq \frac{s}{d-c} = \int_{h_c-l_x}^{h_c} \frac{\varepsilon}{d-c} dx \quad (4-21)$$

Story drift ratio  $\delta_j$  by joint shear deformation is determined from the shear distortion  $\gamma_j$  in Eq. (4-12) (see Eqs. (4-11) and (4-12)).

$$\delta_j = \gamma_j \left( 1 - \frac{h_c}{2L} - \frac{h_b}{2H} \right) \quad (4-22)$$

Story drift ratio of the joint in Eqs. (4-16) - (4-22) is calculated by assuming equal left and right beam shear span and equal top and bottom column height as shown in Fig. 4-7. Thus, the proposed equation should be applied to left and right symmetric beam-column connection. For asymmetric beam-column connection, each deformation of left and right beam should be estimated in Eqs. (4-18) and (4-20).

According to Hakuto et al. (1999), column lateral load  $P_u$  corresponding to beam flexural moments  $M_1$  and  $M_2$  that is applied to left and right joint interface in inelastic story drift ratio  $\delta_T$  is decreased as the joint deformation increases (see Fig. 4-4). This is because, as a bond-slip increases, compression zone of a beam cross-section determined from Eq. (4-2) is lengthen, and beam flexural moments  $M_1$  and  $M_2$  are decreased. The reduced column lateral load  $P_u$  is determined from force equilibrium condition.

$$P_u = \frac{L}{2H} \left( \frac{M_1 + M_2}{L_1} \right) \quad (4-23)$$

In story drift ratio  $\delta_T$  of beam-column connection, load-carrying capacity  $P_n$  of column corresponding to joint shear resistance  $V_{jn}$  is determined from force equilibrium condition of beam-column connection (Paulay and Priestley, 1992).

$$P_n = \frac{V_{jn} \times j_d}{H(1 - j_d/H - h_c/L)} \quad (4-24)$$

where  $j_d$  = moment lever arm length of a beam. As compression zone depth of the beam section in Eq. (4-2) increases,  $j_d$  decreases.



## 4.6 Flexural Deformation Capacity of Beam Section

At the joint interface, flexural failure of a beam is developed by bottom concrete crushing and fracture of bottom flexural bars. Particularly, as the bond-slip of the beam flexural bars increases, early concrete crushing can be occurred by the increased compression zone of the beam cross-section due to anchorage force. Concrete crushing is occurred when the strain at the extreme fiber of beam reaches ultimate strain. To predict the cover concrete failure after bottom concrete crushing, crushing drift ratio was determined from the concrete compression strain  $\varepsilon_{cb}$  at the beam bottom bars where inner concrete was damaged after cover concrete spalling. From the give strain of top re-bar  $\varepsilon_m$ , concrete compression strain at beam bottom bars under negative moment is as follows.

$$\varepsilon_{cb} = -\frac{c' - d'}{d_n - c'} \varepsilon_m \quad (4-25)$$

where  $c'$  = neutral axis depth of beam cross-section under negative moment (=  $c_{bI} / \beta_1$ ,  $\beta_1$  = coefficient between neutral axis and compression zone of equivalent stress block (ACI 318-11, 2011));  $d'$  = distance between compression flexural bars and beam bottom face under negative moment; and  $d_n$  = effective beam depth under negative moment. The neutral axis depth increases with bond-slip of re-bar (see Eq. (4-2)). Beam crushing was defined such that  $\varepsilon_{cb}$  reach -0.004 (Park and Paulay, 1975).

For flexural member subjected to cyclic loading, load-carrying capacity was decreased by re-bar fracture when the tension strain of re-bar reaches the fracture strain 0.04 (Wood, 1989; Park et al., 2012). Thus, in Fig. 4-9, beam flexural moment degradation by re-bar fracture was defined when the tensile strain  $\varepsilon_t$  of the bottom flexural bars with significant plastic deformation reaches 0.04.

## 4.7 Evaluation and Verification of Joint Deformation Capacity

### 4.7.1 Calculation of Joint Deformation and Shear Strength

Because the ratio of the beam top flexural bars to resist flexural moment by gravity load are greater than the ratio of the bottom flexural bars, inelastic deformation is significantly occurred in the bottom flexural bars. Thus, in the proposed model, the deformation and shear strength of the joint are predicted as follows, on the basis of the tension strain of the beam bottom flexural bars. The Matlab code for the proposed model was shown in Appendix A.

- 1) From the given tension strain  $\varepsilon_t$  of the beam bottom flexural bars, bond-slip deformation  $e_b$ , anchorage bond-slip  $s$ , joint shear distortion  $\gamma_j$ , and principle strain of  $\varepsilon_I$  joint concrete are determined using the joint bond strength model.
- 2) According to Chapter 4.5, story drift ratio  $\delta_T$  is determined. When the ratio of beam top and bottom flexural bars is different, effective beam depth  $d$  and neutral axis depth  $c$  ( $= c_{bI}$ ) are determined from the bottom flexural bars with low re-bar ratio.
- 3) Joint shear strength by diagonal compression field  $V_T$  is determined from the bond strength of the bottom beam flexural bars, joint hoop strength, and diagonal compression field of joint concrete.

- 4) Diagonal compression strut is defined by compression zone of beam and column cross-section. Effective compression strength of the diagonal strut is determined from the principal strain  $\varepsilon_l$  calculated by 1). On the basis of the diagonal strut configuration and the effective strength, joint shear resistance by the diagonal strut  $V_c$  is determined.
- 5) From load-deformation relationship in Chapter 4.5, column lateral demand by beam flexural yielding  $P_u$  is compared with column lateral capacity by joint shear resistance  $P_n$ .

#### **4.7.2 Comparison of Predictions and Test Results**

Fig. 4-8 shows the relationship between column lateral demand due to beam flexural yielding  $P_u$  and column lateral capacity due to joint shear resistance  $P_n$ . When the column lateral capacity  $P_n$  is less than column lateral demand  $P_u$  before beam flexural failure, load-carrying capacity of the joint is significantly deteriorated by the joint shear failure. On the other hand, when the column lateral capacity  $P_n$  is greater than column lateral demand  $P_u$  until beam flexural failure, the deformation capacity of the joint is governed by deformation capacity of beam plastic hinge.

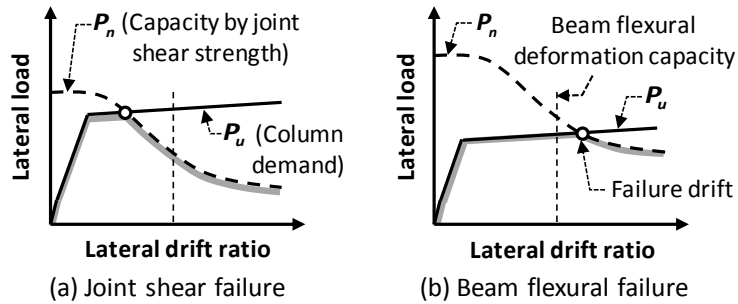


Fig. 4-8. Load-deformation relationship

Table 4-1 shows test parameters and failure modes of 64 existing interior beam-column connections (Lee et al., 2009; Hwang et al., 2013; Hwang et al., 2013; Teraoka et al., 1994; Susanto and Hua, 2003; Durrani and Wight, 1982; Hayashi et al., 1993; Sugano et al., 1991; Oda et al., 1997; Noguchi and Kashiwazaki, 1992; Kawai et al., 1997; Brooke et al., 2006; Xian et al., 1992; Joh et al., 1991; Li et al., 2002; Otani et al., 1984; Kusahara et al., 2004; Walker, 2001; Leon, 1984; Lin, 2000). 57 specimens exhibited joint shear failure (JF), and 7 specimens exhibited beam flexural failure (BC, BF).

Table 4-1. Test parameters of existing test specimens (Continued)

Specimens		Geometric properties <sup>a</sup>						Top re-bar of beam			Bottom re-bar of beam			Joint hoop		Concrete strength	Axial load	Failure mode <sup>c</sup>	
		<i>L</i>	<i>H</i>	<i>h<sub>b</sub></i>	<i>b<sub>b</sub></i>	<i>h<sub>c</sub></i>	<i>b<sub>c</sub></i>	<i>A<sub>s</sub></i>	<i>f<sub>y</sub></i>	<i>d<sub>b</sub></i>	<i>A<sub>s</sub></i>	<i>f<sub>y</sub></i>	<i>d<sub>b</sub></i>	<i>A<sub>h</sub></i>	<i>f<sub>yh</sub></i>	<i>f<sub>c</sub>'</i> (MPa)	<i>N<sub>c</sub></i> / ( <i>f<sub>c</sub>'</i> <i>b<sub>b</sub>h<sub>c</sub></i> )	Test results	Predicti on
Hwang et al. (2013)	S1	5760	2100	500	350	460	500	2040	452	25.4	1020	452	25.4	1548	496	38.3	0.00	JF	BC-JF
Hwang et al. (2013)	S1	4760	2100	500	350	550	500	3110	465	25.4	1524	520	22.2	2064	446	32.0	0.00	JF	BC
	S2	4760	2100	500	350	550	500	1935	710	22.2	1161	710	22.2	2064	446	32.0	0.00	JF	BC
	S3	4760	2100	500	350	450	500	1935	710	22.2	1161	710	22.2	2064	446	32.0	0.00	JF	JF
Teraoka et al. (1994)	NO43	3000	2000	400	300	400	400	1134	382	19.1	1134	382	19.1	785	347	54.0	0.20	N	BC-JF
	NO47	3000	2000	400	300	400	400	1701	382	19.1	1701	382	19.1	785	347	54.0	0.20	JF	BC-JF
Susanto and Hua (2003)	S1	4000	2626	400	200	300	400	995	510	15.9	597	510	15.9	1065	440	33.0	0.08	JF	JF
Durrani and Wight (1982)	X1	2496	2248	419	279	362	362	1548	331	22.0	1136	345	19.0	881	352	34.3	0.06	JF	BC-JF
	X2	2496	2248	419	279	362	362	1548	331	22.0	1136	345	19.0	1321	352	33.7	0.06	JF	BC-JF
	X3	2496	2248	419	279	362	362	1163	331	22.0	855	345	19.0	881	352	31.0	0.05	N	BC-JF
Hayashi et al. (1993)	NO43	3000	2000	400	300	400	400	1136	383	19.1	1136	383	19.1	710	347	49.1	0.20	BC	BC-JF
	NO46	3000	2000	400	300	400	400	568	858	19.1	568	858	19.1	710	347	49.1	0.20	N	BC-JF
	NO47	3000	2000	400	300	400	400	1704	383	19.1	1704	383	19.1	710	347	49.1	0.20	JF	BC-JF
Sugano et al. (1991)	J4-0	2780	1400	400	300	440	440	3096	386	22.2	3096	386	22.2	1024	923	30.4	0.33	JF	BC-JF
	J6-0	2780	1400	400	300	440	440	3096	386	22.2	3096	386	22.2	1024	923	60.5	0.17	JF	BC-JF
	J8-0	2780	1400	400	300	440	440	3096	386	22.2	3096	386	22.2	1024	923	77.6	0.13	JF	BC-JF
Oda et al. (1997)	BN1	2800	1500	475	300	450	450	2322	502	22.2	2322	502	22.2	1016	817	79.0	0.07	N	BC-JF
	BN2	2800	1500	475	300	450	450	3096	502	22.2	3096	502	22.2	1016	817	79.0	0.07	JF	BC-JF
	BN3	2800	1500	475	300	450	450	2550	535	25.4	2550	535	25.4	1016	817	79.0	0.07	N	BC-JF
	BN5	2800	1500	475	300	450	450	2040	535	25.4	2040	535	25.4	1016	817	51.3	0.09	N	BC-JF
Noguchi and Kashiwazaki (1992)	OKJ1	2700	1470	300	200	300	300	1143	718	12.7	889	718	12.7	336	955	70.0	0.12	JF	BC-JF
	OKJ3	2700	1470	300	200	300	300	1270	718	12.7	1270	718	12.7	336	955	107.0	0.12	JF	BC-JF
	OKJ6	2700	1470	300	200	300	300	1016	718	12.7	889	718	12.7	336	955	53.5	0.12	JF	BC-JF

Table 4-1. Test parameters of existing test specimens (Continued)

Specimens		Geometric properties <sup>a</sup>						Top re-bar of beam			Bottom re-bar of beam			Joint hoop		Concrete strength	Axial load	Failure mode <sup>c</sup>	
		<i>L</i>	<i>H</i>	<i>h<sub>b</sub></i>	<i>b<sub>b</sub></i>	<i>h<sub>c</sub></i>	<i>b<sub>c</sub></i>	<i>A<sub>s</sub></i>	<i>f<sub>y</sub></i>	<i>d<sub>b</sub></i>	<i>A<sub>s</sub></i>	<i>f<sub>y</sub></i>	<i>d<sub>b</sub></i>	<i>A<sub>h</sub></i>	<i>f<sub>yh</sub></i>	<i>f<sub>c</sub>'</i> (MPa)	<i>N<sub>c</sub></i> / ( <i>f<sub>c</sub>'</i> <i>b<sub>b</sub>h<sub>c</sub></i> )	Test result	Predicti on
Kawai et al. (1997)	I8C	3800	1600	450	325	475	475	3483	522	22.2	3483	522	22.2	640	928	85.5	0.20	JF	BC-JF
Brooke et al. (2006)	1B	4872	3248	500	200	800	360	1503	552	25.4	1503	552	25.4	3164	300	31.2	0.00	RB	BC-JF
	2B	4872	3248	500	200	800	360	1503	552	25.4	1503	552	25.4	2712	300	40.6	0.00	RB	BC-JF
	3B	4872	3248	500	200	675	360	1503	552	25.4	1503	552	25.4	2712	300	44.8	0.00	N	BC-JF
	4B	4872	3248	500	200	675	360	1503	552	25.4	1503	552	25.4	2712	300	42.8	0.00	N	BC-JF
Xian et al. (1992)	U1	3500	2470	500	250	450	300	791	453	12.0	791	453	12.0	1459	348	30.9	0.00	BC	JF
	U2	3500	2470	500	250	450	300	804	445	15.9	402	445	15.9	1029	348	40.8	0.00	BC	JF
	U3	3500	2470	500	250	450	300	804	445	15.9	804	445	15.9	1459	348	42.5	0.00	N	JF
	U4	3500	2470	500	250	450	300	628	492	20.0	402	445	15.9	1057	348	47.2	0.00	N	JF
	U5	3500	2470	500	250	450	300	942	492	20.0	942	492	20.0	1648	348	60.7	0.00	N	JF
	U6	3500	2470	500	250	450	300	1232	463	28.0	628	492	20.0	1648	348	59.3	0.00	BC	BC-JF
Joh et al. (1991)	B1	3000	1750	350	150	300	300	398	371	12.7	398	371	12.7	170	307	21.3	0.16	JF	BC-JF
	B2	3000	1750	350	300	300	300	398	371	12.7	398	371	12.7	170	307	20.8	0.16	JF	JF
	HH	3000	1750	350	200	300	300	387	404	12.7	387	404	12.7	432	1167	25.6	0.15	N	BF
	HL	3000	1750	350	200	300	300	387	404	12.7	387	404	12.7	432	1167	27.4	0.14	N	BF
	LH	3000	1750	350	200	300	300	387	404	12.7	387	404	12.7	170	377	26.9	0.15	N	BC-JF
	MH	3000	1750	350	200	300	300	387	404	12.7	387	404	12.7	339	377	28.1	0.14	N	BF
Li et al. (2002)	M1	3500	2700	600	300	300	900	995	503	15.9	597	503	15.9	600	499	32.0	0.00	JF	JF
	M2	3500	2700	600	300	900	300	1928	460	25.4	1020	460	25.4	300	499	30.3	0.00	JF	BC-JF
Otani et al. (1984)	J1	2700	1470	300	200	300	300	1062	401	13.0	531	401	13.0	192	368	25.7	0.08	JF	JF
	J2	2700	1470	300	200	300	300	1062	401	13.0	531	401	13.0	384	368	24.0	0.08	JF	BC-JF
	J3	2700	1470	300	200	300	300	1062	401	13.0	531	401	13.0	896	368	24.0	0.08	JF	BC-JF
	J4	2700	1470	300	200	300	300	1062	401	13.0	531	401	13.0	192	368	25.7	0.31	JF	BC-JF
	J6	2700	1470	300	200	300	300	531	401	13.0	398	401	13.0	288	368	28.7	0.21	N	BC-JF

Table 4-1. Test parameters of existing test specimens

Specimens		Geometric properties <sup>a</sup>						Top re-bar of beam			Bottom re-bar of beam			Joint hoop		Concrete strength	Axial load	Failure mode <sup>c</sup>	
		$L$	$H$	$h_b$	$b_b$	$h_c$	$b_c$	$A_s$	$f_y$	$d_b$	$A_s$	$f_y$	$d_b$	$A_h$	$f_{yh}$	$f'_c$ (MPa)	$N_c / (f'_c b_c h_c)$	Test result	Predicti on
Kusuhara et al. (2004)	JE0	2700	1470	300	180	280	320	710	387	9.5	710	387	9.5	192	364	27.0	0.00	JF	JF
	J1	2500	1560	400	300	350	350	1990	510	15.9	1990	510	15.9	1136	510	40.0	0.00	JF	JF
Lee et al. (2009)	BJ1	2500	1560	400	300	350	350	1194	510	15.9	1194	510	15.9	1136	510	40.0	0.00	JF	BC-JF
	BJ2	2500	1560	400	300	350	350	995	510	15.9	995	510	15.9	852	510	40.0	0.00	JF	JF
	BJ3	2500	1560	400	300	350	350	796	510	15.9	796	510	15.9	852	510	40.0	0.00	JF	JF
	B1	2500	1560	400	300	350	350	597	510	15.9	597	510	15.9	852	510	40.0	0.00	BC	JF
Walker (2001)	Peer14	3658	2134	508	406	457	406	1571	423	22.2	787	504	15.9	0	0	31.8	0.11	JF	JF
	Peer22	3658	2134	508	406	457	406	2002	528	20.6	1335	528	20.6	0	0	38.4	0.09	JF	JF
Leon (1984)	BCJ5 <sup>d</sup>	3448	3823	457	330	381	381	1530	414	25.4	852	414	19.1	1016	414	31.1	0.30	N	BC-BF
	BCJ8 <sup>d</sup>	3448	3823	457	330	381	381	1530	414	25.4	852	414	19.1	1016	414	31.1	0.00	N	BC-BF
	BCJ9 <sup>d</sup>	3448	3823	457	330	381	381	1530	414	25.4	852	414	19.1	1016	414	31.1	0.00	N	BC-BF
	BCJ11 <sup>d</sup>	3448	3823	457	224	381	381	1580	414	31.8	1020	414	25.4	1016	414	31.1	0.30	N	BC-BF
	BCJ12 <sup>d</sup>	3448	3823	457	457	381	381	1530	414	25.4	852	414	19.1	1016	414	31.1	0.30	N	BC-BF
Lin et al. (2000)	U1	3190	2450	550	300	390	390	904	525	12.0	904	525	12.0	1188	352	36.8	0.43	JF	JF
	U2	3190	2450	550	300	390	390	904	525	12.0	904	525	12.0	1782	352	36.8	0.43	N	JF
	U3	3190	2450	550	300	390	390	678	525	12.0	678	525	12.0	792	352	35.0	0.10	N	JF
	U4	3190	2450	550	300	390	390	904	525	12.0	452	525	12.0	792	352	35.0	0.10	N	JF

<sup>a)</sup>  $L$ = beam length (mm);  $H$ = column height (mm);  $h_b$ = beam depth (mm);  $b_b$ = beam width (mm);  $h_c$ = column depth (mm); and  $b_c$ = column width (mm)

<sup>b)</sup>  $A_s$ = area of re-bar (mm<sup>2</sup>);  $f_y$ = yield strength of re-bar based on material test result (MPa); and  $d_b$ = re-bar diameter (mm)

<sup>c)</sup> BC: Beam Crushing; RB: BF: Beam Failure; Re-bar Buckling; JF: Joint Failure; and N: No mention

<sup>d)</sup> with transverse beams



In Fig. 4-9, predictions of column lateral demand  $P_u$  and column lateral capacity  $P_n$  by joint shear strength according to story drift ratio  $\delta_T$  are compared with test results. For the column lateral capacity  $P_n$ , on the basis of bond strength model in Chapter 3,  $3\tau_u$  and  $\tau_u$  were applied as the plastic bond stress at 1<sup>st</sup> cycle and beyond 1<sup>st</sup> cycle, respectively, to predict strength degradation. Failure drift ratio was defined as the story drift ratio where the column lateral capacity  $P_n$  reaches the column lateral demand  $P_u$ . In Table 4-1, failure mode BC indicated beam bottom concrete crushing before failure drift ratio, BF indicated tension re-bar fracture before failure drift ratio, and JF was defined such that failure drift is less than beam failure drift ratio. For specimens subjected to one cyclic loading at each drift ratio by Durrani and Wight (1982) and Joh et al. (1991), failure drift ratio was defined by  $P_n$  of 1<sup>st</sup> cycle. For other specimens, the failure drift ratio was defined by  $P_n$  beyond 1<sup>st</sup> cycle.

As shown in Fig. 4-9 and Table 4-1, the proposed model predicts well the load-carrying capacity degradation of column lateral load  $P_n$  by joint shear strength and failure mode as story drift ratio increases. Load-carrying capacity of specimens was significantly decreased near the story drift ratio to predict the fracture of beam tensile bars. At the story drift ratio to predict the crushing of beam bottom concrete, load-carrying capacity decreased.

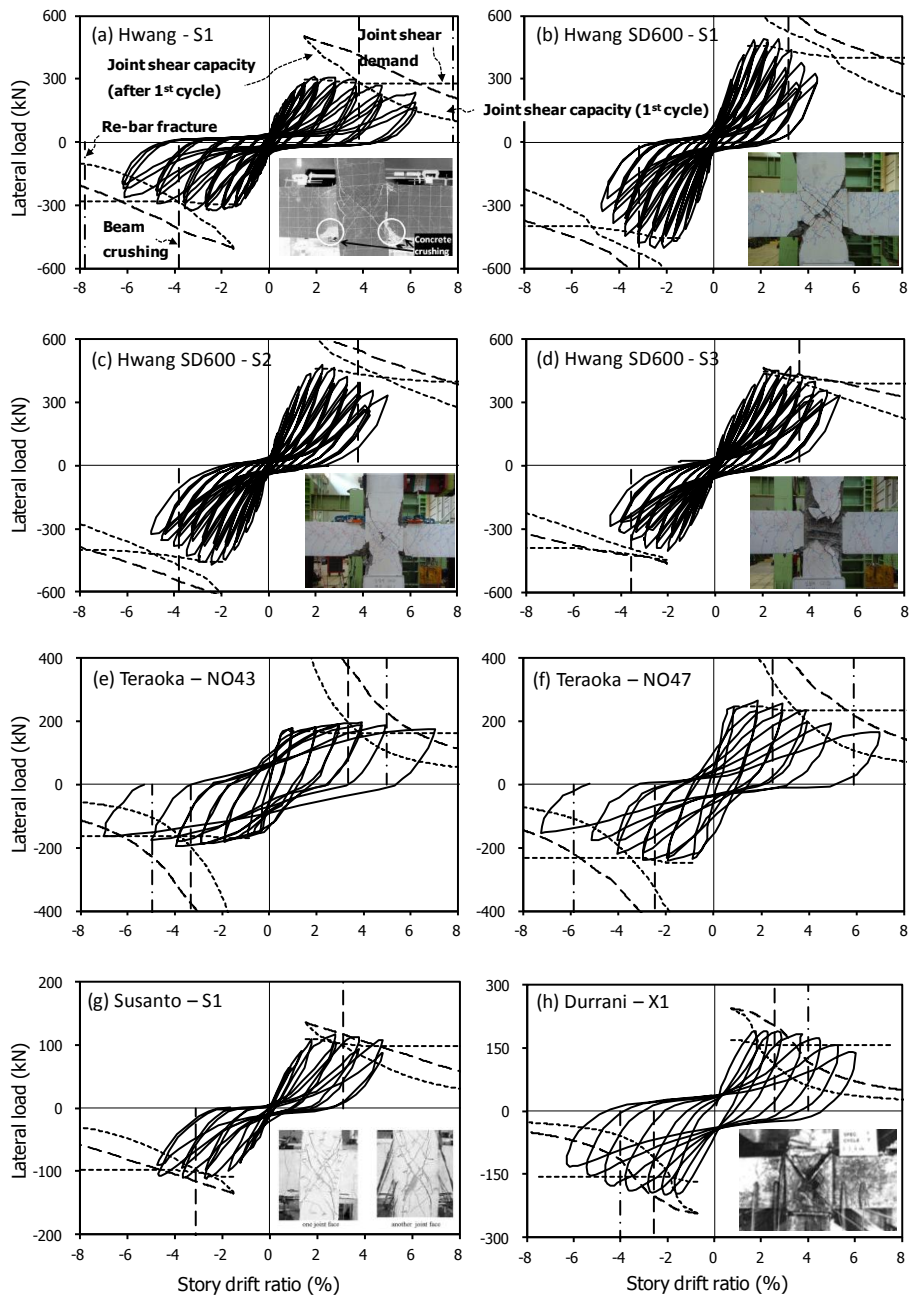


Fig. 4-9. Comparisons between hysteresis curves and predictions (Continued)

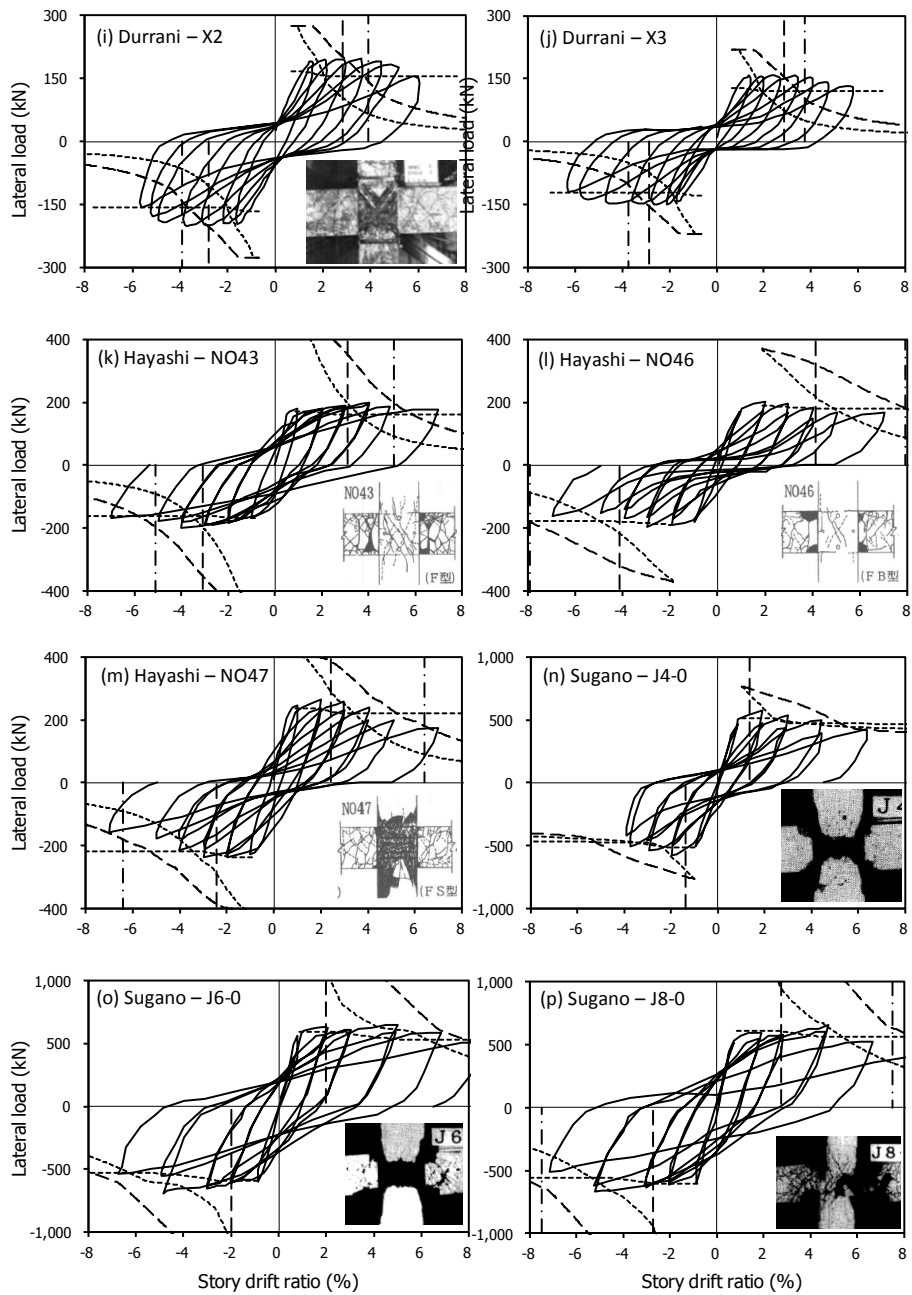


Fig. 4-9. Comparisons between hysteresis curves and predictions (Continued)

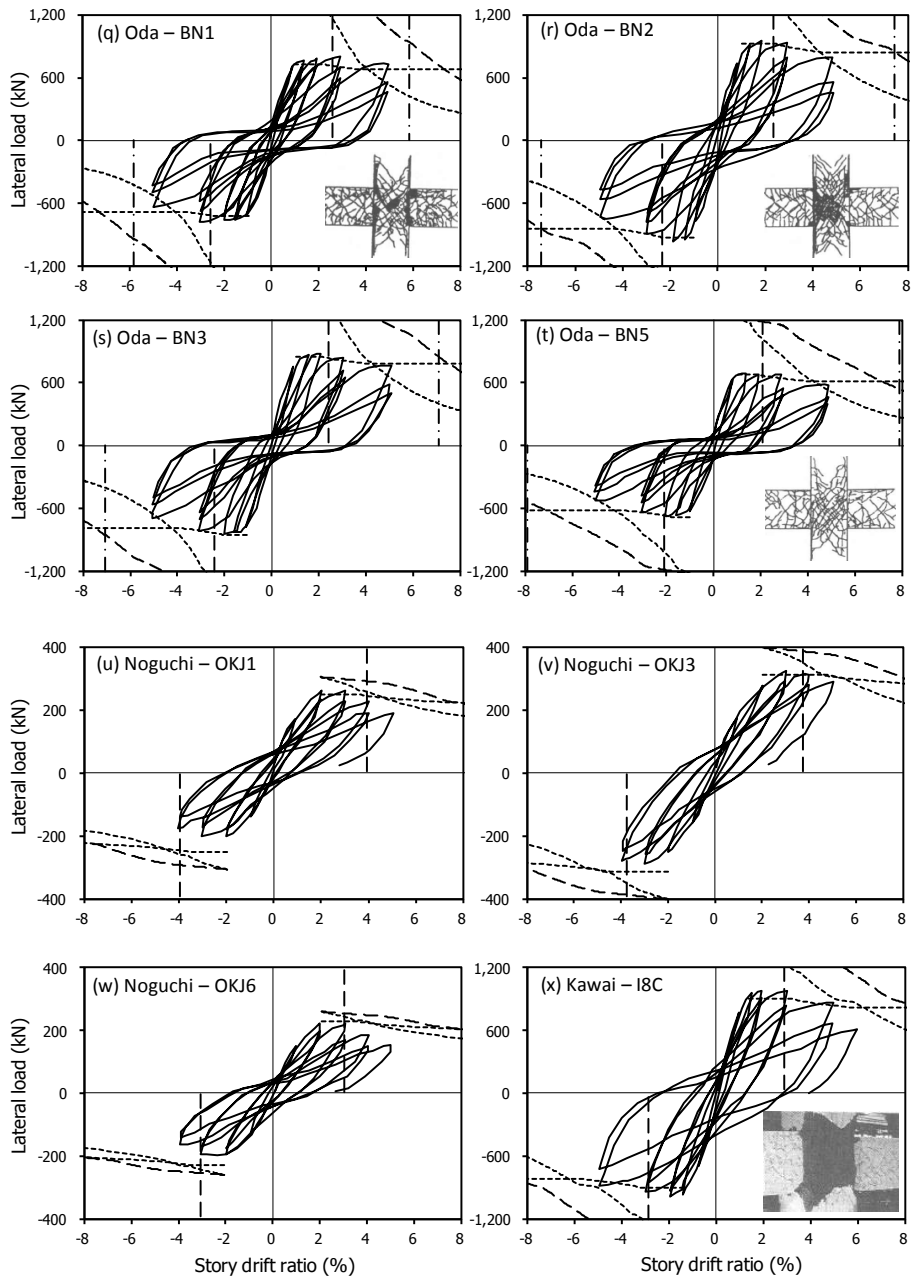


Fig. 4-9. Comparisons between hysteresis curves and predictions (Continued)

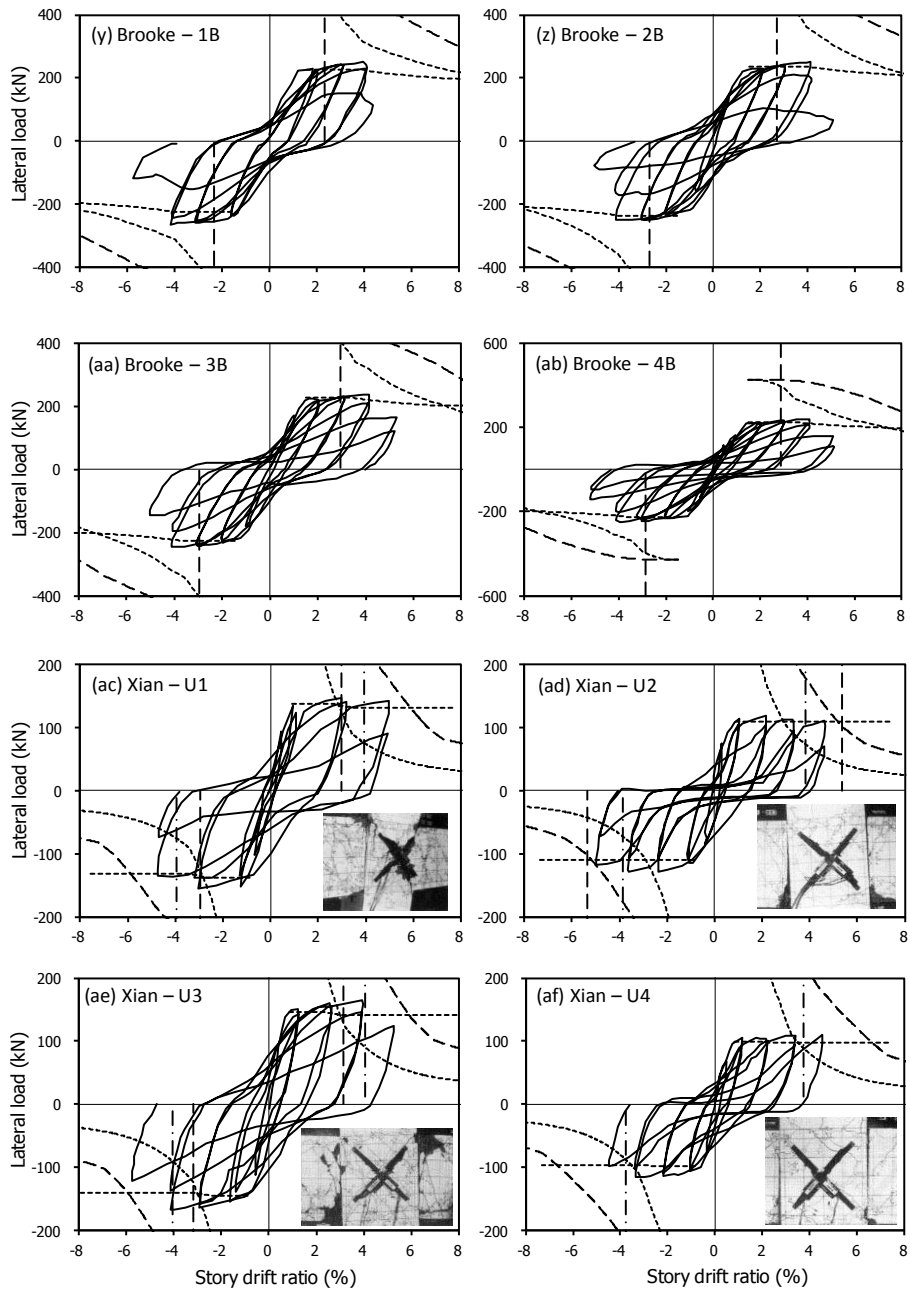


Fig. 4-9. Comparisons between hysteresis curves and predictions (Continued)

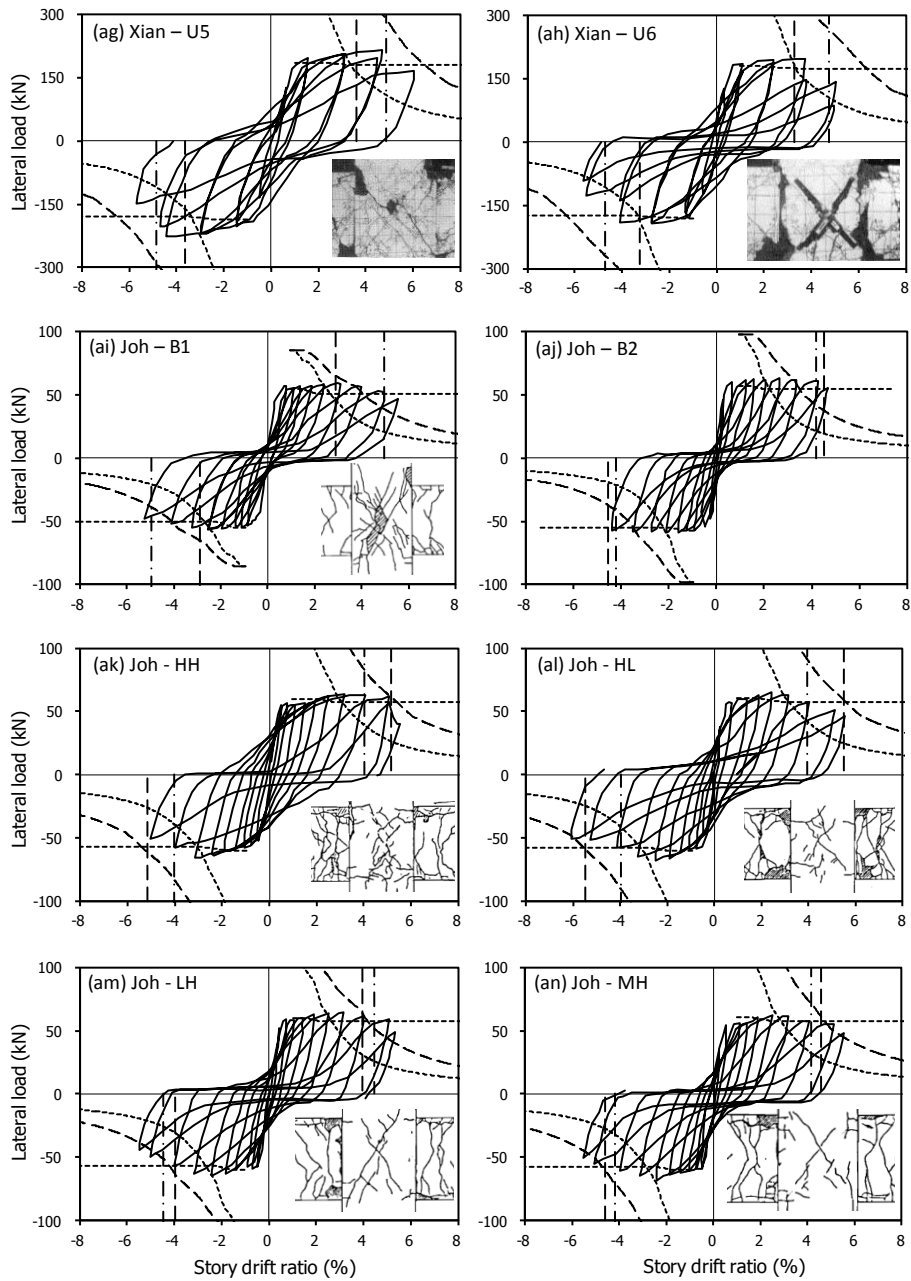


Fig. 4-9. Comparisons between hysteresis curves and predictions (Continued)

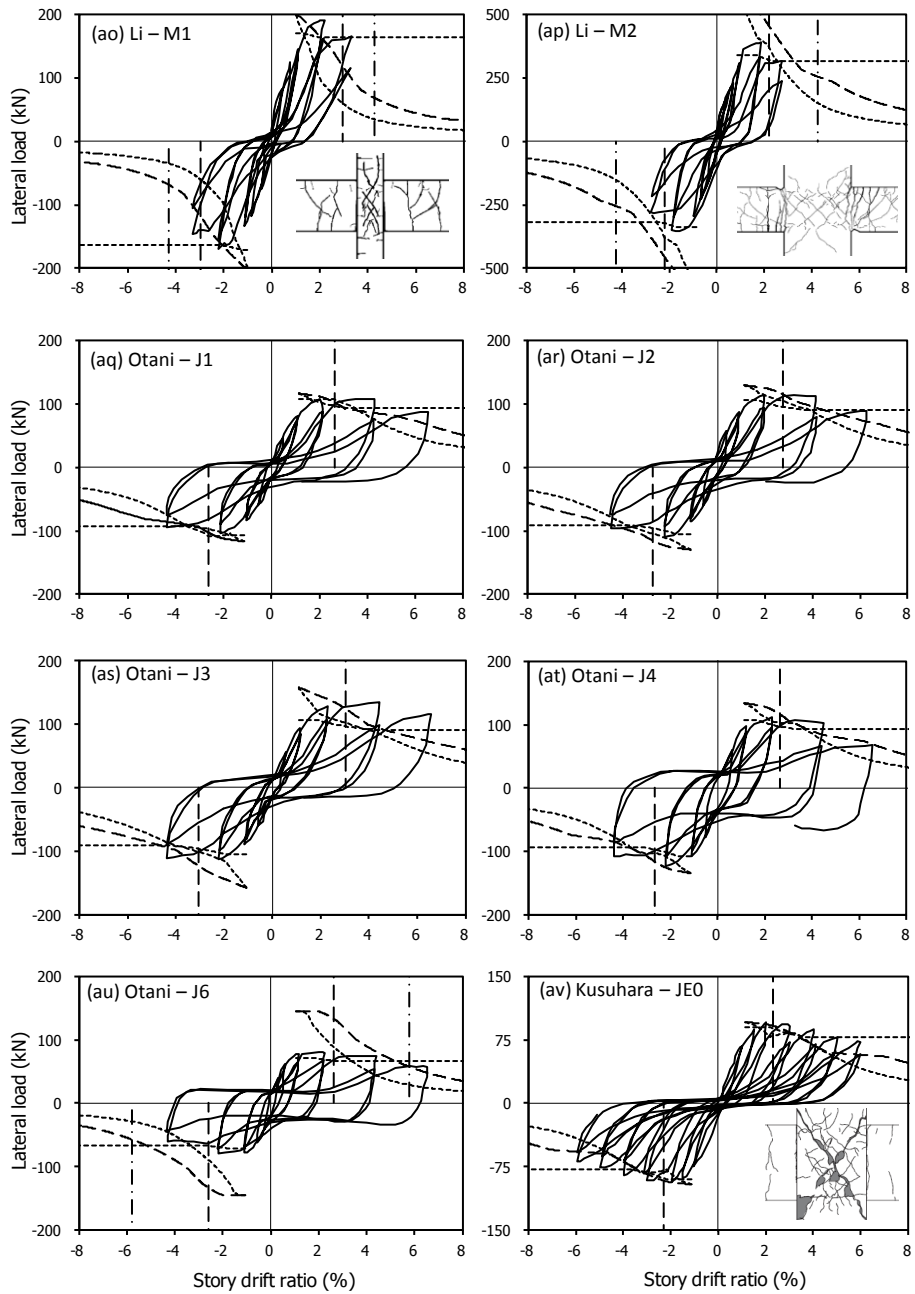


Fig. 4-9. Comparisons between hysteresis curves and predictions (Continued)

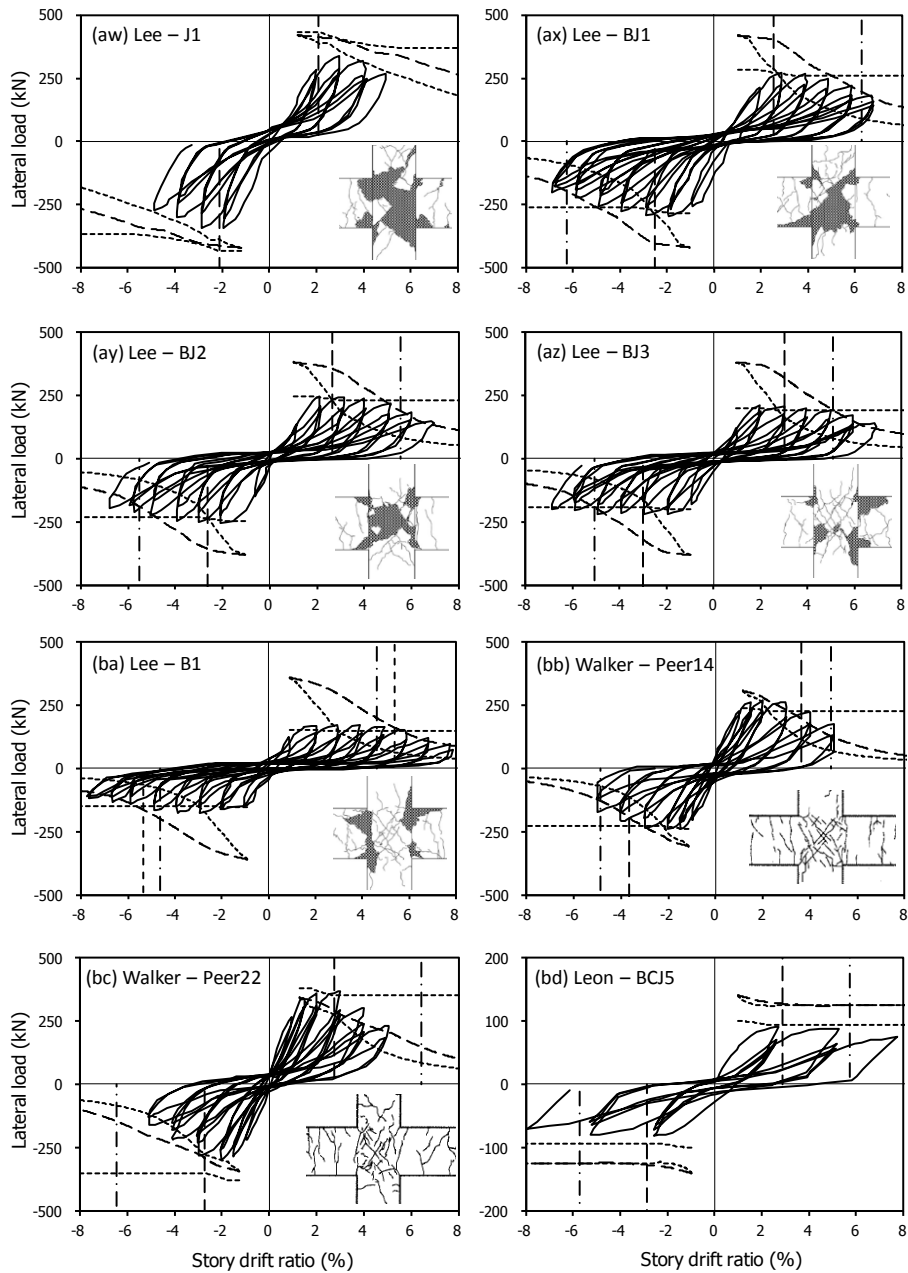


Fig. 4-9. Comparisons between hysteresis curves and predictions (Continued)



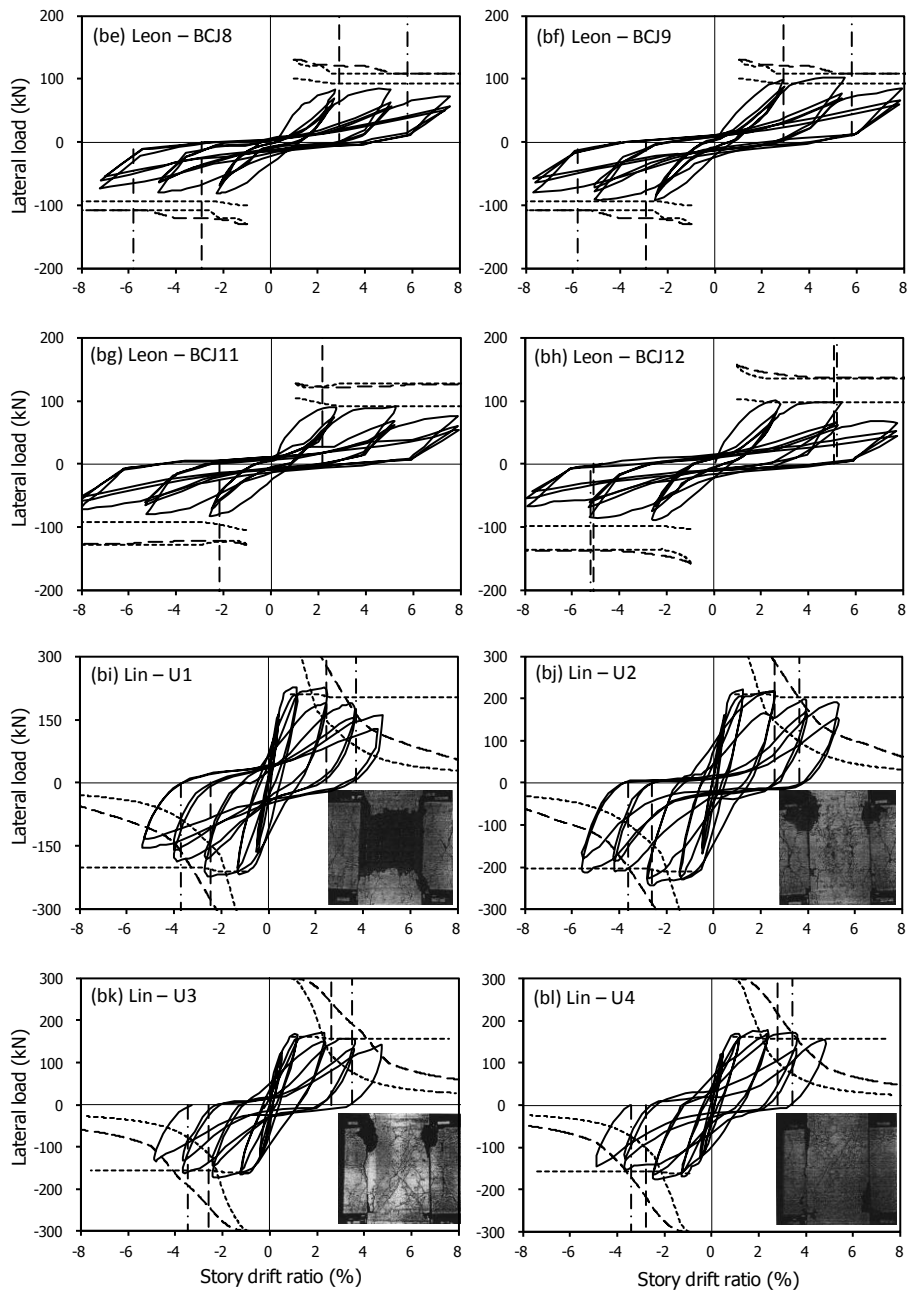


Fig. 4-9. Comparisons between hysteresis curves and predictions

In Fig. 4-9, load-carrying capacity of specimen was decreased by cyclic loading at same story drift ratio. Column lateral capacity  $P_n$  for 1<sup>st</sup> cyclic loading was similar with envelope curve, and  $P_n$  beyond 1<sup>st</sup> cyclic loading agreed well with the load carrying capacity for 2<sup>nd</sup> or 3<sup>rd</sup> cyclic loading.

In Fig. 4-9(b) - (d),  $P_n$  was evaluated to be greater than the load-carrying capacity of specimens. This is because the load-carrying capacity was early decreased when a lot of cyclic loading was applied or displacement increment was very small (Walker, 2001; ACI 374.1-05, 2005). In Figs. 4-9(h) - (j),  $P_n$  was evaluated to be less than the load-carrying capacity of specimens. The reason why is that column demand  $P_u$  was less than peak strength compared to other test results, inaccuracy of material test result, and manufacturing error. In Fig. 4-9(y) - (ab),  $P_n$  was greater than test results because of re-bar buckling and significant bond-slip of re-bars. In Fig. 4-9(bd) - (bh),  $P_n$  was not almost decreased by joint cross-beam. Load-carrying capacity was governed not joint failure but beam flexural failure. This indicates that the cross-beam is effective to prevent joint cracking and joint failure.

## 4.8 Discussion

In the present study, joint shear deformation and load-carrying capacity depending on bond-slip at the joint for interior beam-column connection was studied. Compared with 64 test results of existing interior beam-column connections, the proposed model was verified. The principal findings are as follows.

- 1) Considering the interaction between beam cross-section and joint, joint deformation based shear strength model depending on bond-slip was developed. The developed model predicts early crushing of beam concrete according to bond-slip, flexural failure due to beam re-bar fracture, and failure mechanism of beam-column connection with cross-beam as well as joint shear failure.
- 2) In RC beam-column connections subjected to cyclic loading, bond-slip of beam flexural bars occurs. In the joint with bond-slip, joint shear strength by truss mechanism is significantly decreased by bond strength degradation. In diagonal strut mechanism, bond-slip expands cracking width of the strut, and reduces the effective compressive strength of the diagonal strut. As a result, joint shear resistance is decreased as joint deformation increases. Particularly, in the joint with small column depth, bond-slip is increased, and early shear failure occurs at the joint due to the reduced contribution of truss mechanism.

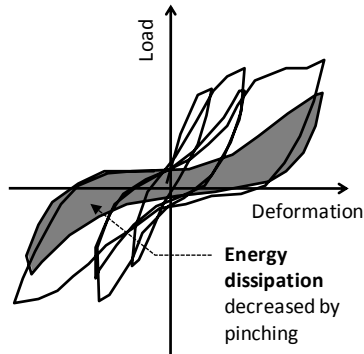
- 3) Predictions of joint shear strength and column lateral demand according to story drift ratio were compared with hysteresis response of beam-column connections with joint shear failure. The proposed model predicted well joint shear strength degradation depending on bond-slip of beam tensile bars after 1<sup>st</sup> cyclic loading and failure mode. However, the shear strength of the joint with the large number of cyclic loading and small displacement step was underestimated than predictions. This is because member strength is decreased early by concrete softening.
- 4) In beam-column connection with cross-beam, diagonal cracking is not occurred at the joint because the joint is fully confined. As a result, even though bond-slip is occurred, shear resistance due to strut mechanism is not decreased, and failure mode is governed by beam flexural failure.

The proposed shear strength model for beam-column connection evaluates the joint deformation capacity addressing bond-slip and joint bars details. The proposed model can be applied to performance based design to satisfy ductility demand. However, further research is needed for exterior beam-column connections.

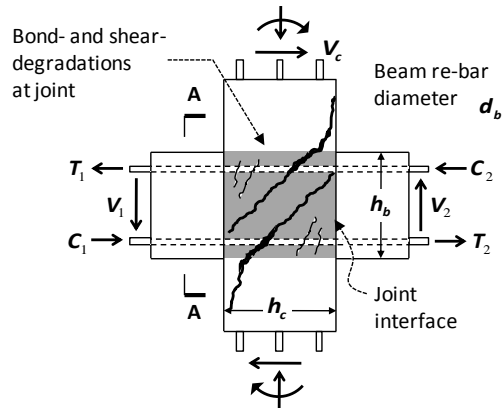
## **Chapter 5. Relationship between Energy Dissipation and Bond Resistance**

### **5.1 Introduction**

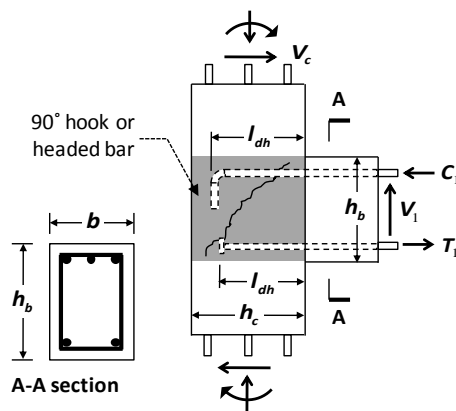
In reinforced concrete moment-resisting frames subjected to cyclic loading, the cyclic response, including stiffness degradation, strength degradation, and energy dissipation, is significantly affected by the behavior of the beam-column joints as well as individual members (Meinheit and Jirsa, 1977; Ehsani, 1982; Leon, 1989; Soleimani et al., 1979). Fig. 5-1 shows the cyclic response and joint load transfer mechanism of beam-column connections that are affected by bar bond-slip and diagonal shear cracking. Under cyclic loading, X-shaped diagonal cracks increase the shear deformation in the joint. Furthermore, due to the plastic strains of the beam flexural bars passing through the joint, the bar bond demand at the interior joint is increased by the compressive force, as well as the tensile forces (bar bond demand =  $T_1 + C_2$  or  $T_2 + C_1$ , in Fig. 5-1(b)). Thus the interior joint is susceptible to bar bond-slip. Once the bond-slip of beam bars and the shear deformation occur in the joint, the unloading/reloading stiffness and energy dissipation are significantly degraded, which appears as pinching in the cyclic response of Fig. 5-1(a).



(a) Cyclic response of beam-column connections



(b) Joint load-transfer of interior connection



(c) Joint load-transfer of exterior connection

Fig. 5-1. Typical cyclic response and joint load-transfer mechanism of beam-column connections

To mitigate bond- and shear strength-degradations in the joint, current earthquake design codes specify the minimum requirement of column depth-to-bar diameter ratio ( $h_c/d_b$ ): ACI 318-11 (2011) and ACI 352R-02 (2002) require  $h_c/d_b > 20$  and  $h_c/d_b > 20 f_y/420$ , respectively. However, previous test results have shown that even when the minimum requirement was satisfied, significant bond slip and shear deformation occurred at the beam-column joints (Kitayama et al. 1987; Leon 1989; Hakuto et al. 1999; Brooke et al. 2006). Thus, to secure the structural performance of beam-column joints, greater development lengths are required for the beam flexural bars as specified in NZS 3101:2006 (2006) and Eurocode 8 (2004).

In order to address the effects of the bond-slip and joint shear deformation, various elaborate models have been developed (Clough, 1966; Takeda et al., 1970; Otani, 1974; El-Metwally and Chen, 1988; Saatcioglu, 1991; Alath and Kunnath, 1995; Kunnath, 1998; Ghobarah and Biddah, 1999; Elmorsi et al., 2000; Fleury et al., 2000; Sivaselvan and Reinhorn, 2000; Song and Pincheira, 2000; Altoontash and Deierlein, 2003; Lowes and Altoontash, 2003; Uma and Prasad, 2004; Anderson et al., 2007; Mitra and Lowes, 2007; Birely et al., 2012). However, these models should be defined considering the complicated mechanisms of bar bond-slip and diagonal shear cracking. As a result, these models require great time and effort in modeling and computations, particularly when numerical analysis of overall moment frames is required.

More conveniently for consideration of bar bond-slip and diagonal shear

cracking, energy-based models for beams and columns were studied by Eom et al. (2009), and Eom and Park (2010). In the energy-based model, the load-displacement relationship was defined such that the area enclosed by the cyclic curve is the same as the predicted energy dissipation. Thus, if the energy dissipation is accurately predicted, the load-displacement relationship can be defined more conveniently.

In this chapter, the energy dissipation of beam-column connections was estimated from existing test results, considering the design parameters. On the basis of the estimation, the relationship between energy dissipation and bond resistance was proposed.



## 5.2 Evaluation of Energy Dissipation Capacity

In order to quantitatively evaluate the energy dissipation capacity of the beam-column connections, existing cyclic test results of 69 cruciform and 63 T-shaped beam-column connections were investigated (Lin, 2000; Brooke et al., 2006; Dai and Park, 1987; Durrani and Wight, 1982; Warcholik and Priestley, 1997; Joh et al., 1991; Milburn and Park, 1982; Xian et al., 1992; Kusuhara et al., 2004; Susanto and Hua, 2003; Shiohara, 2010; Pampanin et al., 2002; Oka and shiohara, 1992; Hwang et al., 2011; Franco et al., 1995; Benavernt et al., 2009; Ehsani et al., 1987; Kaku and Asakusa, 1991; Chutarat and Aboutaha, 2003; Chun et al., 2007; Tsonos et al., 1992; Ehsani and Wight, 1985; Shiohara, 2010). Tables 5-1 and 5-2 present the material and geometric properties of the specimens. The test specimens had conventional reinforcement details at the joints, such as transverse hoops, and no lap splices of beam flexural re-bars. The concrete strengths were  $f'_c = 23.9 - 88.2$  MPa. The yield strength and diameter of the beam bars were  $f_y = 276 - 710$  MPa and  $d_b = 9.5 - 35.8$  mm, respectively. The specimens exhibited various failure modes from the joint failure to the beam failure, depending on the design parameters such as the beam moment-to-column moment ratio, the joint shear capacity-to-demand ratio, and the bar bond parameters.

For parametric study of the existing test results, the energy dissipation ratio  $\kappa$  specified in ACI 374.1-05 (2005) was used. As shown in Fig. 5-2,  $\kappa$  is defined as the ratio of the actual energy dissipation  $E_H$  per load cycle to the

idealized elastic-perfectly plastic energy dissipation  $E_{ep}$ :  $\kappa = E_{II} / E_{ep}$ . Generally, the  $\kappa$  value increases with the deformation (Priestley, 2000). However, at small deformations, the energy dissipation does not significantly affect the shape of the load-displacement relationship. Thus, in the present study, according to ACI 374.1-05 (2005),  $\kappa$  was defined at the third load cycle of relatively large story drift ratio  $\delta = 3.5\%$ . However, when the existing test conditions did not satisfy the requirement of ACI 374.1-05 (2005), the  $\kappa$  was defined differently: when the number of load cycles at  $\delta = 3.5\%$  was less than three,  $\kappa$  was calculated for the second load cycle. When a specimen failed before  $\delta = 3.5\%$ , or when the strength of the second or third load cycle was less than 80 % of that of the first load cycle (this case can be regarded as the failure of the specimen),  $\kappa$  was evaluated at a moderate drift ratio of less than  $\delta = 3.5\%$ . In the calculation of  $E_{ep}$ , the initial stiffness  $k_i$  was defined from the envelop curve (see Fig. 5-2) (ACI 374.1-05, 2005). The  $\kappa$  values of the interior and exterior connection specimens are presented in Tables 5-1 and 5-2, respectively.

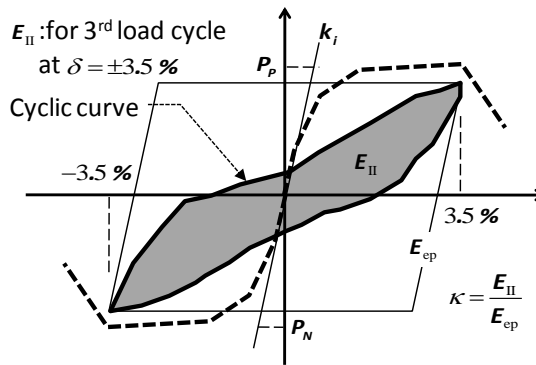


Fig. 5-2. Definition of energy dissipation ratio (ACI 374.01-5)

According to the previous studies (Eom and Park, 2010; Park and Eom, 2006; Eom and Park, 2010; Eom and park, 2013), the energy dissipation capacity of beam-column connections is affected by various design parameters, such as the geometry and reinforcement details of the beams and columns. However, as discussed in Chapter 5.1 and Fig. 5-1, the energy dissipation capacity of beam-column connections is degraded primarily by the bar bond-slip and diagonal cracking at the joint. Thus, the joint shear strength and the bond resistance of the beam flexural bars were considered as the primary design parameters for the evaluation of energy dissipation. In ACI 318-11 (2011), ACI 352R-02 (2002), and NZS 3101:2006 (2006), the requirements for the bond resistance of the beam flexural bars is defined as follows (refer to Figs. 5-1(b) and (c)).

$$\frac{h_c}{d_b} \geq k_1 \quad \text{for interior connections} \quad (5-1a)$$

$$\frac{l_{dh}}{d_b} \geq k_2 \quad \text{for exterior connections} \quad (5-1b)$$

$$V_{jn} \geq \phi V_{ju} \quad \text{for interior connections} \quad (5-2)$$

where  $h_c$  = column depth (or joint depth);  $d_b$  = the greatest bar diameter of the beam flexural bars;  $l_{dh}$  = development length of the beam flexural bars anchored inside the joint in exterior connections;  $k_1$  and  $k_2$  = minimum requirements for the bond resistance of the beam flexural bars specified in the

design codes;  $V_{jn}$  = nominal shear strength of the joint;  $V_{ju}$  = shear demand of the joint; and  $\phi$  = strength reduction factor for shear.

In Eq. (5-1a),  $k_1 = 20$  for ACI 318-11 (2011),  $20 \cdot (f_y/420)$  for ACI352R-02 (2002), and  $1.25f_y/(3.3\alpha_f\alpha_d\gamma\sqrt{f_c})$  for NZS 3101:2006 (2006), where  $\alpha_f$  and  $\alpha_d$  = coefficients addressing the direction of the beam flexural bars and the ductility of beam plastic hinges; and  $\gamma$  = coefficient addressing the story drift ratio demand  $\delta$  of the joint ( $= 1.53 - 0.29\delta$ ,  $\delta$  in %). In Eq. (5-1b),  $k_2 = f_y/(5.4\sqrt{f_c})$  for ACI 318-11 (2011),  $\alpha_f/(6.2\sqrt{f_c})$  for ACI352R-02 (2002), and  $0.24\alpha_1\alpha_2f_y/\sqrt{f_c}$  for NZS 3101:2006 (2006), where  $\alpha$  = overstrength factor of steel reinforcing bars addressing the strain-hardening behavior ( $= 1.25$ );  $\alpha_1$  and  $\alpha_2$  = coefficients addressing the details of hook anchorage and the joint confinement by transverse hoops. In Eq. (5-2),  $V_{jn} = \gamma_j\sqrt{f_c}'A_j$  and  $V_{ju} = T_1 + C_2 - V_c$  for interior connections, or  $C_1 - V_c$  for exterior connections, where,  $\gamma_j$  = coefficients addressing the confinement provided by the beams framing into the joint;  $A_j$  = effective joint shear area;  $T_1$  = resultant tension force at the beam critical section in the negative moment;  $C_2$  = resultant compression force at the beam critical section in the positive moment; and  $V_c$  = shear demand of the column (see Figs. 5-1(b) and (c)).

For parametric study related to bond-slip, from Eq. (5-1a),  $h_c/d_b$ ,  $(h_c/d_b)(\sqrt{f_c}'/f_y)$ , and  $(h_c/d_b)(\gamma\sqrt{f_c}'/f_y)$  were chosen as the bond parameters of the beam flexural bars for interior connections, and from Eq. (5-1b),  $(l_{dh}/d_b)$ ,  $(l_{dh}/d_b)(\sqrt{f_c}'/f_y)$ , and  $(l_{dh}/d_b)(\sqrt{f_c}'/\alpha_1\alpha_2f_y)$  were chosen for exterior connections. In the majority of the existing specimens investigated in this study, the number

of the beam flexural bars placed at the top was greater than at the bottom. In this case, the bond-slip of the bottom bars is greater than that of the top bars, because the inelastic deformation of the bottom bars is greater than that of the top bars, due to the force-equilibrium in the cross-section. Therefore, the bond parameters summarized in Tables 5-1 and 5-2 were defined using the yield strength and maximum diameter of the bottom bars.

Table 5-1. Summary of interior beam-column connection tests (Continued)

Specimens		$f'_c$ (MPa)	$f_y$ (MPa)	$l_s/h_b$	$h_c/d_b$	$\delta$ (%)	$\frac{\sum M_c}{\sum M_b}$	$V_n/V_u$	$\kappa$
Beckingsale (Lin, 2000)	B11	35.9	298	3.62	23.9	3.72	- <sup>1)</sup>	1.62	0.43
	B12	34.6	298	3.62	23.9	3.73	-	1.62	0.43
	B13	31.4	298	3.62	23.9	3.59	-	1.21	0.41
Brooke et al. (2006)	1B	31.2	552	4.07	31.5	3.10	2.05	1.08	0.33
	2B	40.6	552	4.07	31.5	3.06	2.02	1.24	0.35
	3B	44.8	537	4.20	26.6	3.08	1.21	1.35	0.34
	4B	42.8	537	4.20	26.6	3.15	1.21	1.32	0.33
Cheung (Lin, 2000)	1D-1	40.8	283	3.14	25.0	3.60	-	1.84	0.50
Dai and Park (1987)	U1	45.9	294	4.19	25.5	3.52	1.72	2.67	0.50
	U2	36.0	300	4.19	14.5	3.91	1.74	1.70	0.38
	U3	36.2	294	4.19	25.5	3.45	1.55	2.38	0.46
	U4	40.1	300	4.19	14.5	3.72	1.63	1.80	0.42
Durrani and Wight (1982)	S1	41.6	331	2.55	16.3	3.66	1.22	1.22	0.34
	S2	30.8	331	2.55	16.3	3.54	1.21	1.03	0.32
	S3	28.3	331	2.55	16.3	3.66	1.32	1.34	0.30
	X1	34.3	331	2.55	16.3	3.86	1.25	1.14	0.33
	X2	33.7	331	2.55	16.3	3.72	1.37	1.12	0.31
	X3	31.0	331	2.55	16.3	3.47	1.22	1.44	0.33
Warcholik et al.(1997)	6-1	49.6	460	3.50	21.8	3.36	1.25	0.71	0.26
Joh et al. (1991)	HL	27.4	404	3.86	23.6	5.22	1.59	1.94	0.32
	LH	26.9	404	3.86	23.6	5.22	1.59	1.92	0.32
Milburn et al. (1982)	U1	41.3	315	5.84	25.5	3.46	1.02	0.97	0.47
Priestley et al. (Lin, 2000)	P1	48.5	276	3.89	23.9	3.98	-	2.45	0.54
Teraoka et al. (Lin, 2000)	NO43	54.0	382	3.25	20.9	4.00	-	1.83	0.39
	NO47	54.0	382	3.25	20.9	2.92	-	1.20	0.35
	HNO1	88.2	611	3.00	25.2	3.82	-	1.03	0.38
	HNO3	88.2	441	3.00	18.0	3.93	-	0.76	0.38
Stevenson (Lin, 2000)	U1	34.0	338	5.84	25.5	4.25	-	0.82	0.39
Xian et al. (1992)	U1	30.9	453	3.05	37.5	3.22	2.12	1.48	0.44
	U2	40.8	445	3.05	28.3	2.26	1.81	2.30	0.36
	U3	42.5	445	3.05	28.3	2.78	2.27	1.75	0.39
	U4	47.2	492	3.05	22.5	2.21	2.87	2.73	0.40
	U5	60.7	492	3.05	22.5	4.62	1.84	1.62	0.36
	U6	59.3	463	3.05	16.1	2.56	1.95	1.68	0.35
Birss (Lin, 2000)	B1	27.9	288	3.62	17.8	3.46	-	1.00	0.30
	B2	31.5	288	3.62	22.9	3.00	-	1.07	0.37
Otani et al. (Lin, 2000)	J1	25.7	401	4.00	23.6	4.34	-	0.89	0.29
	J2	24.0	401	4.00	23.6	4.33	-	0.86	0.32
	J3	24.0	401	4.00	23.6	4.42	-	0.86	0.30
Kusuhara et al. (2004)	JE0	27.0	387	4.03	29.5	2.97	1.32	0.99	0.36

Table 5-1. Summary of interior beam-column connection tests

Specimens		$f'_c$ (MPa)	$f_y$ (MPa)	$l_s/h_b$	$h_c/d_b$	$\delta$ (%)	$\frac{\sum M_c}{\sum M_b}$	$V_n/V_u$	$\kappa$
Susanto and Hua (2003)	S1	33.0	510	4.63	18.9	3.76	1.90	0.91	0.23
	S2	34.0	510	4.63	18.9	3.78	1.90	0.92	0.21
	S3	35.0	510	4.63	18.9	3.91	1.92	0.94	0.22
	S5	39.0	425	4.75	15.8	3.82	1.60	1.21	0.20
	S6	38.0	425	4.75	15.8	3.83	1.59	1.19	0.21
Shiohara (2010)	B01	29.0	378	2.42	18.9	3.02	1.00	1.19	0.25
	B02	29.0	378	2.42	18.9	3.04	1.00	0.95	0.27
	B03	29.0	425	2.42	15.1	3.02	1.00	0.53	0.24
	B04	29.0	378	2.42	18.9	2.99	1.48	1.19	0.23
	B05	29.0	378	2.42	18.9	3.00	1.35	0.95	0.24
	B06	29.0	378	2.42	18.9	3.02	1.78	0.95	0.23
	B07	29.0	378	2.42	18.9	3.00	1.00	1.19	0.26
	B08	29.0	378	2.42	18.9	2.98	1.00	1.15	0.26
	B09	29.0	425	2.42	15.1	3.00	1.00	0.52	0.22
	B10	29.0	425	2.42	15.1	3.00	1.00	0.51	0.22
	C01	31.0	378	2.42	18.9	3.02	1.03	1.02	0.28
	C03	31.0	378	2.42	18.9	3.00	1.10	0.76	0.30
	D09	32.9	378	2.42	18.9	3.02	1.00	0.96	0.31
	D10	32.9	378	2.42	18.9	2.98	0.98	0.95	0.28
	D11	32.9	378	2.42	18.9	3.01	1.32	0.95	0.22
	E03	61.4	425	2.42	15.1	3.01	1.00	0.92	0.23
Pampanin et al. (2002)	C2	23.9	346	4.85	16.7	3.29	1.18	1.28	0.16
Oka et al. (1992)	J1	81.2	638	4.27	23.6	3.07	1.30	0.84	0.33
	J7	79.2	676	4.27	23.6	2.99	1.53	1.08	0.32
	J9	79.2	676	4.27	23.6	2.97	1.14	1.26	0.28
	J10	39.2	700	4.27	23.6	3.01	1.70	0.50	0.25
Hwang et al. (2011)	S1	32.0	465	4.21	21.7	2.90	1.85	0.89	0.27
	S2	32.0	710	4.21	24.8	3.30	1.86	0.90	0.21
	S3	32.0	710	4.31	20.3	3.49	1.44	0.73	0.17

<sup>1)</sup> The flexural strengths of beams and columns were not reported.

Table 5-2. Summary of exterior beam-column connection tests (Continued)

Specimens		$f'_c$ (MPa)	$f_y$ (MPa)	$l_s/h_b$	$l_{dh}/d_b$	$\alpha_1\alpha_2^{1)}$	$\Sigma M_c$ $/M_b$	$V_n/V_u$	$\kappa$
Franco et al. (1995)	R4	29.7	478	2.96	20.1	0.56	1.30	3.07	0.35
	R4S	38.6	464	2.96	20.1	0.56	1.30	3.73	0.34
	R4T	38.3	464	2.96	20.1	0.56	1.30	4.25	0.38
Benavernt et al. (2009)	EL	24.9	404	7.53	19.0	1.00	1.80	3.76	0.31
	EU	24.9	404	7.53	14.0	1.00	1.10	3.28	0.22
Ehsani et al. (1987)	1	64.7	428	3.28	15.2	0.56	1.89	2.02	0.40
	2	67.3	428	3.28	15.2	0.56	1.83	1.68	0.39
	3	64.7	428	3.58	13.1	0.56	1.90	1.42	0.34
	4	67.3	428	3.58	11.2	0.56	1.67	1.16	0.28
	5	44.6	280	3.47	11.0	0.56	1.41	1.20	0.35
Kaku et al. (1991)	1	31.1	360	4.55	15.2	0.80	2.57	1.36	0.32
	2	41.7	360	4.55	15.2	0.80	2.36	1.58	0.34
	3	41.7	360	4.55	15.2	0.80	1.45	1.58	0.26
	4	44.7	360	4.55	15.2	0.80	3.10	1.64	0.33
	5	36.7	360	4.55	15.2	0.80	2.27	1.48	0.31
	6	40.4	360	4.55	15.2	0.80	1.43	1.56	0.32
	7	32.2	395	4.55	15.7	0.80	2.48	1.39	0.33
	8	41.2	395	4.55	15.7	0.80	2.47	1.57	0.35
	9	40.6	395	4.55	15.7	0.80	1.74	1.56	0.33
	10	44.4	395	4.55	15.7	0.80	3.17	1.63	0.38
	11	41.9	395	4.55	15.7	0.80	2.51	1.58	0.35
	14	41.0	391	4.55	15.3	0.80	2.15	1.57	0.36
	15	39.7	391	4.55	15.3	0.80	2.36	1.54	0.30
	16	37.4	391	4.55	15.3	0.80	2.90	1.50	0.35
Shiohara (2010)	L01	27.7	380	2.42	15.1	0.80	1.01	1.86	0.18
	L02	27.7	380	2.42	15.1	0.80	1.43	1.86	0.23
	L03	27.7	380	2.42	15.1	0.80	1.82	1.86	0.25
	L04	27.7	380	2.42	12.3	0.80	1.01	1.86	0.18
	L05	27.7	380	2.42	12.3	0.80	1.43	1.86	0.21
	L06	27.7	380	2.42	12.3	0.80	1.82	1.86	0.21
	L07	27.7	380	2.42	9.45	0.80	1.01	1.86	0.15
	L08	27.7	380	2.42	9.45	0.80	1.82	1.86	0.15
	L09	27.7	380	2.42	9.45	0.80	2.54	1.86	0.16
	L10	27.7	380	2.42	12.3	0.80	1.23	1.23	0.18
	L11	27.7	380	2.42	12.3	0.80	1.72	1.23	0.22
	M01	29.0	380	2.42	15.1	0.80	1.43	1.91	0.21
	M02	29.0	380	2.42	15.1	0.80	1.43	1.91	0.28
	M03	29.0	380	2.42	12.3	0.80	1.43	1.91	0.19
	M04	29.0	380	2.42	12.3	0.80	1.43	1.91	0.20
	N04	29.0	380	3.12	17.4	0.56	3.19	1.82	0.28
	N05	29.0	380	3.12	13.4	0.56	1.99	1.82	0.20
	O01	29.8	380	2.42	15.1	0.80	1.43	1.94	0.23
	O02	29.8	380	2.42	12.3	0.80	1.01	1.94	0.18
	O03	29.8	380	2.42	12.3	0.80	1.43	1.94	0.17
	O04	29.8	380	2.42	12.3	0.80	1.74	1.28	0.18



Table 5-2. Summary of exterior beam-column connection tests

Specimens		$f'_c$ (MPa)	$f_y$ (MPa)	$l_s/h_b$	$l_{dh}/d_b$	$\alpha_1\alpha_2^{1)}$	$\Sigma M_c/M_b$	$V_n/V_u$	$\kappa$
Chutarat et al. (2003)	S1	27.6	483	4.67	14.3	0.80	1.30	1.00	0.26
	S2	27.6	483	4.67	14.3	0.80	1.30	1.00	0.22
	SA	33.1	483	5.56	28.6	0.80	1.30	3.53	0.51
	SB	33.1	483	5.56	28.6	0.80	1.30	3.53	0.49
Chun et al. (2007)	JC1	61.7	403	3.96	18.0	0.56	2.00	3.27	0.50
	JM1	60.1	403	3.96	17.4	0.56	2.00	3.23	0.48
	JC11	32.8	458	3.96	12.6	0.56	2.00	1.42	0.22
	JM11	32.8	458	3.96	12.6	0.56	2.00	1.42	0.23
Hwang et al. (2011)	S4	32.0	520	4.21	22.4	0.56	3.63	1.62	0.34
	S5	32.0	710	4.21	22.4	0.56	3.69	1.71	0.22
Tsonos et al. (1992)	S2	26.0	529	3.17	14.6	0.80	1.38	1.62	0.18
	S6	33.0	485	3.17	12.5	0.80	1.04	0.95	0.20
Ehsani et al. (1985)	1B	33.6	331	3.17	11.0	0.56	1.01	0.63	0.26
	2B	35.0	331	3.47	11.0	0.56	1.35	0.67	0.27
	3B	40.9	331	3.17	11.0	0.56	1.07	0.75	0.30
	4B	44.6	331	3.47	11.0	0.56	1.41	0.76	0.33
	5B	24.4	331	2.22	13.0	0.56	1.93	0.65	0.27
	6B	39.8	331	2.22	13.0	0.56	1.56	1.14	0.33

<sup>1)</sup>  $\alpha_1 = 0.7$  for 32 mm bars or smaller with side cover normal to the plane of the hook

$\geq 60$  mm, and cover on the tail extension of 90° hooks equal to or greater than 40 mm.

Otherwise,  $\alpha_1 = 1.0$ ;  $\alpha_2 = 0.8$  where confined by closed stirrups or hoops spaced at  $6d_b$  or less. Otherwise,  $\alpha_2 = 1.0$ .

Figs. 5-3 and 5-4 show the relationships between the bond parameters and the energy dissipation ratios  $\kappa$  for the interior and exterior connections, respectively. In the figures, the vertical and horizontal axes indicate the  $\kappa$  values and bond parameters, respectively. The trend lines and correlation coefficients  $R^2$  are presented in Figs. 5-3 and 5-4 ( $R^2$  close to 1.0 indicates a strong correlation).

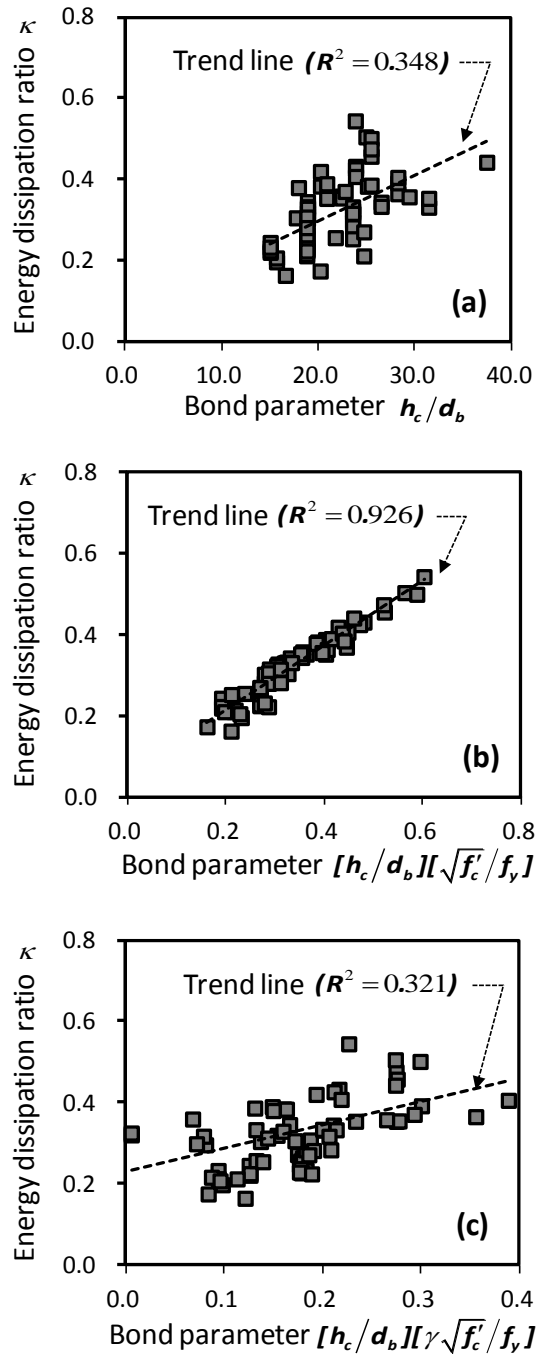


Fig. 5-3. Variation of energy dissipation ratio according to bond parameters: interior connections

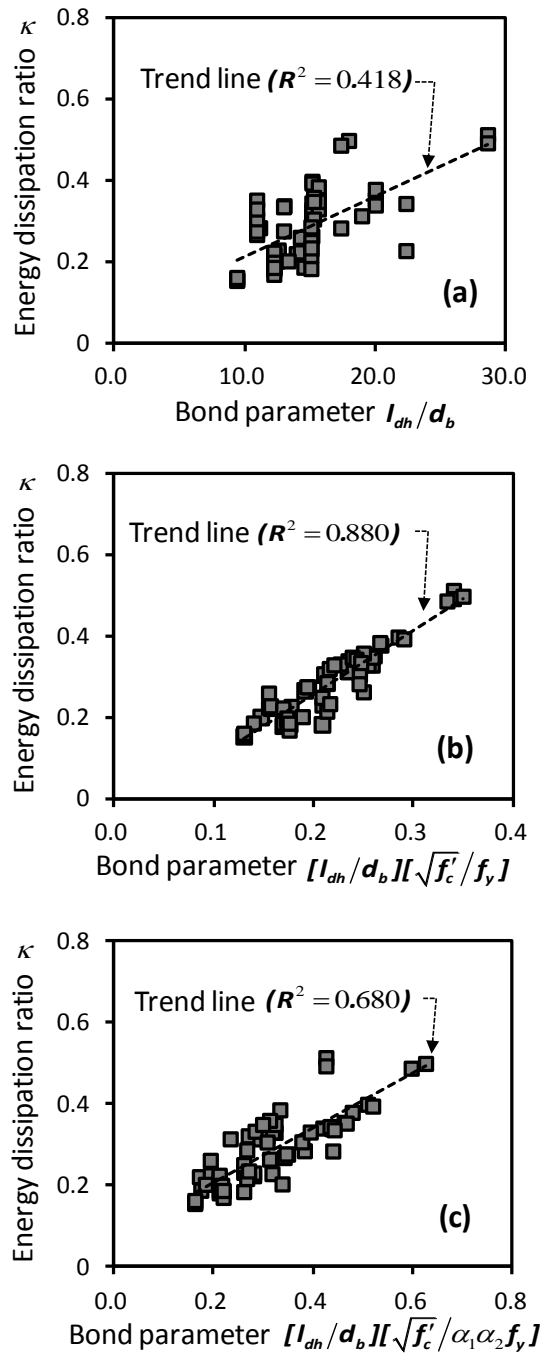


Fig. 5-4. Variation of energy dissipation ratio according to bond parameters: exterior connections

For both interior and exterior connections, the  $\kappa$  values correlated better with the bond parameters  $(h_c/d_b)(\sqrt{f'_c}/f_y)$  and  $(l_{dh}/d_b)(\sqrt{f'_c}/f_y)$ . In Figs. 5-3(b) and 5-4(b), the correlation coefficients,  $R^2 = 0.926$  for the interior connections and 0.880 for the exterior connections, were relatively high, which means good correlations between the energy dissipation capacity and the bond parameters  $(h_c/d_b)(\sqrt{f'_c}/f_y)$  and  $(l_{dh}/d_b)(\sqrt{f'_c}/f_y)$ . On the other hand, in Figs. 5-3(c) and 5-4(c), the parameters, which include the effects of the story drift ratio (i.e.  $\gamma$ ) and the details of hook anchorage and transverse reinforcement (i.e.  $\alpha_1\alpha_2$ ), did not show good correlations with the  $\kappa$  values. Furthermore, even though cyclic behaviors between low-strength bars and high-strength bars were different, re-bar strength discrepancy was not critical to the relationship between the energy dissipation capacity and the bond parameters. This is because the early fracture of the high-strength bars is related to not the energy dissipation capacity but deformation capacity.

For parametric study for the joint shear strength, from Eq. (5-2),  $V_{jn}/V_{ju}$  was chosen as the parameter. The shear parameters of the interior and exterior connection specimens are presented in Tables 5-1 and 5-2. Figs. 5-5(a) and (b) show the relationships between the energy dissipation ratios  $\kappa$  and the joint shear parameter  $V_{jn}/V_{ju}$  for the interior and exterior connections, respectively. As presented in Tables 5-1 and 5-2, in the majority of the connection specimens, the sum of column flexural capacities (i.e.  $\Sigma M_c$ ) was greater than the sum of beam flexural capacities (i.e.  $\Sigma M_b$ ), which indicates that the load-carrying capacity of the specimens was determined by the flexural capacities of the beams. Thus,  $V_{jn}$  and  $V_{ju}$  were calculated by using the beam plastic

hinge mechanism (refer to Tables 5-1 and 5-2). As shown in Fig. 5-5, the  $R^2$  values were much less than those of Figs. 5-3(b) and 5-4(b), which indicates that the correlation between the joint shear parameter and the energy dissipation capacity was significantly weaker than that of the bond parameter.

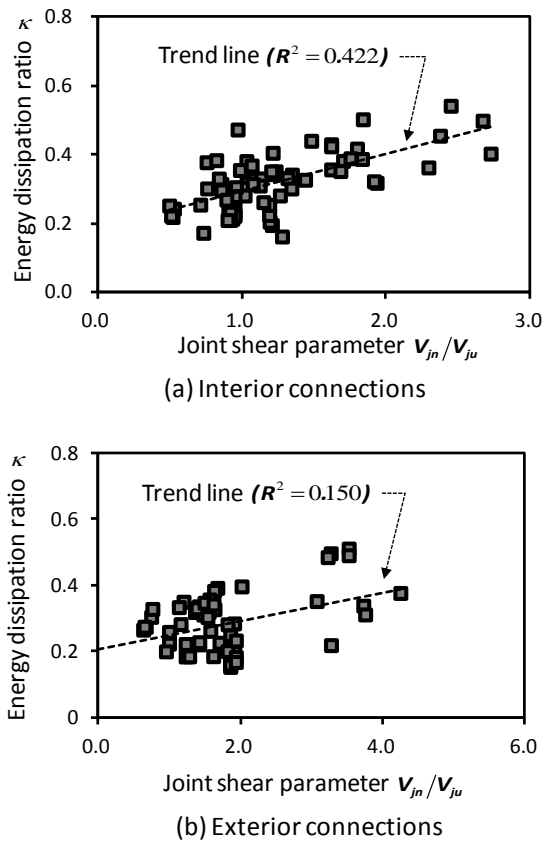


Fig. 5-5. Variation of energy dissipation ratio according to joint shear parameters

The effect of beam reinforcement on the energy dissipation ratio  $\kappa$  was also investigated (see Fig. 5-6). The results showed that the correlation

coefficients in the statistics were not improved, but even worse. This is because, even for the connection specimens designed in accordance with the bar bond requirements specified in ACI 318-11 (2011) and ACI 352R-02 (2002), the cyclic responses were dominated by the joint deformations, rather than by the beams or columns.

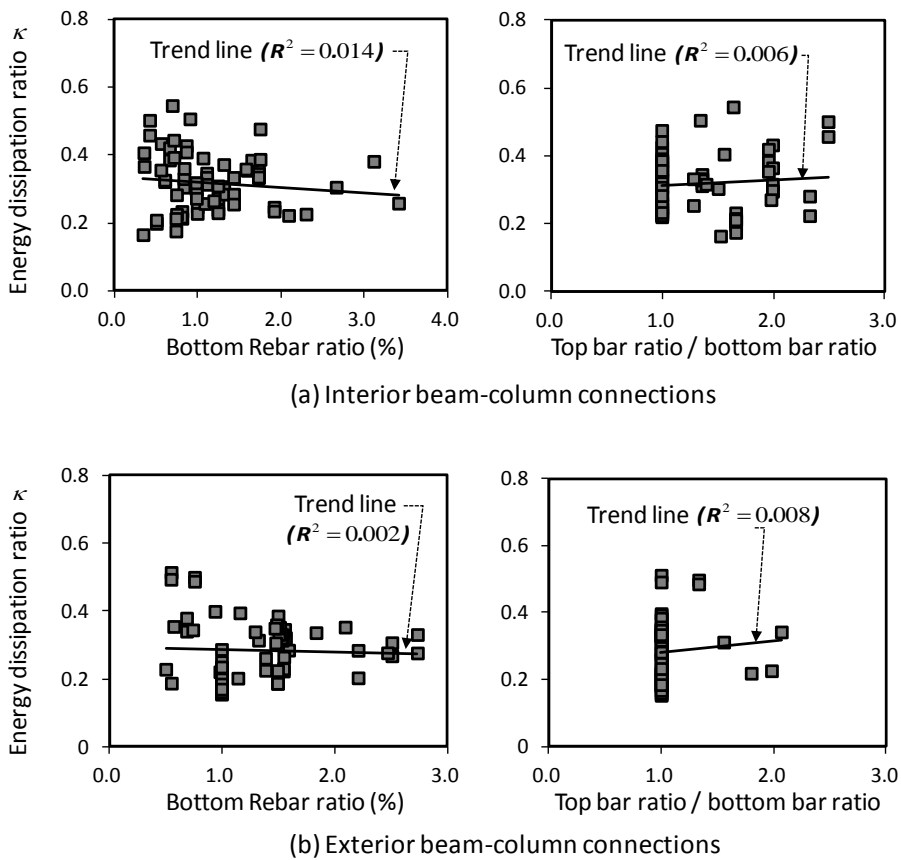


Fig. 5-6. Variations of energy dissipation according to beam rebar ratio

On the basis of the results shown in Figs. 5-3(b) and 5-4(b), the energy dissipation ratios  $\kappa$  of the interior and exterior connections were defined as the linear functions of the bond parameters  $(h_c/d_b)(\sqrt{f'_c}/f_y)$  and  $(l_{dh}/d_b)(\sqrt{f'_c}/f_y)$ , respectively, using the method of least squares.

For interior beam-column connections,

$$\kappa = 0.80 \frac{h_c}{d_b} \frac{\sqrt{f'_c}}{f_y} + 0.053 \quad \left( 0.16 \leq \frac{h_c}{d_b} \frac{\sqrt{f'_c}}{f_y} \leq 0.60 \right) \quad (5-3a)$$

For exterior beam-column connections,

$$\kappa = 1.56 \frac{l_{dh}}{d_b} \frac{\sqrt{f'_c}}{f_y} - 0.058 \quad \left( 0.13 \leq \frac{l_{dh}}{d_b} \frac{\sqrt{f'_c}}{f_y} \leq 0.35 \right) \quad (5-3b)$$

In Eqs. (5-3a) and (5-3b), the upper and lower limits on the bond parameters  $(h_c/d_b)(\sqrt{f'_c}/f_y)$  and  $(l_{dh}/d_b)(\sqrt{f'_c}/f_y)$  were specified as the minimum and maximum values presented in Tables 5-1 and 5-2, which represents the range of the design parameter of the existing tests.

### 5.3 Discussion

In the present study, by analyzing the cyclic test results of 69 interior and 63 exterior beam-column connections, the relationships between the bond resistance of beam flexural bars at the joints and the energy dissipation capacity were quantified.

The energy dissipation capacity (or the energy dissipation per load cycle) of interior and exterior connections correlated better with the bond resistance of beam flexural bars at the joints, than the joint shear resistance. Thus, the energy dissipation ratios  $\kappa$  of interior and exterior connections were defined as the linear functions of the bond parameters of beam flexural bars,  $(h_c/d_b)(\sqrt{f_c}'/f_y)$  and  $(l_{dh}/d_b)(\sqrt{f_c}'/f_y)$ , respectively. The correlation coefficients  $R^2$  for the interior and exterior connections were 0.93 and 0.88, respectively, which indicates very strong correlation.



## **Chapter 6. Energy-Based Hysteresis Model**

### **6.1 Introduction**

In reinforced concrete moment-resisting frames subjected to cyclic loading, bond-slip of beam bars increase the shear deformation in the joint. Once the bond-slip of beam bars and the shear deformation occur in the joint, the unloading/reloading stiffness and energy dissipation are significantly degraded, which appears as pinching in the cyclic response.

In order to address the effects of the bond-slip and joint shear deformation, various elaborate component models have been developed (Lowes and Altoontash, 2003; Elmorsi et al., 2000; Fleury et al., 2000; Altoontash and Deierlein, 2003; Mitra and Lowes, 2007; Uma and Prasad, 2004). Lowes and Altoontash (2003), Elmorsi et al. (2000), and Fleury et al. (2000) used continuum-type elements combined with spring elements, maintaining compatibility with beam and column line elements. Altoontash and Deierlein (2003) and Mirta and Lowes (2007) proposed the models that consist of a shear-panel element and rotational spring elements. Uma and Prasad (2004) proposed joint shear strength-deformation relationship for non-linear dynamic analysis. These models consist of a shear-panel element for the joint, and vertical, horizontal, and rotational spring elements. Although addressing all components affecting the connection behavior, these models require great time and effort in modeling and computations, particularly when

numerical analysis of the entire moment frame structures is required.

More conveniently for numerical analysis of the moment frame structures, lumped plasticity spring elements representing the overall cyclic response of a beam-column connection can be used. El-Metwally and Chen (1988), and Alath and Kunnath (1995) used zero-length rotational spring elements between the joint and beams/columns, to decouple the inelastic response of the beams, columns, and joints. Kunnath (1998) used joint spring elements at the intersection of beams and columns. Ghobarah and Biddah (1999) developed a stress-strain relationship for beam-column joints with transverse reinforcement, and Anderson et al. (2007) expanded the stress-strain relationship to joints without transverse reinforcement. Birely et al. (2012) used dual hinge elements at joint interfaces. Magliulo and Ramasco (2007) used a lumped plasticity model to perform three dimensional nonlinear dynamic analysis.

In the lumped plasticity models, the hysteresis constitutive model of the spring elements should be able to address the degradations of unloading/reloading stiffness, strength degradation, and energy dissipation under cyclic loading, which are significantly affected by the bond-slip and shear cracking at the joint. To describe the strength- and stiffness-degradations, various hysteresis models were developed by Clough (1966), Otani (1974), Saatcioglu (1991), Takeda et al. (1970), Song and Pincheira (2000), and Sivaselvan and Reinhorn (2000). The majority of the existing models are stiffness-based models in which the degradation of

unloading/reloading stiffness and strength under cyclic loading was defined on the basis of existing test results. However, it is very difficult to accurately define the unloading/reloading stiffness considering the complicated joint behavior such as the bar bond-slip and diagonal shear cracking. More importantly, in actual design of new structures without test results, it is not feasible to accurately define the model parameters.

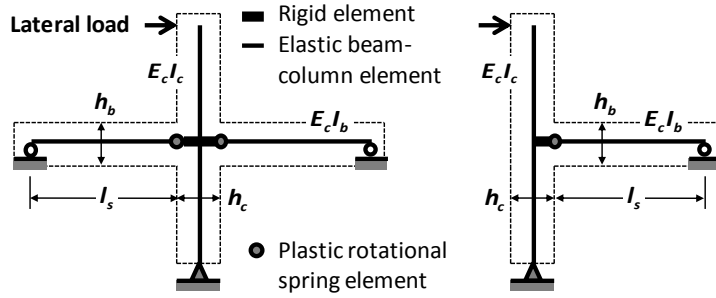
As an alternative, energy-based models for beams and columns were studied by Eom et al. (2009), Eom and Park (2010), Sucuoğlu and Acun (2012), Sucuoğlu and Erberik (2004), Kwak and Kim (2001). Ibarra et al. (2005) proposed the energy-based model for beam-column connection. Particularly, in the energy-based model proposed by Eom et al. (2009) and Eom and Park (2010), the load-displacement relationship was defined such that the area enclosed by the cyclic curve is the same as the predicted energy dissipation. Thus, if the energy dissipation is accurately predicted considering the bar bond-slip and diagonal shear cracking, the load-displacement relationship with pinching can be reversely created from the energy dissipation.

In this chapter, the concept of the energy-based model was applied to beam-column connections, to define the load-displacement relationship under cyclic loading. For this purpose, the energy-based hysteresis model was defined using the predicted energy dissipation. In the proposed model, the existing backbone curve of FEMA 356 (2000) was used, and the Pinching 4 model of OpenSees (Mazzoni et al., 2006) was modified to implement the

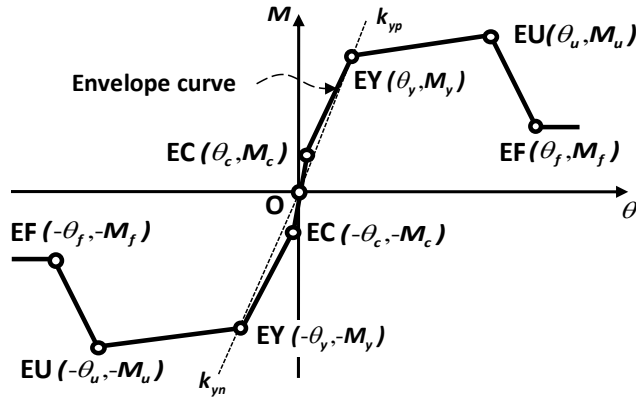
predicted energy dissipation. For verification, the proposed model was applied to existing test specimens, and the results were compared with the test results. Limitations on the application of the proposed method were also discussed.

## 6.2 Energy-Based Hysteresis Model

Fig. 6-1(a) shows the proposed lumped plasticity model for the interior and exterior beam-column connections. The proposed model comprises the elastic beam-column elements, rigid elements in the joint region, and rotational spring elements at the joint interface. If plastic hinges are expected to develop in columns, additional rigid and rotational spring elements can be used in the columns. The elastic beam-column elements simulate elastic flexural responses of beams and columns. The rigid elements are used to address the offset effect corresponding to the joint depth or height. The rotational spring elements at the joint interface are used to simulate the combined responses of the beams and joint. The advantage of the proposed model over the existing lumped plasticity approaches (El-Metwally and Chen, 1988; Alath and Kunnath, 1995; Kunnath, 1998; Ghobarah and Biddah, 1999; Anderson et al., 2007; Magliulo and Ramasco, 2007; Birely et al., 2012), is the simplicity: the rotational spring elements describe the combined cyclic responses of the beam-column connections, rather than the separate responses of the beams and the joint. Thus, the number of the spring elements can be reduced. Although simple spring models are used, by using the constraint condition of energy dissipation, the effect of the bar bond-slip and shear deformation can be directly addressed in the proposed load-displacement relationship.



(a) Analysis model for interior and exterior connections



(b) Envelope curve for plastic rotational spring element

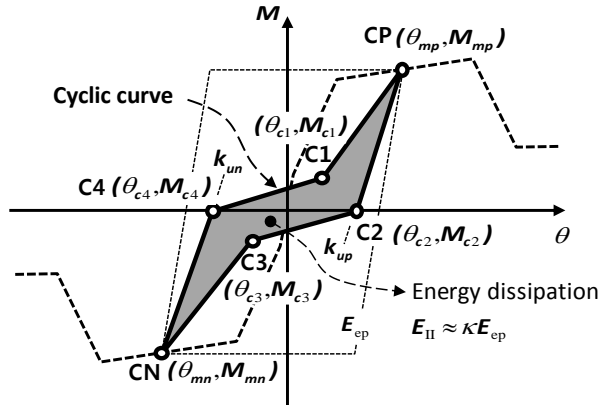
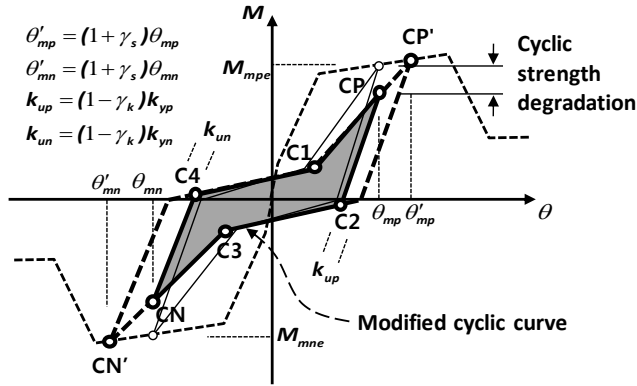

 (c) Cyclic curve for plastic rotational spring element without cyclic strength degradation ( $\gamma_s = 0$ )

Fig. 6-1. Energy-based hysteresis model for beam-column connections (Continued)



(d) Modified cyclic curve with cyclic strength degradation ( $\gamma_s \neq 0$ )

Fig. 6-1. Energy-based hysteresis model for beam-column connections

The proposed load-displacement relationship consists of an envelope curve and cyclic curves (see Fig. 6-1(b) and (c)). The envelop curve was developed modifying the backbone curve specified in FEMA 356 (2000). In the backbone curve, the parameters, except peak strength, yield strength, and initial stiffness, need to be determined empirically on the basis of available test results. Thus, in the present study, the parameters were determined on the basis of the existing test results reported in this paper. On the other hand, the cyclic curve was developed by modifying the Pinching 4 model of OpenSees (2006). When the parameters for the cyclic curve are determined, the proposed model used a very important constraint condition: the energy dissipation capacity which indicates the area of a cyclic curve. Thus, although the specific unloading/reloading stiffness is not exactly the same as each test result, the shape and area of the cyclic load-displacement relationship can be predicted without big mistakes.

Fig. 6-1(b) illustrates the envelope curve (i.e. a moment-plastic deformation angle relationship by monotonic loading) defined by modifying the backbone curve of FEMA 356 (2000). When the responses of the positive and negative loadings are different (i.e. when the number of bars is different at the top and bottom of the beam cross-section), the positive and negative envelope curves can be defined differently. In Fig. 6-1(b), EC, EY, EU, and ER indicate characteristic points corresponding to initial cracking, yielding, ultimate, and residual states, respectively. To define the cracking moment  $M_c$  at EC and yield moment  $M_y$  at EY, the flexural cracking moment  $M_{cr}$  and nominal yield moment  $M_{ny}$  at the critical section of beams (i.e. at the joint interface) are used as follows (see Fig. 6-1(b)).

$$M_c = M_{cr} \quad \text{and} \quad M_y \approx M_{ny} \quad (6-1a)$$

The ultimate moment  $M_u$  at EU and the residual moment  $M_r$  at ER are defined as functions of the nominal flexural capacity  $M_n$ .

$$M_u = \beta_u M_n \quad \text{and} \quad M_r = \beta_r M_n \quad (6-1b)$$

In Eq. (6-1b),  $\beta_u$  can be theoretically determined from nonlinear section analysis addressing reinforcement details, load conditions, and actual material strengths. When detailed analysis is not performed,  $\beta_u$  can be approximated as 1.25, considering the tensile stress  $1.25f_y$  of re-bars increased by the cyclic strain-hardening behavior (ACI 318-11, 2011). For the residual moment,  $\beta_r = 0.2$  was defined according to FEMA 356 (2000).



The elastic beam-column element represents the flexural rigidity and deformations of the beams and columns. The effective stiffness of the beams and columns,  $E_c I_c$  or  $E_c I_b$  shown in Fig. 6-1 (a), is determined addressing the stiffness degradation associated with flexural cracking and inelastic deformation before yielding. On the other hand, the rotational spring elements represent the elastic deformation of the joint, along with the pure plastic deformation of the joint and beams. According to Shin and LaFave (2004), the deformation angles at the initial cracking and yielding,  $\theta_c$  ( $= 0.0002 - 0.0003$  rad.) and  $\theta_y$  ( $= 0.002 - 0.01$  rad.), respectively, can be theoretically estimated by using the compression field theory or the softened truss model. In the present study,  $\theta_c$  at EC and  $\theta_y$  at EY addressing the elastic shear deformations of the joint before the yielding point are approximated as  $0.0002$  rad. and  $0.002$  rad., respectively. Generally, the elastic shear deformations of the joint are much less than the yield drift ratio of the connection, provided that appropriate transverse reinforcement is used in the joint. Therefore, relatively small deformation angles are used for  $\theta_c$  and  $\theta_y$  for simplicity. The validity of  $\theta_c = 0.0002$  rad. and  $\theta_y = 0.002$  rad. is demonstrated in Chapter 6.3 Applications. Note that if uncracked stiffness is used for the elastic beam-column elements of the beams and columns, the angles  $\theta_c$  at EC and  $\theta_y$  at EY of the rotational spring elements should include the pre-yield deformations of the beams and columns, as well as the elastic deformation of the joint.

The plastic deformation angles  $\theta_u$  at EU and  $\theta_r$  at ER were determined according to FEMA 356 (2000). However, FEMA 356 (2000) separately defines the plastic rotation angle at the beam plastic hinges and the plastic

shear angle at the joint, addressing the reinforcement detail and loading condition. In the proposed method, on the other hand, the rotational spring elements (Fig. 6-1(a)) represent the overall plastic deformation angle of a beam-column connection, including the beam plastic hinge zone and the joint. Therefore,  $\theta_u$  at EU for the rotational spring elements can be defined as the sum of the  $\theta_{bu}$  and  $\theta_{ju}$  specified in FEMA 356 (2000).

$$\theta_u = \theta_{bu} + \theta_{ju} \quad (6-2)$$

where  $\theta_{bu}$  = maximum plastic rotation angle of the beam, and  $\theta_{ju}$  = maximum shear angle of the joint. For more accurate analysis, the maximum plastic deformation angle  $\theta_u$  at EU can be determined from other advanced methods (Fischinger et al, 2008). The plastic deformation angle  $\theta_r$  at ER, which defines the post-peak descending slope of the envelope curve, was determined from the existing test results. For simplicity,  $\theta_r$  was approximated as  $\theta_r = 2.0\theta_u$ .

Fig. 6-1(c) shows the cyclic curve of the moment-plastic deformation angle relationship, connecting six characteristic points CP, C1, C2, CN, C3, and C4, which are defined such that the area enclosed by the cyclic curve is the same as the predicted energy dissipation (Eom et al., 2009; Eom and Park, 2010). CP ( $\theta_{mp}$ ,  $M_{mp}$ ) and CN ( $\theta_{mn}$ ,  $M_{mn}$ ) denote the positive and negative peak points, respectively, where the unloading and reloading behaviors begin. C2 ( $\theta_{c2}$ ,  $M_{c2}$ ) and C4 ( $\theta_{c4}$ ,  $M_{c4}$ ) denote the points where the unloading stiffness significantly decreases, causing pinching in the cyclic response. C1 ( $\theta_{c1}$ ,  $M_{c1}$ ) and C3 ( $\theta_{c3}$ ,  $M_{c3}$ ) denote the points where the reloading stiffness is recovered.

To ease the use in practice, the cyclic curve including stiffness- and strength-degradations was proposed by modifying the Pinching 4 model of OpenSees (Mazzoni et al., 2006).

The unloading behavior continues from points CP to C2 and from points CN to C4, where the moments are zero ( $M_{c2} = M_{c4} = 0$ , see Fig. 6-1(c)). The unloading stiffness  $k_{up}$  and  $k_{un}$  are defined as

$$k_{up} = (1 - \gamma_k) k_{yp} \quad \text{and} \quad k_{un} = (1 - \gamma_k) k_{yn} \quad (6-3)$$

where  $k_{yp}$  and  $k_{yn}$  = secant stiffnesses connecting point O and the positive and negative yield points EY, respectively (Fig. 6-1(b)), and  $\gamma_k$  = coefficient representing the degradation of the unloading stiffness under cyclic loading. In the present study, the degradation of the unloading stiffness is defined as the function of the load cycle number,  $i$  ( $= 0, 1, 2, \dots$ ), accumulated during the entire loading history (Mazzoni et al., 2006).

$$\gamma_k = 0.05 \times i \leq 0.8 \quad (6-4)$$

The original definition of  $\gamma_k$  in the reference (OpenSees manual) is  $K1 \cdot \delta_{\max}^{K2} + K3 \cdot i^{K4} \leq \gamma_{k, \max}$ , and the coefficients are determined on the basis of test results, user's experience, or engineering judgment. In the present study, the coefficients  $K1$ ,  $K2$ ,  $K3$ ,  $K4$ , and  $\gamma_{k, \max}$  were defined as 0, 0, 0.05, 1, and 0.8, respectively, from the comparison between the predicted hysteresis curves and the existing test results.

As shown in Fig. 6-1(c), the hysteretic energy dissipation per load cycle  $E_H$  of the connection is affected by the moments and deformation angles at points C1 and C3. Therefore, the moments and plastic deformation angles,  $(\theta_{c1}, M_{c1})$  at point C1 and  $(\theta_{c3}, M_{c3})$  at point C3, are defined as the functions of the predicted energy dissipation ratio  $\kappa$  of Eqs. (5-3a) and (5-3b) in Chapter 5 as follows.

$$\theta_{c1} = \lambda_{\theta} \theta_{mp} \quad \text{and} \quad \theta_{c3} = \lambda_{\theta} \theta_{mn} \quad (6-5)$$

$$M_{c1} = \lambda_M M_{mp} \quad \text{and} \quad M_{c3} = \lambda_M M_{mn} \quad (6-6)$$

where  $(\theta_{mp}, M_{mp})$  and  $(\theta_{mn}, M_{mn})$  = plastic deformation angles and moments at the peak points CP and CN, respectively, where the unloading behavior starts; and  $\lambda_{\theta}$  and  $\lambda_M$  = coefficients defined as the functions of the energy dissipation ratio  $\kappa$ , as follows.

$$\lambda_{\theta} = -0.95\kappa + 0.5 \quad (6-7)$$

$$\lambda_M = 1.5\kappa - 0.12 \quad (6-8)$$

The coefficients  $\lambda_{\theta}$  and  $\lambda_M$  are defined such that the energy dissipation per load cycle  $E_H$  enclosed by the cyclic curve (C1-CP-C2-C3-CN-C4) is the same as  $\kappa E_{ep}$ , where  $E_{ep}$  = energy dissipation by the elastic-perfectly plastic behavior between CP and CN (refer to Fig. 6-1(c)). Curve fitting between the

cyclic curves of Fig. 6-1(c) and the test results was performed for various  $\kappa$  values and drift levels. On the basis of the results,  $\lambda_\theta$  and  $\lambda_M$  were defined as the linear functions of  $\kappa$ , in Eqs. (6-7) and (6-8).

The validity of the definitions of  $\lambda_\theta$  (Eq. (6-7)) and  $\lambda_M$  (Eq. (6-8)) can be verified by comparing the energy dissipation ratios  $\kappa$  resulting from the proposed cyclic curve and the experimental cyclic curve. The comparisons were performed for the specimens Durrani S3 (Durrani et al., 1982), Xian U5 (Xian et al., 1992), and Dai U1 (Dai and Park, 1987). The results are shown in Fig. 6-2. The horizontal and vertical axes indicate the drift ratios and the energy dissipation ratios  $\kappa$ , respectively. As shown in Fig. 6-2, at all drift levels, the predicted  $\kappa$  values agreed with the test results, and notable discrepancy according to the drift levels was not observed. Note that the predicted  $\kappa$  values were not uniform, but greater or smaller than the  $\kappa$  values of Table 6-1 calculated by Eq. (5-3) in Chapter 5. This is because the coefficients  $\lambda_\theta$  and  $\lambda_M$  were approximated in Eqs. (6-7) and (6-8) when the proposed cyclic curve was defined.

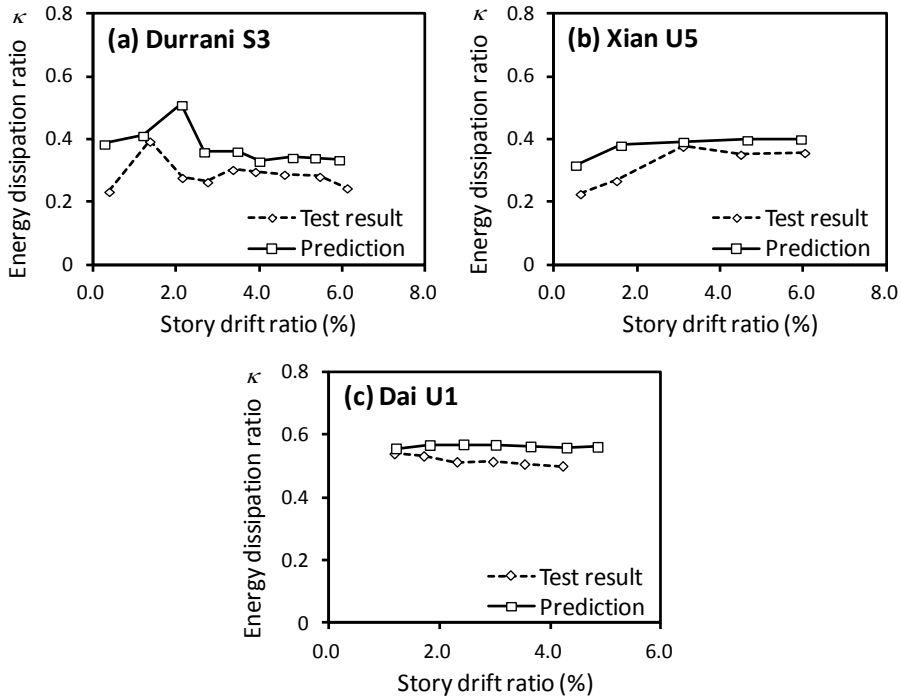


Fig. 6-2. Comparison of predicted energy dissipation ratios with test results

In the existing test results in Tables 5-1 and 5-2 in Chapter 5, as the  $\kappa$  value ranges 0.15 - 0.54,  $\lambda_\theta$  and  $\lambda_M$  vary from 0.36 to -0.01 and from 0.11 to 0.69, respectively. The cyclic curve defined in Eqs. (6-3) - (6-8) is applicable to both interior and exterior connections.

Strength degradation can occur during repeated load cycles between the peak points CP and CN, which is defined as the cyclic strength degradation in FEMA 440 (2005). The cyclic strength degradation (i.e. a delay in strength development) is caused by the bond deterioration of beam flexural bars, and the concrete crushing at the joint interface. Modifying the Pinching 4 model

of OpenSees (Mazzoni et al., 2006), the cyclic strength degradation was addressed as follows. As shown in Fig. 6-1(d), the cyclic curves after the first load cycle are defined with the modified peak points CP' and CN' corresponding to  $\theta'_{mp}$  and  $\theta'_{mn}$ , respectively. Since the plastic deformation angles at CP' and CN' are greater than those at CP and CN, the moments corresponding to  $\theta_{mp}$  and  $\theta_{mn}$  of the second and third load cycles are less than those of the first load cycle. Here, the plastic rotation angles  $\theta'_{mp}$  and  $\theta'_{mn}$  at the modified peak points CP' and CN' are defined as follows (see Fig. 6-1(d)).

$$\theta'_{mp} = (1 + \gamma_s) \theta_{mp} \quad \text{and} \quad \theta'_{mn} = (1 + \gamma_s) \theta_{mn} \quad (6-9)$$

The coefficient  $\gamma_s$  is defined by the number of load cycles,  $i$  ( $= 0, 1, 2, \dots$ ) accumulated during the entire loading history (Mazzoni et al., 2006).

$$\gamma_s = 0.1 \times i^{0.2} \leq 0.5 \quad (6-10)$$

The original definition of  $\gamma_s$  in the reference (OpenSees manual) is  $S1 \cdot \delta_{\max}^{S2} + S3 \cdot i^{S4} \leq \gamma_{s,\max}$ , and the coefficients are determined on the basis of test results, user's experience, or engineering judgment. In the present study, the coefficients  $S1$ ,  $S2$ ,  $S3$ ,  $S4$ , and  $\gamma_{s,\max}$  were defined as 0, 0, 0.1, 0.2 and 0.5, respectively, from the comparison between the predictions and the existing test results.

The advantages of the proposed model can be summarized as follows.

- 1) For simplicity, beam-column connections were modeled with rotational springs of limited numbers. Thus, the proposed model can be conveniently used for the numerical analysis of overall moment-frames.
- 2) The proposed model is able to accurately predict the energy dissipation capacity. In the present study, the energy dissipation of beam-column connection was accurately defined by the bar bond-slip parameters.
- 3) The proposed model defines the cyclic behavior of beam-column connections, using a constraint condition of energy dissipation capacity. Thus, the cyclic load-displacement relationship can be directly and accurately predicted without big mistakes.
- 4) The proposed model defines the cyclic behavior of beam-column connections, as the function of the energy dissipation capacity. Thus, the proposed model can be conveniently used for the performance-based design/analysis of structures; in actual design, if a target energy dissipation ratio  $\kappa$  is determined considering the design parameters, the beam-column connection model for numerical analysis can be directly determined according the target value.



### 6.3 Applications

The proposed lumped plasticity model (Fig. 6-1(a)), using the energy-based hysteresis moment-rotation relationship, was applied to existing interior and exterior connection specimens (Brooke et al., 2006; Dai and Park, 1987; Durrani and Wight, 1982; Xian et al., 1992; Hwang et al., 2011; Ehsani et al., 1987; Kaku and Asakusa, 1991; Chutarat and Aboutaha, 2003; Tsonos et al., 1992; Shiohara, 2010). In all specimens, the column flexural capacities (i.e.  $\Sigma M_c$ ) were greater than the beam flexural capacities (i.e.  $\Sigma M_b$ ). Thus, the rotational spring elements were used only for the beams. The cross sections of beams at the joint interface are shown in Figs. 6-3 and 6-4. The dimensions and modeling parameters of the specimens are presented in Table 6-1. In order to highlight the advantage of the proposed model, the specimens that exhibited various shapes in the cyclic responses from significant pinching (i.e. low energy dissipation ratio) to no-pinching (i.e. high energy dissipation ratio) were used in these examples.

Table 6-1. Modeling parameters for existing test specimens

Specimens <sup>1)</sup>	Bond resistance parameter		Modeling parameter			
	$(l_{dj}/d_b)(\sqrt{f_c'}/f_y)^2$	$\kappa^3$	$\lambda_\theta$	$\lambda_M$	$\theta_u (= \theta_{bu} + \theta_{fu})$ (rad.)	
Interior	Hwang S3 (2011)	0.162	0.182 (0.174)	0.327	0.153	0.040 (=0.025+0.015)
	Durrani S3 (1982)	0.292	0.287 (0.303)	0.227	0.311	0.040 (=0.025+0.015)
	Brooke 4B (2006)	0.324	0.312 (0.333)	0.204	0.348	0.040 (=0.025+0.015)
	Xian U5 (1992)	0.356	0.338 (0.358)	0.179	0.387	0.040 (=0.025+0.015)
	Xian U3 (1992)	0.415	0.385 (0.391)	0.134	0.458	0.040 (=0.025+0.015)
	Dai U1 (1987)	0.588	0.524 (0.500)	0.002	0.666	0.040 (=0.025+0.015)
Exterior	Tsonos S2 (1992)	0.141	0.161 (0.184)	0.347	0.122	0.035 (=0.025+0.010)
	Shiohara L06 (2010)	0.170	0.207 (0.212)	0.303	0.191	0.035 (=0.025+0.010)
	Ehsani 4 (1987)	0.215	0.277 (0.281)	0.237	0.296	0.035 (=0.025+0.010)
	Kaku 2 (1991)	0.251	0.333 (0.342)	0.184	0.380	0.035 (=0.025+0.010)
	Ehsani 2 (1987)	0.291	0.397 (0.391)	0.123	0.476	0.035 (=0.025+0.010)
	Chutarat SA (2003)	0.341	0.474 (0.510)	0.050	0.591	0.035 (=0.025+0.010)

<sup>1)</sup> The material and geometric properties are presented in Tables 5-1 and 5-2.

<sup>2)</sup>  $l_{dj} = h_c$  for interior connections, and  $l_{dh}$  for exterior connections.

<sup>3)</sup> The values are the predictions estimated from Eqs. (5-3a) and (5-3b), and the values inside the brackets are the test results.

As shown in Fig. 6-1(a), the specimens were modeled with the elastic beam-column elements, rotational spring elements, and rigid elements. For the elastic beam-column elements, to consider the effect of flexural cracking,  $0.35E_cI_g$  ( $E_c$  = modulus of concrete ( $=4700\sqrt{f'_c}$ ) and  $I_g$  = second-order moment of inertia of the gross cross section) was used for the flexural rigidity of the beams, as specified in ACI 318-11 (2011). Since the columns of the specimens were not subjected to axial compression load, the flexural rigidity of the columns was also defined as  $0.35E_cI_g$ , though ACI 318-11 (2011) recommends  $0.7E_cI_g$  for columns which are subjected to axial load. To address the offset effects by the joint depths, infinite flexural rigidity was assigned to the rigid elements.

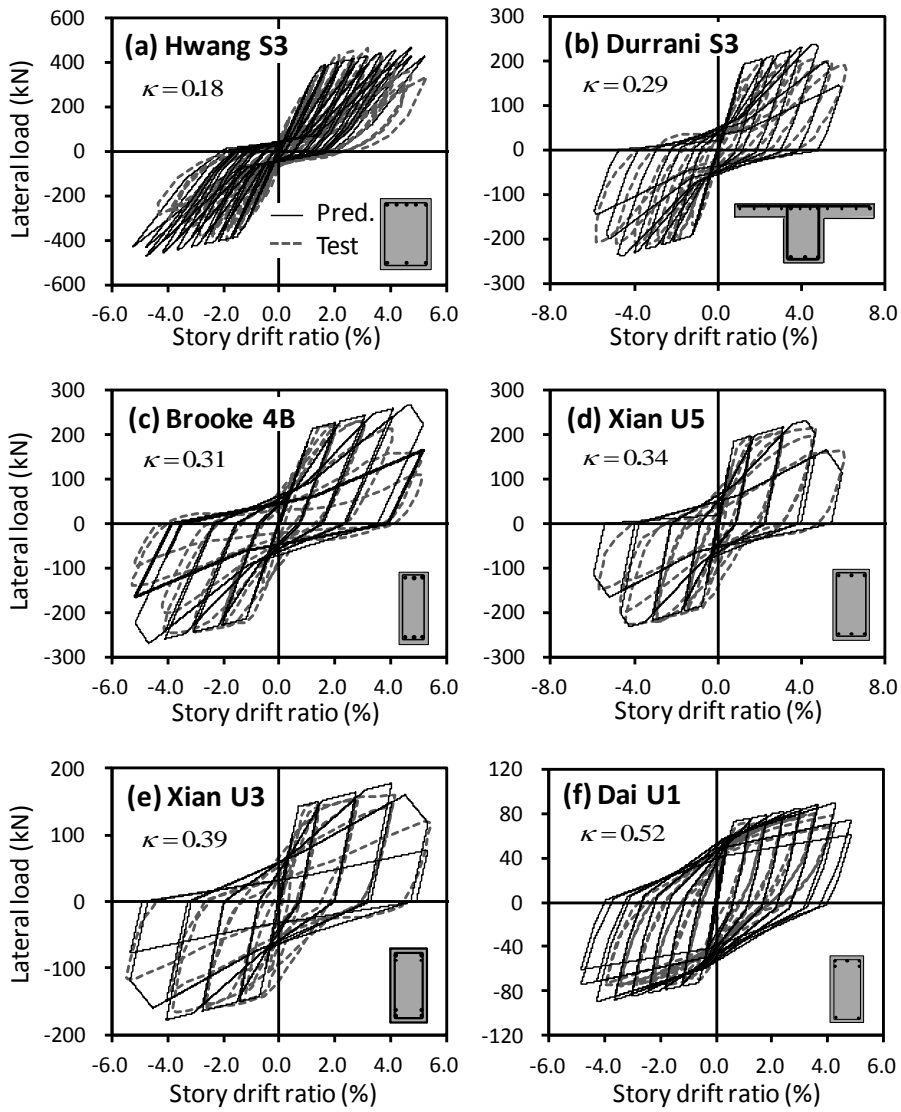


Fig. 6-3. Predicted cyclic responses vs. test results for interior connections (Brooke et al., 2006; Dai and Park, 1987; Durrani and Wight, 1982; Xian et al., 1992; Hwang et al., 2011)

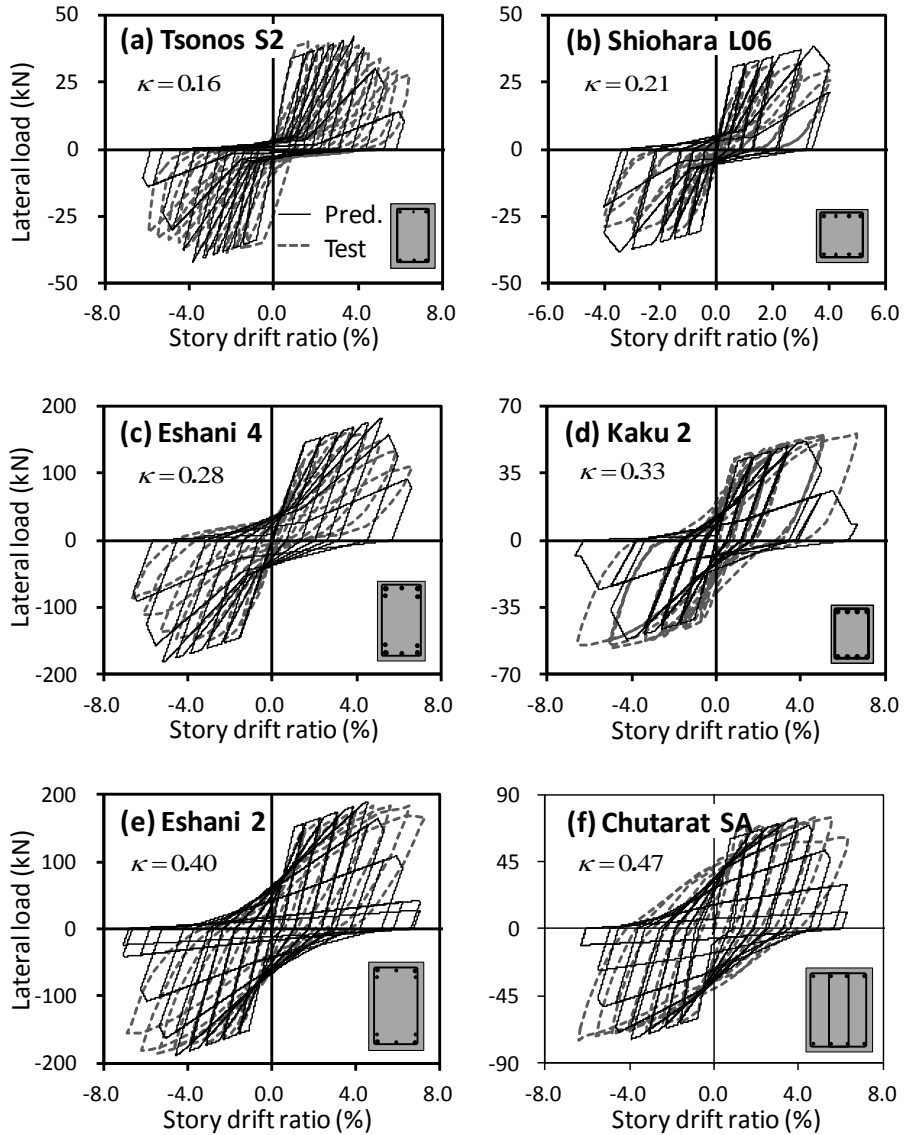


Fig. 6-4. Predicted cyclic responses vs. test results for exterior connections (Ehsani et al., 1987; Kaku and Asakusa, 1991; Chutarat and Aboutaha, 2003; Tsonos et al., 1992; Shiohara, 2010)

For the rotational spring elements located at the joint interface, the moments at the characteristic points of the envelope curves,  $M_c$ ,  $M_n$ ,  $M_u$ , and  $M_r$ , were determined from section analysis of the beam cross-sections: the flexural cracking moment  $M_{cr}$  ( $=0.63\sqrt{f'_c} I_g / y_t$ , where  $y_t$  = distance between the neutral axis and the tension end) and the nominal flexural strength  $M_n$  were used for  $M_c$  and  $M_y$ , respectively; by using  $\beta_u = 1.25$  and  $\beta_f = 0.2$ ,  $M_u$  and  $M_r$  were determined as  $1.25M_y$  and  $0.2M_y$ , respectively.  $\theta_c = 0.0002$  rad and  $\theta_y = 0.002$  rad were used for the plastic deformation angles at the cracking and yield points, respectively. The maximum plastic deformation angles  $\theta_u$  of the connection specimens were determined by using Eq. (6-2):  $\theta_u = \theta_{bu} + \theta_{ju}$ . Table 6-1 presents the maximum beam plastic rotation angles  $\theta_{bu}$ , and the maximum joint shear angles  $\theta_{ju}$  of the connection specimens.  $\theta_{bu}$  and  $\theta_{ju}$  corresponding to the reinforcement details and load conditions were determined from FEMA 356 (2000).

The cyclic curves of the rotational spring elements were determined from the properties of Eqs. (6-3) - (6-8), which were defined as the functions of the energy dissipation ratio  $\kappa$  in Eqs. (5-3a) and (5-3b) in Chapter 5. The  $\kappa$  values of the specimens are presented in Table 6-1. In Table 6-1, for instance, the predicted  $\kappa$  of the specimen Ehsani 2 was 0.474, which was very close to the test result 0.510. For the specimen Chutarat SA, the predicted  $\kappa$  was 0.397, which was very close to the test result 0.391. This result indicates that the proposed model predicted the test results with reasonable precision. Detailed calculations for the envelope curves and the cyclic curves are presented as follows.

The energy-based hysteresis model was applied to an interior connection specimen U1 tested by Dai and Park (1987). The configuration of the connection and the reinforcement details of the beam at the joint face are shown in Fig. 6-5(a). The yield strength of re-bars was  $f_y = 294$  MPa, and the concrete strength was  $f'_c = 45.9$  MPa. Fig. 6-5(b) shows the envelope curve of the plastic rotational spring element (see the dashed line). The characteristic points EC, EY, and EU are marked on the figure. Since the area of the bottom bars was two-fifths the area of the top bars, the envelope curves were asymmetric. The cracking and ultimate moment capacities calculated from the section analysis for the negative loading (i.e. top bars in tension) were  $M_{cr} = 33.9$  kN·m and  $M_n = 114$  kN·m, respectively. Therefore, the cracking and yield moments of the negative envelope curve were  $M_c = 33.9$  kN·m and  $M_y = 114$  kN·m. The ultimate and residual moments were determined as  $M_u (= 1.25M_y) = 143$  kN·m, and  $M_r (= 0.2M_y) = 22.8$  kN·m (see Fig. 6-5(b)). The cracking and ultimate moment capacities for the positive loading (i.e. bottom re-bars in tension) were 33.9 and 48.1 kN·m, respectively. The maximum and residual strengths of the positive loading were determined in the same manner.

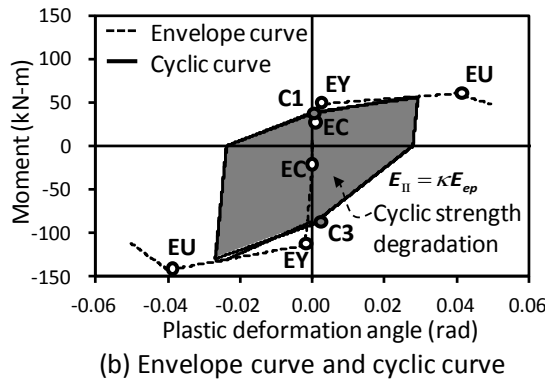
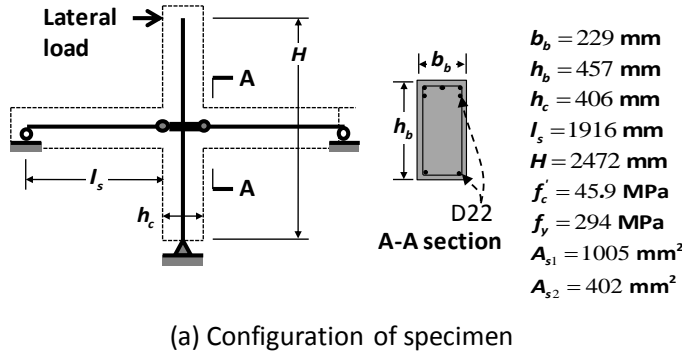


Fig. 6-5. Interior connection Dai and Park U1 (Dai and Park, 1987)

The cracking and yield plastic deformation angles of the positive and negative envelope curves were defined as  $\theta_c = 0.0002$  rad. and  $\theta_y = 0.0013$  rad., respectively. According to FEMA 356 (2000), the maximum plastic rotation angle of the beam and the maximum plastic shear angle of the beam-column joint were determined as  $\theta_{bu} = 0.025$  rad. and  $\theta_{ju} = 0.015$  rad., respectively (see Table 6-1). Therefore, the maximum plastic deformation angle of the connection specimen U1 was  $\theta_u = \theta_{bu} + \theta_{ju} = 0.040$  rad.  $\theta_r = 2.0\theta_u = 0.080$  rad. was used.

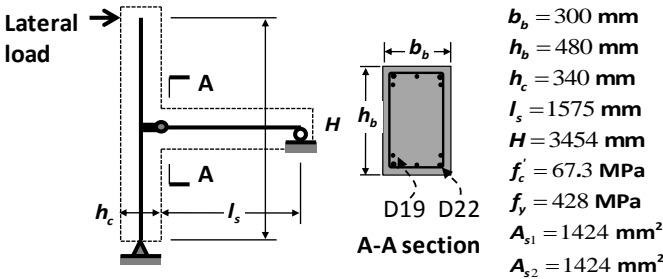


Fig. 6-5(b) shows the cyclic curve of the plastic rotational spring element for  $\theta_{mp} = 0.03$  rad. and  $\theta_{mn} = -0.03$  rad. The overall depth of the column cross section was  $h_c = 406$  mm, and the maximum diameter of the bottom re-bars of the beam was  $d_b = 15.9$  mm. Therefore, the energy dissipation ratio  $\kappa$  of the specimen U1 was calculated as (see Eq. (5-3a) and Table 5-1 in Chapter 5)

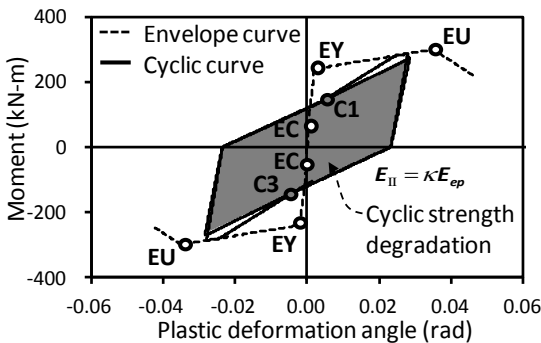
$$\kappa = 0.8 \frac{h_c}{d_b} \frac{\sqrt{f'_c}}{f_y} + 0.053 = 0.8 \frac{406}{15.9} \frac{\sqrt{45.9}}{294} + 0.053 = 0.524 \quad (6-11)$$

The coefficients defining the cyclic curve were determined as  $\lambda_\theta = 0.002$  and  $\lambda_M = 0.666$  from Eqs. (6-7) and (6-8) ( $\kappa = 0.524$ ). In the cyclic curve, the coefficients  $\gamma_s = 0.155$  and  $\gamma_k = 0.450$  representing the stiffness- and strength-degradations were calculated using  $i = 9$ . The entire cyclic response of U1 predicted by the proposed method is shown in Fig. 6-3(f).

The energy-based hysteresis model was applied to the exterior connection 2 tested by Ehsani et al. (1987) (Fig. 6-6(a)). The yield strength of re-bars was  $f_y = 428$  MPa, and the concrete strength was  $f'_c = 67.3$  MPa. From the section analysis for the negative loading,  $M_{cr} = 59.5$  kN·m and  $M_n = 239$  kN·m. Thus,  $M_c = 59.5$  kN·m and  $M_y = 239$  kN·m. The ultimate and residual moments were  $M_u (= 1.25M_y) = 299$  kN·m, and  $M_r (= 0.2M_y) = 47.8$  kN·m (see Fig. 6-6(b)). Since the area of the top and bottom bars was identical, the positive envelope curve was the same as the negative envelope curve. The cracking and yield plastic deformation angles of the positive and negative envelope curves were  $\theta_c = 0.0002$  rad. and  $\theta_y = 0.0018$  rad., respectively. The

$$\theta_{bu} + \theta_{ju} = 0.035 \text{ rad. } (\theta_r = 2.0\theta_u = 0.070 \text{ rad.}).$$


(a) Configuration of specimen



(b) Envelope curve and cyclic curve

Fig. 6-6. Exterior connection: Ehsani 2 (Ehsani et al., 1987)

The embedment length of the beam re-bars was  $l_{dh} = 290$  mm, and the maximum diameter of the bottom bars of the beam was  $d_b = 19.1$ . Therefore,

the energy dissipation ratio  $\kappa$  was calculated as (see Eq. (5-3b) in Chapter 5)

$$\kappa = 1.56 \frac{l_{dh}}{d_b} \frac{\sqrt{f'_c}}{f_y} - 0.058 = 1.56 \frac{290}{19.1} \frac{\sqrt{67.3}}{428} - 0.058 = 0.397 \quad (6-12)$$

The coefficients defining the cyclic curve were calculated as  $\lambda_\theta = 0.123$  and  $\lambda_M = 0.476$  from Eqs. (6-7) and (6-8) ( $\kappa = 0.397$ ). Fig. 6-6(b) shows the cyclic curve corresponding to  $\theta_{mp} = 0.03$  rad. and  $\theta_{mn} = -0.03$  rad. In the cyclic curve, the coefficients  $\gamma_s = 0.148$  and  $\gamma_k = 0.350$  representing the stiffness- and strength- degradations were calculated using  $i = 7$ . The entire cyclic response of the specimen predicted by the proposed energy-based hysteresis model is shown in Fig. 6-4(e).

Figs. 6-3 and 6-4 compare the predicted cyclic responses of the interior and exterior connection specimens with the test results. As shown in the figures, the proposed lumped plasticity method using the proposed energy-based hysteresis model predicted the cyclic responses of the specimens with reasonable precision, including the energy dissipation, pinching, and strength- and stiffness- degradations during cyclic loading. In particular, the energy-based hysteresis model was applicable to various cyclic curves, from the significantly-pinched cyclic curves with lower  $\kappa$  values to the less-pinched cyclic curves with higher  $\kappa$  values. However, in the predictions shown in Figs. 6-4(e) and (f), strength degradation occurred earlier than the test results. The difference between the prediction and the test result is attributed to the underestimation of the maximum deformation by FEMA 356 (2000). As

mentioned, the present study focused on the energy dissipation ratio, while the maximum deformation was predicted following FEMA 356 (2000).

The application of the proposed model is limited to the joints with transverse hoops and beam re-bars without lap splices at the joint. Further, it is assumed that beams show stable flexural behavior without deficiency in shear strength, and thus the overall cyclic response of the connections is affected by the bond-slip damage of the joint region and the flexural damage of the beam end, rather than the shear damage of the beam. In addition, further research is required for the connections with columns subjected to moderate or high compressive load, because the specimens analyzed in the present study were mostly free from axial compressive load. The ranges of the design parameters are limited to those of existing test specimens that were used to develop the proposed model: the column moment-to-beam moment ratio  $\sum M_{nc} / \sum M_{nb} \geq 1.0$ , the joint shear capacity-to-demand ratios  $0.5 \leq V_n / V_u \leq 4.25$ , the column depth-to-beam bar diameter ratios  $14.5 \leq h_c / d_b \leq 37.5$  for interior connection, and the embedment length-to-beam bar diameter ratios  $9.5 \leq l_{dh} / d_b \leq 28.6$  for exterior connection. Regarding other design parameters, including the reinforcement details of joints, material and geometric properties of beams, and story drift ratio, further research is required.

## 6.4 Discussion

In the present study, a simplified method to model the beam-column connections subjected to cyclic loading was investigated. On the basis of the relationships between the bond resistance of beam flexural bars at the joints and the energy dissipation capacity, an energy-based hysteresis model was proposed, by modifying the backbone curves of FEMA 356 (2000), and the Pinching 4 model of OpenSees (Mazzoni et al., 2006). For verification, the cyclic responses of the existing connections predicted by the proposed method were compared with the test results. The major conclusions of the present study are summarized as follows.

- 1) The energy-based hysteresis model was defined such that the area enclosed by the cyclic curve was the same as the predicted energy dissipation capacity. The unloading and reloading behaviors, pinching, and strength- and stiffness-degradations under cyclic loading were described by using the functions of the energy dissipation ratio  $\kappa$  and the loading history.
- 2) To simulate the cyclic responses of the connections including the joint responses, a lumped plasticity model, which consists of elastic beam-column elements, rigid elements, and plastic rotational spring elements, was investigated. For the rotational spring elements, the proposed energy-based hysteresis model was used. The proposed method was applied to

existing test specimens. The results showed that the predicted cyclic responses by the proposed method correlated well with the test results of the interior and exterior connections, which range from significantly-pinched cyclic curves, to less-pinched cyclic curves.

## **Chapter 7. Nonlinear Time History Analysis Using Energy-Based Model**

### **7.1 Introduction**

In current earthquake design codes (KBC 2009, 2009; IBC 2009, 2009; ASCE/SEI 07-5, 2005), design earthquake load applied to buildings is decreased using response modification factors defined with respect to deformation capacity. However, the inelastic hysteretic response and energy dissipation of beam-column connection affect the earthquake demand of the buildings. In nonlinear static method such as capacity spectrum method (ATC, 1996) and direct displacement-based design (Priestley, 2000), the earthquake demand of buildings is determined using energy dissipation due to hysteretic behavior of the joint.

Song and Pincheira (2000) investigated the effect of stiffness and strength degradation on the maximum inelastic displacement of single degree of freedom system. The prediction by FEMA 273 (1997) underestimated the peak displacement for periods below 0.3 seconds on rock or firm soil and below 1.5 seconds on soft soil. Sucuoğlu and Erberik (2004) evaluated the earthquake performance of inelastic single degree of freedom system using energy-based strength deterioration model. As the cyclic behavior was deteriorated, spectral displacement of deteriorated structure system was significantly increased for periods below 1.5 seconds. Ibarra et al. (2005)

performed the dynamic analysis of single degree of freedom system with strength- and stiffness-deteriorated hysteretic response, which reduces energy dissipation capacity, for 40 earthquake acceleration. It was reported that the deterioration of component is critical to the response of structure system that undergo large inelastic deformation. FEMA 440 (2005) performed the dynamic analysis of single degree of freedom system with various hysteretic behaviors (Elasto-plastic; Stiffness degradation; Strength and stiffness degradation) for 240 earthquake acceleration. It was reported that the maximum deformation was greatly increased as the energy dissipation decreased in the structures with the natural period below 1.0 second, and the maximum deformation was significantly increased in the structures with shorter natural period. That is, in short natural period structures, the energy dissipation capacity affects significantly to the earthquake response of the structures.

It indicates that, to determine the seismic response and design earthquake load in reinforced concrete (RC) low-rise moment frame structure with short period, not only the deformation capacity but the hysteretic behavior and energy dissipation including strength- and stiffness-degradation should be considered. However, all of existing studies performed the nonlinear dynamic analysis for single degree of freedom system. Earthquake response depending on the hysteretic behavior of system needs to be evaluated for multi degree of freedom system.

In RC moment frame structures, hysteretic behavior and energy



dissipation are significantly affected by inelastic behavior of beam-column connections. This is because most inelastic deformation is concentrated to the connection. The inelastic behavior depends on bond strength between beam flexural bars and joint concrete. Particularly, the energy dissipation capacity of the joint increases with bond resistance of the beam flexural bars (see Chapter 5). In this chapter, using the energy-based hysteresis model proposed in Chapter 6, nonlinear time history analysis for low-rise RC moment frame structures below 5 stories was performed. On the basis of the nonlinear dynamic analysis result, the earthquake response according to energy dissipation capacity of the joint was evaluated.

## 7.2 Analysis Model Using OpenSees

### 7.2.1 Moment Frame Structure

For moment frame structures with short period, to evaluate the earthquake response of the structures according to energy dissipation ratio of the joint, nonlinear time history analysis was performed using OpenSees program (2006). Three types of moment frame structures, which are 3 stories-1 bay structures, 3 stories-3 bay structures, and 5 stories-3 bay structures, were analyzed. Fig. 7-1 shows structure modeling for dynamic analysis. Each story height is 3600 mm, and span between columns is 6000 mm. Natural periods are  $T_n = 0.331$  seconds for 3 stories-1 bay structures,  $T_n = 0.355$  seconds for 3 stories-3 bay structures, and  $T_n = 0.606$  seconds for 5 stories-3 bay structures. Beam-column connection modeling was based on the energy-based hysteretic model proposed in Chapter 6. Assuming plastic hinges at column face from strong column-weak beam concept, the plastic hinge of a beam was located at column depth /2 apart from the joint node. The plastic hinge of a column was applied to the bottom node of 1<sup>st</sup> floor column.

Beam cross-section is 400 mm × 600 mm, and column cross-section is 500 mm × 500 mm. Concrete strength is 24 MPa. Positive and negative moment of the beam are 250 kN·m and 400 kN·m, respectively. Positive and negative moment of the column are 440 kN·m.

According to FEMA 273 (1997), 100 % of dead load and 25 % of live

load were applied to initial gravity load and structure mass. The initial load was applied to beams as uniform load. The mass was applied to the joint node as lumped mass. As a second effect of the structures,  $P-\Delta$  effect (second effect due to gravity load) was considered.

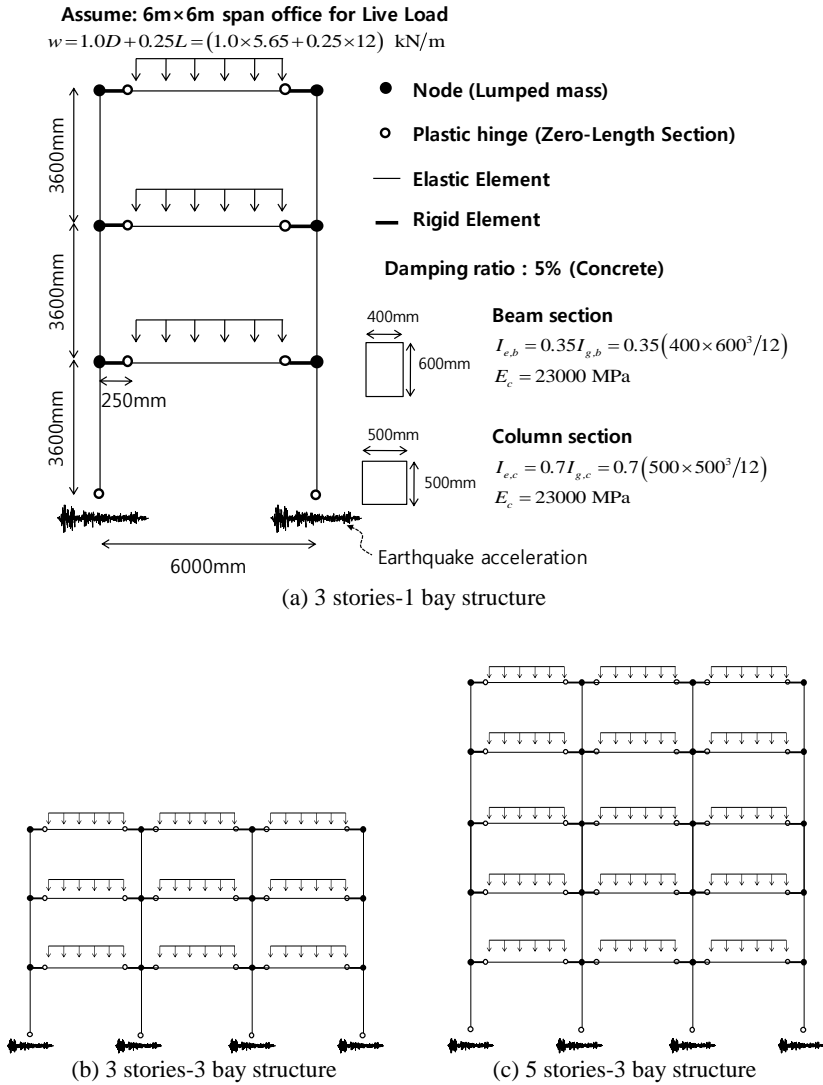


Fig. 7-1. Structure modeling for dynamic analysis of OpenSees

Fig. 7-2 shows the cyclic behaviors of beam-column connections and columns. For interior beam-column connections, the plastic deformation angles  $\theta_c$ ,  $\theta_y$ ,  $\theta_u$ , and  $\theta_r$  were approximated as 0.0002, 0.002, 0.04, and 0.08 rad., respectively. For exterior beam-column connections and columns, the plastic deformation angles  $\theta_c$ ,  $\theta_y$ ,  $\theta_u$ , and  $\theta_r$  were approximated as 0.0002, 0.002, 0.035, and 0.07 rad., respectively. For energy dissipation capacity of beam-column connections, four types joints (Elasto-Perfectly Plastic; energy dissipation ratio  $\kappa = 0.2$ ;  $\kappa = 0.4$ ; and  $\kappa = 0.6$ ) were considered. Elasto-Perfectly Plastic joint is generally used in the dynamic analysis, and the nonlinear behavior of moment frame structures was studied using the energy-based joint model. The joint with  $\kappa = 0.2$  shows significant pinching behavior in beam-column connection. It is general cyclic behavior of beam-column connections in low-rise building because of insufficient bond resistance of beam flexural bars at the joint. The joint with  $\kappa = 0.6$  shows good energy dissipation capacity. When perfect bond is provided in the joint, the energy dissipation ratio is approximately limited by the inherent maximum value of reinforced concrete beams:  $\kappa = 0.6$  (ATC 40, 2006; Park and Eom, 2006; Eom and Park, 2010). For energy dissipation capacity of column, two types columns (Elasto-Perfectly Plastic; and  $\kappa = 0.4$ ) was considered. The column with  $\kappa = 0.4$  was assumed to be earthquake designed column.

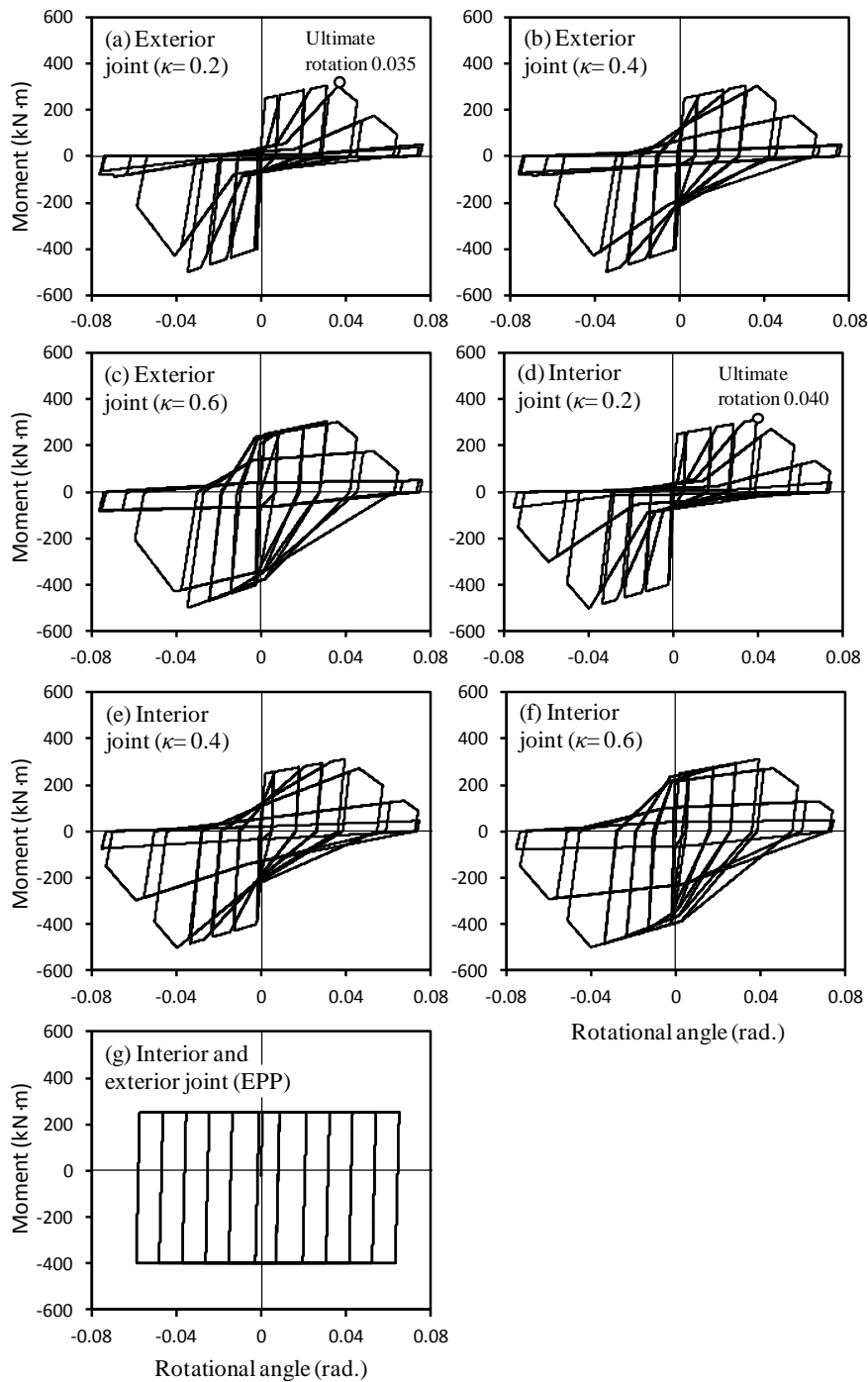


Fig. 7-2. Hysteretic behaviors of interior and exterior joint and column (Continued)

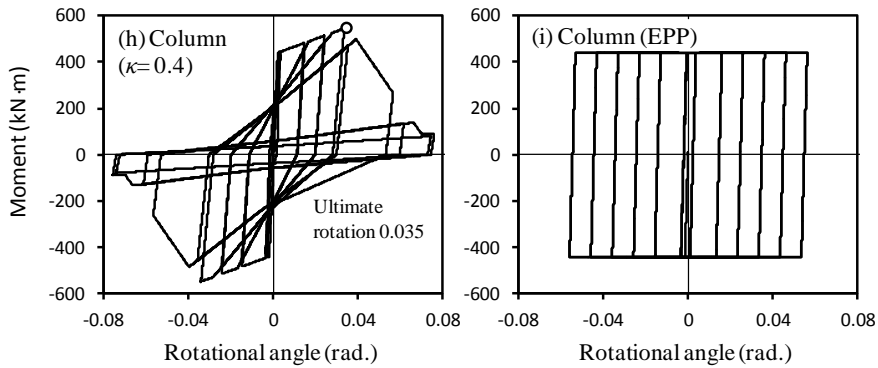
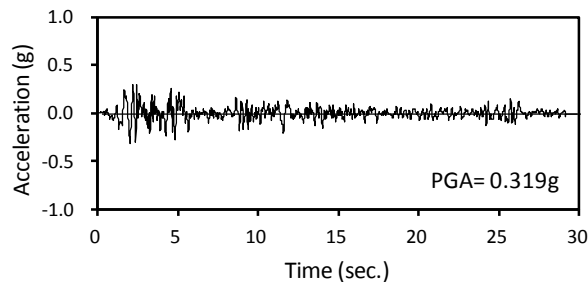


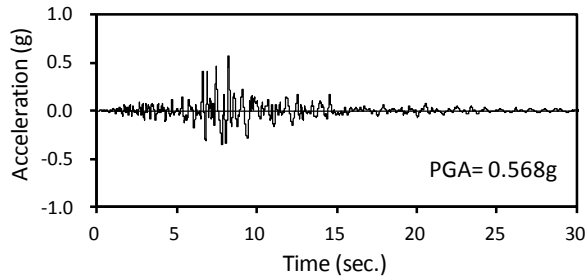
Fig. 7-2. Hysteretic behaviors of interior and exterior joint and column

As a ground acceleration, El-Centro earthquake acceleration (18.05.1940, NS; Peak Ground Acceleration(PGA)= 0.319g), Northridge earthquake acceleration (17.01.1994, 0RR090; PGA= 0.568g), and Kobe earthquake acceleration (16.01.1995, KJM000; PGA= 0.821g) were applied to bottom nodes of 1<sup>st</sup> story columns for nonlinear time history analysis (see Figs. 7-1 and 7-3). Dynamic analysis was performed at interval of 0.001 second to avoid the convergence problem.

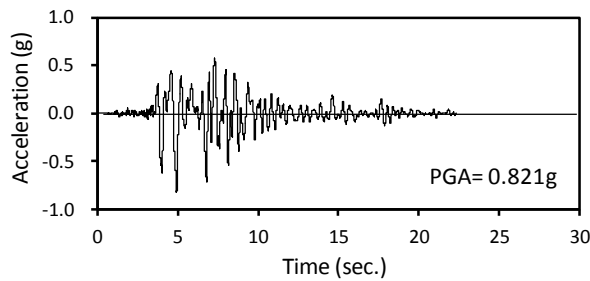


(a) El-Centro earthquake acceleration

Fig. 7-3. Ground acceleration (Continued)



(b) Northridge earthquake acceleration



(c) Kobe earthquake acceleration

Fig. 7-3. Ground acceleration

Fig. 7-4 shows load-displacement relationship for nonlinear system. For the earthquake load greater than load-carrying capacity of structure, nonlinear deformation of structures is significantly increased. In the nonlinear response, ductility  $\mu$  is defined as the ratio of the maximum displacement  $u_m$  to the yield displacement  $u_y$ . Generally, as ductility demand  $\mu$  increases, design load can be reduced in inelastic earthquake design. Thus, the increased yield strength reduction factor  $R$  (= decreased normalized strength) requires the higher ductility demand in building structures. Here,  $R = 1$  was defined such that the structure reaches the yield state under earthquake acceleration.

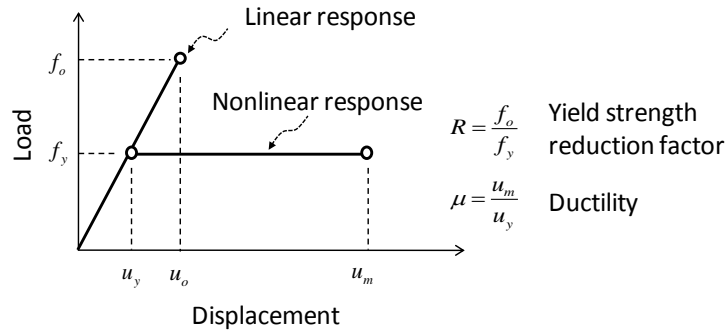


Fig. 7-4. Load-displacement relationship for nonlinear system

For nonlinear dynamic analysis, first, the peak acceleration ( $R= 1$ ) that induces elastic behavior of structure was determined. And then, using the increased peak acceleration ( $R= 2$  and  $4$ ), nonlinear dynamic analysis was performed to evaluate the discrepancy of the energy dissipation capacity at the joint. Peak accelerations for  $R= 1$  were  $0.644\text{ g}$ ,  $0.577\text{ g}$ ,  $0.348\text{ g}$  in 3 stories-1 bay structure, 3 stories-3 bay structure, 5 stories-3 bay structure, respectively, in El-Centro earthquake load. Peak accelerations for  $R= 1$  were  $0.574\text{ g}$ ,  $0.585\text{ g}$ ,  $0.598\text{ g}$  in 3 stories-1 bay structure, 3 stories-3 bay structure, 5 stories-3 bay structure, respectively, in Northridge earthquake load. Peak accelerations for  $R= 1$  were  $0.473\text{ g}$ ,  $0.446\text{ g}$ ,  $0.342\text{ g}$  in 3 stories-1 bay structure, 3 stories-3 bay structure, 5 stories-3 bay structure, respectively, in Kobe earthquake load.

### 7.2.2 Nonlinear Analysis Algorithm

Eq. (7-1) shows dynamic equilibrium equation for multi degree of freedom system.



$$[M]\{\ddot{u}\} + [C]\{\dot{u}\} + [K]\{u\} = -[M]\{\ddot{u}_g\} \quad (7-1)$$

where  $[M]$  = mass matrix;  $[C]$  = viscous damping coefficient matrix;  $[K]$  = stiffness matrix;  $\{\ddot{u}\}$  = acceleration matrix;  $\{\dot{u}\}$  = velocity matrix;  $\{u\}$  = displacement matrix; and  $\{\ddot{u}_g\}$  = earthquake acceleration.

To solve Eq. (7-1) for nonlinear system, average acceleration method by Newmark was used (Chopra, 2001). Solution procedure for nonlinear system is as follows.

*Initial calculations*

$$\ddot{u}_0 = \frac{p_0 - [C]\dot{u}_0 - (f_s)_0}{[M]} \quad (7-2a)$$

$$\Delta t = 0.001 \text{ sec.} \quad (7-2b)$$

$$a = \frac{4}{\Delta t}[M] + 2[C] \quad (7-2c)$$

$$b = 2[M] \quad (7-2d)$$

*Calculations for each time step,  $i$*

$$\Delta \hat{p}_i = \Delta p_i + a\dot{u}_i + b\ddot{u}_i \quad (7-3a)$$

Determine the tangent stiffness  $k_i$  in cyclic curve (7-3b)

$$\hat{k}_i = k_i + \frac{2}{\Delta t}[C] + \frac{4}{(\Delta t)^2}[M] \quad (7-3c)$$

Solve for  $\Delta u_i$  from  $\hat{k}_i$  and  $\Delta \hat{p}_i$  using the iterative procedure of Eq. (7-3d)

$$\Delta \dot{u}_i = \frac{2}{\Delta t} \Delta u_i - 2\dot{u}_i \quad (7-3e)$$

$$\Delta \ddot{u}_i = \frac{4}{(\Delta t)^2} \Delta u_i - \frac{4}{\Delta t} \dot{u}_i - 2\ddot{u}_i \quad (7-3f)$$

$$u_{i+1} = u_i + \Delta u_i \quad (7-3g)$$

$$\dot{u}_{i+1} = \dot{u}_i + \Delta \dot{u}_i \quad (7-3h)$$

$$\ddot{u}_{i+1} = \ddot{u}_i + \Delta \ddot{u}_i \quad (7-3i)$$

*Repetition for the next time step.* Replace  $i$  by  $i+1$  and implement Eqs. (7-3a) to (7-3i) for the next time step.

In nonlinear analysis procedure, modified Newton-Raphson iteration was used to solve the displacement increment over the time step. Iterative procedure is as follows.

*Initialize data*

$$\mathbf{u}_{i+1}^{(0)} = \mathbf{u}_i \quad (7-4a)$$

$$\mathbf{f}_s^{(0)} = (\mathbf{f}_s)_i \quad (7-4b)$$

$$\Delta \mathbf{R}^{(1)} = \Delta \hat{\mathbf{p}}_i \quad (7-4c)$$

$$\hat{k}_T = \hat{k}_i \quad (7-4d)$$

*Calculations for each iterations,  $j= 1, 2, 3, \dots$*

$$\Delta \mathbf{u}^{(j)} = \frac{\Delta \mathbf{R}^{(j)}}{\hat{k}_T} \quad (7-4e)$$

$$\mathbf{u}_{i+1}^{(j)} = \mathbf{u}_{i+1}^{(j-1)} + \Delta \mathbf{u}^{(j)} \quad (7-4f)$$

$$\Delta \mathbf{f}^{(j)} = \mathbf{f}_s^{(j)} - \mathbf{f}_s^{(j-1)} + (\hat{k}_T - k_T) \Delta \mathbf{u}^{(j)} \quad (7-4g)$$

$$\Delta R^{(j+1)} = \Delta R^{(j)} - \Delta f^{(j)} \quad (7-4h)$$

*Repetition for next iteration.* Replace  $j$  by  $j+1$  and repeat Eqs. (7-4e) to (7-4h).

Eq. (7-5) shows Rayleigh damping matrix for viscous damping coefficient  $C$  in Eq. (7-1).

$$C = a_0 M + a_1 K \quad (7-5a)$$

$$a_0 = \zeta \frac{2\omega_i \omega_j}{\omega_i + \omega_j} \quad (7-5b)$$

$$a_1 = \zeta \frac{2}{\omega_i + \omega_j} \quad (7-5c)$$

where  $a_0$  = mass proportional damping coefficient;  $a_1$  = stiffness proportional damping coefficient;  $\zeta$  = damping ratio (=0.05 for RC structures); and  $\omega_i$  and  $\omega_j$  = natural frequencies of  $i^{\text{th}}$  and  $j^{\text{th}}$  mode of structure, respectively. Here,  $i = 1$  and  $j = 3$  was used. When initial stiffness is used in Eq. (7-5), artificial damping may be generated in the lower modes (Charney, 2008). It produces extreme errors in nonlinear analysis. Thus, the stiffness matrix  $K$  at current state determination was used to calculate Rayleigh damping as well as average acceleration method. As a result, damping matrix  $C$  and stiffness matrix  $K$  are changed according to structure nonlinearity. The OpenSees code

for the proposed model was shown in Appendix B.

## **7.3 Earthquake Response According to Energy Dissipation Capacity on El-Centro Earthquake Loading**

### **7.3.1 3 Stories-1 Bay Structure**

Fig. 7-5 shows displacements at 3<sup>rd</sup> floor for the yield strength reduction factor  $R=2$ . The peak displacement of inelastic response at  $\kappa=0.2$  was greater than that of elastic response. As the energy dissipation ratio increased, the peak displacement was reduced from 123.5 mm ( $\kappa=0.2$ ) to 105.7 mm ( $\kappa=0.6$ ) (see Fig. 7-5(b)-(d)). Particularly, when the energy dissipation ratio was larger than  $\kappa=0.2$ , inelastic displacement was less than elastic displacement. This is because the energy dissipation capacity of the structure was behaved as the damping of the structure. For elastic perfectly plastic beam-column connection and column with  $\kappa=0.4$  (EPP), the peak displacement of the structure was 96.9 mm (see Fig. 7-5(e)). For elastic perfectly plastic beam-column connection and elastic perfectly plastic column (EPP+EPP), the peak displacement of the structure was 94.4 mm that was the minimum response (see Fig. 7-5(f)). This result indicates that the energy dissipation capacity is critical to the inelastic deformation of the moment frame structures. Particularly, the inelastic response of the structure with significant pinching joint ( $\kappa=0.2$ ) was increased to 31 % of that of EPP+EPP structure that is generally assumed in dynamic analysis.

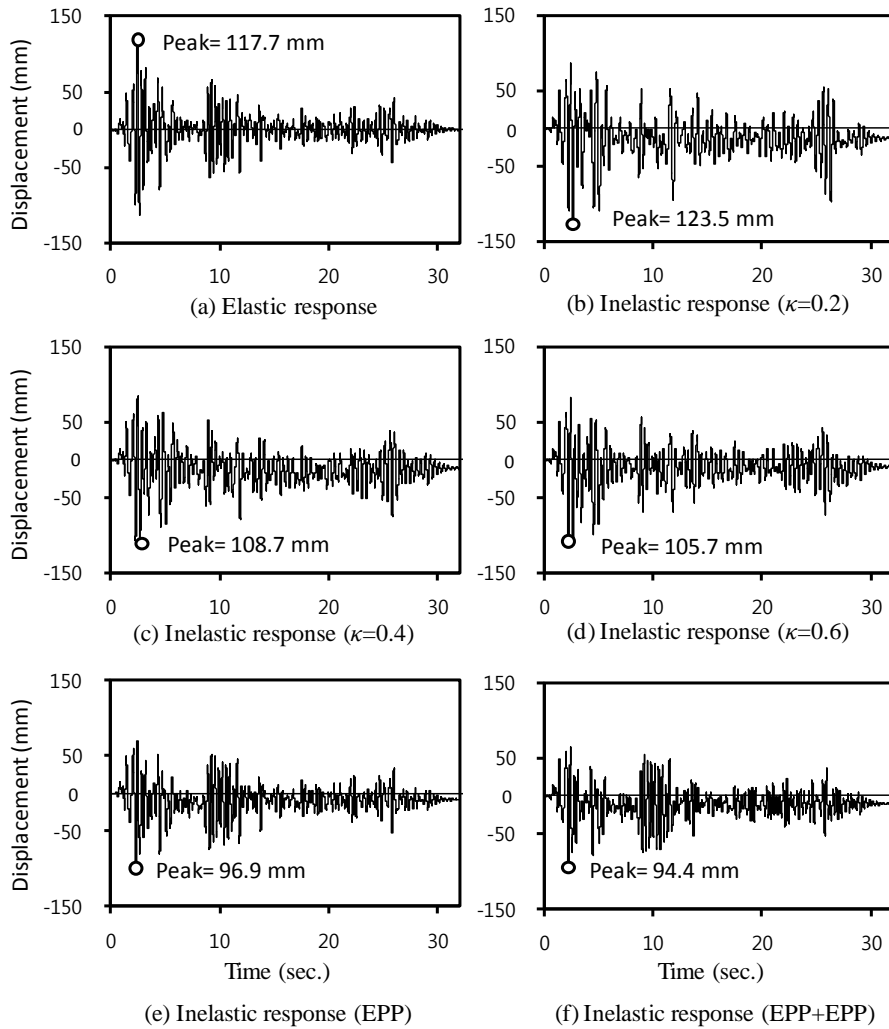


Fig. 7-5. Displacements at 3<sup>rd</sup> floor in 3 stories-1 bay structure ( $R=2$ )

Fig. 7-6 shows displacements at 3<sup>rd</sup> floor for the yield strength reduction factor  $R=4$ . Compared to the displacement of elastic response, the displacement of inelastic response at  $\kappa=0.2$  was increased to 1.5 times. As the energy dissipation ratio increases, the peak displacement was reduced from 344.5 mm to 294.3 mm (see Fig. 7-6(b)-(d)). Unlike Fig. 7-5, the inelastic peak displacement was not less than the elastic peak displacement. For EPP structure, the peak displacement was 249.3 mm (see Fig. 7-6(e)). For EPP+EPP structure, the peak displacement was decreased to 214.9 mm (see Fig. 7-6(f)). The inelastic response of the structure with significant pinching joint ( $\kappa=0.2$ ) was increased to 60 % of that of EPP+EPP structure. It was greater than the increment of the displacement for  $R=2$ . This is because the increased inelastic deformation for  $R=4$  requires more energy dissipation in the structure. That is, in the structure designed with the large yield strength reduction factor, the peak displacement of the structure is significantly affected by the energy dissipation of the structure.



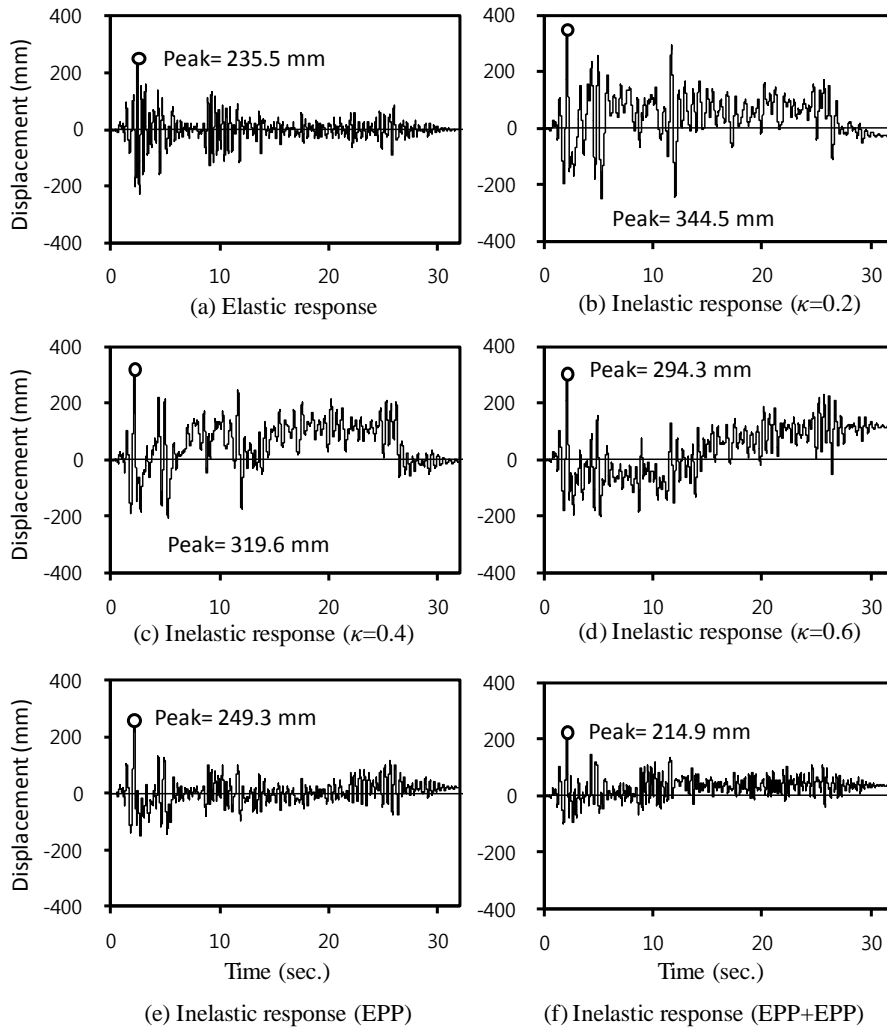


Fig. 7-6. Displacements at 3<sup>rd</sup> floor in 3 stories-1 bay structure ( $R=4$ )

Fig. 7-7 shows the peak displacement of each floor from Figs. 7-5 and 7-6. Compared to the displacement of the EPP+EPP structure, the peak displacement of the structure with the energy dissipation ratio  $\kappa = 0.2 - 0.6$  was increased from 11 % ( $\kappa = 0.6$ ) to 38 % ( $\kappa = 0.2$ ) for  $R= 2$  and from 37 % ( $\kappa = 0.6$ ) to 61 % ( $\kappa = 0.2$ ) for  $R=4$ .

Fig. 7-8 shows ductility of each floor. The ductility was determined from the peak drift of each floor divided into the maximum drift of 1<sup>st</sup> floor. Compared to the ductility of the EPP+EPP structure, the ductility of the structure with  $\kappa = 0.2 - 0.6$  increased from 12 % ( $\kappa = 0.6$ ) to 38 % ( $\kappa = 0.2$ ) for  $R= 2$  and from 34 % ( $\kappa = 0.6$ ) to 72 % ( $\kappa = 0.2$ ) for  $R=4$ .

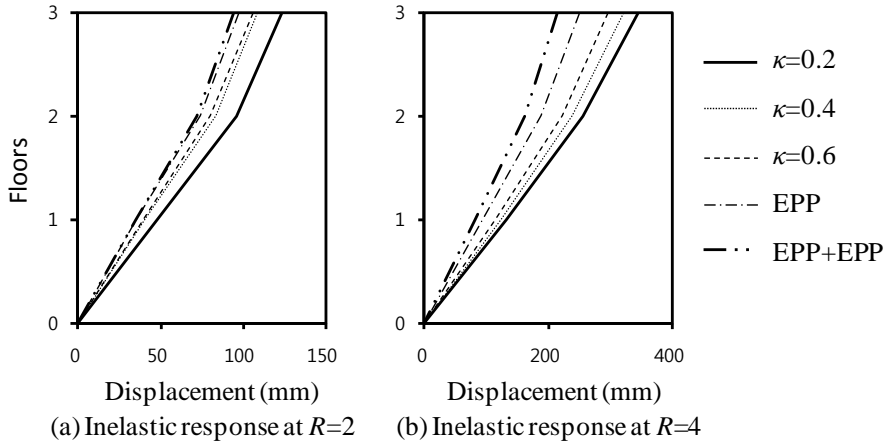


Fig. 7-7. Comparison of displacement according to energy dissipation ratio of 3 stories-1 bay structure

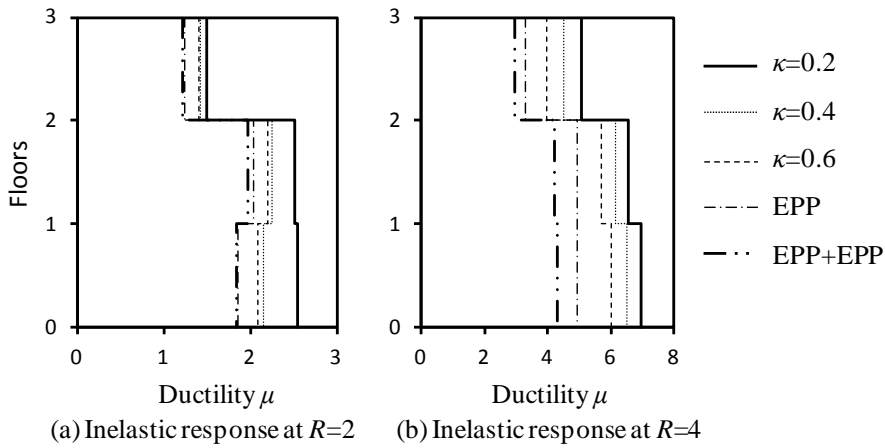


Fig. 7-8. Comparison of ductility according to energy dissipation ratio of 3 stories-1 bay structure

Figs. 7-9 and 7-10 shows moment-rotation relationship in the beam plastic hinge at the end of the dynamic analysis. As shown in Fig. 7-9, the plastic hinge with low energy dissipation capacity exhibited the large rotation angle. As a result, the displacement of the structure was increased. For the

yield strength reduction factor  $R=4$ , the rotation angle was significantly increased (see Fig. 7-10). Particularly, the negative rotation angle at  $\kappa=0.2$  was almost two times that of EPP+EPP.

The stiffness degradation by pinching in the joint decreased the damping coefficient in Eq. (7-5). In Eq. (7-2a), the reduced  $C$  matrix and load-carrying capacity  $(f_s)_0$  in pinching region increase the acceleration  $\ddot{u}$  of the structure. The increased acceleration  $\ddot{u}$  and the decreased stiffness  $K$  induce the displacement increment (see Eqs. (7-3a) - (7-3d)). As a result, because the stiffness and load-carrying capacity are decreased in the joint with low energy dissipation capacity, the earthquake response of the structure is increased.

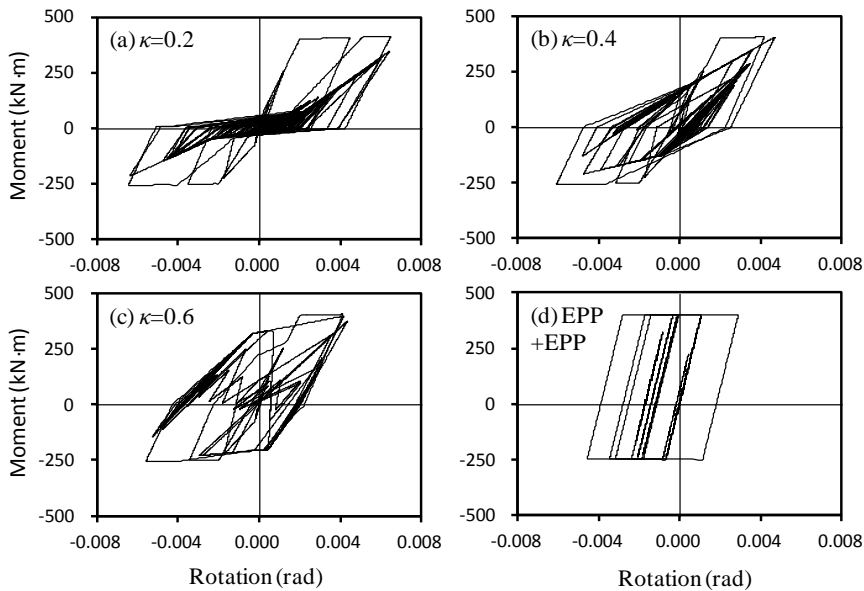


Fig. 7-9. Moment-rotation relationship according to energy dissipation ratio for  $R=2$

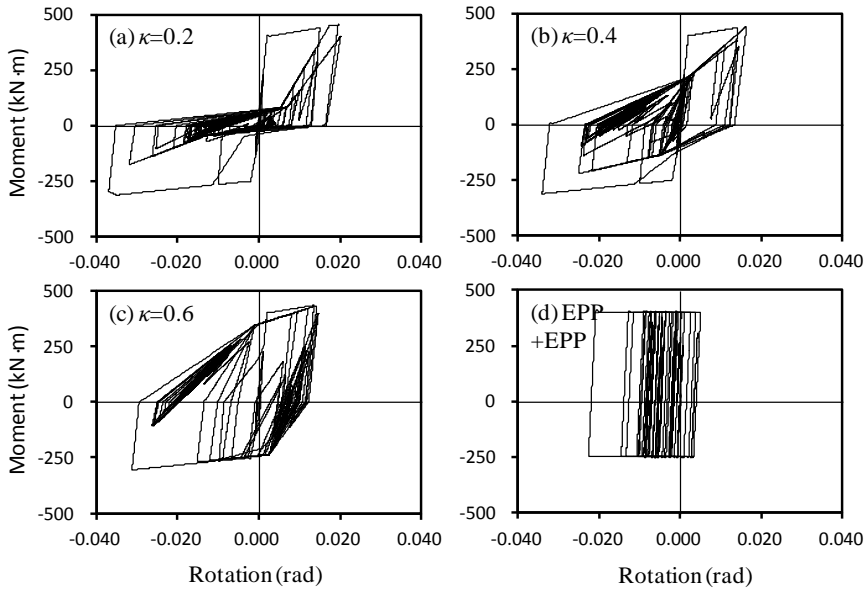


Fig. 7-10. Moment-rotation relationship according to energy dissipation ratio for  $R=4$

### 7.3.2 3 Stories-3 Bay Structure

Figs. 7-11 and 7-12 show the displacement variations at 3<sup>rd</sup> floor of the 3 stories-3 bay structure according to time for the yield strength reduction factor  $R=2$  and  $R=4$ , respectively. Fig. 7-13(a) shows the peak displacement of each floor with respect to the energy dissipation capacity of the joint in the 3 stories-3 bay structure for the yield strength reduction factor  $R=2$ . The peak displacement of inelastic response at 3<sup>rd</sup> floor for  $\kappa=0.2$  was 0.97 times that of elastic response. As the energy dissipation ratio increased, the peak displacement was reduced from 108.6 mm ( $\kappa=0.2$ ) to 102.9 mm ( $\kappa=0.6$ ). For elastic perfectly plastic beam-column connection and column with  $\kappa=0.4$  (EPP), the peak displacement of the structure was 95.4 mm. For elastic perfectly plastic beam-column connection and elastic perfectly plastic column (EPP+EPP), the peak displacement of the structure was the minimum (= 93.5

mm). Compared to the peak displacement of the EPP+EPP structure, the peak displacements of the structure with  $\kappa=0.2-0.6$  were increased from 8 % ( $\kappa=0.6$ ) to 17 % ( $\kappa=0.2$ ) according to the energy dissipation ratio.

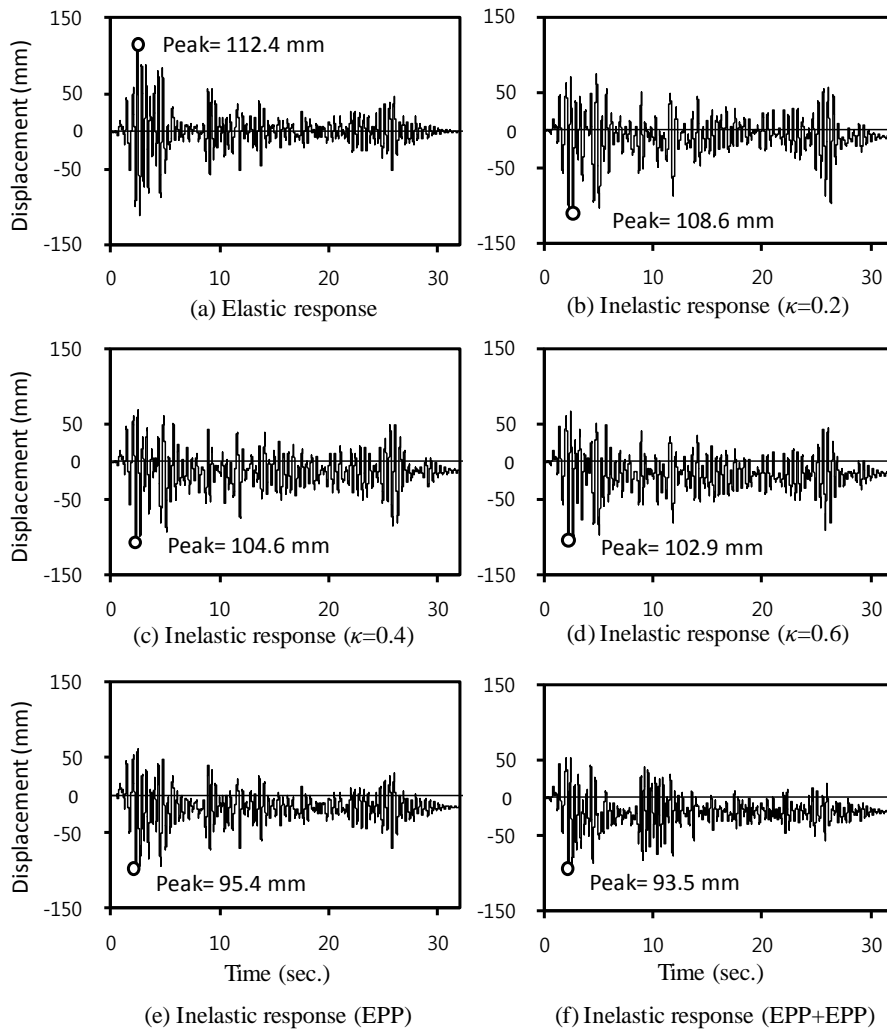


Fig. 7-11. Displacements at 3<sup>rd</sup> floor in 3 stories-3 bay structure (R= 2)

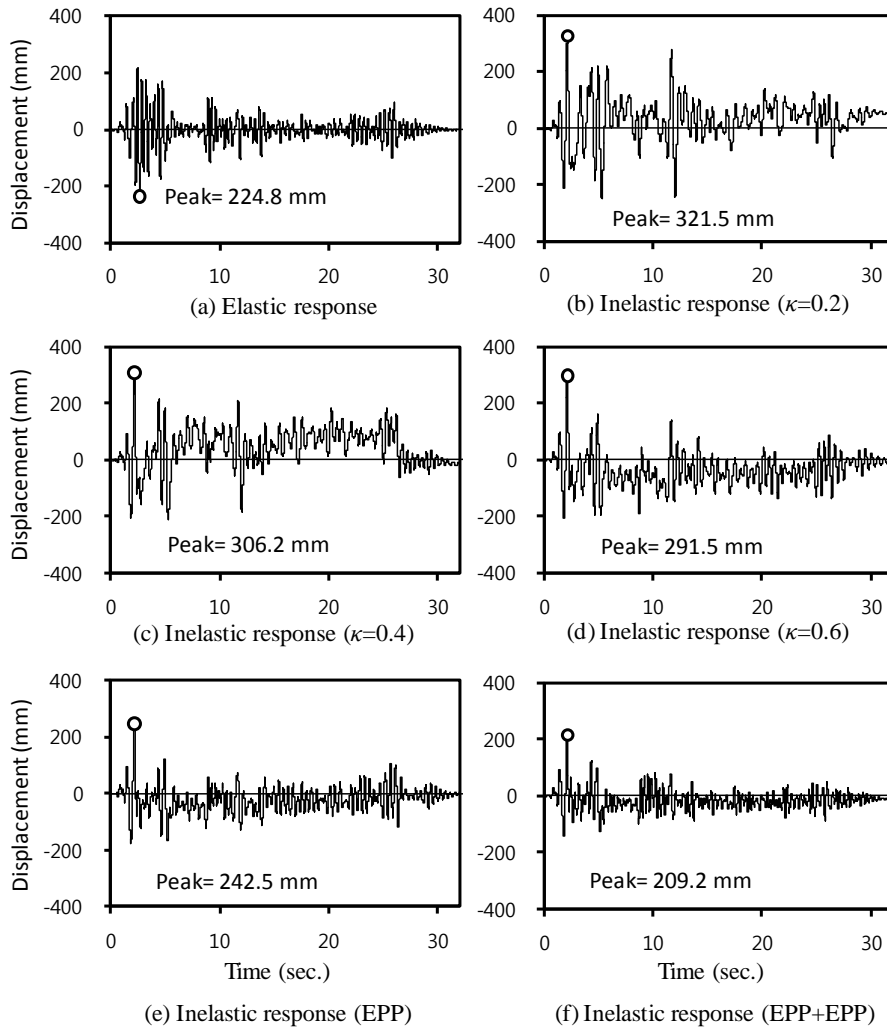


Fig. 7-12. Displacements at 3<sup>rd</sup> floor in 3 stories-3 bay structure ( $R=4$ )

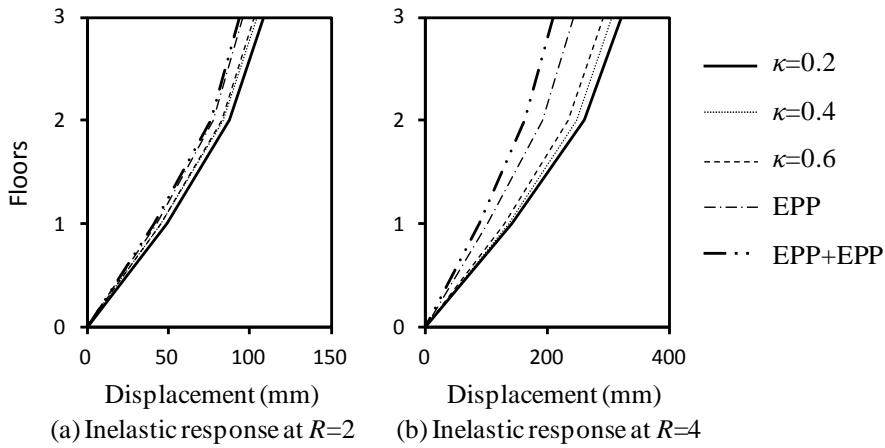


Fig. 7-13. Comparison of displacement according to energy dissipation ratio of 3 stories-3 bay structure

Fig. 7-13(b) shows the peak displacement of each floor with respect to energy dissipation capacity of the joint in 3 stories-3 bay structure for the yield strength reduction factor  $R=4$ . Compared to the elastic response, the inelastic response at 3<sup>rd</sup> floor in the structure with  $\kappa=0.2$  was increased to 1.43 times. As the energy dissipation ratio increases, the peak displacement was reduced from 321.5 mm ( $\kappa=0.2$ ) to 291.5 mm ( $\kappa=0.6$ ). For elastic perfectly plastic beam-column connection and column with  $\kappa=0.4$  (EPP), the peak displacement of the structure was 242.5 mm. For elastic perfectly plastic beam-column connection and elastic perfectly plastic column (EPP+EPP), the peak displacement of the structure was the minimum (= 209.1 mm). Compared to EPP+EPP structure, the displacement of the structure with  $\kappa=0.2 - 0.6$  increased from 39 % ( $\kappa=0.6$ ) to 63 % ( $\kappa=0.2$ ). These results are similar to the response of 3 stories-1 bay structure. However, compared with



the displacement in 3 stories-1 bay structure, the displacement increment due to the discrepancy of the energy dissipation capacity in the 3 stories-3 bay structure was slightly decreased.

Fig. 7-14 shows the ductility of each floor in the 3 stories-3 bay structure. Compared to EPP+EPP structure, the ductility of the structure with  $\kappa=0.2$  - 0.6 increased from 9 % ( $\kappa=0.6$ ) to 17 % ( $\kappa=0.2$ ) for  $R=2$  and from 21 % ( $\kappa=0.6$ ) to 63 % ( $\kappa=0.2$ ) for  $R=4$ .

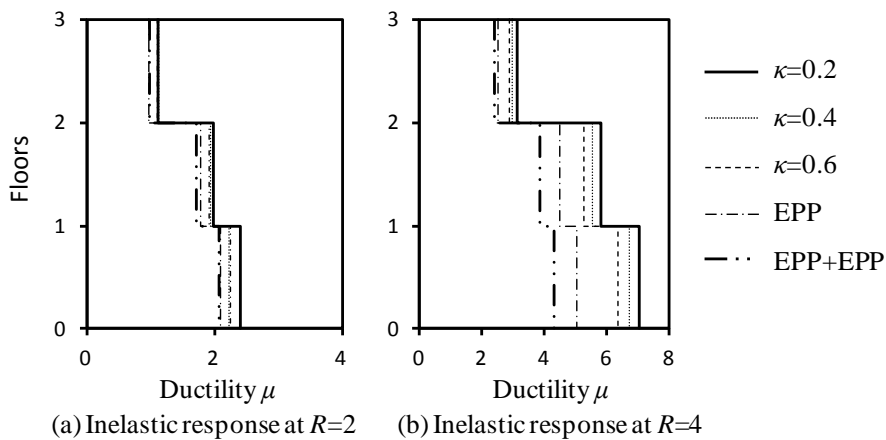


Fig. 7-14. Comparison of displacement according to energy dissipation ratio of 3 stories-3 bay structure

### 7.3.3 5 Stories-3 Bay Structure

Figs. 7-15 and 7-16 show the displacements at 5<sup>th</sup> floor in 5 stories-3 bay structure for the yield strength reduction factor  $R=2$  and  $R=4$ , respectively.

Fig. 7-17(a) shows the peak displacement of each floor with respect to energy dissipation capacity of the joint in 5 stories-3 bay structure for the yield strength reduction factor  $R=2$ . Compared to the elastic response, the inelastic response at 5<sup>th</sup> floor in the structure with  $\kappa=0.2$  was 0.88 times. As the energy dissipation ratio increases, the peak displacement was slightly decreased from 165.5 mm ( $\kappa=0.2$ ) to 160.5 mm ( $\kappa=0.6$ ). For elastic perfectly plastic beam-column connection and column with  $\kappa=0.4$  (EPP), the peak displacement was 138.5 mm. For elastic perfectly plastic beam-column connection and elastic perfectly plastic column (EPP+EPP), the peak displacement was the minimum (= 136.7 mm). Compared to EPP+EPP structure, the displacement of the structure with  $\kappa=0.2-0.6$  increased from 17 % ( $\kappa=0.6$ ) to 21 % ( $\kappa=0.2$ ).

Fig. 7-17(b) shows the peak displacement of each floor with respect to energy dissipation capacity at the joint in 5 stories-3 bay structure for the yield strength reduction factor  $R=4$ . Compared to elastic response, inelastic response at 3<sup>rd</sup> floor in the structure with  $\kappa=0.2$  was 0.97 times. As the energy dissipation ratio increases, the peak displacement was reduced from 296.5 mm ( $\kappa=0.2$ ) to 290.7 mm ( $\kappa=0.4$ ). However, even though the energy dissipation capacity was increased in the joint with  $\kappa=0.6$ , the peak displacement was increased to 316.8 mm. For elastic perfectly plastic beam-column connection and column with  $\kappa=0.4$  (EPP), the peak displacement of the structure was 269.4 mm. For elastic perfectly plastic beam-column connection and elastic perfectly plastic column (EPP+EPP), the peak displacement of the structure was the minimum (= 252.4 mm). Compared to EPP+EPP structure, the displacement of the structure with  $\kappa=0.2-0.6$  increased from 17 % ( $\kappa=0.2$ )

to 26 % ( $\kappa= 0.6$ ). Unlike the existing results, the peak displacement in the structure with  $\kappa= 0.6$  was greater than that of the structure with  $\kappa= 0.2$ . Furthermore, compared to the displacement in the 3 stories-3 bay structure, the displacement increment according to the energy dissipation capacity was significantly decreased in the 5 stories-3 bay structure.

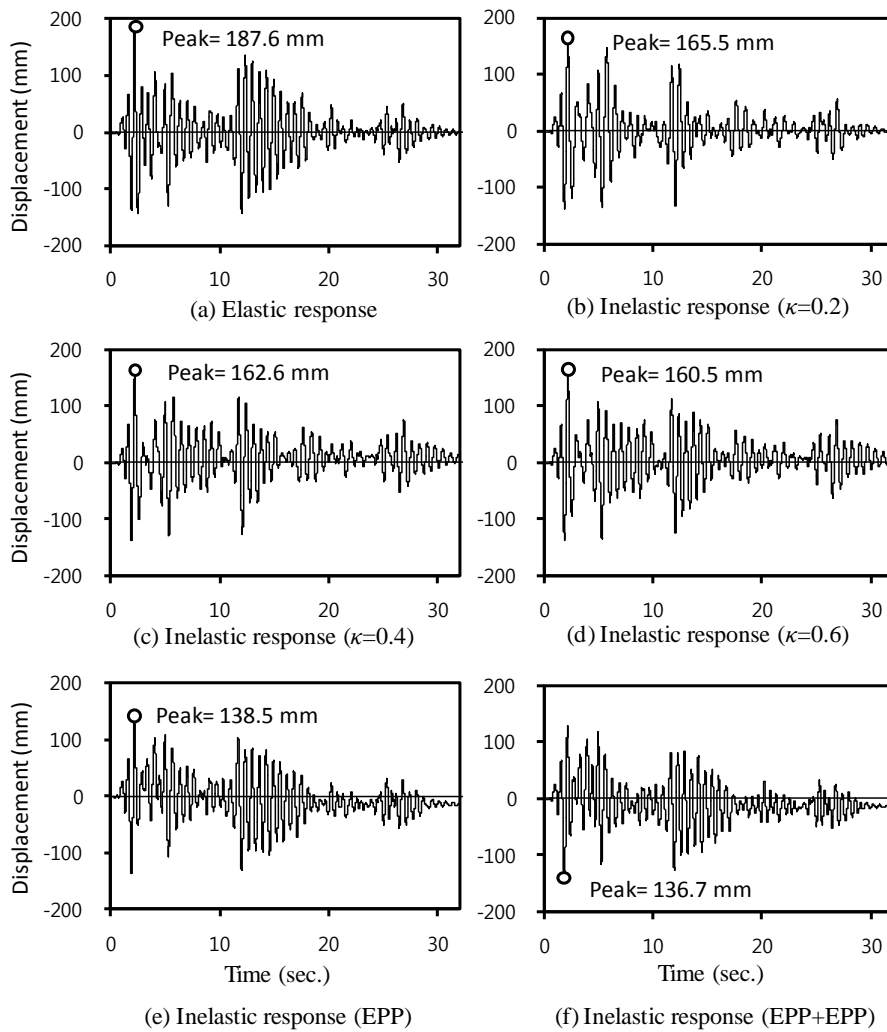


Fig. 7-15. Displacements at 5<sup>th</sup> floor in 5 stories-3 bay structure ( $R= 2$ )

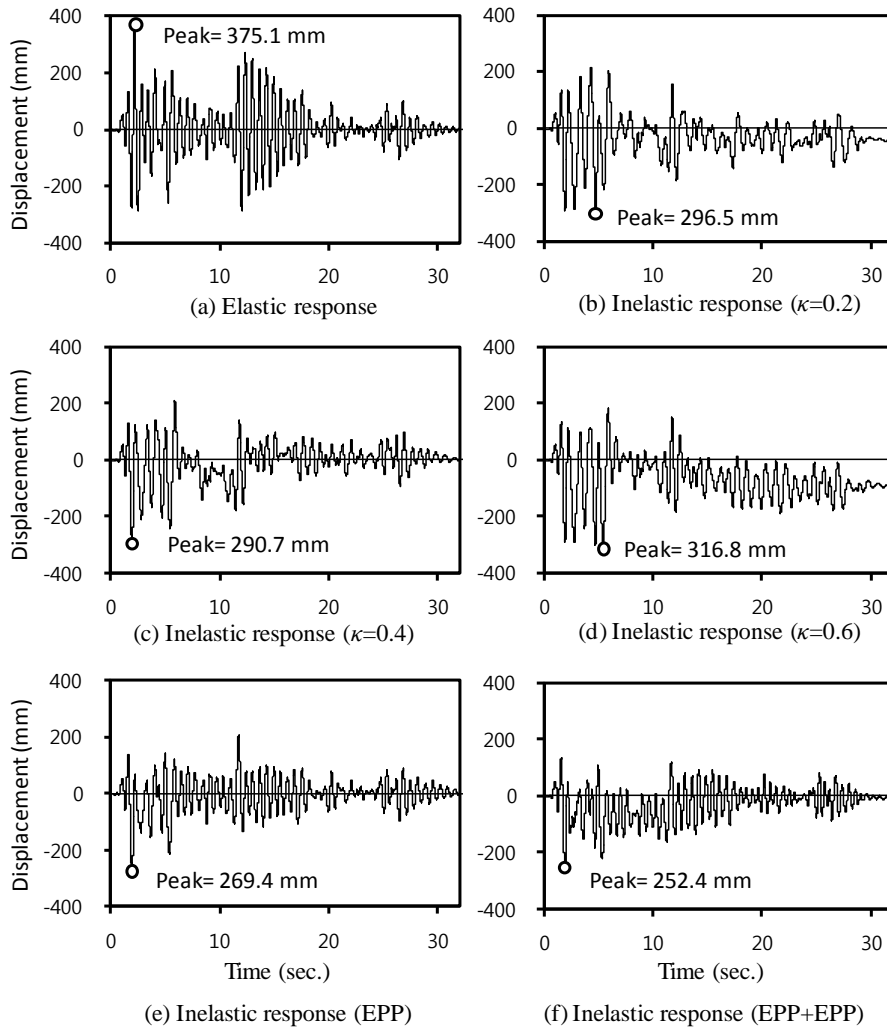


Fig. 7-16. Displacements at 5<sup>th</sup> floor in 5 stories-3 bay structure ( $R=4$ )

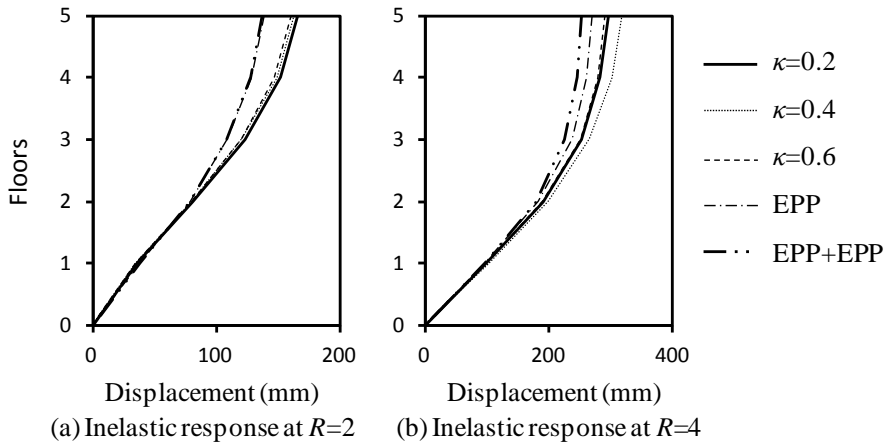


Fig. 7-17. Comparison of displacement according to energy dissipation ratio of 5 stories-3 bay structure

Fig. 7-18 shows the ductility of each floor in 5 stories-3 bay structure. Compared to EPP+EPP structure, the ductility of the structure with  $\kappa=0.2$  - 0.6 was increased from 11 % ( $\kappa=0.6$ ) to 15 % ( $\kappa=0.2$ ) for  $R=2$  and from 37 % ( $\kappa=0.2$ ) to 41 % ( $\kappa=0.6$ ) for  $R=4$ .

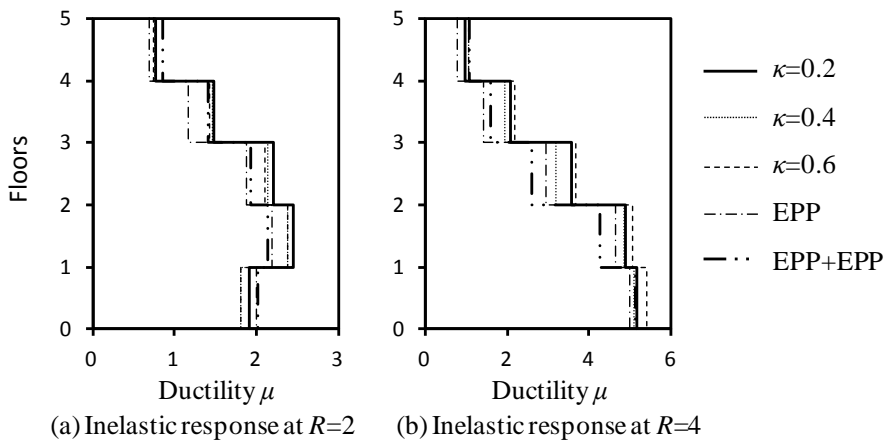


Fig. 7-18. Comparison of ductility according to energy dissipation ratio of 5 stories-3 bay structure

### 7.3.4 Plastic Hinge Distributions

Figs. 7-19 and 7-20 show the plastic hinge distribution and the rotational angle at positive and negative direction for  $R=4$  in 3 stories-1 bay moment frame structure, respectively. Figs. 7-21 and 7-22 show the plastic hinge distribution and the rotational angle at positive and negative direction for  $R=4$  in 3 stories-3 bay moment frame structure, respectively. Figs. 7-23 and 7-24 show the plastic hinge distribution and the rotational angle at positive and negative direction for  $R=4$  in 5 stories-3 bay moment frame structure, respectively. Plastic hinge was developed when the rotational angle was greater than yield rotation 0.002. When the rotational angle was greater than ultimate rotation 0.04 for interior joint and 0.035 for exterior joint and column, the load-carrying capacity of the joint and column was decreased. As shown in Figs. 7-19 - 7-24, the rotational angle requirement was decreased in the structure with large energy dissipation capacity. Thus, in low-rise moment frame structure, when the energy dissipation capacity is increased in the beam-column connections, the inelastic deformation and damage in the joint can be reduced.

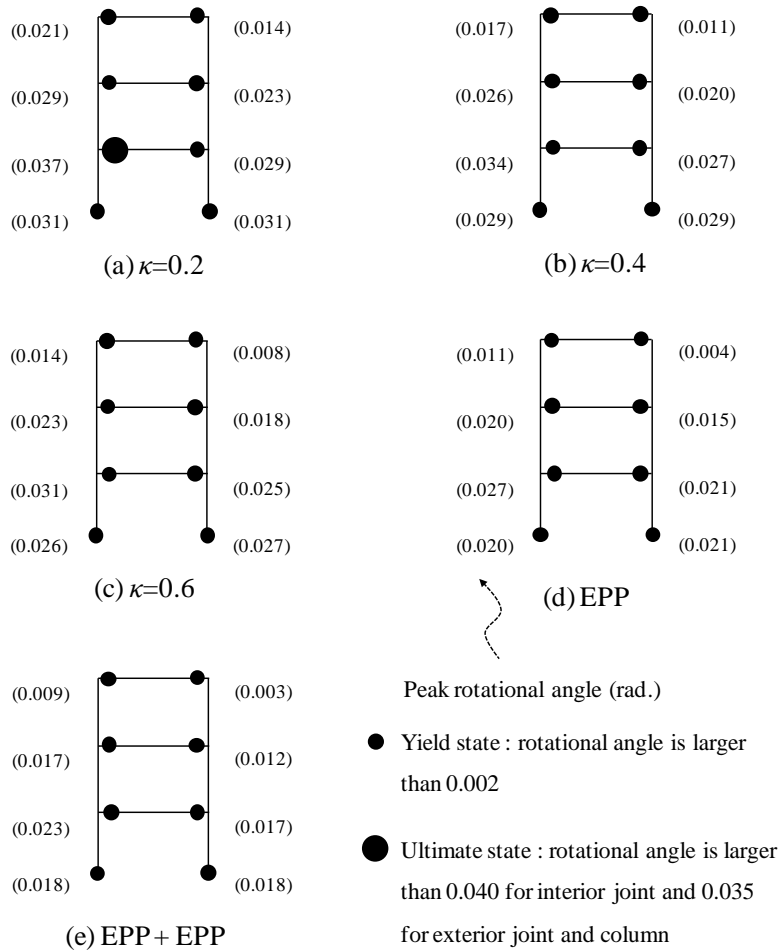


Fig. 7-19. Plastic hinge distribution at positive direction for  $R=4$  in 3 stories-1 bay structure

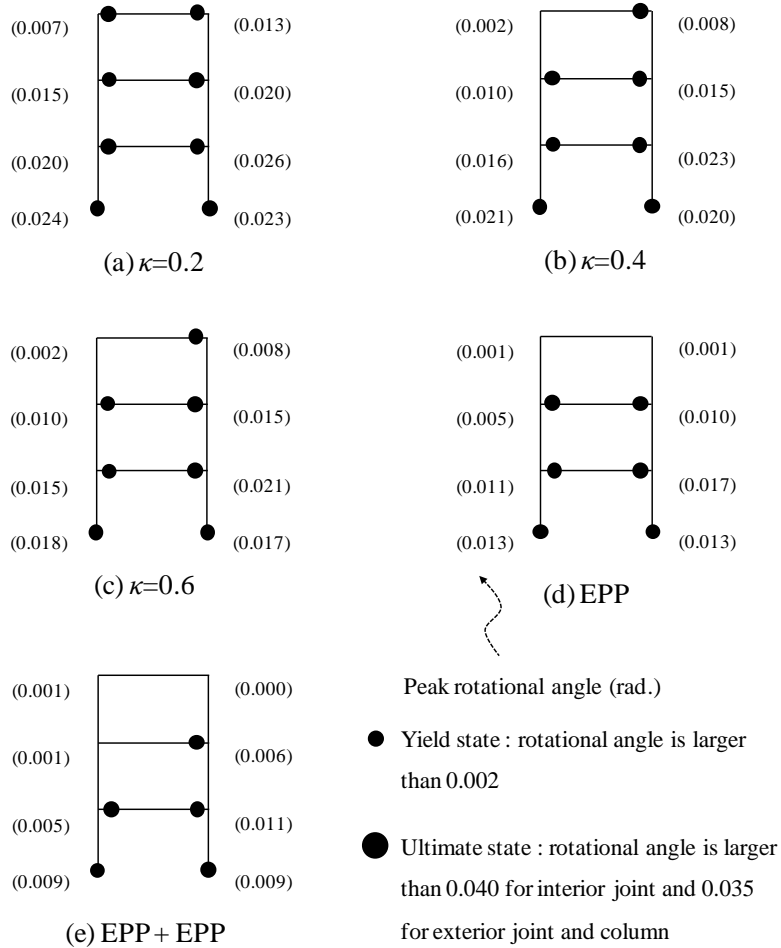


Fig. 7-20. Plastic hinge distribution at negative direction for  $R=4$  in 3 stories-3 bay structure



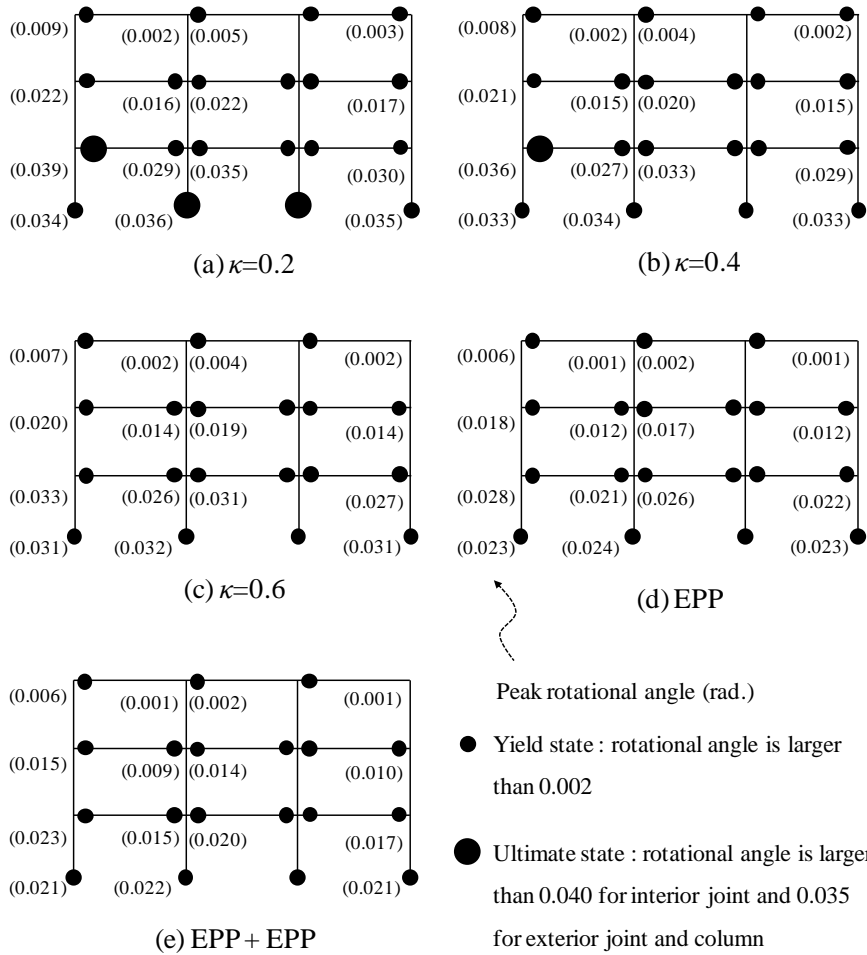


Fig. 7-21. Plastic hinge distribution at positive direction for  $R=4$  in 3 stories-3 bay structure

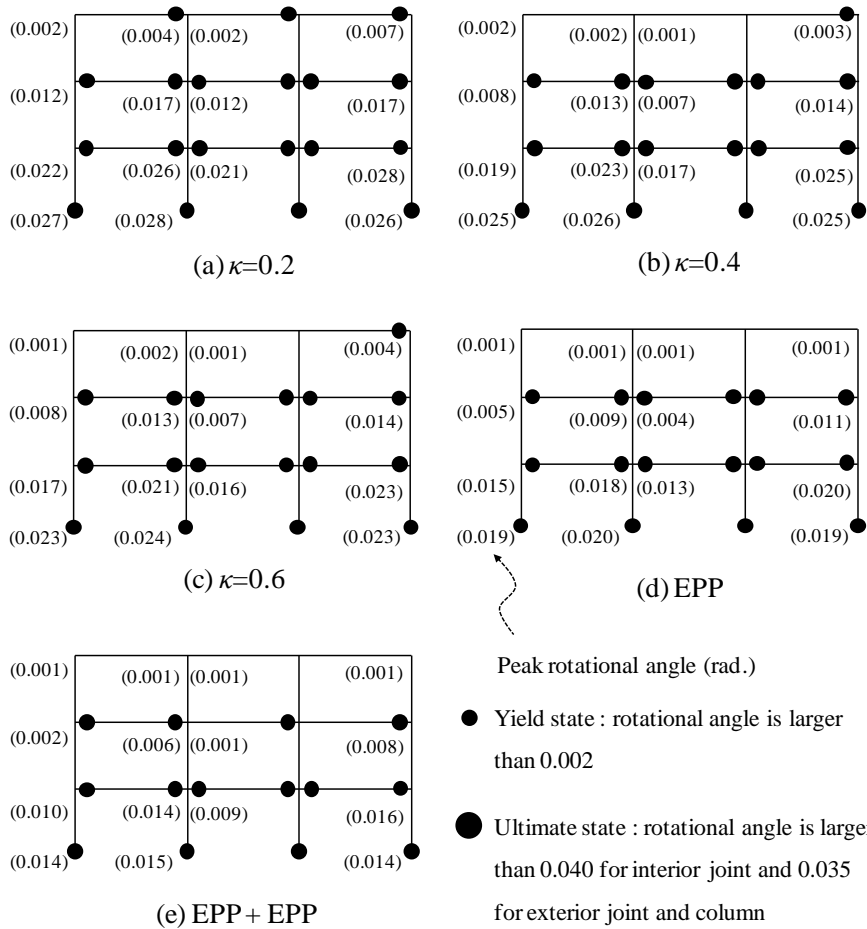


Fig. 7-22. Plastic hinge distribution at negative direction for  $R=4$  in 3 stories-3 bay structure

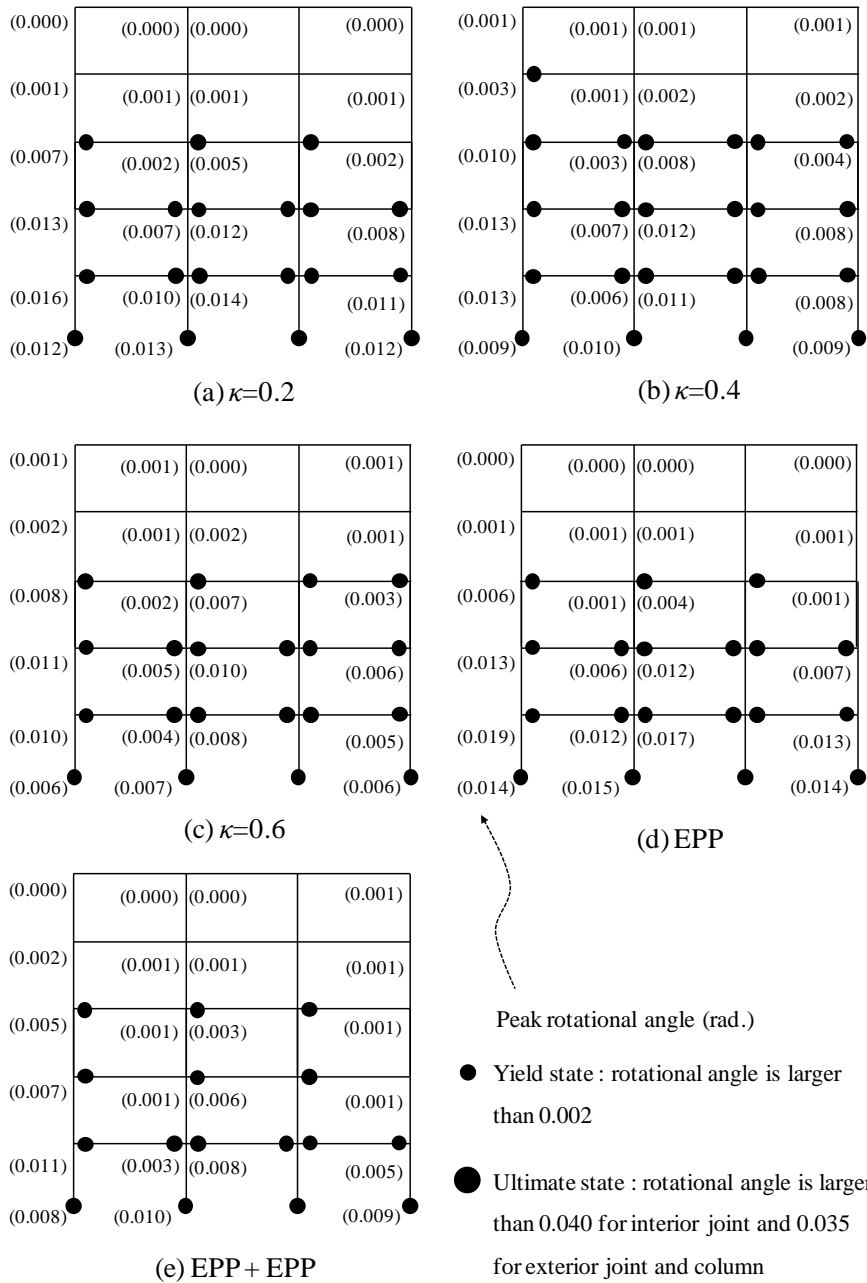


Fig. 7-23. Plastic hinge distribution at positive direction for  $R=4$  in 5 stories-3 bay structure

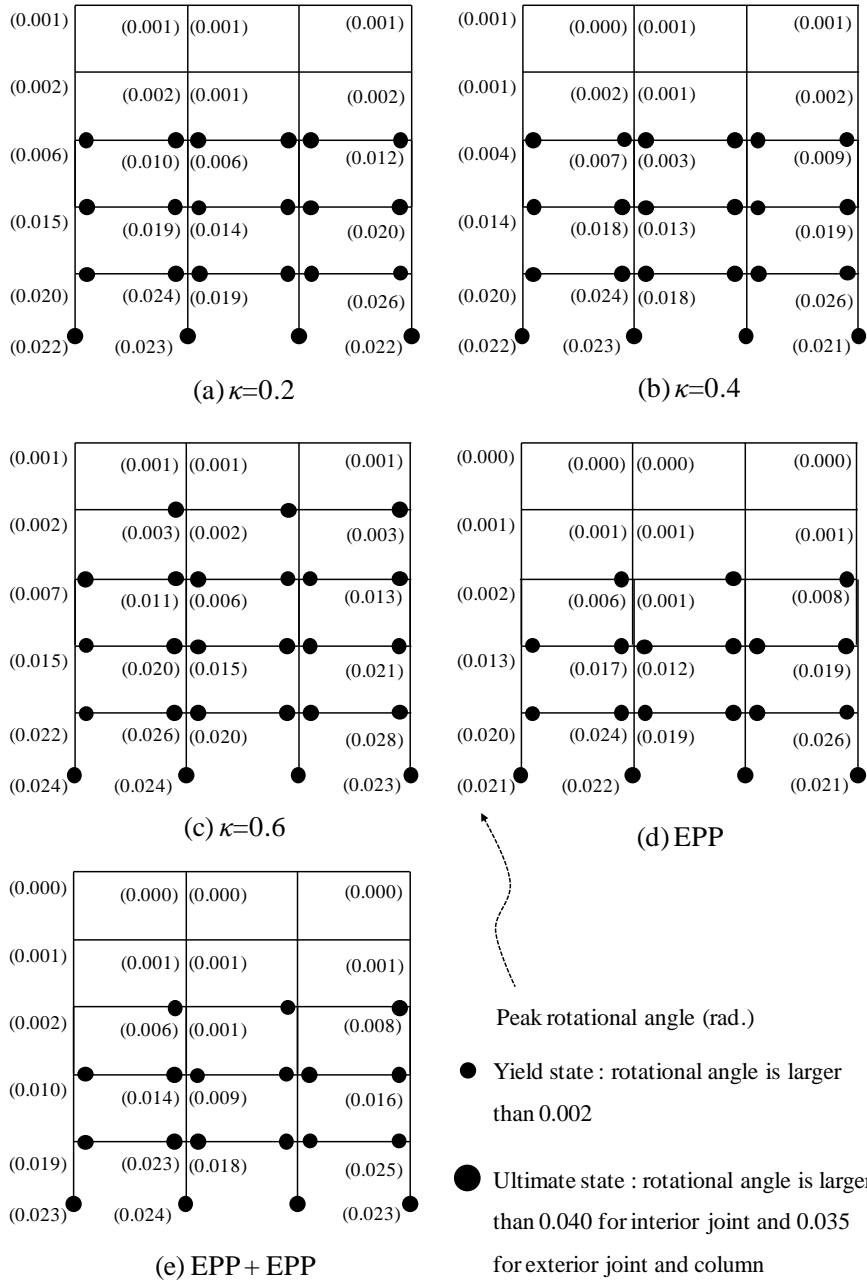


Fig. 7-24. Plastic hinge distribution at negative direction for  $R=4$  in 5 stories-3 bay structure

## **7.4 Earthquake Response According to Energy Dissipation Capacity on Northridge and Kobe Earthquake Loadings**

### **7.4.1 3 Stories-1 Bay Structure**

Fig. 7-25 shows displacements at 3<sup>rd</sup> floor for the yield strength reduction factor  $R=2$  and 4 in the 3 stories-1 bay structure subjected to Northridge earthquake load. Fig. 7-25(a) shows the peak displacement of each floor with respect to energy dissipation capacity in the 3 stories-1 bay structure for the yield strength reduction factor  $R=2$ . The peak displacement of the inelastic response at 3<sup>rd</sup> floor in the structure with  $\kappa=0.2$  was 0.93 times that of the elastic response. As the energy dissipation ratio increased, the peak displacement of the structure was slightly increased from 102.2 mm ( $\kappa=0.2$ ) to 104.9 mm ( $\kappa=0.6$ ). Even though the energy dissipation capacity was increased in the joint, the peak displacement of the structure with  $\kappa=0.6$  was increased. For elastic perfectly plastic beam-column connection and column with  $\kappa=0.4$  (EPP), the peak displacement of the structure was 113.7 mm. For elastic perfectly plastic beam-column connection and elastic perfectly plastic column (EPP+EPP), the peak displacement of the structure was 113.5 mm. Compared to the displacement of the EPP+EPP structure, the displacements of the structure with  $\kappa=0.2-0.6$  were decreased from 10 % ( $\kappa=0.6$ ) to 7.6 % ( $\kappa=0.2$ ).

Fig. 7-25(b) shows the peak displacement of each floor with respect to

energy dissipation capacity in the 3 stories-1 bay structure for the yield strength reduction factor  $R=4$ . The peak displacement of the inelastic response at 3<sup>rd</sup> floor in the structure with  $\kappa=0.2$  was 1.45 times that of the elastic response. As the energy dissipation ratio increased, the peak displacement of the structure was reduced from 320.0 mm ( $\kappa=0.2$ ) to 272.9 mm ( $\kappa=0.6$ ). For elastic perfectly plastic beam-column connection and column with  $\kappa=0.4$  (EPP), the peak displacement of the structure was 221.1 mm. For elastic perfectly plastic beam-column connection and elastic perfectly plastic column (EPP+EPP), the peak displacement of the structure was the minimum (= 190.7 mm). Compared to the displacement of the EPP+EPP structure, the displacements of the structure with  $\kappa=0.2-0.6$  were increased from 43 % ( $\kappa=0.6$ ) to 68 % ( $\kappa=0.2$ ).

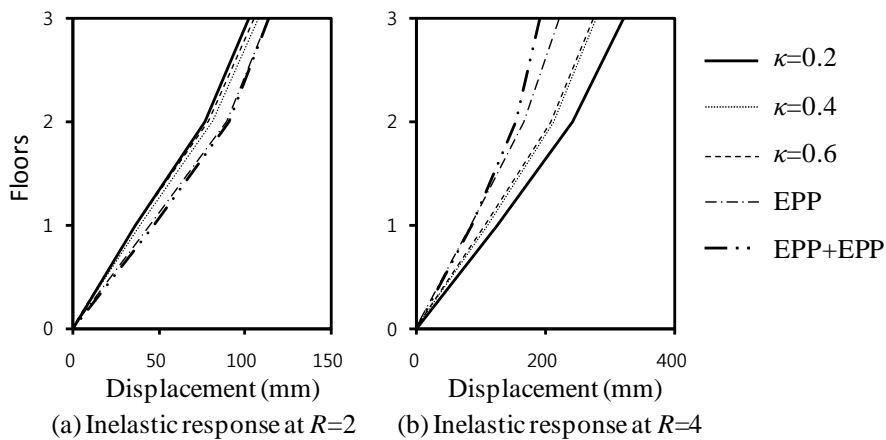


Fig. 7-25. Comparison of displacement according to energy dissipation ratio of 3 stories-1 bay structure subjected to Northridge earthquake load

Fig. 7-26 shows the ductility of each floor in 3 stories-1 bay structure. Compared to the ductility of the EPP+EPP structure, the ductility of the structure with  $\kappa=0.2 - 0.6$  were increased from -20.5 % ( $\kappa=0.2$ ) to 4 % ( $\kappa=0.6$ ) for  $R=2$  and from 48 % ( $\kappa=0.6$ ) to 89 % ( $\kappa=0.2$ ) for  $R=4$ .

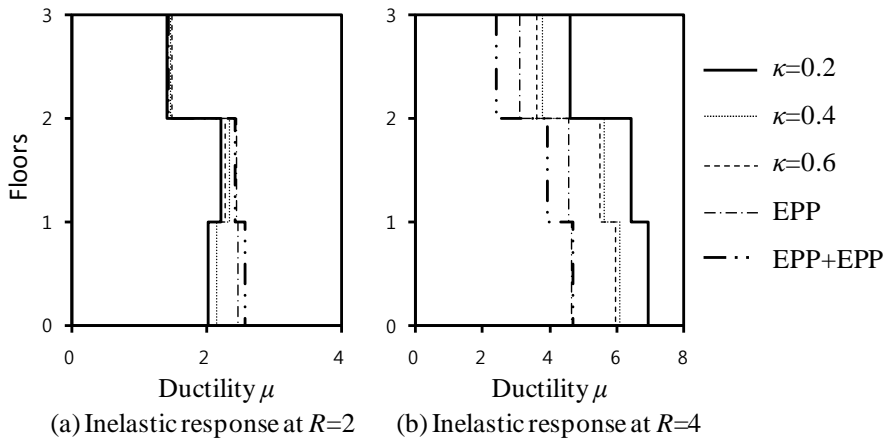


Fig. 7-26. Comparison of ductility according to energy dissipation ratio of 3 stories-1 bay structure subjected to Northridge earthquake load

Fig. 7-27 shows the displacement at 3<sup>rd</sup> floor for the yield strength reduction factor  $R=2$  and 4 in the 3 stories-1 bay structure subjected to Kobe earthquake load. Fig. 7-27(a) shows the peak displacement of each floor with respect to energy dissipation capacity in the 3 stories-1 bay structure for the yield strength reduction factor  $R=2$ . Compared to elastic response, inelastic response at 3<sup>rd</sup> floor in the structure with  $\kappa=0.2$  was 1.03 times. As the energy dissipation ratio increased, the peak displacement was slightly decreased from 116.2 mm ( $\kappa=0.2$ ) to 101.6 mm ( $\kappa=0.6$ ). For elastic perfectly plastic beam-

column connection and column with  $\kappa=0.4$  (EPP), the peak displacement of the structure was 92.6 mm. For elastic perfectly plastic beam-column connection and elastic perfectly plastic column (EPP+EPP), the peak displacement of the structure was the minimum (= 88.8 mm). Compared to the displacement of the EPP+EPP structure, the displacements of the structure with  $\kappa=0.2-0.6$  were increased from 14 % ( $\kappa=0.6$ ) to 31 % ( $\kappa=0.2$ ).

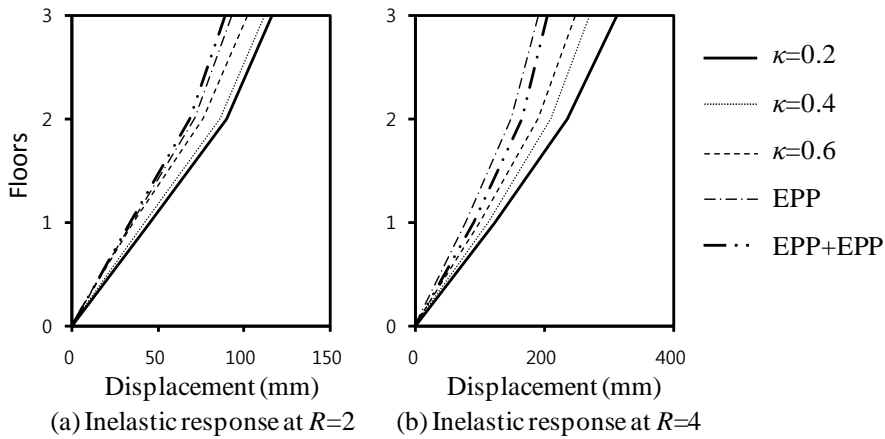


Fig. 7-27. Comparison of displacement according to energy dissipation ratio of 3 stories-1 bay structure subjected to Kobe earthquake load

Fig. 7-27(b) shows the peak displacement of each floor with respect to energy dissipation capacity in 3 stories-1 bay structure for the yield strength reduction factor  $R=4$ . Compared to elastic response, inelastic response at 3<sup>rd</sup> floor in the structure with  $\kappa=0.2$  was 1.38 times. As the energy dissipation ratio increased, the peak displacement was reduced from 311.8 mm ( $\kappa=0.2$ ) to 246.7 mm ( $\kappa=0.6$ ). For elastic perfectly plastic beam-column connection and



column with  $\kappa=0.4$  (EPP), the peak displacement of the structure was 190.8 mm. For elastic perfectly plastic beam-column connection and elastic perfectly plastic column (EPP+EPP), the peak displacement of the structure was 204.5 mm. Compared to the displacement of the EPP+EPP structure, the displacements of the structure with  $\kappa=0.2-0.6$  were increased from 21 % ( $\kappa=0.6$ ) to 52 % ( $\kappa=0.2$ ).

Fig. 7-28 shows the ductility of each floor in 3 stories-1 bay structure. Compared to the ductility of the EPP+EPP structure, the ductility of the structure with  $\kappa=0.2-0.6$  were increased from 22 % ( $\kappa=0.6$ ) to 34 % ( $\kappa=0.2$ ) for  $R=2$  and from 25 % ( $\kappa=0.6$ ) to 74 % ( $\kappa=0.2$ ) for  $R=4$ .

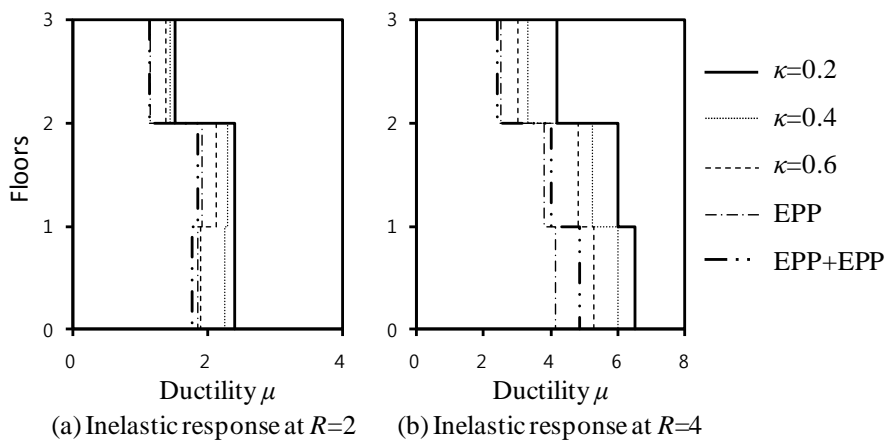


Fig. 7-28. Comparison of ductility according to energy dissipation ratio of 3 stories-1 bay structure subjected to Kobe earthquake load

### 7.4.2 3 Stories-3 Bay Structure

Figs. 7-29 shows the displacements at 3<sup>rd</sup> floor for the yield strength reduction factor  $R= 2$  and 4 in the 3 stories-3 bay structure subjected to Northridge earthquake load. Fig. 7-29(a) shows the peak displacement of each floor with respect to energy dissipation capacity in the 3 stories-3 bay structure for the yield strength reduction factor  $R= 2$ . Compared to elastic response, inelastic response at 3<sup>rd</sup> floor in the structure with  $\kappa= 0.2$  was 1.06 times. As the energy dissipation ratio increases, the peak displacement of the structure was slightly decreased from 118.1 mm ( $\kappa= 0.2$ ) to 110.2 mm ( $\kappa= 0.6$ ). Even though the energy dissipation capacity was increased in the joint, the peak displacement of the structure was increased. For elastic perfectly plastic beam-column connection and column with  $\kappa= 0.4$  (EPP), the peak displacement of the structure was 103.4 mm. For elastic perfectly plastic beam-column connection and elastic perfectly plastic column (EPP+EPP), the peak displacement of the structure was the minimum (= 102.0 mm). Compared to the displacement of the EPP+EPP structure, the displacements of the structure with  $\kappa= 0.2 - 0.6$  were increased from 8 % ( $\kappa= 0.6$ ) to 16 % ( $\kappa= 0.2$ ).

Fig. 7-29(b) shows the peak displacement of each floor with respect to energy dissipation capacity in the 3 stories-3 bay structure for the yield strength reduction factor  $R= 4$ . Compared elastic response, inelastic response at 3<sup>rd</sup> floor in the structure with  $\kappa= 0.2$  was 1.52 times. As the energy dissipation ratio increases, the peak displacement was reduced from 338.0 mm

( $\kappa = 0.2$ ) to 248.5 mm ( $\kappa = 0.6$ ). For elastic perfectly plastic beam-column connection and column with  $\kappa = 0.4$  (EPP), the peak displacement of the structure was 184.0 mm. For elastic perfectly plastic beam-column connection and elastic perfectly plastic column (EPP+EPP), the peak displacement of the structure was the minimum (= 179.3 mm). Compared to the displacement of the EPP+EPP structure, the displacements of the structure with  $\kappa = 0.2 - 0.6$  were increased from 39 % ( $\kappa = 0.6$ ) to 89 % ( $\kappa = 0.2$ ).

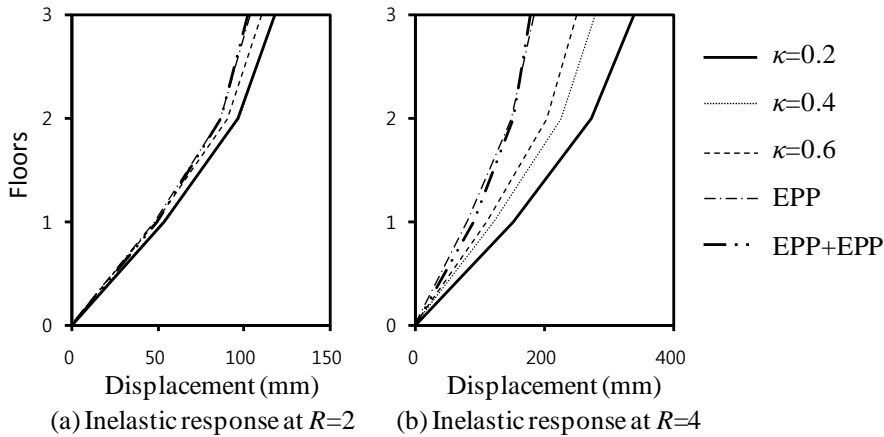


Fig. 7-29. Comparison of displacement according to energy dissipation ratio of 3 stories-3 bay structure subjected to Northridge earthquake load

Fig. 7-30 shows the ductility of each floor in the 3 stories-3 bay structure. Compared to the ductility of the EPP+EPP structure, the ductility of the structure with  $\kappa = 0.2 - 0.6$  were increased from 4 % ( $\kappa = 0.6$ ) to 13 % ( $\kappa = 0.6$ ) for  $R = 2$  and from 41 % ( $\kappa = 0.6$ ) to 89 % ( $\kappa = 0.2$ ) for  $R=4$ .

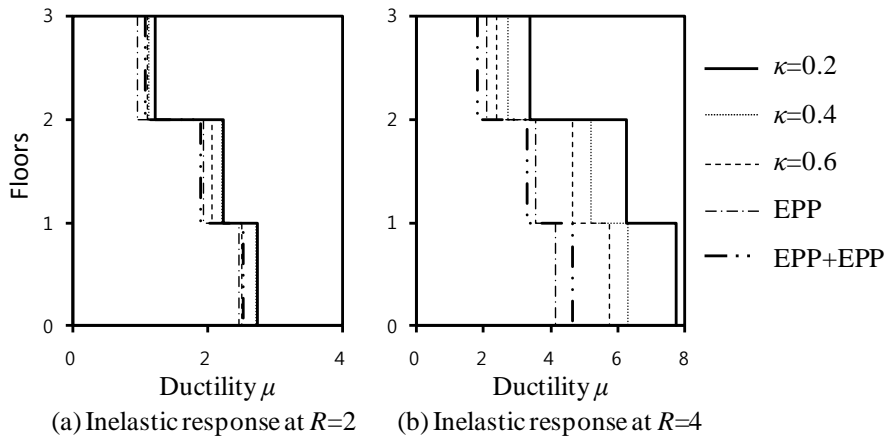


Fig. 7-30. Comparison of ductility according to energy dissipation ratio of 3 stories-3 bay structure subjected to Northridge earthquake load

Figs. 7-31 shows the displacements at 3<sup>rd</sup> floor for the yield strength reduction factor  $R= 2$  and 4 in the 3 stories-3 bay structure subjected to Kobe earthquake load. Fig. 7-31(a) shows the peak displacement of each floor with respect to energy dissipation capacity in the 3 stories-3 bay structure for the yield strength reduction factor  $R= 2$ . Compared to elastic response, inelastic response at 3<sup>rd</sup> floor was 0.87 times at  $\kappa= 0.2$ . As the energy dissipation ratio increased, the peak displacement was slightly decreased from 96.8 mm ( $\kappa= 0.2$ ) to 93.7 mm ( $\kappa= 0.6$ ). For elastic perfectly plastic beam-column connection and column with  $\kappa= 0.4$  (EPP), the peak displacement of the structure was 106.0 mm. For elastic perfectly plastic beam-column connection and elastic perfectly plastic column (EPP+EPP), the peak displacement of the structure was 95.8 mm. Compared to EPP+EPP structure, the displacement of the structure with  $\kappa= 0.2 - 0.6$  increased from -2 % ( $\kappa= 0.6$ ) to 1 % ( $\kappa= 0.2$ ).

Fig. 7-31(b) shows the peak displacement of each floor with respect to energy dissipation capacity at the joint in 3 stories-3 bay structure for the yield strength reduction factor  $R=4$ . Compared elastic response, inelastic response at 3<sup>rd</sup> floor was 1.56 times at  $\kappa=0.2$ . As the energy dissipation ratio increased, the peak displacement was reduced from 348.7 mm ( $\kappa=0.2$ ) to 311.1 mm ( $\kappa=0.6$ ). For elastic perfectly plastic beam-column connection and column with  $\kappa=0.4$  (EPP), the peak displacement was 261.1 mm. For elastic perfectly plastic beam-column connection and elastic perfectly plastic column (EPP+EPP), the peak displacement was the minimum (= 240.7 mm). Compared to EPP+EPP structure, the displacement of the structure with  $\kappa=0.2 - 0.6$  increased from 29 % ( $\kappa=0.6$ ) to 45 % ( $\kappa=0.2$ ).

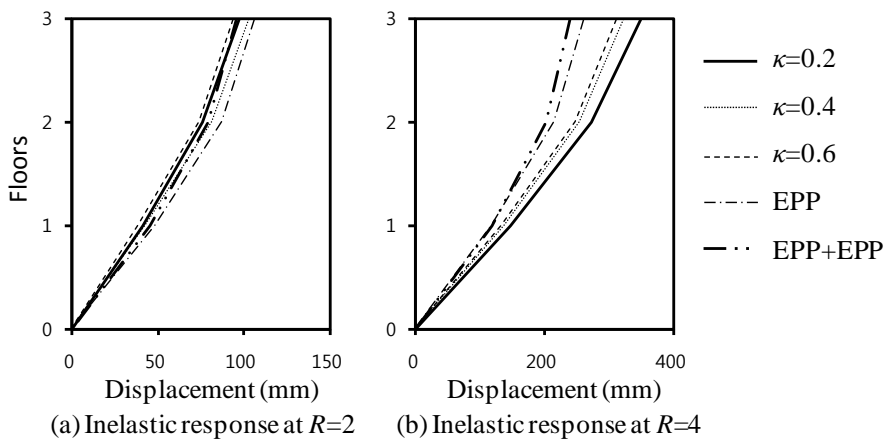


Fig. 7-31. Comparison of displacement according to energy dissipation ratio of 3 stories-3 bay structure subjected to Kobe earthquake load

Fig. 7-32 shows the ductility of each floor in the 3 stories-3 bay structure. Compared to the ductility of the EPP+EPP structure, the ductility of the structure with  $\kappa = 0.2 - 0.6$  were increased from -14 % ( $\kappa = 0.6$ ) to 2 % ( $\kappa = 0.2$ ) for  $R = 2$  and from 44 % ( $\kappa = 0.6$ ) to 70 % ( $\kappa = 0.2$ ) for  $R = 4$ .

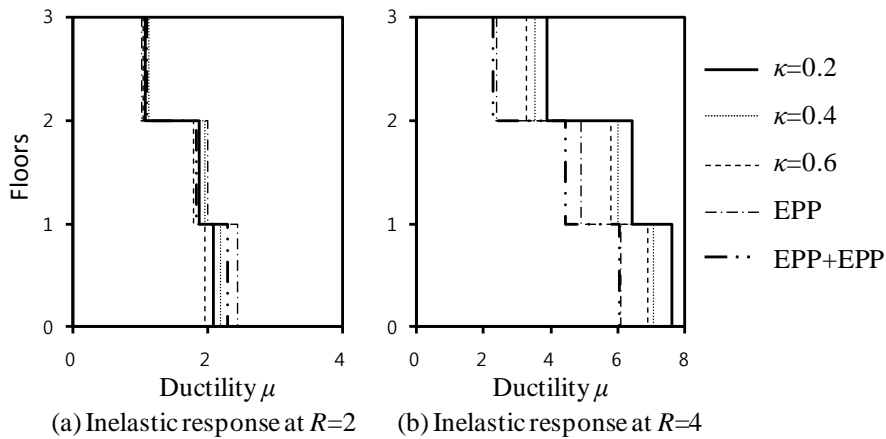


Fig. 7-32. Comparison of ductility according to energy dissipation ratio of 3 stories-3 bay structure subjected to Kobe earthquake load

### 7.4.3 5 Stories-3 Bay Structure

Figs. 7-33 shows displacements at 5<sup>th</sup> floor for the yield strength reduction factor  $R = 2$  and 4 in the 5 stories-3 bay structure subjected to Northridge earthquake load. Fig. 7-33(a) shows the peak displacement of each floor with respect to energy dissipation capacity at the joint in 5 stories-3 bay structure for the yield strength reduction factor  $R = 2$ . Compared to elastic response, inelastic response at 5<sup>th</sup> floor in the structure with  $\kappa = 0.2$  was 1.11 times. As the energy dissipation ratio increases, the peak displacement was

slightly decreased from 224.3 mm ( $\kappa=0.2$ ) to 208.8 mm ( $\kappa=0.6$ ). For elastic perfectly plastic beam-column connection and column with  $\kappa=0.4$  (EPP), the peak displacement of the structure was 176.4 mm. For elastic perfectly plastic beam-column connection and elastic perfectly plastic column (EPP+EPP), the peak displacement of the structure was the minimum (= 152.0 mm). Compared to the displacement of the EPP+EPP structure, the displacements of the structure with  $\kappa=0.2 - 0.6$  were increased from 37 % ( $\kappa=0.6$ ) to 49 % ( $\kappa=0.2$ ).

Fig. 7-33(b) shows the peak displacement of each floor with respect to energy dissipation capacity at the joint in 5 stories-3 bay structure for the yield strength reduction factor  $R=4$ . Compared to elastic response, inelastic response at 5<sup>th</sup> floor in the structure with  $\kappa=0.2$  was 1.35 times. As the energy dissipation ratio increased, unlike Fig. 7-33(a), the peak displacement of the structure was increased from 547.2 mm ( $\kappa=0.2$ ) to 566.8 mm ( $\kappa=0.6$ ). For elastic perfectly plastic beam-column connection and column with  $\kappa=0.4$  (EPP), the peak displacement of the structure was 486.7 mm. For elastic perfectly plastic beam-column connection and elastic perfectly plastic column (EPP+EPP), the peak displacement of the structure was the minimum (= 396.5 mm). Compared to the displacement of the EPP+EPP structure, the displacements of the structure with  $\kappa=0.2 - 0.6$  were increased from 38 % ( $\kappa=0.2$ ) to 50 % ( $\kappa=0.6$ ).

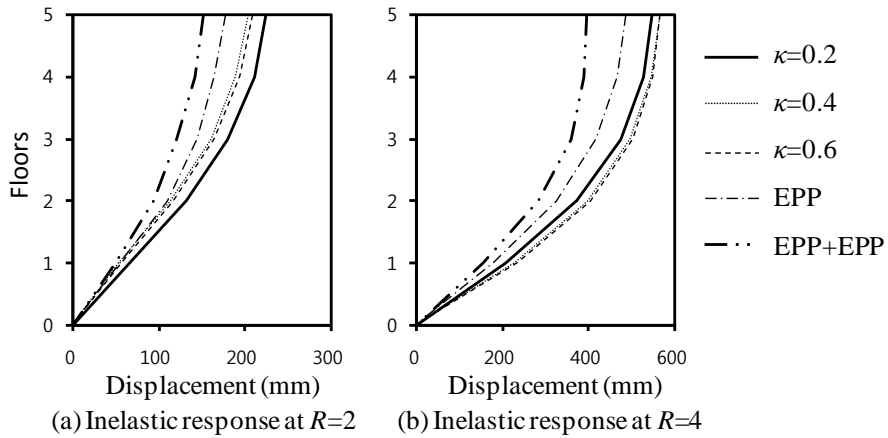


Fig. 7-33. Comparison of displacement according to energy dissipation ratio of 5 stories-3 bay structure subjected to Northridge earthquake load

Fig. 7-34 shows the ductility of each floor in 5 stories-3 bay structure. Compared to the ductility of the EPP+EPP structure, the ductility of the structure with  $\kappa=0.2-0.6$  were increased from 32 % ( $\kappa=0.6$ ) to 46 % ( $\kappa=0.6$ ) for  $R=2$  and from 47 % ( $\kappa=0.2$ ) to 50 % ( $\kappa=0.6$ ) for  $R=4$ .

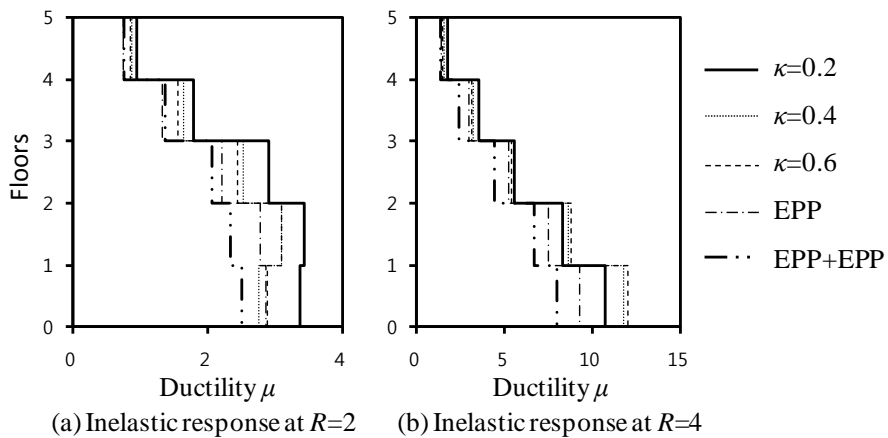


Fig. 7-34. Comparison of ductility according to energy dissipation ratio of 5 stories-3 bay structure subjected to Northridge earthquake load



Figs. 7-35 shows the displacements at 5<sup>th</sup> floor for the yield strength reduction factor  $R= 2$  and 4 in the 5 stories-3 bay structure subjected to Kobe earthquake load. Fig. 7-35(a) shows the peak displacement of each floor with respect to energy dissipation capacity in the 5 stories-3 bay structure for the yield strength reduction factor  $R= 2$ . Compared to elastic response, inelastic response at 3<sup>rd</sup> floor in the structure with  $\kappa= 0.2$  was 0.72 times. As the energy dissipation ratio increases, the peak displacement was slightly decreased from 145.9 mm ( $\kappa= 0.2$ ) to 140.5 mm ( $\kappa= 0.6$ ). For elastic perfectly plastic beam-column connection and column with  $\kappa= 0.4$  (EPP), the peak displacement of the structure was 136.2 mm. For elastic perfectly plastic beam-column connection and elastic perfectly plastic column (EPP+EPP), the peak displacement of the structure was the minimum (= 134.3 mm). Compared to the displacement of the EPP+EPP structure, the displacements of the structure with  $\kappa= 0.2 - 0.6$  were increased from 12 % ( $\kappa= 0.6$ ) to 15 % ( $\kappa= 0.2$ ).

Fig. 7-35(b) shows the peak displacement of each floor with respect to energy dissipation capacity in the 5 stories-3 bay structure for the yield strength reduction factor  $R= 4$ . Compared to elastic response, inelastic response at 5<sup>th</sup> floor in the structure with  $\kappa= 0.2$  was 1.36 times. As the energy dissipation ratio increased, the peak displacement was reduced from 549.9 mm ( $\kappa= 0.2$ ) to 479.7 mm ( $\kappa= 0.6$ ). For elastic perfectly plastic beam-column connection and column with  $\kappa= 0.4$  (EPP), the peak displacement of the structure was 474.4 mm. For elastic perfectly plastic beam-column connection and elastic perfectly plastic column (EPP+EPP), the peak displacement of the structure was 528.7 mm. Compared to the displacement of the EPP+EPP

structure, the displacements of the structure with  $\kappa=0.2 - 0.6$  were increased from -22 % ( $\kappa=0.6$ ) to 4 % ( $\kappa=0.2$ ).

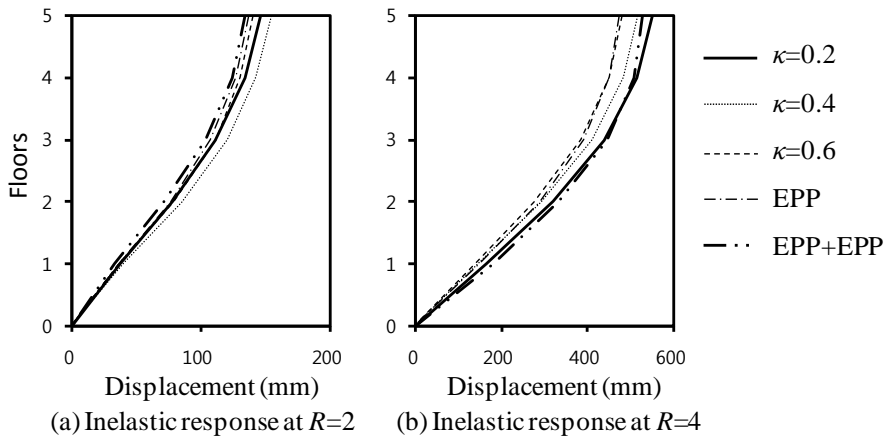


Fig. 7-35. Comparison of displacement according to energy dissipation ratio of 5 stories-3 bay structure subjected to Kobe earthquake load

Fig. 7-36 shows the ductility of each floor in the 5 stories-3 bay structure. Compared to the ductility of the EPP+EPP structure, the ductility of the structure with  $\kappa=0.2 - 0.6$  were increased from 12 % ( $\kappa=0.6$ ) to 15 % ( $\kappa=0.2$ ) for  $R=2$  and from 1 % ( $\kappa=0.6$ ) to 13 % ( $\kappa=0.2$ ) for  $R=4$ .

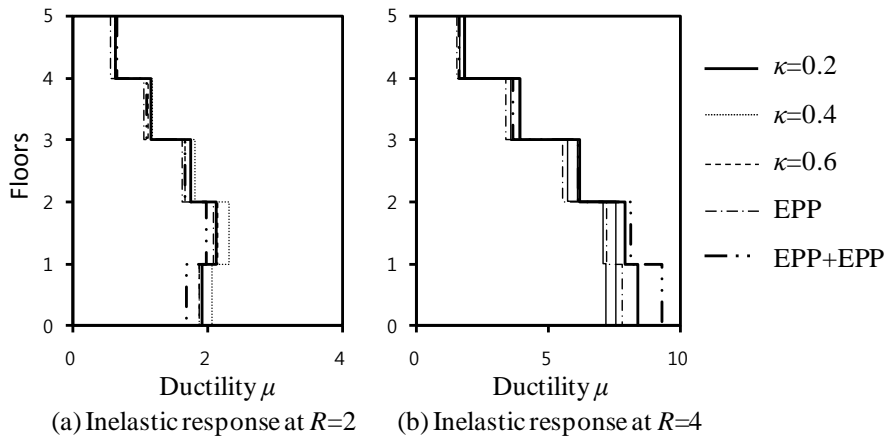


Fig. 7-36. Comparison of ductility according to energy dissipation ratio of 5 stories-3 bay structure subjected to Kobe earthquake load

## **7.5 Influence Parameters of Earthquake Response**

### **7.5.1 Relationship between Energy Dissipation of Structures and Earthquake Response**

Fig. 7-37 shows the energy dissipation at each floor in 3 stories-1 bay structures. The energy dissipation was determined from moment-rotation relationship in Figs. 7-9 and 7-10. All energy dissipation of columns in 1<sup>st</sup> floor and beam-column connections in each floor were cumulated with floors. For El-Centro earthquake load, the energy dissipation of the structure was greater than those of the structure subjected to other earthquake loads. The structure subjected to larger earthquake load ( $R=4$ ) induced the more energy dissipation. In most cases, as the energy dissipation ratio of beam-column connections decreased, the energy dissipation of the moment frame structure was increased. This is because the energy dissipation is increased by the increased deformation of beam-column connections and columns in the moment frames with low energy dissipation ratio (see Figs. 7-9 and 7-10).

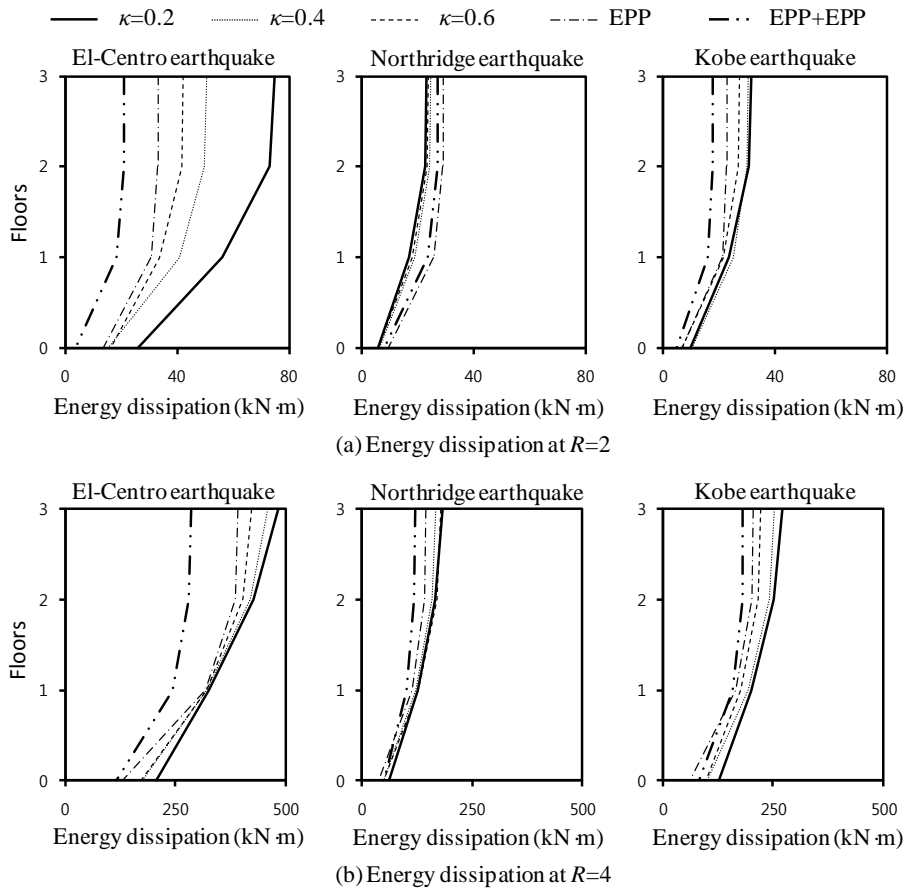


Fig. 7-37. Energy dissipation in 3 stories-1 bay structures

Fig. 7-38 shows the energy dissipation at each floor in 3 stories-3 bay structures. For El-Centro earthquake load, the energy dissipation of the structure was greater than those due to other earthquake loads. In most cases, as the energy dissipation ratio of beam-column connections decreased, the energy dissipation of the structure was increased.

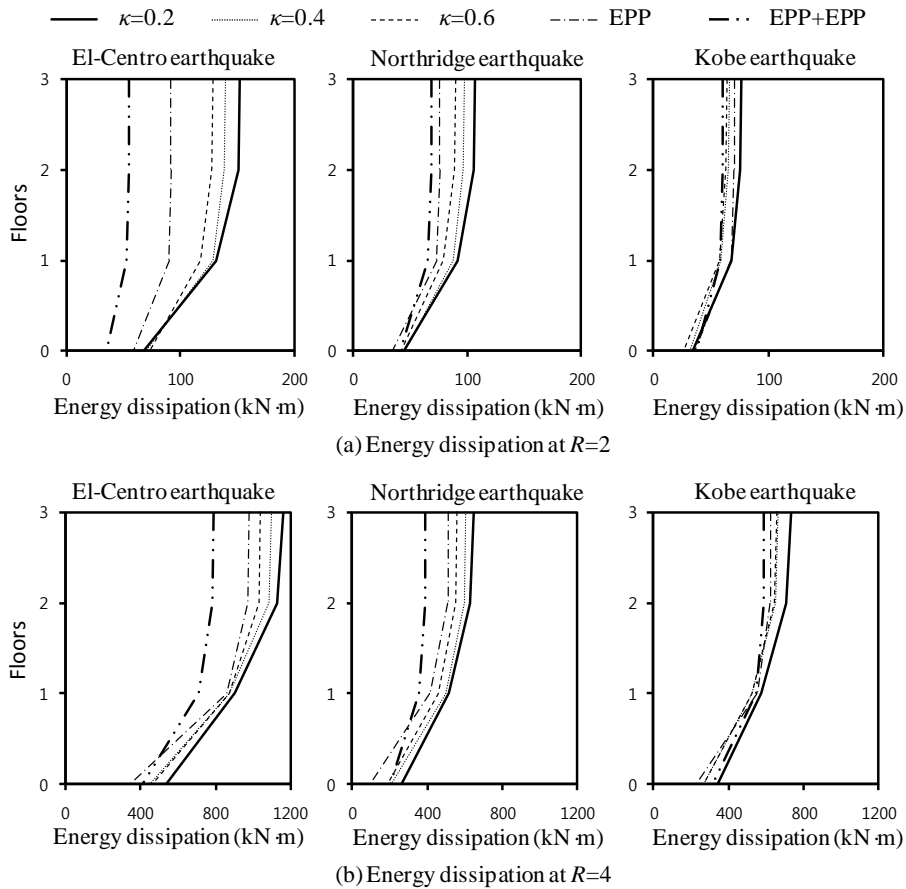


Fig. 7-38. Energy dissipation in 3 stories-3 bay structures

Fig. 7-39 shows the energy dissipation at each floor in 5 stories-3 bay structures. Unlike Figs. 7-37 and 7-38, for Northridge earthquake load, the energy dissipation of the structure was greater than those due to other earthquake loads. Furthermore, as the energy dissipation ratio of beam-column connections decreased, the energy dissipation was not increased. The energy dissipation of the structure depending on the energy dissipation ratio of beam-column connections was affected by structure types and earthquake

loading types.

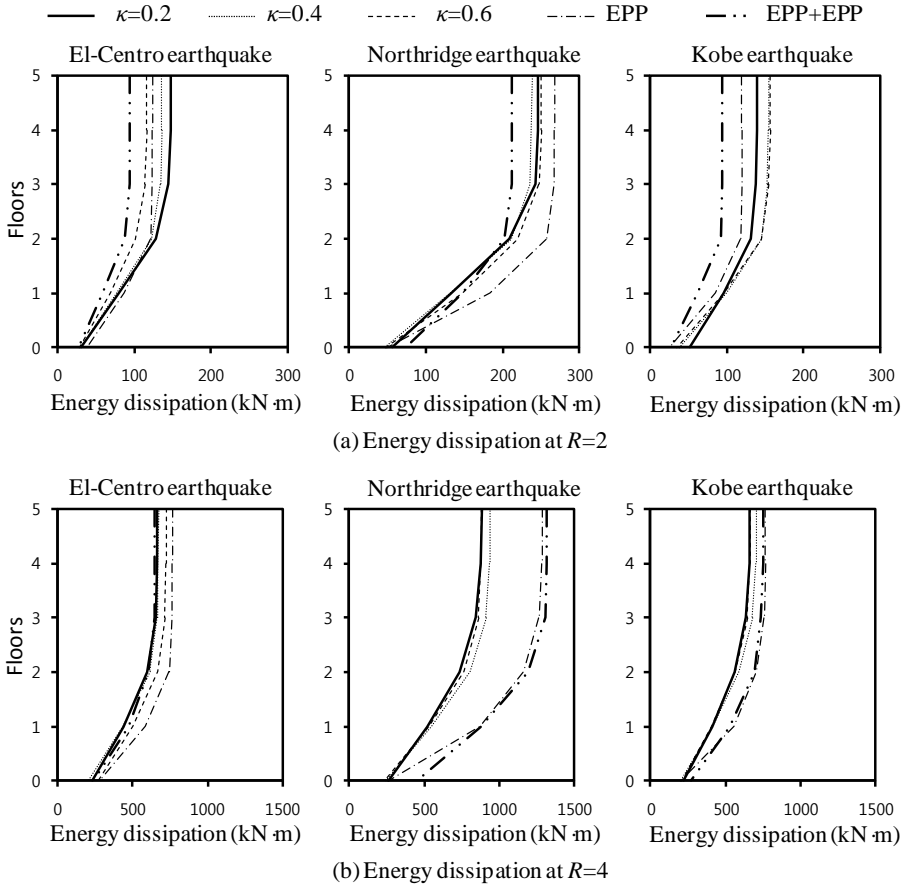


Fig. 7-39. Energy dissipation in 5 stories-3 bay structures

Fig. 7-40 shows the relationship between energy dissipation and plastic rotation in beam-column connections and columns. The energy dissipation was defined as average values at each floor, and the plastic rotation was defined as the peak rotation. As shown in Fig. 7-40, the plastic rotation was proportional to the energy dissipation in beam-column connections and

columns. However, the plastic rotation due to Northridge earthquake load was significantly increased in the energy dissipation 50 kN·m. The reason why is that the number of large earthquake acceleration close to the peak ground acceleration was less in Northridge earthquake load. As a result, although the peak rotation was increased by the peak ground acceleration, the energy dissipation was decreased by the reduced number of cyclic behavior undergoing large deformation. That is, earthquake loading property influences the relationship between the energy dissipation of the structure and the deformation.

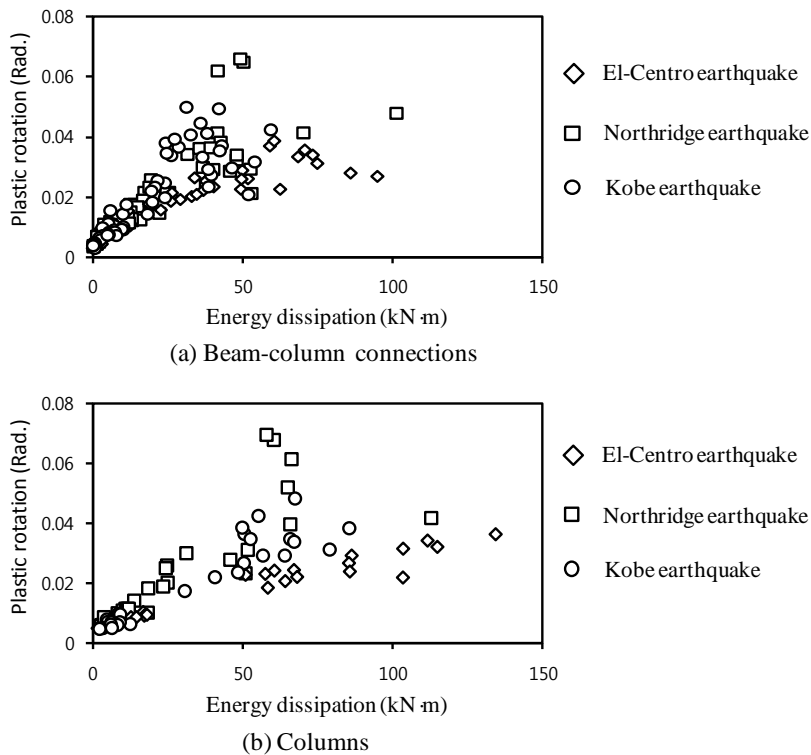


Fig. 7-40. Relationship between energy dissipation and plastic rotation



### 7.5.2 Relationship between Energy Dissipation Ratio of Beam-Column Connections and Earthquake Response

Fig. 7-41(a) shows the average lateral drift ratio depending on energy dissipation ratio of structure. The average lateral drift ratio was defined as the peak displacement at the top floor divided by the height of the moment frame structures for three earthquake load. For the yield strength reduction factor  $R=4$ , as the energy dissipation ratio increased, the lateral drift ratio was decreased. The increased ratios of lateral drift for  $R=4$  (ratio of  $\kappa=0.2$  to EPP) were 48 %, 47 %, and 13 % for  $T_n=0.331$  sec,  $T_n=0.335$  sec, and  $T_n=0.606$  sec, respectively. On the other hand, the lateral drift ratio increment depending on the energy dissipation ratio for  $R=2$  was less than that of  $R=4$ . The increased ratios of lateral drift for  $R=2$  were 13 %, 6 %, and 19 % for  $T_n=0.331$  sec,  $T_n=0.335$  sec, and  $T_n=0.606$  sec, respectively.

As shown in Fig. 7-41(b), the relationship between energy dissipation ratio and ductility  $\mu$  correlates with the relationship between energy dissipation ratio and lateral drift ratio in Fig. 7-41(a). The increased ratios of ductility for  $R=2$  (ratio of  $\kappa=0.2$  to EPP) were 11 %, 3 %, and 12 % for  $T_n=0.331$  sec,  $T_n=0.335$  sec, and  $T_n=0.606$  sec, respectively. The increased ratios of ductility for  $R=4$  were 48 %, 47 %, and 10 % for  $T_n=0.331$  sec,  $T_n=0.335$  sec, and  $T_n=0.606$  sec, respectively.

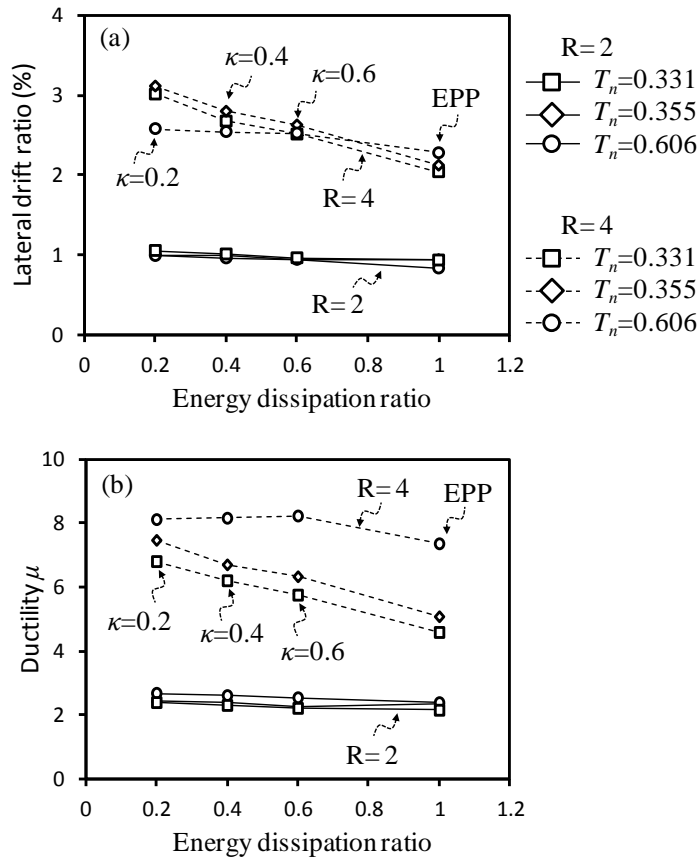


Fig. 7-41. Earthquake responses according to energy dissipation ratio

### 7.5.3 Relationship between Natural Period of Structures and Earthquake Response

Fig. 7-42(a) shows the lateral drift ratio depending on natural period of structure. For the yield strength reduction factor  $R=4$ , as the natural period increased, the lateral drift ratio discrepancy depending on energy dissipation ratio was decreased. The increased ratios of lateral drift for  $R=4$  (ratio of lateral drift at  $T_n=0.331$  to lateral drift at  $T_n=0.606$ ) were 17 %, 5 %, 0 %, and -10 % for  $\kappa=0.2$ ,  $\kappa=0.4$ ,  $\kappa=0.6$ , and EPP, respectively. On the other

hand, the lateral drift ratio increment depending on the energy dissipation ratio for  $R=2$  was less than that of  $R=4$ . The increased ratios of lateral drift for  $R=2$  were 6 %, 5 %, 2 %, and 12 % for  $\kappa = 0.2$ ,  $\kappa = 0.4$ ,  $\kappa = 0.6$ , and EPP, respectively.

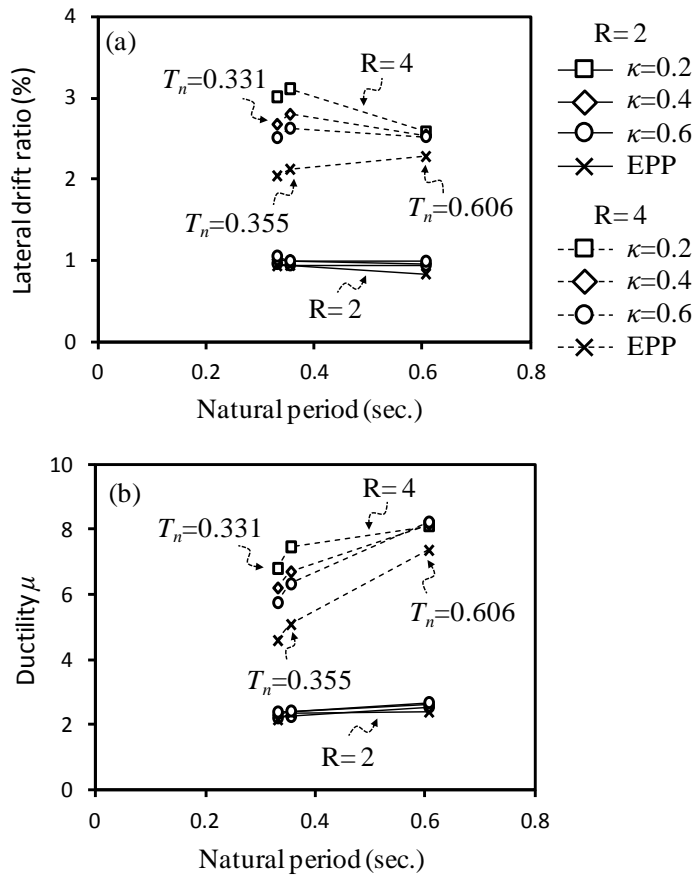


Fig. 7-42. Earthquake responses according to natural period

As shown in Fig. 7-42(b), the relationship between natural period and

ductility  $\mu$  did not correlate with that in Fig. 7-42(a). The increased ratios of ductility for  $R=2$  (ratio of ductility at  $T_n = 0.331$  to ductility at  $T_n = 0.606$ ) were -11 %, -12 %, -13 %, and -10 % for  $\kappa = 0.2$ ,  $\kappa = 0.4$ ,  $\kappa = 0.6$ , and EPP, respectively. The increased ratios of ductility for  $R=4$  were -16 %, -24 %, -30 %, and -38 % for  $\kappa = 0.2$ ,  $\kappa = 0.4$ ,  $\kappa = 0.6$ , and EPP, respectively. The ductility of the structure subjected to El-Centro earthquake load was larger in the structure with short natural period. On the other hand, under Northridge and Kobe earthquake loads, the ductility of the structure with short natural period was less than that of the structure with long natural period. This is because the earthquake load influences the relationship between the natural period and the ductility of the structure. That is, the earthquake response of the structure is related to the natural period of the structure and the period of earthquake acceleration. However, it is very difficult to define the relationship between the earthquake acceleration and the earthquake response of the structure, because the irregular earthquake acceleration consists of various waves. Thus, a number of nonlinear time history analyses should be performed for various ground acceleration, natural period of the structure, and structure types.

Figs. 7-41 and 7-42 indicate that the earthquake response such as lateral drift and ductility is increased in the structure with larger inelastic deformation (i.e. larger yield strength reduction factor  $R$ ). Furthermore, as the natural period is short and the energy dissipation ratio decreases, the lateral drift of the structure are increased more than those of the structure dissipating elasto-perfectly plastic energy.

## 7.6 Discussion

In this chapter, earthquake response of low-rise moment frame structures with respect to energy dissipation capacity in the beam-column connections was investigated. Using the developed energy-based model, nonlinear dynamic analysis was performed. Energy dissipation capacity degradation at the joint increases the lateral drift and ductility of moment frame structures. Furthermore, as the natural period of the structure is short, the lateral drift of the structure with low energy dissipation ratio were significantly increased more than those of the structure with large energy dissipation ratio. In the moment resisting frame structure that undergoes large inelastic deformation, structure performance was greatly affected by the energy dissipation capacity of the structure. Thus, the energy dissipation ratio of beam-column connections should be considered in earthquake design of low-rise moment frame structures. However, a further study is required to define accurately the relationship between the energy dissipation ratio of beam-column connections and the earthquake response of the structure in various earthquake accelerations.

## Chapter 8. Plastic Hinge Relocation Method Using Strengthening Bars

### 8.1 Introduction

In reinforced concrete moment-resisting frame structures, the overall earthquake resistance including stiffness, strength, deformation capacity, and energy dissipation capacity is significantly affected by the beam-column joints. Under cyclic loading, when yielding of the beam flexural bars penetrates into the joint panel and X-type diagonal cracking occurs in the joint panel (Fig. 8-1), significant bond slip and shear strength degradation occur in the joint (Kitayama et al., 1987; Leon, 1989; Hakuto et al., 1999; Brooke et al., 2006).

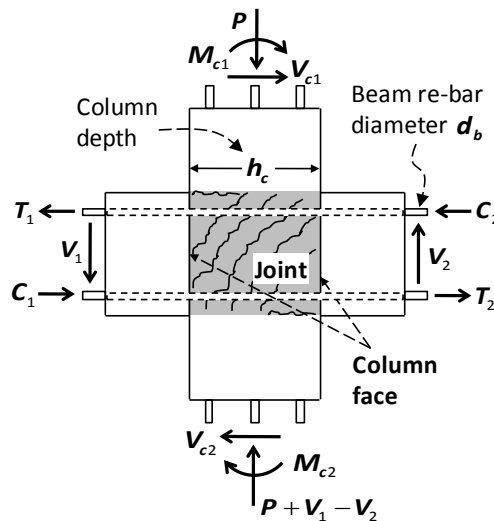


Fig. 8-1. Load transfer of interior beam-column joint

To mitigate bar bond-slip in the joint, current earthquake design codes specify the minimum requirement of column depth-to-bar diameter ratio ( $h_c/d_b$ ): ACI 318-11 (2011) and ACI 352R-02 (2002) require  $h_c/d_b > 20$  and  $h_c/d_b > 20 f_y/420$ , respectively. However, previous test results showed that even when the minimum requirement was satisfied, significant bond slip and shear deformation occurred at the beam-column joints (Kitayama et al., 1987; Leon, 1989; Hakuto et al., 1999; Brooke et al. 2006). Thus, to secure the structural performance of beam-column joints, NZS 3101:2006 (2006) and Eurocode 8 (2004) require greater development lengths for the beam flexural bars. However, such large development length frequently causes difficulty in architectural design when small columns or shallow depth columns (i.e. wall-columns) are preferred in low-rise buildings.

Alternatively, strengthening methods using additional strengthening bars in the joint can be used to enhance the bond resistance and shear strength (Galunic et al., 1977; Park and Milburn, 1983; Abdel-Fattah and Wight, 1987; Joh et al., 1991; Fenwick and Irvine, 1997; Yamamoto et al., 2008). Galunic et al. (1977) compared the effects of straight bars and 60° bent bars to strengthen the beam-column joints. The bent bars showed better performance in reducing joint shear distortion. Park and Milburn (1983) and Joh et al. (1991) used 90° hooked bars to relocate the beam plastic hinge zone (i.e. the critical section) to a distance of 0.5 - 1.0 times the beam depth from the column face. Abdel-Fattah and Wight (1987) used additional straight bars passing through the joint to reduce the yield penetration of beam re-bars. Fenwick and Irvine (1997) used the bond plates welded to the beam and column bars. Yamamoto

et al. (2008) used the U-shaped bars to relocate the slab plastic hinge zone to a distance of 1.8 times the slab depth from the wall face.

The existing test results showed that the strengthening methods efficiently enhanced the bond-resistance and shear strength in the beam-column joints. However, the following studies are required to expand the use of the strengthening methods.

- 1) Even with an identical strengthening method, the structural performance of beam-column connections can significantly vary according to the design parameters. Thus, the effects of the design parameters on the performance need to be quantified in order to apply the strengthening method to the performance-based design of beam-column connections. For example, the variation of energy dissipation capacity according to the length and strength of the strengthening bars need to be studied.
- 2) Current design codes specify the details of the strengthening methods and the bar anchorage. NZS 3101:2006 (2006) requires that the length of the strengthening bars be extended to a distance not less than the beam depth or 500 mm from the column face. ACI 318-11 (2011) Sec. 12 requires that the development length of the 90° hooked bars be not less than  $8d_b$  and 150 mm. However, a large development length may cause inconvenience in the design and construction of strengthening bars. Thus, the validity of such requirements needs to be verified.

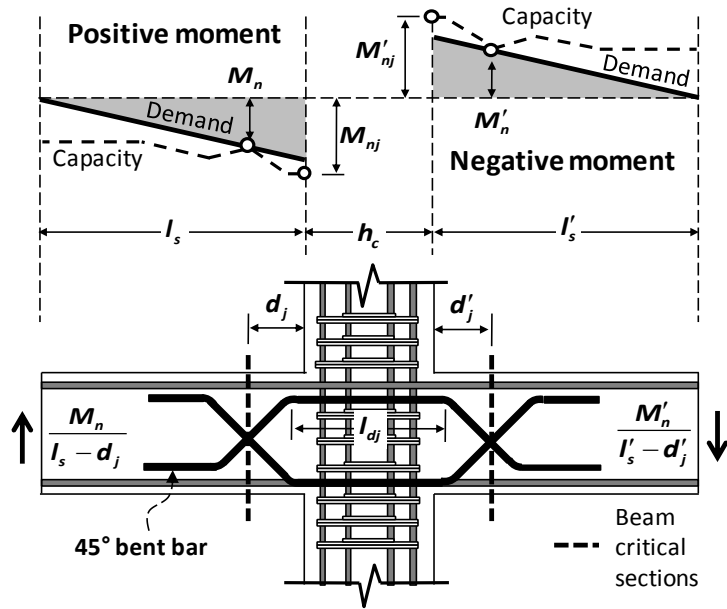


- 3) Unless special design provisions are provided, the bond resistance and joint shear strength of beam-column joints with strengthening bars should satisfy the requirements of the current design codes for conventional beam-column connections. In this case, the requirements of the current design methods or the relevant design parameters need to be modified, considering the enhanced performance and details of the strengthening methods.

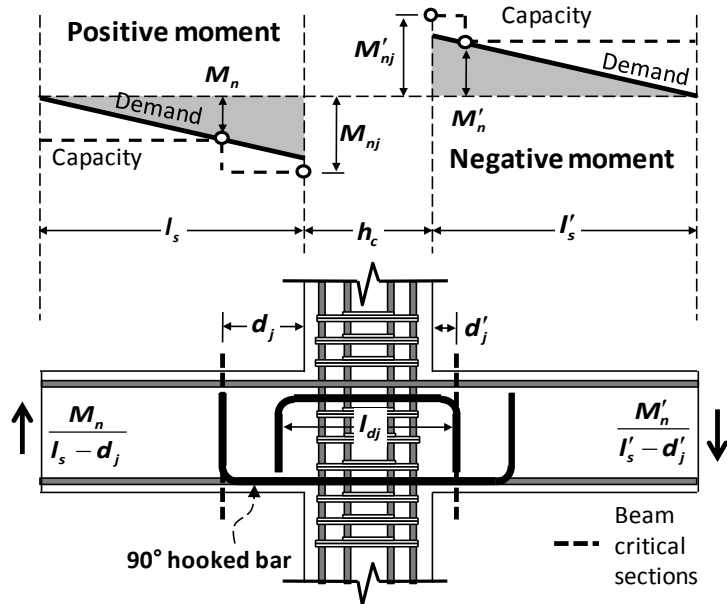
In the present study, cyclic loading tests for beam-column connections were performed to evaluate the effects and details of the strengthening methods and the relevant code-requirements. To verify the effect of the strengthening methods, the test specimens were intentionally designed with small  $h_c/d_b$  ratios less than 20, which is the minimum requirement of ACI 318. For the strengthening methods, 45° bent bars and 90° hooked bars were used in the joints. On the basis of existing test results from the present study and previous studies, design recommendations were proposed for the bar bond- and joint shear-design of beam-column connections with the strengthening methods.

## 8.2 Relocation of Beam Plastic Hinge Zone

Fig. 8-2 shows the concept of the joint strengthening methods using  $45^\circ$  bent bars and  $90^\circ$  hooked bars (Park and Milburn, 1983; Joh et al., 1991; NZS 3101, 2006). The flexural capacity of the beams at the column face is increased by the strengthening bars (i.e. the  $45^\circ$  bent bars and  $90^\circ$  hooked bars) (see dotted lines in Figs. 8-2(a) and (b)). Therefore, the beam critical section and plastic hinge zone are relocated to the distance  $d_j$  where the moment capacity of the beam is the same as the demand (see Figs. 8-2(a) and (b)). Consequently, yielding of the beams doesn't significantly influence the behavior of the joint.



(a) 45° bent bars



(b) 90° hooked bars

Fig. 8-2. Strengthening methods for beam-column joint

To prevent early yielding of beam flexural bars at the column face, the beam moment capacity  $M_{nj}$  at the column face should be greater than the demand which is developed by the moment capacity  $M_n$  at the critical section (Fig. 8-2):

$$M_{nj} > M_n \left( \frac{l_s}{l_s - d_j} \right) \quad \text{or} \quad M'_{nj} > M'_n \left( \frac{l'_s}{l'_s - d'_j} \right) \quad (8-1)$$

where  $l_s$  = the distance from the column face to the location of zero moment in the beams; and  $d_j$  = the distance from the column face to the beam critical section. In Eq. (8-1) and Fig. 8-2,  $M_n'$ ,  $M_{nj}'$ ,  $d_j'$ , and  $l'_s$  are the quantities corresponding to the negative moment. Here,  $M_{nj}$  and  $M_{nj}'$  at the column face are calculated from sectional analysis, addressing the contribution of the strengthening bars (i.e. the 45° bent bars and 90° hooked bars). In the calculation of  $M_n$  and  $M_n'$  at the critical section, the contribution of the 45° bent bars located at the center of the cross section is included, while the contribution of the 90° hooked bars is neglected because of the short development length.

The area of strengthening bars should be determined from Eq. (8-1). According to ACI 318-11 (2011) Sec 21, the actual tensile stress of beam flexural bars can be increased to 1.25 times the yield strength due to the cyclic strain-hardening behavior of the re-bars. Therefore, it is recommended that the total area of the 45° bent bars and 90° hooked bars be greater than at least 25 % of the total area of the beam flexural bars.

When the strengthening methods are used in the beam-column joint, flexural yielding of the beams occurs at the critical section relocated to the distance  $d_j$  and  $d'_j$  from the column face, as shown in Fig. 8-3. Therefore, the development length of the beam flexural bars passing through the joint can be increased to the distance between the left and right critical sections. Thus, even when a small column depth  $h_c$  is used, the bond resistance of the beam flexural bars can be increased to the modified development length  $l_{dj}$ . In the present study, the minimum length of the straight part of the  $45^\circ$  bent bars and  $90^\circ$  hooked bars is defined as the modified development length  $l_{dj}$  of the beam flexural bars (see Figs. 8-2 and 8-3).

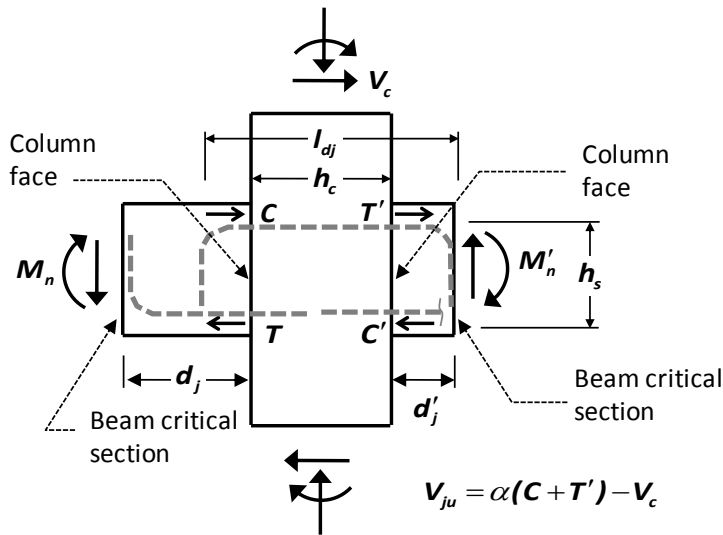


Fig. 8-3. Shear demand of beam-column joint with strengthening bars

The shear strength of the joint with strengthening bars can be increased by restraining the bar yield penetration and diagonal concrete cracking. In the present study, the enhanced joint shear strength  $V_{jn}$  is defined as follows, modifying the provisions of ACI318-11 (2011) and ACI352R-02 (2002).

$$V_{jn} = \beta\gamma\sqrt{f'_c}A_j \leq 1.7\sqrt{f'_c}A_j \quad (8-2)$$

$$\beta = \frac{l_{dj}}{h_c} \geq 1.0 \quad (8-3)$$

where  $A_j$  = effective joint shear area ( $= b_j h_c$ );  $b_j = \min\{0.5(b_b + b_c), b_b + h_c, b_c\}$  (ACI352R-02, 2002) or  $\min\{b_b + 2x, b_b + h_c, b_c\}$  (ACI 318-11, 2011);  $b_b$  = width of the beam cross section;  $b_c$  = width of the column cross section;  $x$  = the smaller perpendicular distance from the longitudinal axis of the beam to the column side; and  $\gamma$  = coefficient addressing the confinement effect by the beams framed into the joint. According to ACI 318-11 (2011) and ACI352R-02 (2002) and,  $\gamma = 1.2$  is used for the cruciform beam-column connections.

In Eqs. (8-2) and (8-3),  $\beta$  ( $\geq 1.0$ ) is the new coefficient introduced to address the joint shear strength enhanced by the use of the strengthening bars. The  $\beta$  value increases as the distance  $l_{dj}$  between the two beam plastic hinge zones increases. The validity of the definition is discussed in Chapter 8.4.3. In Eq. (8-2), the product  $\beta\gamma$  should not be greater than 1.7, which is the maximum value for interior beam-column joints (ACI318-11, 2011; ACI352R-02, 2002).

Flexural yielding of the beams occurs at the relocated critical sections away from the column face. Thus, the joint shear demand  $V_{ju}$  at the column face is calculated using the moments,  $M_n l_s / (l_s - d_j)$  and  $M'_n l'_s / (l'_s - d'_j)$ , which are developed by the beam moment capacity at the critical sections (refer to Eq. (8-1) and Fig. 8-2). The joint shear demand  $V_{ju}$  is calculated as follows (see Fig. 8-3).

$$V_{ju} = \alpha (C + T') - V_c \approx \alpha \left( \frac{M_n l_s}{l_s - d_j} + \frac{M'_n l'_s}{l'_s - d'_j} \right) \frac{1}{h_s} - V_c \quad (8-4)$$

where  $C$  and  $T'$  = resultant compression and tension forces of the beam cross-sections, respectively, at the column face (refer to Fig. 8-3);  $\alpha$  = coefficient addressing the effects of material over-strength and cyclic strain-hardening (= 1.25);  $V_c$  = the shear demand of the column; and  $h_s$  = the distance between the top and bottom flexural bars of the beams.

### 8.3 Test Program

For cyclic loading tests, five full-scale cruciform specimens, S1 - S5, were prepared. Fig. 8-4 shows the dimensions and re-bar details of the specimens. The re-bar details of the beams and columns were designed to satisfy the requirements of the special moment frame specified in ACI 318-11 (2011), except for the requirements of beam-column joints. Table 8-1 presents the measured strengths of concrete and re-bars. The compressive strength of concrete was  $f'_c = 29.4 - 38.3$  MPa, and the yield strengths of the re-bars were  $f_y = 462, 496, 452,$  and  $475$  MPa for D10, D13, D25(A), and D25(B) bars, respectively.

Fig. 8-4(a) shows the conventional beam-column connection S1 without strengthening bars. The net beam length between the vertical supports was  $l = 5760$  mm. The net column height was  $h = 2100$  mm. The dimensions of the column and beam cross-sections were  $500 \text{ mm} \times 460 \text{ mm}$  and  $350 \text{ mm} \times 500 \text{ mm}$ , respectively. Four D25 and two D25 bars were used at the top and bottom of the beam cross-section, respectively ( $\rho_t = 0.013$  and  $\rho_b = 0.0065$ ). D10 bars were used for the hoops in the plastic hinge region at a spacing of  $100 \text{ mm}$  ( $\rho_v = 0.0041$ ). In the column, twelve D25 bars were used for the longitudinal reinforcement ( $\rho = 0.0266$ ), and D13 bars were used for the ties at a spacing of  $100 \text{ mm}$  ( $\rho_h = 0.0103$ ). The  $h_c/d_b$  ratio of the beam flexural bars was intentionally designed as a small value,  $18.1$  ( $h_c = 460 \text{ mm}$  and  $d_b = 25.4 \text{ mm}$ ), which did not satisfy the requirement of ACI 318-11 (2011) Sec. 21



(see Table 8-1).

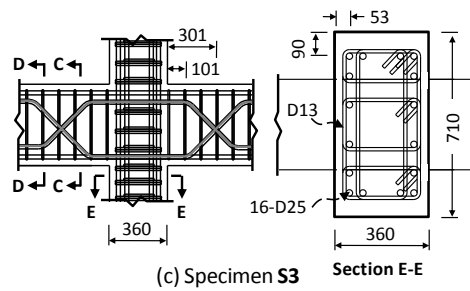
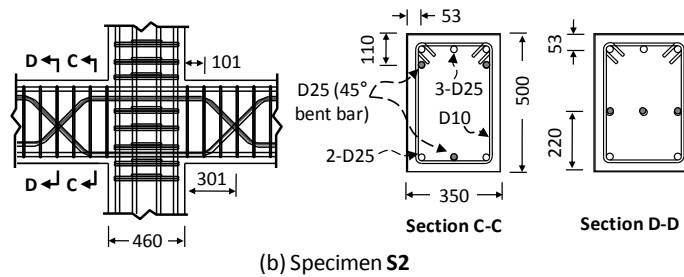
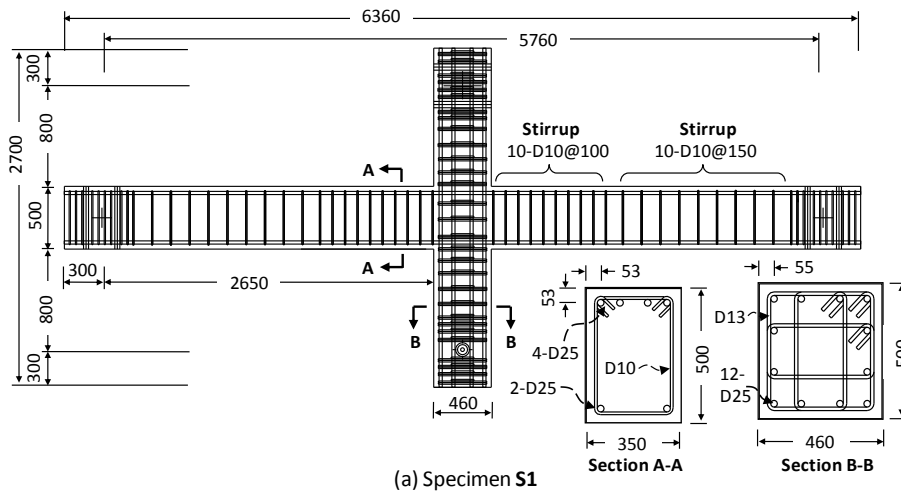
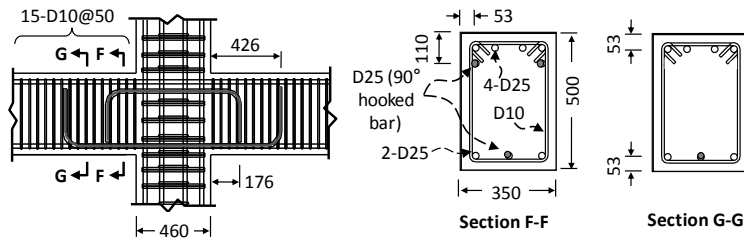
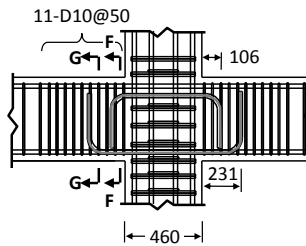


Fig. 8-4. Dimensions and re-bar details of connection specimens (Continued)



(d) Specimen S4



(e) Specimen S5

Fig. 8-4. Dimensions and re-bar details of connection specimens

Table 8-1. Properties of test specimens (mm, %, MPa, kN, and kN-m)

Specimens		S1	S2	S3	S4	S5
Materials strengths	Concrete strength $f'_c$	38.3	32.0	35.9	29.4	37.5
	Re-bar yield strength $f_y$ <sup>1)</sup>	462, 496, 452, and 475 MPa for D10, D13, D25(A), and D25(B)				
Beam	Dimensions ( $b_b \times h_b$ )	350 × 500	350 × 500	350 × 500	350 × 500	350 × 500
	Top / bottom bars	4D25 / 2D25	3D25 / 2D25	3D25 / 2D25	4D25 / 2D25	4D25 / 2D25
	Joint-strengthening bars	-	45° bent bars	45° bent bars	90° hooked bars	90° hooked bars
	( $d_j$ / $d_j'$ / $l_{dj}$ )	-	(301/301/662)	(301/301/562)	(426/176/812)	(231/106/672)
	Stirrups at plastic hinge	D10@100	D10@100	D10@100	D10@50	D10@50
	$M_n$ and $M_{nj}$ <sup>2)</sup>	197 / -	249 <sup>3)</sup> / 297	252 <sup>3)</sup> / 300	194 / 282	206 / 301
	$M_n'$ and $M_{nj}'$ <sup>2)</sup>	375 / -	369 <sup>3)</sup> / 437	377 <sup>3)</sup> / 445	364 / 483	391 / 527
Joint	$h_c/d_b$ and $l_{dj}/d_b$	18.1 and N/A	18.1 and 26.1	14.2 and 22.1	18.1 and 32.0	18.1 and 26.5
	$V_{ju}$	1419	1807	1854	1639	1677
	$\beta$ and $\beta\gamma$	1.0 and 1.2	1.44 and 1.7	1.56 and 1.7	1.77 and 1.7	1.46 and 1.7
	$V_{jn}$	1452	1880	1943	1802	2035

<sup>1)</sup> D25(A) and D25(B) were used for specimens S1 and S4, and for specimens S2, S3, and S5, respectively.

<sup>2)</sup> Measured material strengths were used for the calculation of the flexural capacities.

<sup>3)</sup> 45° bent bars were included in the calculation (see Section D-D in Fig. 8-4(b)).

Fig. 8-4(b) shows the re-bar details of specimen S2 strengthened with 45° bent bars (three D25 bars). Dimensions and re-bar details of the column were identical to those of S1. In the beam, three D25 and two D25 bars were used at the top and bottom of the cross-section, respectively ( $\rho_t = 0.0098$  and  $\rho_b = 0.0065$ ). Although the number of the top bars was decreased, due to the 45° bent bars, the predicted load-carrying capacity of S2 was 22% greater than that of S1 (see  $P_n$  in Table 8-2). The beam critical sections were relocated to  $d_j = d_j' = 301$  mm from the column face, as shown in Fig. 8-4(b). The 45° bent bars were bent at 101 mm from the column face. Thus, the modified development length of the beam flexural bars, which is defined as the length of the straight part of the 45° bent bars, was  $l_{dj} = h_c + 101 + 101 = 662$  mm (see Fig. 8-4(b)). As a result, the development length-to-bar diameter ratio of the beam bars,  $l_{dj}/d_b$ , was increased to 26.1 which was greater than the conventional ratio,  $h_c/d_b = 18.1$  ( $d_b = 25.4$  mm). D10 bars were used for the hoops in the beam plastic hinge region at a spacing of 100 mm ( $\rho_v = 0.0041$ ).

Fig. 8-4(c) shows the re-bar details of specimen S3 strengthened with 45° bent bars (three D25 bars). The details of S3 were the same as those of S2, except for the column dimension of 360 mm × 710 mm. To investigate the effect of the strengthening bars on the beam-column joint with a small column depth, the column depth was decreased to  $h_c = 360$  mm ( $h_c/d_b = 14.2$ ), which was the least among the specimens. However, by using the 45° bent bars, the development length  $l_{dj}$  of the beam flexural bars and the  $l_{dj}/d_b$  ratio were increased to 562 mm ( $= h_c + 101$  mm + 101 mm) and 22.1 ( $d_b = 25.4$  mm, see Table 8-1), respectively, when compared to those of S1. The column width

was increased to 710 mm to ensure the strong column-weak beam behavior and the joint shear strength.

Fig. 8-4(d) shows the re-bar details of specimen S4 strengthened with 90° hooked bars (three D25 bars). The dimensions and re-bar details of the column and beam were the same as those of S1. The top strengthening bars (two D25 bars) and the bottom strengthening bar (one D25 bar) were anchored at 176 mm ( $= 6.9d_b$ ) and 426 mm ( $= 16.8d_b$ ) from the column face, respectively ( $d_j = 426$  mm and  $d'_j = 176$  mm, see Fig. 8-4(d)). The top and bottom 90° hooks were intentionally placed at different locations to mitigate the concentration of plastic deformation and anchorage force. The bottom hooked bars were designed with a greater length because under cyclic loading, greater plastic strains develop in the bottom beam bars with the smaller area. The modified development length of the beam bars was conservatively determined as  $l_{dj} = h_c + 176 + 176 = 812$  mm, using the length of the top hooked bars. Thus, the  $l_{dj}/d_b$  ratio was increased to 32.0 ( $d_b = 25.4$  mm, refer to  $h_c/d_b = 18.1$  in Table 8-1). To prevent premature concrete failure in the beam plastic hinge, the spacing of the D10 hoops was decreased to 50 mm ( $\rho_v = 0.0098$ ).

Fig. 8-4(e) shows the re-bar details of specimen S5 strengthened with 90° hooked bars (three D25 bars). The dimensions and details of S5 were the same as those of S4, except for the smaller length of the strengthening bars. The top and bottom strengthening bars were anchored at 106 mm ( $= 4.2d_b$ ) and 231 mm ( $= 9.1d_b$ ) from the column face, respectively ( $d_j = 231$  mm and  $d'_j = 106$

mm, see Fig. 8-4(e)). The development length of the beam bars was determined as  $l_{dj} = h_c + 106 + 106 = 672$  mm using the length of the top hooked bar. Thus, the  $l_{dj}/d_b$  was increased to 26.5 (refer to  $h_c/d_b = 18.1$ ).

In this test, the following details of the strengthening bars were evaluated.

- 1) NZS3101:2006 (2006) recommends that beam plastic hinges be relocated at a distance not less than the greater of the beam depth  $h_b$  and 500 mm from the column face, on the basis of existing test results (Park and Milburn, 1983; Joh et al., 1991; Galunic et al., 1997). In this test, on the other hand, the relocated plastic hinges were designed with shorter distances: the distance  $d_j$  (or  $d'_j$ ) between the critical section and the column face was 301 mm ( $= 0.60h_b$ ) for S2 and S3 and 106 - 426 mm ( $= 0.21h_b - 0.85h_b$ ) for S4 and S5.
- 2) ACI 318-11 Sec. 12 (2011) requires that the development length  $l_{dh}$  of the 90° hooked bars be not less than the greater of  $8d_b$  ( $= 203$  mm) and 150 mm. In this test, the development lengths of S4 and S5 were 176 and 106 mm, respectively, which were shorter than  $8d_b$  ( $= 203$  mm) (see Fig. 8-4). The end hook extension of the 90° hooked bars ( $= 313$  mm) satisfied the requirement of ACI 318-11 (2011),  $12d_b$  for the standard hooks.
- 3) To avoid the concentration of plastic deformation and anchorage force, the top and bottom 90° hooks were anchored at different locations. The distance of the two end hooks were 250mm for S4 and 125mm for S5.

Fig. 8-5 shows the test set-up. Cyclic lateral loading was applied to the top hinge of the column. The cyclic loading program was planned according to ACI 374.1-05 (2005). Load cycles were repeated three times at each displacement level. No axial load was applied to the column. The beams were laterally supported to prevent out-of-plane displacement. LVDTs were used to measure the shear deformation of the beam-column joint, the lateral displacement at the loading point, and the slip deformations at the supports of the column and beams.

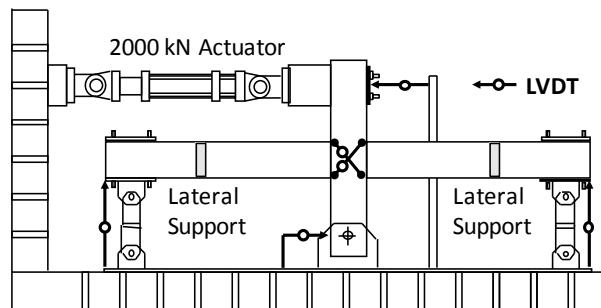


Fig. 8-5. Test setup

## 8.4 Test Results

### 8.4.1 Lateral Load-Drift Ratio Relationship and Failure Mode

Fig. 8-6 shows the lateral load - drift ratio relationships of the specimens. The lateral drift ratio was calculated by dividing the measured net lateral displacement at the loading point by the net column height (= 2100 mm). The failure modes of the specimens at the end of the test are shown in Fig. 8-7 and Table 8-2. The specimens exhibited different responses and failure modes according to the strengthening methods and the details. In S1 without the strengthening bars, significant bond-slip and diagonal cracking occurred in the joint (see Fig. 8-7(a)). As the bond-slip and yield penetration of the beam reinforcement increased, a gap occurred at the column face. Due to the repeated opening and closing of the gap and the diagonal cracking in the joint, S1 showed significant pinching in the cyclic response (see Fig. 8-6(a)). As shown in Fig. 8-7, the diagonal cracks in the joint eventually propagated to the vertical cracks at the top and bottom columns. Such cracks and damages of the joint and columns might be even worse if the column is subjected to high axial load. Ultimately, S1 failed at 6.2 % drift ratio due to concrete crushing at the column face (see Fig. 8-7(a)).



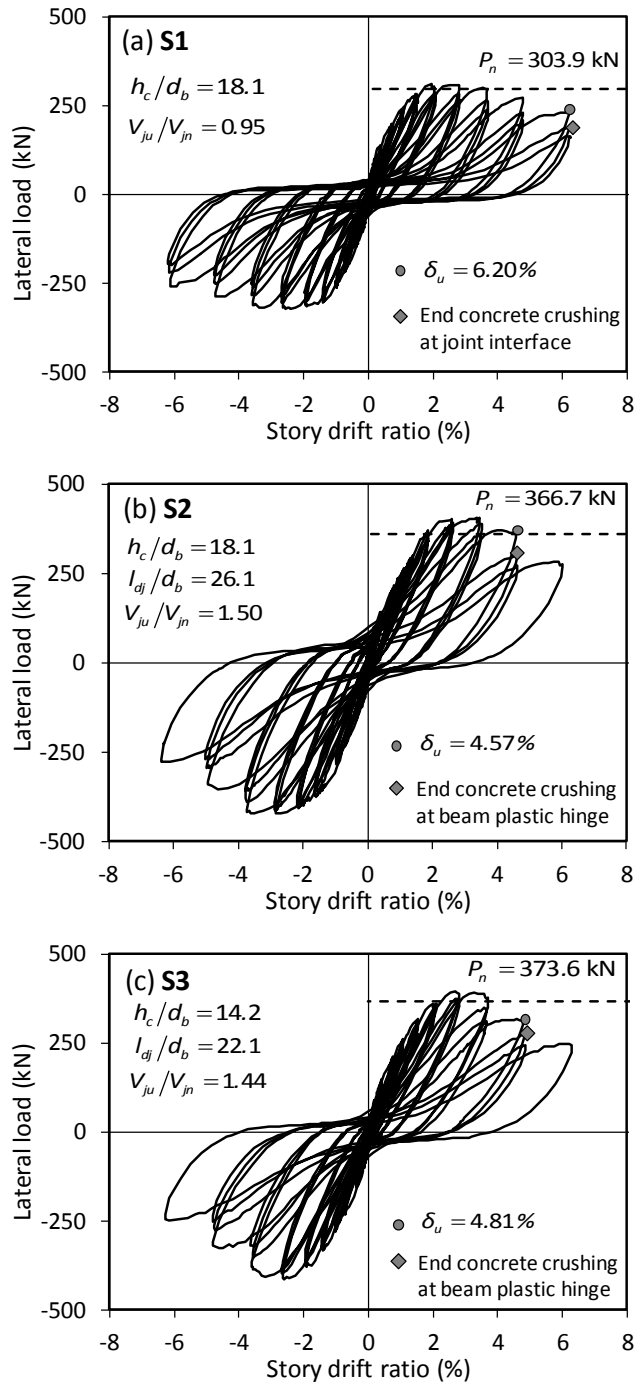


Fig. 8-6. Lateral load-drift ratio relationship of connection specimens (Continued)

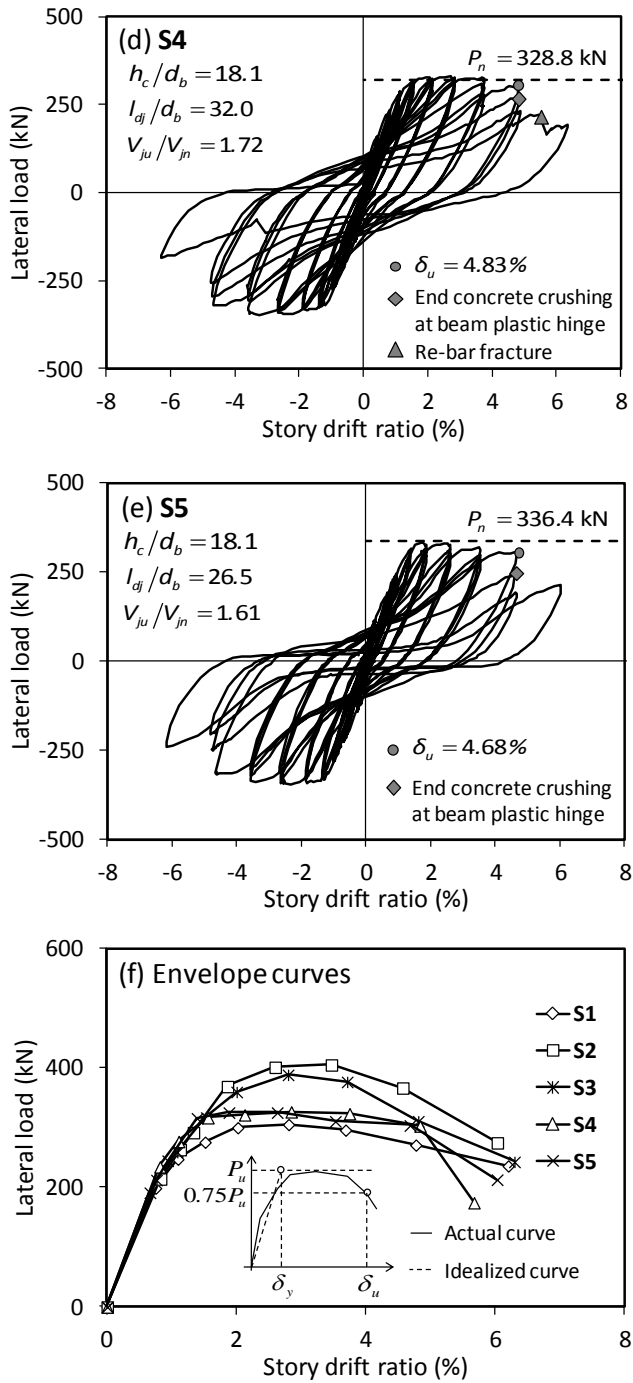


Fig. 8-6. Lateral load-drift ratio relationship of connection specimens

Table 8-2. Test results (kN, kN/mm, and %)

Specimen	Load-carrying capacity			Deformation capacity		Stiffness	Acceptance criteria for cyclic loading by ACI374.1-05				Failure mode
	$P_u$	$P_n$	$P_u/P_n$	$\delta_v$	$\delta_u$		$k_i^{1)}$	$k_s^{1)}$	$k_s/k_i^{1)}$	$\kappa^{1)}$	
S1	310	296	1.05	1.27	6.20	11.6	23.0	0.72	0.03	0.206	Joint failure <sup>2)</sup>
S2	406	361	1.12	1.85	4.57	10.4	19.2	2.56	0.13	0.254	Beam failure <sup>3)</sup>
S3	394	367	1.07	1.77	4.81	10.6	20.2	1.50	0.07	0.206	Beam failure <sup>3)</sup>
S4	330	321	1.03	1.22	4.83	12.9	22.8	2.28	0.10	0.322	Beam failure <sup>3)</sup>
S5	332	328	1.01	1.27	4.68	12.4	23.6	1.98	0.08	0.281	Beam failure <sup>3)</sup>

<sup>1)</sup>  $k_i$  was calculated according to the definition of ACI374.1-05 Sec. 7.3.  $k_s$  and  $\kappa$  were evaluated for the third load cycle at 3.5 % drift ratio.

<sup>2)</sup> Concrete crushing at column face

<sup>3)</sup> Concrete crushing at the bottom of beam plastic hinges

Figs. 8-6(b) and 8-7(b) show the cyclic response and failure mode of S2 strengthened with 45° bent bars. Since the plastic hinge zones of the beams were relocated, pinching in the cyclic response was not as significant as S1. Thus, the hysteretic energy dissipation of S2 increased. At 4.6 % drift ratio, S2 failed due to concrete crushing in the beam plastic hinge zones. The concrete crushing occurred at the beam bottom which was subjected to greater compressive stresses and strains due to the greater area of the top flexural bars. However, despite the use of strengthening bars, substantial diagonal and vertical cracks developed in the joint and columns, though they were not as significant as that of S1.

Figs. 8-6(c) and 8-7(c) show the cyclic response and failure mode of S3 with 45° bent bars and a smaller column depth ( $h_c = 360$  mm). Despite the smaller joint depth, the overall cyclic response and the failure aspects of S3 were similar to those of S2. S3 failed at 4.81 % drift ratio by concrete crushing at the beam plastic hinge zones.

Figs. 8-6(d) and (e) show the cyclic responses of S4 and S5 strengthened with 90° hooked bars. Pinching was significantly decreased in the cyclic responses. As a result, the hysteretic energy dissipations of S4 and S5 substantially increased when compared with the cyclic response of S1. Fig. 8-7(d) shows the failure mode of S4. In the beam plastic hinge zones, concrete crushing initiated at the bottom of the beams. Ultimately, the concrete crushing propagated into the beam web along the hook anchorage. In the joint, diagonal cracking decreased. Ultimately, S4 failed at 4.8 % drift ratio due to

concrete crushing and bar fracture at the beam bottom. The cyclic response and failure mode of S5 were similar to those of S4 (compare Fig. 8-6(e) and Fig. 8-7(e)). However, since the development length of the strengthening bars was shorter and the locations of the hook anchorages were closer to the joint, concrete crushing was more concentrated at the smaller plastic hinge zones of the beams (see  $d_j$  and  $d_j'$  in Table 8-1).

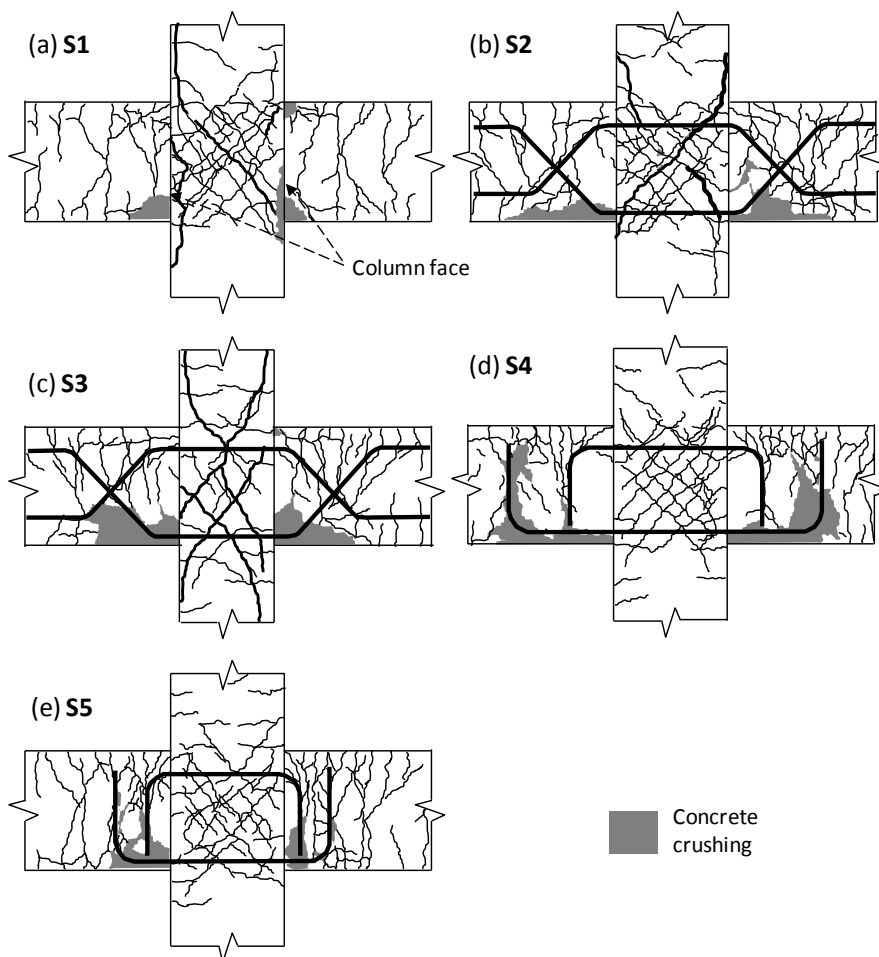


Fig. 8-7. Failure modes of specimens at the end of the test

### 8.4.2 Load-carrying Capacity and Deformation Capacity

Table 8-2 presents the maximum strength  $P_u$  of the specimens measured from the test. Although S1, S4, and S5 had the same area of beam flexural bars, the maximum strengths of S4 and S5 with the 90° hooked bars were about 7 % greater than that of S1, due to the relocation of the beam critical sections. In S2 and S3 with 45° bent bars,  $P_u$  was increased by about 30 % because, in addition to the effect of the beam plastic hinge relocation, the 45° bent bars significantly contributed to the flexural strength in the beam plastic hinge zones. In S4 and S5, the hooked bars did not contribute to the flexural strength in the plastic hinge zone.

The nominal strengths  $P_n$  of the specimens were predicted by assuming flexural yielding at the beam critical sections which were relocated to the distances of  $d_j$  and  $d'_j$  from the column face (see Table 8-1, Fig. 8-2, and Fig. 8-8).

$$P_n = \left( \frac{M_n}{l_s - d_j} + \frac{M'_n}{l'_s - d'_j} \right) \left( \frac{l}{2h} \right) \quad (8-5)$$

where  $l$  = net beam length between the two end supports;  $h$  = net column height between the top and bottom hinges; and  $M_n$  and  $M'_n$  = the nominal moment capacities at the critical sections. Table 8-2 compares the test strengths  $P_u$  and the predicted strengths  $P_n$ . The  $P_u/P_n$  ratios ranged from 1.01 to 1.12, which indicates that the predictions based on the relocated plastic

hinge mechanism agreed well with the test results.

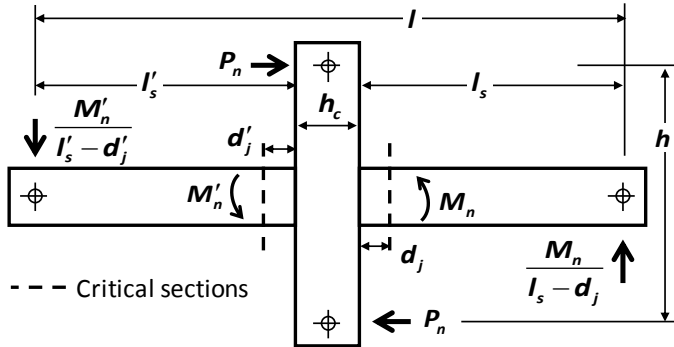


Fig. 8-8. Calculation of load-carrying capacity

Table 8-2 also compares the yield and maximum lateral drift ratios of the specimens measured by the tests. As shown in Fig. 8-6(f), the yield stiffness  $k_y$  was defined as the secant stiffness connecting the origin and the point corresponding to 75 % of the maximum strength  $P_u$ . The yield drift ratio  $\delta_y$  was then calculated as  $\delta_y = P_u / k_y$  (Park, 1988). The maximum drift ratio  $\delta_u$  was determined as the post-peak drift ratio corresponding to 75 % of the maximum strength  $P_u$ . The maximum drift ratio of S1 without strengthening bar was  $\delta_u = 6.20\%$ . On the other hand, in S2 - S5 with the strengthening bars, the maximum drift ratios were decreased to  $\delta_u = 4.57 - 4.83\%$ . This result indicates that the bar bond-slip does not necessarily result in a poor deformation capacity. However, the high deformation capacity of S1 was attributed to the rigid body motion caused by the bar bond-slip. Thus, the increased deformation capacity did not contribute to the energy dissipation of

the beam-column connection.

Table 8-2 compares the yield stiffness  $k_y$  and yield drift ratios  $\delta_y$ . Since the number of beam flexural bars in S4 and S5 was the same as that of S1,  $k_y$  and  $\delta_y$  in S1, S4, and S5 were almost the same. On the other hand,  $k_y$  of S2 and S3 using 45° bent bars was about 10 % less than that of S1 because of the reduced number of beam flexural bars. Unlike the 90° hooked bars, the 45° bent bars significantly contributed to the flexural capacity at the beam plastic hinge zone. Thus, the maximum strengths  $P_u$  of S2 and S3 were 31.0 and 27.1 % greater than that of S1. As a result, the yield drift ratios  $\delta_y (= P_u/k_y)$  of S2 and S3 were significantly increased (see Table 8-2).

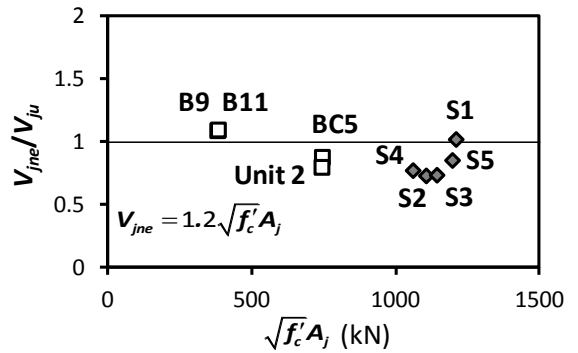
#### 8.4.3 Shear Strength of Beam-Column Joints

Table 8-1 compares the joint shear demand  $V_{ju}$  and the modified joint strength  $V_{jn} (= \beta\gamma\sqrt{f'_c}A_j \leq 1.7\sqrt{f'_c}A_j)$ . The joint shear strength  $V_{jn}$  of S1 without strengthening bars was calculated from Eq. (8-2), using  $\beta = 1.0$  and  $\gamma = 1.2$  for the cruciform connection. For S2 - S5 with the strengthening bars,  $V_{jn}$  was calculated by using  $\beta = l_{dj}/h_c = 1.44 - 1.77$ ,  $\gamma = 1.2$ , and the condition of  $\beta\gamma \leq 1.7$  (refer to Eq. (8-3) and Table 8-1). The shear demand  $V_{ju}$  of the specimens were evaluated by Eq. (8-4), using  $h_s = 394$  mm (see Table 8-1). In the calculations of  $V_{ju}$ ,  $\alpha = 1.25$  was used to address the cyclic strain-hardening of the beam flexural bars. The test strengths  $P_u$  in Table 8-2 were used for the shear force  $V_c$  of the columns.

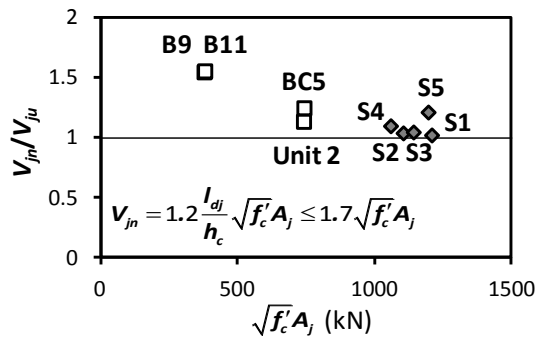


Fig. 8-9 (a) shows the joint shear capacity-to-demand ratios  $V_{jne}/V_{ju}$  of test specimens with strengthening bars, where  $V_{jne}$  indicates the joint shear strength specified in ACI 352R-02 (2002):  $V_{jne} = 1.2\sqrt{f'_c}A_j$ . The test specimens included existing specimens B9, B11, Unit 2, BC5 (refer to Table 8-3) used in previous studies (Galunic et al. 1977; Park and Milburn 1983; Joh et al. 1991), as well as S1 – S5 tested in this study. In the majority of the test specimens, the  $V_{jne}/V_{ju}$  ratios were less than 1.0, which indicates that the specimens were expected to be unsafe against the joint shear demand. However, in reality, joint shear failure did not occur in all the test specimens.

Fig. 8-9(b) shows the modified joint shear capacity ratios of the test specimens,  $V_{jn}/V_{ju}$ , where  $V_{jn}$  indicates the modified joint shear strength (Eq. (8-2)). As shown in the figure, in all specimens, the  $V_{jn}/V_{ju}$  ratios were greater than 1.0, which agree with the test results which did not show joint shear failure. This result indicates that the modified definition  $V_{jn} (= \beta\gamma\sqrt{f'_c}A_j \leq 1.7\sqrt{f'_c}A_j)$  can be safely used to define the joint shear strength. However, since the purpose of the existing tests was not the investigation of the joint shear strength, further studies are required to accurately define the joint shear strength enhanced by strengthening bars. It is noted that in the majority of the test specimens, the product  $\beta\gamma$  in Eq. (8-2) was limited by the maximum value 1.7 (see  $\beta\gamma$  in Table 8-1).



(a) Existing joint shear strength (ACI 352R-02)



(b) Proposed joint shear strength

Fig. 8-9. Shear strength of beam-column joints with strengthening bars

#### 8.4.4 Secant Stiffness and Energy Dissipation Capacity

ACI 374.1-05 (2005) specifies that, as an acceptance criterion for the beam-column connection subjected to cyclic loading, the secant stiffness from -0.35 % to +0.35 % drift ratio should not be less than 0.05 times the initial stiffness. Table 8-2 compares the initial stiffness  $k_i$ , the secant stiffness  $k_s$ , and the ratio ( $=k_s/k_i$ ). The  $k_i$  and  $k_s$  were calculated according to ACI 374.1-05 (2005), and  $k_s$  was evaluated for the third load cycle at 3.5 % drift ratio. The  $k_s$

$/k_i$  ratio of S1 was 0.03, which was less than the acceptance criterion 0.05. On the other hand, the ratios of S2, S3, S4, and S5 were 0.07 - 0.13 which satisfied the criterion.

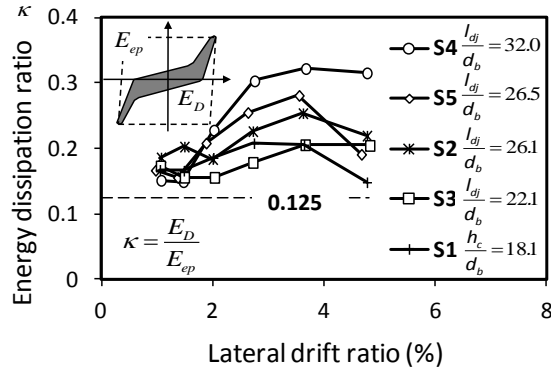
Fig. 8-10(a) shows the energy dissipation ratios  $\kappa$  at each drift level. The energy dissipation ratio  $\kappa$  was defined as the ratio of the actual energy dissipation  $E_D$  per load cycle (i.e. the area enclosed by a complete load cycle at each drift ratio) to the idealized elastic-perfectly plastic energy dissipation  $E_{ep}$ :  $\kappa = E_D / E_{ep}$  (see Fig. 8-10(a), ACI 374.1-05, 2005). The  $\kappa$  values were estimated for the third load cycle at each drift level. In Fig. 8-10(a), the  $\kappa$  values increased with the lateral drift ratios until 3.5 %. ACI 374.1-05 (2005) requires that the  $\kappa$  values at a given drift ratio, which is not less than 3.5 %, should not be less than 0.125. As shown in Fig. 8-10(a), all specimens satisfied the minimum requirement of ACI 374.1-05 (2005). The modified development length-to-bar diameter ratios of beam bars,  $l_{dj} / d_b$ , are also presented in Fig. 8-10(a). Apparently, the  $\kappa$  values increased as the  $l_{dj} / d_b$  ratios increased. S4 with the greatest  $l_{dj} / d_b$  ( $= 32.0$ ) showed the greatest  $\kappa$  value.

To further investigate the correlation between the modified development length  $l_{dj}$  and the energy dissipation capacity, the energy dissipation ratios  $\kappa$  of existing test specimens with or without strengthening bars were plotted in Fig. 8-10(b) with respect to the bond parameter (Beckingsale, 1980; Stevenson, 1980; Otani et al., 1984; Xian et al., 1992; Teraoka et al., 1994; Warcholik and Priestley, 1997; Pampanin et al., 2002; Teng and Zhou, 2003; Oka and Shiohara, 2004; Kusahara et al., 2004; Brooke et al., 2006; Kusahara et al.,

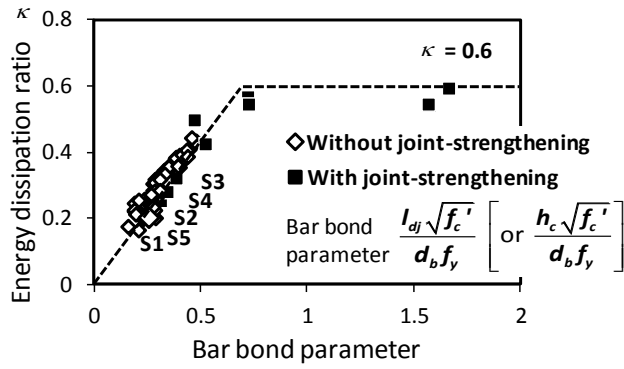
2010; Hwang et al., 2011). For the bond parameter of the specimens without strengthening bars,  $h_c(\sqrt{f_c}')/(d_b f_y)$  was used, while  $l_{dj}(\sqrt{f_c}')/(d_b f_y)$  was used for the specimens with strengthening bars. The bond parameter was defined considering the relevant provisions of ACI 318-11 (2011) and NZS 3101 (2006). The  $\kappa$  values were calculated at 3.5 % drift ratio or a drift ratio close to 3.5 %, as suggested in ACI 374.1-05 (2005). The bond parameters  $[l_{dj}(\sqrt{f_c}')/(d_b f_y)$  and  $h_c(\sqrt{f_c}')/(d_b f_y)]$  and the energy dissipation ratios  $\kappa$  of the specimens are presented in Tables 8-2 and 8-3.

In Fig. 8-10(b), for the specimens without strengthening bars, the  $\kappa$  values increased in proportion to the bond parameter  $(h_c/d_b)(\sqrt{f_c}'/f_y)$ , and the correlation was very good without significant scatters. Fig. 8-10(b) also shows the trend line and the correlation coefficients  $R^2$  defined by the method of least squares. The correlation coefficient was  $R^2 = 0.926$ , which indicates good correlation ( $R^2$  close to 1.0 indicates a strong correlation).

As shown in Fig. 8-10(b), the test results of the specimens with strengthening bars also follow the trend line. The  $\kappa - l_{dj}(\sqrt{f_c}')/(d_b f_y)$  relationship is the same as the  $\kappa - h_c(\sqrt{f_c}')/(d_b f_y)$  relationship. This result indicates that for the beam-column connections with strengthening bars, the modified development length  $l_{dj}$  can be used to define the bond parameter. However, in Fig. 8-10(b), the energy dissipation ratio is limited by  $\kappa = 0.6$ . This  $\kappa$  value is the possible maximum energy dissipation which can be developed by pure beam yielding mechanism without damage in the beam-column joint (ATC 40, 2006; Park and Eom, 2006; Eom and Park, 2010).



(a) Energy dissipation ratio vs. lateral drift ratio



(b) Energy dissipation ratio vs. bar bond parameter at joint

Fig. 8-10. Energy dissipation ratio of specimens

On the basis of the test results in Fig. 8-10(b), the energy dissipation ratio  $\kappa$  of the interior beam-column connections was defined as the linear function of the bond parameter  $(h_c/d_b)(\sqrt{f'_c}/f_y)$ , using the method of least squares.

$$\kappa = 0.80 \frac{h_c}{d_b} \frac{\sqrt{f'_c}}{f_y} + 0.053 \quad \left( 0.1 \leq \frac{h_c}{d_b} \frac{\sqrt{f'_c}}{f_y} \leq 0.6 \right) \quad (8-6)$$

For beam-column connections with strengthening bars, the bond parameter is replaced by  $l_{dj}(\sqrt{f_c})/(d_b f_y)$ . Eq. (8-6) can be used for energy performance-based design of beam-column connections with or without strengthening bars; for a given condition of strengthening bar, the energy dissipation capacity of the beam-column connection can be estimated from Eq. (8-6), and the result can be compared with the target energy dissipation ratio.

Table 8-3. Summary on existing test results (Continued)

Specimens		$f'_c$ (MPa)	$f_y$ (MPa)	$h_c/d_b$	$l_{dj}/d_b$	BP <sup>2)</sup>	$\kappa$ <sup>3)</sup>
Galunic et al. (1977)	BC5 <sup>1)</sup>	14.5	441	-	54.4	0.47	0.50
Beckingsale (1980)	B11	35.9	298	23.9	-	0.48	0.43
	B12	34.6	298	23.9	-	0.47	0.43
	B13	31.4	299	23.9	-	0.45	0.41
Warcholik et al. (1997)	6-1	49.6	645.9	21.8	-	0.24	0.26
Park and Milburn (1983)	Unit 1	41.3	315	25.5	-	0.52	0.43
	Unit 2 <sup>1)</sup>	46.9	307	-	70.3	1.57	0.55
Pampanin et al. (2002)	C2	23.9	387	16.7	-	0.21	0.16
Yamamoto et al. (2008)	PP1 <sup>1)</sup>	69.0	361	-	72.3	1.66	0.59
Joh et al. (1991)	B1	21.3	371	23.6	-	0.29	0.26
	B2	20.8	371	23.6	-	0.29	0.20
	HL	27.4	404	23.6	-	0.31	0.32
	LH	26.9	404	23.6	-	0.30	0.32
	B9 <sup>1)</sup>	25.6	404	-	57.5	0.72	0.57
	B11 <sup>1)</sup>	25.9	404	-	57.5	0.72	0.55
Teraoka et al. (1994)	NO43	54.0	382	20.9	-	0.40	0.39
	NO47	54.0	382	20.9	-	0.40	0.35
	HNO1	88.2	611	25.2	-	0.39	0.38
	HNO3	88.2	441	18.0	-	0.38	0.38
Xian et al. (1992)	U1	30.9	453	37.5	-	0.46	0.44
	U2	40.8	445	28.3	-	0.41	0.36
	U3	42.5	445	28.3	-	0.41	0.39
	U4	47.2	445	28.3	-	0.44	0.40
	U5	60.7	492	22.5	-	0.36	0.36
	U6	59.3	492	22.5	-	0.35	0.35
Stevenson (1980)	U1	34.0	337.8	25.5	-	0.44	0.39
Otani et al. (1984)	J1	25.7	401	23.6	-	0.30	0.29
	J2	24.0	401	23.6	-	0.29	0.32
	J3	24.0	401	23.6	-	0.29	0.30
Teng et al. (2003)	S1	33.0	510	18.9	-	0.21	0.23
	S2	34.0	510	18.9	-	0.22	0.21
	S3	35.0	510	18.9	-	0.22	0.22
	S5	39.0	425	15.8	-	0.23	0.20
	S6	38.0	425	15.8	-	0.23	0.21
Oka et al. (2004)	J1	81.2	638	23.6	-	0.33	0.33
	J7	79.2	676	23.6	-	0.31	0.32
	J9	79.2	676	23.6	-	0.31	0.28
	J10	39.2	700	23.6	-	0.21	0.26
Hwang et al. (2011)	S1	32.0	520	24.8	-	0.27	0.27
	S2	32.0	710	24.8	-	0.20	0.21
	S3	32.0	710	20.3	-	0.16	0.17

Table 8-3. Summary on existing test results

Specimens		$f'_c$ (MPa)	$f_y$ (MPa)	$h_c/d_b$	$l_{dj}/d_b$	BP <sup>2)</sup>	$\kappa$ <sup>3)</sup>
Brooke et al. (2006)	1B	31.2	552	31.5	-	0.32	0.33
	2B	40.6	552	31.5	-	0.36	0.35
	3B	44.8	537	26.6	-	0.33	0.34
	4B	42.8	537	26.6	-	0.32	0.33
Kusuhara et al. (2010)	B01	29.0	378	18.9	-	0.27	0.25
	B02	29.0	378	18.9	-	0.27	0.27
	B03	29.0	425	15.1	-	0.19	0.24
	B04	29.0	378	18.9	-	0.27	0.23
	B05	29.0	378	18.9	-	0.27	0.24
	B06	29.0	378	18.9	-	0.27	0.23
	B07	29.0	378	18.9	-	0.27	0.26
	B08	29.0	378	18.9	-	0.27	0.26
	B09	29.0	425	15.1	-	0.19	0.22
	B10	29.0	425	15.1	-	0.19	0.22
	C01	31.0	378	18.9	-	0.28	0.28
	C03	31.0	378	18.9	-	0.28	0.30
	D09	32.9	378	18.9	-	0.29	0.31
	D10	32.9	378	18.9	-	0.29	0.28
	D11	32.9	378	18.9	-	0.29	0.22
	E03	61.4	425	15.1	-	0.28	0.23
Kusuhara et al. (2004)	JE0	27.0	387	29.5	-	0.40	0.36

<sup>1)</sup> Connection specimens with joint-strengthening methods

<sup>2)</sup> Bond parameter  $h_c(\sqrt{f'_c})/(d_b f_y)$  or  $l_{dj}(\sqrt{f'_c})/(d_b f_y)$

<sup>3)</sup> Energy dissipation ratio at  $\delta = 3.5\%$  or the closest  $\delta$  to 3.5%.



## 8.5 Deformations at Beam-Column Joints

### 8.5.1 Re-bar Strain

Fig. 8-11 shows the strains of the beam flexural bottom bars in the beam-column joints. The vertical and horizontal axes indicate the re-bar strains and the distances from the center of the joints, respectively. Due to the malfunction of the strain gauges, the re-bar strains were measured until the drift ratio of  $\delta = 2.7\%$ . The strain profiles of the re-bars along the joint depth ( $= h_c$ ) correspond to the negative loading (see Fig. 8-11). As shown in Fig. 8-11(a), in S1 without strengthening bars, the strains of the beam re-bars were in tension and compression at the left and right column faces, respectively, until  $\delta = 1.47\%$ . However, as the drift ratio increased further to  $2.0\%$ , the strains of the beam re-bars at the left column face significantly exceeded the yield strain in tension. At  $\delta = 2.73\%$ , all the re-bar strains in the entire joint depth remained in tension, which indicates that complete bond-failure occurred in the joint after  $\delta = 2.73\%$ .

In S2 - S5 with strengthening bars, the strains of the beam re-bars at the left and right column faces were significantly less than those of S1 (see Fig. 8-11, note that the scales of the vertical axes are different). At  $\delta = 2.71\%$ , the maximum strains of S2 and S3 with the  $45^\circ$  bent bars were 0.0043 and 0.0034, respectively, which were slightly greater than the yield strain ( $\epsilon_y = 0.0023$ ). In S4 and S5 with the  $90^\circ$  hooked bars, the re-bar strains were even less (see Figs. 8-11(d) and (e)). This result indicates that bond-slip in the joints was

significantly reduced by the strengthening bars, particularly by using the 90° hooked bars. In the case of S3 using a smaller column depth, all re-bar strains in the joint were in tension, which indicates that the joint was subjected to yield penetration. Nevertheless, the re-bar strains were less than those of S1, because the  $l_{dj}/d_b$  ratio of S3 (= 22.1) was greater than the  $h_c/d_b$  ratio of S1 (= 18.1) (compare Figs. 8-11(a) and (c)).

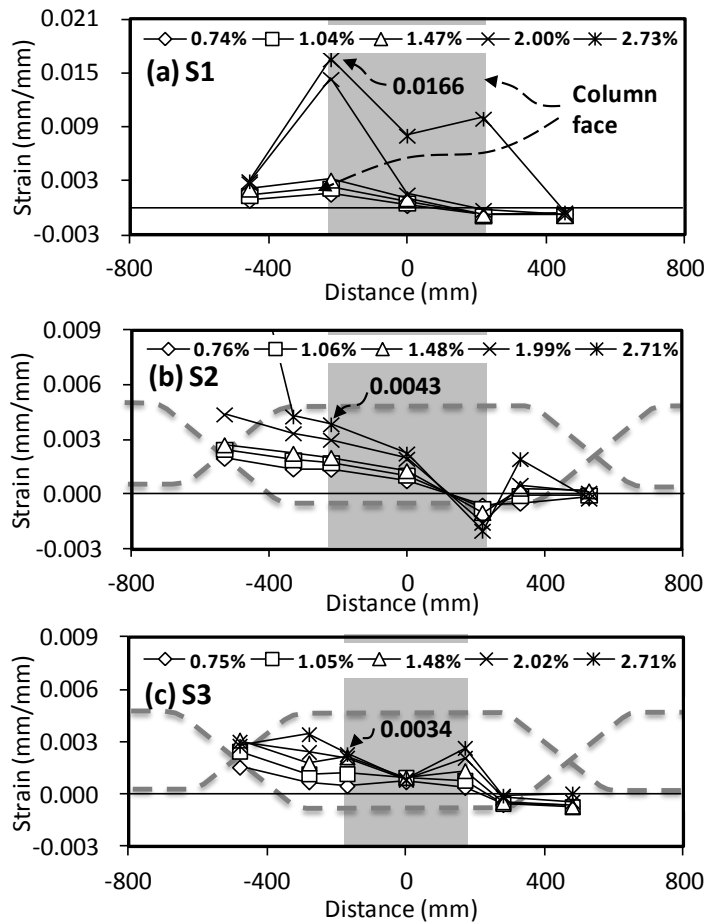


Fig. 8-11. Strains of beam flexural bars (Continued)

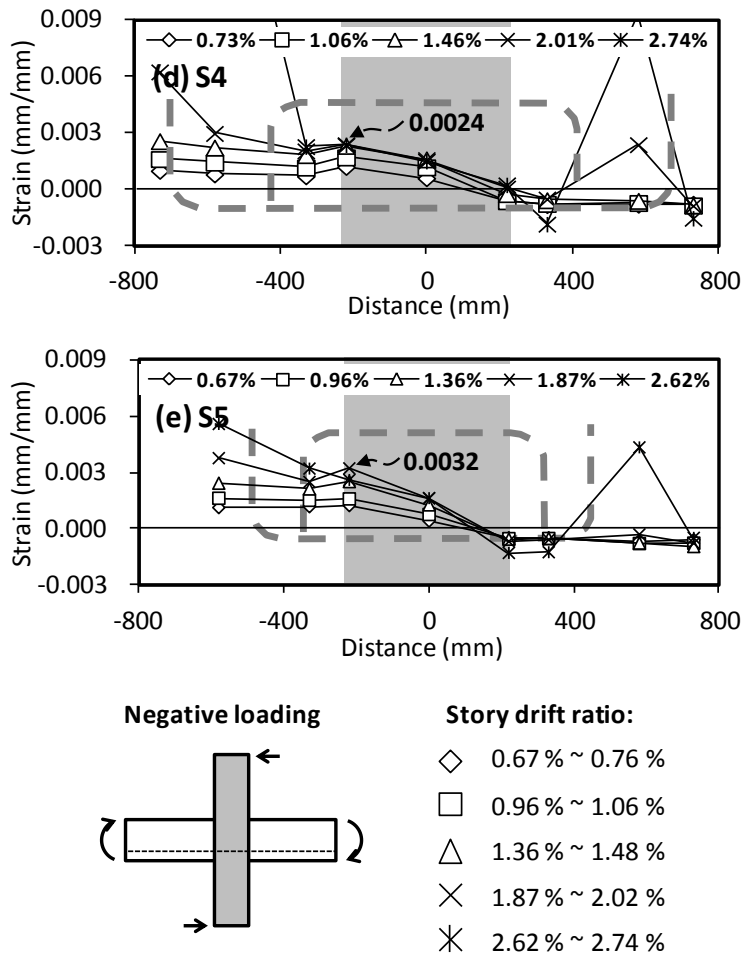


Fig. 8-11. Strains of beam flexural bars

Fig. 8-12 shows the strains of the strengthening bars (i.e. the  $45^\circ$  bent bars and  $90^\circ$  hooked bars) placed in the bottom of the joints. The strain profiles of the strengthening bars at each drift level correspond to the negative loading. In S2 and S3, at  $\delta = 2.71\%$ , the strains of the  $45^\circ$  bent bars at the column faces were greater than the yield strain. This result indicates that, unlike the  $90^\circ$  hooked bars, the  $45^\circ$  bent bars significantly contributed to the

beam flexural capacity of S2 and S3. On the other hand, in S4 and S5 using the 90° hooked bars, the strains of the hooked bars at the column faces were less than the yield strain (see Figs. 8-12(c) and (d)).

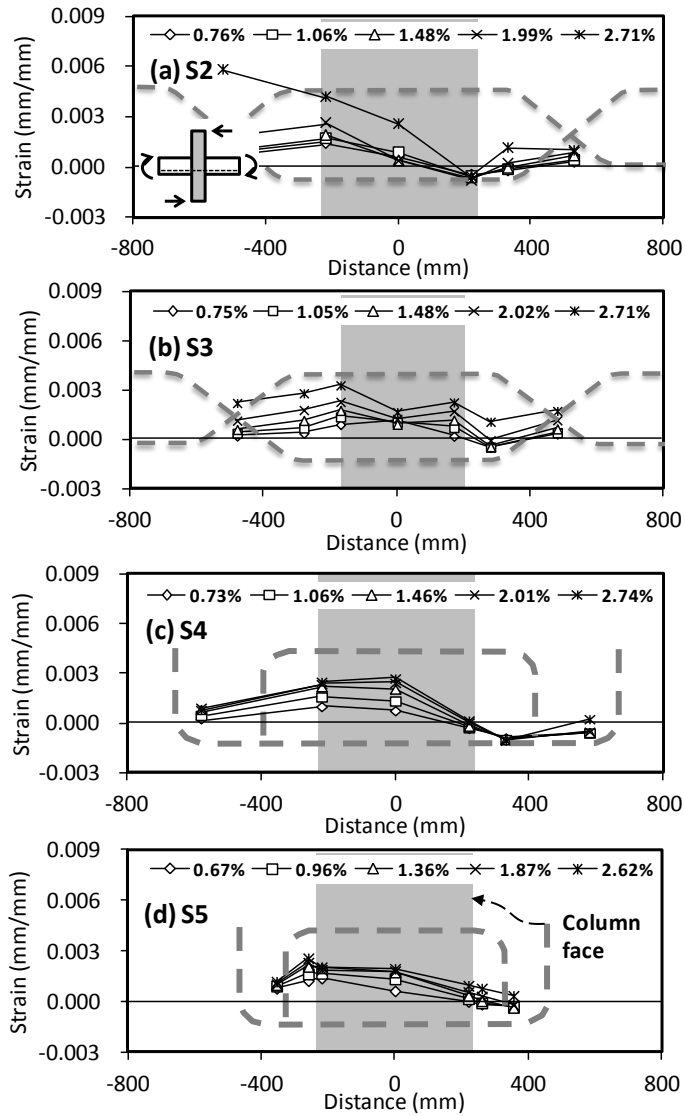


Fig. 8-12. Strains of strengthening bars

### 8.5.2 Shear Deformation

Fig. 8-13 shows the variation of the joint shear deformation  $\gamma_j$  according to the lateral drift ratio. The joint shear deformation was calculated using the diagonal elongation and shortening measured from LVDTs (refer to  $e_j$  and  $e_j'$  in Fig. 8-13, Lin, 2000). In S2, the measurement was stopped at  $\delta = 1.99\%$  due to unexpected malfunction of the LVDTs. As shown in Fig. 8-13, relatively large shear deformations occurred in S1, S2, and S3 where diagonal shear cracking was significant at the joints (refer to Figs. 8-7(a), (b), and (c)). Particularly, the joint shear deformation was the greatest in S1 which showed significant bar bond-slip. On the other hand, in S4 and S5 with  $90^\circ$  hooked bars, joint shear deformation was not significant even at large drift ratios. In the specimens with the strengthening bars, except S2, the joint shear deformations remained almost uniform at large inelastic drift ratios greater than  $3.0\%$  (see Fig. 8-13). This is because the majority of the plastic deformations was concentrated at the relocated plastic hinge zones of the beams, rather than at the joints. On the other hand, the joint shear deformation of S1 without the strengthening bar increased proportionally to the drift ratio until  $4.5\%$ .

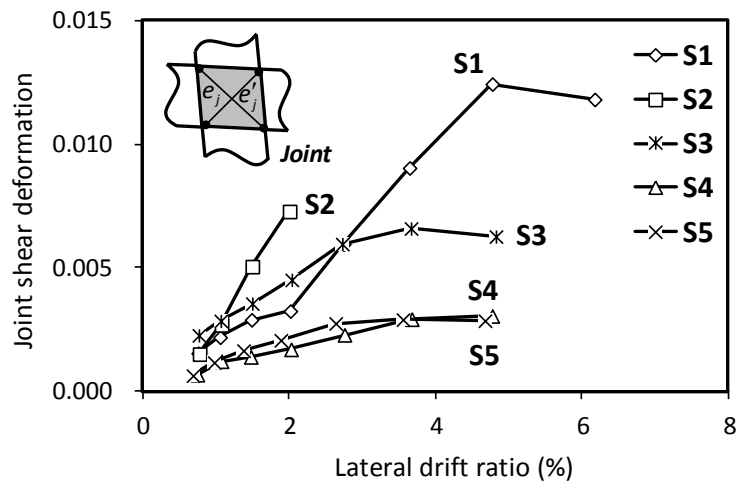


Fig. 8-13. Shear deformation at beam-column joints

## 8.6 Design Recommendations

On the basis of the test results and investigations reported in the present study and previous studies, considerations for the seismic design of interior beam-column connections with strengthening bars are recommended as follows.

- 1) The area of the strengthening bars (45° bent bars and 90° hooked bars) should be determined such that the beam flexural capacity  $M_{nj}$  (or  $M_{nj}'$ ) at the column face is not less than the demand corresponding to the flexural capacity  $M_n$  (or  $M_n'$ ) at the relocated critical section (see Eq. (8-1) and Fig. 8-2). It is also recommended that the total area of the 45° bent bars and 90° hooked bars be greater than at least 25 % of the total area of the beam flexural bars, considering cyclic strain hardening and.
- 2) In beam-column joints, the development length of beam flexural bars can be increased to the modified development length  $l_{dj}$ , which is defined as the least length of the straight part of the strengthening bars. Thus, for the evaluation of bond-resistance according to ACI 318-11 (2011) and ACI 352R-02 (2002), the  $l_{dj}/d_b$  ratio can be used (instead of using  $h_c/d_b$ ).
- 3) The joint shear demand  $V_{ju}$  at the column face should be evaluated using the flexural capacities  $M_n$  and  $M_n'$  of the relocated critical sections. Addressing the enhanced bond resistance, the shear strength of cruciform

beam-column joints can be increased to  $V_{jn} = \beta\gamma\sqrt{f'_c}A_j$  where  $\gamma = 1.2$ ,  $\beta = l_{dj}/h_b$ , and  $\beta\gamma \leq 1.7$ .

- 4) Unlike the 90° hooked bars, the 45° bent bars significantly contribute to the flexural capacity in the beam plastic hinge zone, which causes significant over-strength in the beam-column joints. The effect of the over-strength should be addressed in the flexural and shear design of the beam, column, and joint.
- 5) In the case of 45° bent bars, the minimum distance of the beam critical section from the column face can be decreased to the greater of 300 mm and  $0.60h_b$ , which is less than the requirement of NZS 3101:2006 (2006), the greater of 500 mm and  $h_b$ .
- 6) In the case of the 90° hooked bars, the minimum distance of the beam critical section from the column face can be decreased to the greater of 106 - 231 mm and  $0.21 - 0.46h_b$  (conservatively the greater of 231 mm and  $0.46h_b$ ), which is less than the requirement of NZS 3101:2006 (2006), the greater of 500 mm and  $h_b$ . In this case, it is recommended that as illustrated in Fig. 8-2(b), the end hooks of the top and bottom 90° hooked bars be anchored at different locations in order to mitigate the concentration of plastic deformation and anchoring force. The length of the bottom 90° hooked bars needs to be longer than that of the top bars. In this study, the minimum distance between the top and bottom anchorage hooks was 125 mm.



- 7) The development length of the  $90^\circ$  hooked bars from the column face to the end hook can be decreased to  $4.2d_b$  ( $= 106$  mm), which is less than the minimum requirement,  $8d_b$  and  $150$  mm, specified in ACI 318-11 (2011).
- 8) To prevent premature concrete failure and to enhance the bond strength of the strengthening bars, the hoop spacing in the beam plastic hinges is recommended to be decreased to  $100$  mm ( $= 0.22d$ ) for the  $45^\circ$  bent bars and  $50$  mm ( $= 0.11d$ ) for the  $90^\circ$  hooked bars, respectively ( $d$  = effective depth of the beam cross section).
- 9) For energy performance-based design of beam-column connections, Eq. (8-4) can be used. The energy dissipation ratio is related to the equivalent damping of structures showing inelastic deformation.

## 8.7 Discussion

In the present study, the strengthening methods for beam plastic hinge relocation in beam-column connections were studied. To study the details and design method of the strengthening bars, cyclic loading tests were performed for five cruciform beam-column connections with and without strengthening bars. For the strengthening methods, 45° bent bars and 90° hooked bars were used. The results of this study are summarized as follows.

- 1) In S1 without strengthening bars ( $h_c/d_b = 18.1$ ), significant bond-slip and diagonal cracking occurred at the beam-column joint. Ultimately, S1 failed due to concrete crushing at the column face. On the other hand, in S2 - S5 with strengthening bars ( $h_c/d_b = 14.2$  and  $18.1$ ), bar bond-slip and diagonal cracking were significantly decreased in the joint, though the  $h_c/d_b$  ratios were less than the minimum requirements of ACI 318-11 (2011) and NZS 3101:2006 (2006).
- 2) Specimens S2 - S5 with strengthening bars exhibited significantly improved energy dissipation capacities as a result of the reduced bond-slip and diagonal cracking. However, the maximum drift ratios of S2 - S5, 4.57 - 4.83 %, were less than 6.20 % of S1 (without strengthening bars) which showed large bond-slip and shear deformation. The maximum strengths of S2 - S5, which were predicted on the basis of the relocated plastic hinge mechanism, correlated well with the test results.

- 3) Unlike the 90° hooked bars, the 45° bent bars significantly contributed to the beam flexural capacity at the critical section (i.e. plastic hinge zone). Thus, the maximum strengths of S2 and S3 with the 45° bent bars were 23 % greater than those of S4 and S5 with 90° hooked bars. As a result of the unnecessary over-strength, the joint shear demand force increased, and bond-slip and diagonal cracking increased.
- 4) S1 without strengthening bars did not satisfy the secant stiffness requirement of ACI 374.1-05 (2005). On the other hand, S2 - S5 with strengthening bars satisfied the secant stiffness requirement. All specimens including S1 satisfied the energy dissipation requirement of ACI 374.1-05 (2005).
- 5) To address the enhanced bond resistance, the development length of beam flexural bars was defined as the length of the straight part of the strengthening bars, which is greater than the column depth  $h_c$ . Existing test results showed that the relationship between the energy dissipation ratio and the modified development length was the same as that of specimens without strengthening bars. This result indicates that for the design of connections with strengthening bars, the bond parameter can be defined as  $l_{dj}/d_b$  rather than the conventional parameter  $h_c/d_b$ .
- 6) On the basis of existing test results, the energy dissipation ratio of beam-column connections was defined as the function of the bond parameter  $l_{dj}\sqrt{f_c'}/(d_b f_y)$ , considering the increased development length  $l_{dj}$ . The design

equation can be used for the performance-based design of beam-column connections with strengthening bars.

- 7) To address the enhanced shear strength, the shear strength of cruciform beam-column connections was defined as  $V_{jn} = \beta \gamma \sqrt{f'_c} A_j$  modifying the provision of ACI 318-11 (2011). Existing test results showed that the modified joint shear strengths can be safely used.

On the basis of the test results and investigations, considerations for the design and detailing for the strengthening bars were recommended.

## **Chapter 9. Summary and Conclusions**

### **9.1 Summary**

Analytical and experimental studies of reinforce concrete (RC) beam-column connection were conducted to evaluate structural performance of the joint in this dissertation. To improve the structural performance of beam-column connections, high-strength re-bars were applied to beam flexural bars. On the basis of existing test results, to predict the structural performance capacity of beam-column connections, relationship between bond-slip and bond-strength for beam-column connection was proposed. Using the proposed bond-slip model, joint shear strength capacity and deformation capacity were evaluated. To predict the structural performance demand of moment frame structures, energy-based hysteresis models for interior and exterior beam-column connections were developed. Using the energy-based model, nonlinear time history analysis for moment frame structures was performed to predict earthquake response with respect to hysteretic behavior of the joint. Finally, design recommendation for beam-column connections with the strengthening methods to enhance the structure performance was proposed. As the earthquake demand and capacity of the moment frame structure with RC joint are accurately estimated, performance based earthquake design can be applied to the RC moment frames.

An experiment study was performed to investigate the validity of high

strength re-bars on the structural performance of beam-column connections. To evaluate the structural performance of beam-column connections, full scale four cruciform interior connections and three T-shaped exterior connections using Grade 400 or 600 bars were designed as part of the special moment frame and were tested under cyclic lateral loading. In the case of the interior connections, the load-carrying capacity and maximum deformation were close to those of the specimen with 400 MPa bars. On the other hand, the energy dissipation capacity of the specimens with 600 MPa bars decreased by a maximum of 25% due to the increased bond-slip at the joints. In the case of the exterior connections, significant bond-slip occurred at the beam bottom bars due to insufficient development length, which decreased the deformation capacity and energy dissipation capacity of the specimens. Except the exterior beam-column connection with insufficient tension and compression development length, however, all beam-column connections using Grade 600 bars satisfied the structural performance requirements specified on ACI 374.1-05.

For performance based design to satisfy ductility demand of RC beam-column connections, joint shear deformation and load-carrying capacity depending on bar bond-slip for interior beam-column connection was studied. Because existing bond models were not appropriate for beam-column connections, on the basis of cyclic test results of 67 existing beam-column joint, bond stress and bond failure mechanism were redefined, and the simplified bond strength model and bond-slip relationship of re-bar in interior beam-column joint subjected to cyclic loading were developed. Then, on the

basis of existing theories and test results, joint deformation based shear strength evaluation model was developed. The prediction results were compared with test results. The proposed shear strength model for beam-column connection evaluates the joint deformation capacity addressing bond-slip and joint bars details.

For performance based design to predict ductility demand of moment frame structures, an analytical study was performed to estimate the hysteretic behavior of beam-column connections and nonlinear response of moment frame structures. To evaluate the earthquake response in building structure level, a beam-column connection model which can be conveniently used for practical design/analysis of reinforced concrete moment frames was developed. By analyzing the cyclic test results of 69 interior and 63 exterior beam-column connections, a design equation was developed to accurately predict the energy dissipation capacity, using bar bond-slip parameters which are used in current design codes. Modifying pinching 4 model of OpenSees, energy-based hysteresis model was developed. The proposed hysteresis model can directly and accurately define the cyclic load-displacement relationship of beam-column connections. The predictions of cyclic behaviors were compared with test results of beam-column connections. Using the developed energy-based model with various energy dissipation capacities, nonlinear dynamic analysis was performed for three types of low-rise moment frame structures.

Finally, an experiment study was performed to improve structure

performance of RC beam-column connections using strengthening methods. To verify the effect of strengthening methods using  $45^\circ$  bent bars and  $90^\circ$  hooked bars in the joints, full scale five cruciform interior connections were designed with small  $h_c/d_b$  ratios less than 20 and were tested under cyclic lateral loading. On the basis of the test results and investigations, considerations for the design and detailing for the strengthening bars were recommended.



## **9.2 Conclusions**

In this dissertation, performance based earthquake design/analysis methods for reinforced concrete beam-column connections were studied. Full scale twelve beam-column connection specimens were tested for cyclic lateral loading. On the basis of the test results and existing test results, for predictions of structural performance capacity of beam-column connections, an evaluation model for joint shear strength and deformation capacity was developed. To estimate the structural performance demand of moment frame structures, an energy-based hysteresis model for nonlinear dynamic analysis of moment frames was developed, and nonlinear dynamic analysis was performed for three typed low-rise moment frame structures. Finally, to improve the structural performance of beam-column connections with insufficient earthquake structural performance, design recommendation for beam-column connections with the strengthening methods was proposed. The primary test results are summarized as follows.

### **9.2.1 Behavior of Beam-Column Connections**

- 1) In the interior connections with Grade 600 bars, the damage mode was diagonal cracking at the joint – yielding of beam flexural bars - bond-slip of beam flexural bars. Ultimately, concrete crushing occurred at the bottom of the beam end. This is because a large compressive force developed at the bottom of the beam end due to the asymmetric re-bar

layout and significant bond-slip. The damage and failure modes were the same as those of specimen with Grade 400 bars. However, in specimen with Grade 600 bars which had the smallest column depth ( $h_c/d_b = 20.5$ ), joint shear failure occurred after concrete delamination, because of the unsatisfactory joint shear strength. This result demonstrates the adequacy of the joint shear strength specified in ACI 318-11 (2011).

- 2) In the exterior connection with Grade 400 bars, the specimen failed due to concrete crushing at the bottom of the beam end. In specimens with Grade 600 bars, in addition to the concrete crushing at the beam bottom, concrete cover spalling and punching occurred at the location of the beam bottom bars in the exterior face of the column, due to the insufficient bar development length in compression. However, such negative effect of bond-slip was not observed in the beam top bars. Thus, the development length for beam bottom bars should be satisfied in compression as well as tension. In this case, the development length of 90° hook bars in ACI 318-11 (2011) needs to be revised.
- 3) In the evaluation by ACI 374.1-05 (2005), all specimens satisfied the requirements of deformation capacity and energy dissipation at 3.5% story drift ratio. However, neither the specimens with Grade 600 bars or Grade 400 bars satisfied the secant stiffness criteria.
- 4) At the 3.5% story drift angle, the hysteretic energy dissipation of the interior connections with Grade 600 bars was 7% - 25% less than that of

the interior connection with Grade 400 bars, due to the less rebar area and the increased bond-slip. The hysteretic energy dissipation of the exterior connections with Grade 600 bars was only 42% - 58% of the exterior connection with Grade 400 bars, due to the insufficient bar development length.

- 5) In the test specimens, despite the absence of cross-ties, buckling did not occur in the beam longitudinal bars, and concrete spalling was not severe. However, the majority of inelastic deformation was caused by the bond-slip of the beam longitudinal bars, without significant flexural deformation of the beams. Thus, further study is required to confirm the need of cross-ties.
- 6) The test results herein are valid for the following design parameters: Grade 600 MPa bars for beam longitudinal re-bars; bar diameters less than 25 mm; beam re-bar ratios less than 1.30 %; and the column depth to bar diameter ratio  $h_c / d_b \geq 22$ .

### 9.2.2 Joint Shear Strength Depending on Bar Bond-Slip

- 1) To consider bond-slip of beam flexural bars in RC beam-column joint subjected to cyclic loading, strain distribution of re-bar due to yield penetration was proposed. For RC beam-column joint with complete bond failure, bond-slip is occurred without the load increment at unloading/reloading behaviors, and constant load is remained by residual friction bond stress  $\tau_u$ . On the basis of the hysteresis curves of the RC beam-column joint with complete bond failure,  $\tau_u$  was determined from joint hoop bar strength and joint shear demand force as well as concrete tensile strength. The residual friction bond stress  $\tau_u$  at the both sides of the joint was decreased equally by cyclic loading.
- 2) In the component test using concrete block and beam-column joint, the proposed model predicts well the bond-slip, bond stress degradation, strain distribution, and elongation of the re-bar subjected to cyclic loading. On the basis of the bond stress model, joint depth-to-diameter of beam flexural bar ratio  $h_c/d_b$  was proposed to restrain the bond-slip of re-bar. As concrete strength increases, the requirement of  $h_c/d_b$  was decreased, and as the ductility demand of a beam increases, the requirement of  $h_c/d_b$  was increased. Particularly, the proposed equation at curvature ductility demand 6 and 9 was similar to the requirements specified on NZS 3101:2006 (2006) and Eurocode 8 (2004), respectively.
- 3) In RC beam-column connections subjected to cyclic loading, joint shear

strength by truss mechanism is significantly decreased by bond strength degradation. In diagonal strut mechanism, bond-slip expands cracking width of the strut, and reduces the effective compressive strength of the diagonal strut. At the same time, beam tensile bars are anchored to compression zone of opposite beam by bond-slip, and the beam compression zone increased. As a result, the strength degradation of the diagonal strut is mitigated, and most of joint shear strength is developed by the diagonal strut. Particularly, in the joint with small column depth, bond-slip is increased, and premature shear failure occurs in the joint due to the reduced contribution of truss mechanism.

- 4) Predictions of joint shear strength and column lateral demand according to story drift ratio were compared with hysteresis response of beam-column connections with joint shear failure. The proposed model predicted well the joint shear strength degradation depending on bond-slip of beam tensile bars and failure mode.

### 9.2.3 Dynamic Response of Structures Using Energy-Based Model

- 1) The energy dissipation capacity of interior and exterior connections correlated better with the bond resistance of beam flexural bars at the joints. Thus, the energy dissipation ratios  $\kappa$  of interior and exterior connections were defined as the linear functions of the bond parameters of beam flexural bars,  $(h_c/d_b)(\sqrt{f'_c}/f_y)$  and  $(l_{dh}/d_b)(\sqrt{f'_c}/f_y)$ , respectively.
- 2) The energy-based hysteresis model was defined such that the area enclosed by the cyclic curve was the same as the predicted energy dissipation capacity. The unloading and reloading behaviors, pinching, and strength- and stiffness-degradations under cyclic loading were described by using the functions of the energy dissipation ratio  $\kappa$  and the loading history. To simulate the cyclic responses of the connections including the joint responses, a lumped plasticity model incorporating with the energy-based hysteresis model was investigated.
- 3) The proposed method was applied to existing test specimens. The results showed that the predicted cyclic responses by the proposed method correlated well with the test results of the interior and exterior connections, which range from significantly-pinched cyclic curves, to less-pinched cyclic curves.
- 4) For three types of low-rise moment resisting frame structures, nonlinear time history analysis was performed using the energy-based model. In the

energy-based model, energy dissipation ratios  $\kappa = 0.2, 0.4, 0.6$ , and  $1.0$  (elasto-perfectly plastic) and  $\kappa = 0.4$  and  $1.0$  were applied to beam-column connections and columns on ground, respectively. As a ground motion for dynamic analysis, El-Centro earthquake acceleration, which was increased two to four times the structure yield strength, was applied. During dynamic analysis, second effect ( $P-\Delta$  effect) due to gravity load and current state stiffness for Rayleigh damping were considered.

- 5) Energy dissipation capacity degradation at the joint increases the lateral drift and ductility demand of moment frame structures. Furthermore, in the short period, the lateral drift was increased. For larger yield strength reduction factor, structure performance was greatly affected by the energy dissipation capacity of the structure.

### 9.2.4 Design Recommendations for Strengthening Methods

- 1) In specimen without strengthening bars, significant bond-slip and diagonal cracking occurred at the beam-column joint. Ultimately, S1 failed due to concrete crushing at the column face. On the other hand, in specimens with the strengthening bars, the bond-slip of the beam flexural bars and diagonal cracking at the joints were significantly decreased by the increased development length of the beam flexural bars, although the  $h_c/d_b$  ratios were less than the minimum requirements of ACI 318-11 (2011) and NZS 3101:2006 (2006). Thus, the use of strengthening bars contributes to prevent the bond-slip of beam flexural bars in the beam-column connection.
- 2) The maximum strengths of the specimens with the strengthening bars, which were predicted on the basis of the relocated plastic hinge mechanism, correlated well with the test results. Unlike the 90° hooked bars, however, the 45° bent bars significantly contributed to the beam flexural capacity at the critical section (i.e. plastic hinge zone). Thus, the maximum strengths of specimens with the 45° bent bars were about 23 % greater than those of specimens with 90° hooked bars. As a result of the unnecessary over-strength, as the joint shear demand force increased, the bond-slip and joint diagonal cracking was significant.
- 3) Specimens with the strengthening bars exhibited significantly improved energy dissipation capacities. The reason why is that the development



length of the beam flexural bars is increased to  $l_{dj}$  (= the least length of the straight part of the strengthening bars), which reduced the bond-slip and joint shear damage. Existing test results showed that the  $\kappa - l_{dj}\sqrt{f'_c}/(d_b f_y)$  relationship of specimens with strengthening bars correlated well with the  $\kappa - h_c\sqrt{f'_c}/(d_b f_y)$  relationship of specimens without strengthening bars. This result indicates that in the current design codes, the development length can be defined as  $l_{dj}/d_b$  rather than the conventional  $h_c/d_b$  ratio.

- 4) Existing test results showed that the shear strength  $V_{jn}$  of the cruciform beam-column joints with the strengthening bars can be increased to  $V_{jn} = \beta\gamma\sqrt{f'_c}A_j$  where  $\gamma = 1.2$  and  $\beta = l_{dj}/h_b$ , but the product  $\beta\gamma$  not greater than 1.7.

### 9.2.5 Performance Based Earthquake Design

For performance based earthquake design, in initial design step, column depth to beam bar diameter ratio  $h_c/d_b$  can be determined from the curvature ductility demand of a beam using the proposed bond requirement model in Chapter 3. On the basis of the designed beam-column connections, deformation capacity and joint shear capacity of beam-column connections are evaluated by the proposed joint shear strength evaluation model in Chapter 4. To predict the earthquake response of moment frame structures, energy dissipation ratio of beam-column connections is estimated by bond parameters, and cyclic behavior of beam-column connections is determined from the proposed energy-based hysteretic model in Chapters 5 and 6. Using the energy-based hysteretic model, the earthquake response of moment frame structures is evaluated by nonlinear time history analysis proposed in Chapter 7.

For performance improvement, strengthening bars can be applied to relocate plastic hinge in beam-column connections. Design recommendations for strengthening bars are given in Chapter 8. Furthermore, to improve the economics and constructability of beam-column connections, the use of high-strength re-bars, Grade 600 bars, in beam-column connections was verified in Chapter 2.

## References

- American Concrete Institute (ACI), “Building Code Requirements for Structural Concrete (ACI 318-11) and Commentary”, ACI Committee 318, 2011.
- ACI-ASCE Committee 352, “Recommendations for Design of Beam-Column Connections in Monolithic Reinforced Concrete Structures”, ACI 352R-02, *American Concrete Institute*, 2002, pp.1-37.
- ACI Committee 374, “Acceptance Criteria for Moment Frames Based on Structural Testing and Commentary”, ACI 374.1-05, *American Concrete Institute*, 2005.
- Adbel-Fattah, B., and Wight, J. K., “Study of Moving Beam Hinging Zones for Earthquake Resistant Design of R/C Buildings”, *ACI Structural Journal*, V. 84, No. 1, 1987, pp. 31-39.
- Alath, S., and Kunnath, S. K., “Modeling Inelastic Shear Deformation in RC Beam-Column Joints”, *Proceedings of the 10<sup>th</sup> Conference on Engineering Mechanics*, University of Colorado at Boulder, Colorado, 1995, pp. 822-825.
- Alsiwat, J. M., and Saatcioglu, M., “Reinforcement Anchorage Slip under Monotonic Loading”, *Journal of Structural Engineering*, ASCE, V. 118, No. 9, 1992, pp. 2421-2438.
- Altoontash, A., and Deierlein, G. D., “A Versatile Model for Beam-Column Joints”, *ASCE Structures Congress*, Seattle, WA, 2003.

- Anderson, M., Lehman, D., and Stanton, J., "A Cyclic Shear Stress-Strain Model for Joints Without Transverse Reinforcement", *Engineering Structures*, V. 30, No. 4, 2007, pp. 941-954.
- Applied Technology Council (ATC), "Seismic Evaluation and Retrofit of Concrete Buildings," *Redwood City, CA*, 1996.
- Asou, N., Nagashima, T., and Sugano, S., "Force Characteristic of Beam Column Connection using High Strength Concrete (Fc600) and Reinforcement (SD490) (in Japanese)", *Proceedings of the Japan Concrete Institute*, V. 15, No. 2, 1993, pp. 553-558.
- Beckingsale, C. W., "Post-Elastic Behaviour of Reinforced Concrete Beam-Column Joints", *Department of Civil Engineering, University of Canterbury*, Research Report No.80-20, 1980.
- Benavernt, C. A., Cahis, X., and Zahran, R., "Exterior wide beam-column connections in existing RC frames subjected to lateral earthquake loads", *Engineering Structures*, V. 31, No. 7, 2009, pp. 1414-1424.
- Birely, A. C., Lowes, L. N., and Lehman, D. E., "A Model for The Practical Nonlinear Analysis of Reinforced-Concrete Frames Including Joint Flexibility", *Engineering Structures*, V. 34, 2012, pp. 455–465.
- Birss, G. R., "The Elastic Behaviour of Earthquake Resistance Reinforced Concrete Interior Beam-Column Joints", *Research Report 78-13*, Department of Civil Engineering, University of Canterbury, Christchurch, 1978.
- Bonacci, J. and Pantazopoulou, S., "Parametric Investigation of Joint Mechanics", *ACI Structural Journal*, V. 90, No. 1, 1993, pp. 61-71.
- British Standards, "Eurocode 2: Design of concrete structures", *BS EN 1992-*

- 1-1:2004*, 2004, pp.1-225.
- British Standard, “Eurocode 8: Design of Structures for Earthquake Resistance”, *BS EN 1998-1:2004*, 2004.
- Brooke N. J., Megget L. M., and Ingham J. M., “Bond performance of Interior Beam-Column Joints with High-Strength Reinforcement”, *ACI Structural Journal*, V. 103, No. 4, 2006, pp. 596-603.
- Charney, F. A., “Unintended Consequences of Modeling Damping in Structures”, *Journal of Structural Engineering*, ASCE, V. 134, No. 4, 2008, pp. 581-592.
- Chopra, A. K., “Dynamics of Structures: Theory and Applications to Earthquake Engineering, 2<sup>nd</sup> Edition”, *Prentice-Hall, Inc.*, 2001.
- Chun, S. C., Lee, S. H., Kang, T. H. K., and Wallace, J. W., “Mechanical Anchorage in Exterior Beam-Column Joints Subjected to Cyclic Loading”, *ACI Structural Journal*, V. 104, No. 1, 2007, pp. 102-112.
- Chutarat, N. and Aboutaha, R. S., “Cyclic Response of Exterior Reinforced Concrete Beam-Column Joints Reinforced with Headed Bars Experimental Investigation”, *ACI Structural Journal*, V. 100, No. 2, 2003, pp. 259-264.
- Ciampi, V., Eligehausen, R., Bertero, V. V., and Popov, E. P., “Analytical Model for Concrete Anchorages of Reinforcing Bars Under Generalized Excitations”, *Earthquake Engineering Research Council Rep. No. 82/23*, Univ. of California, Berkeley, Calif, 1982.
- Clough, R. W., “Effects of Stiffness Degradation on Earthquake Ductility Requirement”, *Rep. No. 6614*, Struct. and Mat. Res., University of California, Berkeley, Calif., 1966.

- Dai, R. and Park, R., "A comparison of the Behaviour of Reinforced Concrete Beam-Column Joints Designed for Ductility and Limited Ductility", *Research Report*, No. 87-4, Department of Civil Engineering, University of Canterbury, 1987.
- Durrani, A. J. and Wight, J. K., "Experimental and Analytical Study of Internal Beam to Column Connections Subjected to Reversed Cyclic Loading", *Report UmEE82R3*, Department of Civil Engineering, University of Michigan, Ann Arbor, 1982.
- Ehsani, M. R., "Behavior of Exterior Reinforced Concrete Beam to Column Connections Subjected to Earthquake Type Loading", *Report No. UMEE 82R5*, Department of Civil Engineering, University of Michigan, Ann Arbor, MI, 1982.
- Ehsani, M. R., Moussa, A. E., and Vallenilla, C. R., "Comparison of Inelastic Behavior of Reinforced Ordinary and High-Strength Concrete Frames", *ACI Structural Journal*, V. 84, No. 2, 1987, pp. 161-169.
- Ehsani, M. R. and Wight, J. K., "Exterior Reinforced Concrete Beam-to-Column Connections Subjected to Earthquake-Type Loading", *ACI Structural Journal*, V. 82, No. 4, 1985, pp. 492-499.
- Eligehausen, R., Popov, E. P., and Bertero, V. V., "Local Bond Stress-Slip Relationships of Deformed Bars under Generalized Excitations", *Earthquake Engineering Research Council Rep. No. 83/23*, Univ. of California, Berkeley, Calif, 1983.
- El-Metwally, S. E., and Chen, W. F., "Moment-Rotation Modeling of Reinforced Concrete Beam-Column Connections", *ACI Structural Journal*, V. 85, No. 4, 1988, pp. 384-394.

- Elmorsi, M., Kianoush, M. R., Tso, W. K., "Modeling Bond-Slip Deformation in Reinforced Concrete Beam-Column Joints", *Canadian Journal of Civil Eng.*, V. 27, No. 3, 2000, pp. 490-505.
- Eom, T., Park, H., "Elongation of Reinforced Concrete Members Subjected to Cyclic Loading", *Journal of Structural Engineering*, ASCE, V. 136, No. 9, 2010, pp. 1044-1054.
- Eom, T., Park, H., "Evaluation of Energy Dissipation of Slender Reinforced Concrete Members and Its Applications", *Engineering Structures*, V. 32, No. 9, 2010, pp. 2884-2893.
- Eom, T., Park, H., "Evaluation of Shear Deformation and Energy Dissipation of RC Members Subjected to Cyclic Loading", *ACI Structural Journal*, in Press.
- Eom T., Park H., and Kang, S. "Energy-based cyclic force-displacement relationship for reinforced concrete short coupling beams", *Engineering Structures*, V. 31, No. 9, 2009, pp. 2020-2031.
- FEMA 273, "NEHRP Guidelines for the Seismic Rehabilitation of Buildings", *Federal Emergency Management Agency*, 1997.
- FEMA 356, "Prestandard and Commentary for the Seismic Rehabilitation of Buildings", *Federal Emergency Management Agency*, 2000.
- FEMA 440, "Improvement of Nonlinear Static Seismic Analysis Procedures", *Federal Emergency Management Agency*, 2005.
- Fenwick, R. C., and Irvine, H. M., "Reinforced Concrete Beam-Column Joints for Seismic Loading", *Department of Civil Engineering, University of Auckland*, Research Report 142, Auckland, New Zealand, 1997, pp. 1-50.
- Fischinger, M., Kramar, M., and Isaković, T., "Cyclic response of slender RC

- columns typical of precast industrial buildings," *Bulletin of Earthquake Engineering*, vol. 6, no. 3, pp. 519-534, 2008.
- Fleury, F., Reynouard, J. M., and Merabet, O., "Multi-Component Model of Reinforced Concrete Joints for Cyclic Loading", *Journal of Engineering Mechanics*, V. 126, No. 8, 2000, pp. 804-811.
- Franco, M. A. D., Mitchell, D., and Paultre, P., "Role of Spandrel Beams on Response of Slab-Beam-Column Connections", *Journal of Structural Eng.*, ASCE, V. 121, No. 3, 1995, pp. 408-419.
- Galunic, B., Bertero, V. V., and Popov, E. P., "An Approach for Improving Seismic Behavior of Reinforced Concrete Interior Joints", *Report of Earthquake Engineering Research Center, UCB/EERC-70/30*, 1977, pp. 1-94.
- Ghobarah, A., and Biddah, A., "Dynamic Analysis of Reinforced Concrete Frames Including Joint Shear Deformation", *Engineering Structures*, V. 21, No. 11, 1999, pp. 971-987.
- Hakuto, S., Park, R., and Tanaka, H., "Effect of Deterioration of Bond of Beam Bars Passing through Interior Beam-Column Joints of Flexural Strength and Ductility", *ACI Structural Journal*, V. 96, No. 5, 1999, pp. 858-864.
- Hayashi, K., Teraoka, M., Mollick, A. A., and Kana, Y., "Bond Characteristic of Interior RC Beam-Column Connections Using High Strength materials (in Japanese)", *Proceeding of the Japan Concrete Institute*, V. 15, No. 2, 1993, pp. 583-588.
- Hong, S. G., Lee, S. G., and Kang, T. H. K., "Deformation-Based Strut-and-Tie Model for Interior Joints of Frames Subject to Load Reversal", *ACI*



- Structural Journal*, V. 108, No. 4, 2011, pp. 423-433.
- Hwang, S. J., and Lee, H. J., “Analytical Model for Predicting Shear Strengths of Interior Reinforced Concrete Beam-Column Joints for Seismic Resistance”, *ACI Structural Journal*, V. 97, No. 1, 2000, pp. 35-44.
- Hwang, H. J., Eom, T. S., and Park, H. G., “Effect of Plastic Hinge Relocation on Bar Bond-Slip at Beam-Column Joint”, *ACI Structural Journal*, Reviewing.
- Hwang, H. J., Park, H. G., Choi, W. S., Kim, J. K., and Chung, L., “Seismic Performance of Beam-Column Connections for Special Moment Frame using 600 MPa Flexural Reinforcement (in Korean)”, *KCI Journal*, V. 23, No. 5, 2011, pp.591-601.
- Hwang, H. J., Park, H. G., Choi, W. S., Chung, L., and Kim, J. K., “Cyclic Loading Test for Beam-Column Connections with 600 MPa Beam Flexural Re-bars”, *ACI Structural Journal*, Reviewing.
- Ibarra, L. F., Medina, R. A., and Krawinkler, H., “Hysteretic Models that Incorporate Strength and Stiffness Deterioration”, *Earthquake Engineering & Structural Dynamics*, V. 34, No. 12, 2005, pp.1489-1511.
- Joh, O., Goto, Y., and Shibata, T., “Influence of Transverse Joint and Beam Reinforcement and Relocation of Plastic Hinge Region on Beam-Column Joint Stiffness Deterioration”, *ACI Special Publication*, SP 123-8, 1991, pp. 187-223.
- Kaku, T. and Asakusa, H., “Ductility Estimation of Exterior Beam-Column Subassemblages in Reinforced Concrete Frames”, *ACI Special Publication*, SP 123-7, 1991, pp. 167-185.
- Kaku, A., Maso, K., Kutoka, T., and Muguruma, T., “Experimental Study

- about deformation characteristic of beam column connection in RC structure (in Japanese)", *Proceedings of the Japan Concrete Institute*, V. 15, No. 2, 1993, pp. 559-564.
- Kawai, T., Kimura, H., Iwata, M., and Watai, T., "Experimental Study of Resistance Mechanism of RC Beam-Column Connections Using High Strength Materials (in Japanese)", *Proceeding of the Japan Concrete Institute*, V. 19, 1997, pp. 1011-1016.
- Kawasazaki, T., Kitayama, K., and Noguchi, H., "Bond characteristic of Reinforced Concrete beam-Column Connections using Ultra High Strength Materials (in Japanese)", *Proceedings of the Japan Concrete Institute*, V. 14, No. 2, 1992, pp. 397-400.
- Kitayama, K., Kojima, C., Otani, S., and Aoyama, H., "Behavior of Reinforced Concrete Interior Beam-Column Connection Subjected to High Shear (in Japanese)", *Proceedings of the Japan Concrete Institute*, V. 11, No. 2, 1989, pp. 531-536.
- Kitayama, K., Otani, S., and Aoyama, H., "Earthquake Resistant Design Criteria For Reinforced Concrete Interior Beam-Column Joints", *Pacific Conference on Earthquake Engineering, New Zealand*, V. 1, 1987, pp. 315-326.
- KS B 0802, "Method of Tensile Test for Metallic Materials", *Korean Agency for Technology and Standards*, 2008.
- Kunnath, S. K., "Macromodel-Based Nonlinear Analysis of Reinforced Concrete Structures", *Structural Engineering Worldwide*, No. T101-5, Oxford, England, Elsevier Science, Ltd., 1998.
- Kusuhara, F., Azukawa, K., and Shiohara, H., Otani, S., "Tests of Reinforced

- Concrete Interior Beam-Column Joint Subassemblage with Eccentric Beams”, *13th World Conference on Earthquake Engineering*, Canada, No. 185, 2004.
- Kusuhara, F., Shiohara, H., Tazaki, W., and Park, S., “Seismic Performance of Reinforced Concrete Interior Beam-Column Joint under Low Ratio of Column to Beam Moment Capacity”, *Journal of Structural and Construction Engineering (Transactions of AIJ)*, V. 75, No. 656, 2010, pp. 1873-1882. (in Japanese)
- Kwak, H., and Kim, S., “Nonlinear Analysis of RC Beam Subjected to Cyclic Loading”, *Journal of Structural Engineering*, ASCE, V. 127, No. 12, 2001, pp. 1436-1444.
- Lee, H. J. and Lin, Y. R., “Preliminary Design Recommendations for RC Beam-Column Joints with High-Strength Reinforcement”, *13th SEEBUS*, Seoul, Korea, 2011, pp. 1-10.
- Lee, J. Y., Kim, J. Y., and Oh, G. J., “Strength Deterioration of Reinforced Concrete Beam-Column Joints Subjected to Cyclic Loading”, *Engineering Structures*, V. 31, No. 9, 2009, pp. 2070-2085.
- Leon, R. T., “Interior Joints with Variable Anchorage Lengths”, *Journal of Structural Eng.*, ASCE, V. 115, No. 9, 1989, pp. 2261-2275.
- Leon, R., “Shear Strength and Hysteretic Behavior of Interior Beam-Column Joints”, *ACI Structural Journal*, V. 87, No. 1, 1990, pp. 3-11.
- Leon, R., “The Effect of Floor Member Size on the Behavior of Reinforced Concrete Beam-Column Joints”, *8<sup>th</sup> World Conference on Earthquake Engineering*, San Francisco, 1984, pp. 445-452.
- Li, B., Wu, Y., and Pan, T. C., “Seismic Behavior of Nonseismically Detailed

- Interior Beam-Wide Column Joints-Part 1: Experimental Results and Observed Behavior”, *ACI Structural Journal*, V. 99, No. 6, 2002, pp. 791-802.
- Lin, C. M., “Seismic Behaviour and Design of Reinforced Concrete Interior Beam Column Joints”, *Research Report*, No. 2000-1, Department of Civil Engineering, University of Canterbury, Christchurch, New Zealand, 2000.
- Lowes, L. N., Altoontash, A., “Modeling Reinforced-Concrete Beam-Column Joints Subjected to Cyclic Loading”, *Journal of Structural Eng.*, ASCE, V. 129, No. 12, 2003, pp. 1686-1697.
- Marti, P., Alvarez, M., Kaufmann, W., and Sigrist, V., “Tension Chord Model for Structural Concrete”, *Structural Engineering International*, V. 8, No. 4, 1998, pp. 287-298.
- Magliulo, G., and Ramasco, R., “Seismic Response of Three-Dimensional R/C Multi-Storey Frame Building Under Uni- and Bi-Directional Input Ground Motion”, *Earthquake Engineering and Structural Dynamics*, V. 36, No. 12, 2007, pp. 1641–1657.
- Mazzoni, S., McKenna, F., Scott, M. H., Fenves, G. L., “OpenSees Command Language Manual”, *The University of California*, 2006.
- Megget L. M., Fenwick R. C., and Amso N., “Seismic Performance of Internal Beam-Column Joints with 500 Grade Reinforcement”, *Pacific Conference on Earthquake Engineering, Christchurch, New Zealand*, 2003, pp. 1-10.
- Meinheit, D. F. and Jirsa, J. O., “Shear Strength of Reinforced Concrete Beam-Column Joints”, *Report No. 77-1, Department of Civil*

- Engineering, Structures Research Laboratory, University of Texas at Austin, TX, 1977.*
- Milburn, J. R. and Park, R., “Behaviour of R.C. Beam Column Joints Designed to NZS 3101”, *Research Report 82-7*, Department of Civil Engineering, University of Canterbury, Christchurch, 1982.
- Mitra, N., and Lowes, L. N., “Evaluation, Calibration, and Verification of A Reinforced Concrete Beam-Column Joint”, *Journal of Structural Eng.*, ASCE, V. 133, No. 1, 2007, pp. 105-120.
- Murakami, H., Fujii, S., Ishiwata, Y., and Morita, S., “Shear Strength and Deformation Capacity of Interior R/C Beam-Column Joint Subassembly”, *12<sup>th</sup> World Conference on Earthquake Engineering*, New Zealand, No. 679, 2000.
- Noguchi, H. and Kashiwazaki, T., “Experimental Studies on Shear Performances of RC Interior Column-Beam Joints with High-Strength Materials”, *10<sup>th</sup> World Conference on Earthquake Engineering*, Balkema, Rotterdam, 1992, pp. 3163-3168.
- NZS 3101:1995, “The Design of Concrete Structures”, *Standards New Zealand*, Wellington, New Zealand, pp.256.
- NZS 3101:2006, “The Design of Concrete Structures”, *Standards New Zealand*, New Zealand, pp.698.
- Oda, M., Kosugi, K., Yamanoka, H., and Tano, K., “Bond Characteristic of Flexural Beam Reinforcement in Beam Column Connection for High Strength Reinforced Concrete Structure (in Japanese)”, *Proceeding of the Japan Concrete Institute*, V. 19, No. 2, 1997, pp. 993-998.
- Oka, K. and Shiohara, H., “Tests of High-Strength Concrete Interior Beam-

- Column-Joint Subassemblages”, *10th World Conference on Earthquake Engineering*, Madrid, Spain, 1992, pp. 3211-3217.
- Otani, S., “Inelastic Analysis of R/C Frame Structures”, *Journal of the Structural Division*, ASCE, V. 100, No. 7, 1974, pp. 1433-1449.
- Otani, S., Kobayashi, Y., and Aoyama, H., “Reinforced Concrete Interior Beam-Column Joints Under Simulated Earthquake Loading”, *Proc. 1st US-NZ-Japan Seminar on Design of R.C. Beam-Column Joints*, Monterey, 1984.
- Pampanin, S., Calvi, G. M., and Moratti, M., “Seismic Behaviour of R.C. Beam-Column Joints Designed for Gravity Loads”, *12th European Conference on Earthquake Engineering*, Rotterdam, 2002.
- Park, H., and Eom, T., “A simplified method for estimating the amount of energy dissipated by flexure-dominated reinforced concrete members for moderate cyclic deformations”, *Earthquake Spectra*, V. 22, No. 2, 2006, pp. 459–490.
- Park, H., Yu, E., and Choi, K., “Shear-Strength Degradation Model for RC Columns Subjected to Cyclic Loading”, *Engineering Structures*, V. 34, 2012, pp. 187–197.
- Park, J., Yun, S., Kim, B., and Lee, J., “A Study for Shear Deterioration of Reinforced Concrete Beam-Column Joints Failing in Shear after Flexural Yielding of Adjacent Beams (in Korean)”, *Journal of the Korea Concrete Institute*, V. 24, No. 4, 2012, pp. 399–406.
- Park R., “State-of-the Art Report: Ductility Evaluation from Laboratory and Analytical Testing”, *Proceedings of 9<sup>th</sup> World Conference on Earthquake Engineering*, V. 8, 1988, pp. 605-616.

- Park, R. and Milburn, J. R., "Comparison of Recent New Zealand and United States Seismic Design Provisions for Reinforced Concrete Beam-Column Joints and Test Results for Four Units Designed According to the New Zealand Code", *Bulletin of the New Zealand National Society for Earthquake Engineering*, V. 16, No. 1, 1983, pp. 21-42.
- Park, R. and Paulay, T., "Reinforced Concrete Structures", *John Wiley & Sons, Inc.*, New York, 1975.
- Paulay, T., "Seismic Design of Concrete Structures: The Present Needs of Societies", *Proceedings of 11<sup>th</sup> World Conference on Earthquake Engineering*, Acapulco, Mexico, 1996.
- Paulay, T. and Priestley, M. J. N., "Seismic Design of Reinforced Concrete and Masonry buildings", *John Wiley & Sons, Inc.*, New York, 1992.
- Priestley, M. J. N., "Brief Comments on Elastic Flexibility of Reinforced Concrete Frames and Significance to Seismic Design", *Bulletin of the New Zealand National Society for Earthquake Engineering*, V. 31, No. 4, 1998, pp. 246-259.
- Priestley, M. J. N., "Performance Based Seismic Design", *Proceedings, 12<sup>th</sup> WCEE*, Auckland, New Zealand, No. 2831, 2000, pp. 1-22.
- Saatcioglu, M., "Modeling Hysteretic Force-Deformation Relationships for Reinforced Concrete Elements", *ACI Special Publication*, ACI, V. 127, 1991, pp. 153-198.
- Shima, H., Chou, L. L., and Okamura, H., "Bond Characteristics in Post-Yield Range of Deformed Bars", *Concr. Libraracy Jpn. Soc. Civ. Eng.*, V. 10, 1987, pp. 113-124.
- Shin, M. and LaFave, J. M., "Modeling of Cyclic Joint Shear Deformation

- Contributions in RC Beam-Column Connections to Overall Frame Behavior”, *Structural Engineering and Mechanics*, Vol. 18, No. 5, 2004, pp.645-669.
- Shiohara, H., “Comprehensive Series of Tests on Seismic Performance of Reinforced Concrete Interior Beam-Column Joints: Part 1”, *Seismic performance of concrete joints and connections, ACI Fall Convention*, 2010.
- Shiohara, H., “Comprehensive Series of Tests on Seismic Performance of Reinforced Concrete Interior Beam-Column Joints : Part 2”, *Seismic performance of concrete joints and connections, ACI Fall Convention*, 2010.
- Shiohara, H., “New Model for Shear Failure of RC Interior Beam-Column Connections”, *Journal of Structural Engineering*, ASCE, V. 127, No. 2, 2001, pp. 152-160.
- Shiohara, H., “Reinforced Concrete Beam-Column Joints: An Overlooked Failure Mechanism”, *ACI Structural Journal*, V. 109, No. 1, 2012, pp. 65-74.
- Shiohara, H., Zaid, S., and Otani, S., “Test of An Innovative Reinforcing Detail for R/C Interior Beam-Column Connections Subjected to Seismic Action”, *Proceedings of the Third International Conference on Concrete under Severe Conditions*, University of British Columbia, Vancouver, Canada, 2001, pp. 739-746.
- Sivaselvan, M. V., and Reinhorn, A. M., “Hysteretic Models for Deteriorating Inelastic Structures”, *Journal of Engineering Mechanics*, ASCE, V. 126, No. 6, 2000, pp. 633-640.



- Soleimani, D., Popov, E. P., and Bertero, V. V., “Hysteretic Behavior of Reinforced Concrete Beam-Column Subassemblages”, *ACI Structural Journal*, V. 76, No. 11, 1979, pp. 1179-1196.
- Song, J. K., and Pincheira, J. A., “Spectral Displacement Demands of Stiffness- and Strength-Degrading Systems”, *Earthquake Spectra*, V. 16, No. 4, 2000, pp. 817-851.
- Stevenson, E. C., “Fibre Reinforced Concrete in Seismic Design”, *Research Report*, No.80-7, Department of Civil Engineering, University of Canterbury, 1980.
- Sucuoğlu, H., Acun, B., “Energy-Based Hysteresis Model for Flexural Response of Reinforced Concrete Columns”, *ACI Structural Journal*, V. 109, No. 4, 2012, pp. 541-549.
- Sucuoğlu, H., and Erberik, A., “Energy-Based Hysteresis and Damage Models for Deteriorating Systems”, *Earthquake Engineering & Structural Dynamics*, V. 33, No. 1, 2004, pp.69-88.
- Sugano, S., Nagashima, T., Kimura, H., and Ichikawa, A., “Behavior of Beam-Column Joints Using High-Strength Materials”, *ACI Special Publication*, V. 123, 1991, pp.359-378.
- Susanto, T. and Hua, Z., “Eccentric Reinforced Concrete Beam-Column Joints Subjected to Cyclic Loading”, *ACI Structural Journal*, V. 100, No. 2, 2003, pp. 139-148.
- Takeda, T., Sozen, M. A., and Nielsen, N. N., “Reinforced Concrete Response to Simulated Earthquakes”, *J. Struct. Div.*, ASCE, V. 96, No. 12, 1970, pp. 2557-2573.
- Tateishi, M. and Ishibashi, K., “Experimental Study about Failure Type in

- Beam Column Connection after Reaching Yielding of Beam Reinforcement (in Japanese)", *Proceedings of the Japan Concrete Institute*, V. 20, No. 3, 1998, pp. 517-522.
- Teng, S. and Zhou, H., "Eccentric Reinforced Concrete Beam-Column Joints Subjected to Cyclic Loading", *ACI Structural Journal*, V. 100, No. 2, 2003, pp. 139-148.
- Teraoka, M., Kanoh, Y., Taraka, K., and Hayoshi, K., "Shear Strength and Deformation Behaviour of R.C. Interior Beam-Column Joint Using High Strength Concrete", *Proc. 2nd US-NZ-Japan-China Multilateral Meeting on structural Performance of High Strength Concrete in Seismic Resions*, Honolulu, 1994.
- Tsonos, A. G., Tegos, I. A., and Penelis, G. Gr., "Seismic Resistance of Type 2 Exterior Beam-Column Joints Reinforced with Inclined Bars", *ACI Structural Journal*, V. 89, No. 1, 1992, pp. 3-12.
- Uma, S. R., and Prasad, A. M., "Seismic Evaluation of R/C Moment Resisting Frame Structures Considering Joint Flexibility", *13<sup>th</sup> World Conference on Earthquake Engineering Conference Proceedings*, Vancouver, Canada, No. 2799, 2004.
- Vecchio, F. J. and Collins, M. P., "Modified Compression-Field Theory for Reinforced Concrete Elements Subjected to Shear", *ACI Structural Journal*, V. 83, No. 2, 1986, pp. 219-231.
- Viathanatepa, S., Popov, E. P., and Bertero, V. V., "Effects of Generalized Loadings on Bond of Reinforcing Bars Embedded in Confined Concrete Blocks", *Earthquake Engineering Research Council Rep. No. 79/22*, Univ. of California, Berkeley, Calif, 1979.

- Walker, S. G., “Seismic Performance of Existing Reinforced Concrete Beam-Column Joints”, *MS Thesis, Department of Civil and Environmental Engineering*, University of Washington, Seattle, 2001, pp. 308.
- Warcholik, G. and Priestley, M. J. N., “Structural Systems Research Project: High Strength Concrete Joints Tests”, *University of California*, San Diego, Report No. TR-97/10, 1997.
- Wong, P. K. C., Priestley, M. J. N., and Park, R., “Seismic Resistance of Frames with Vertically Distributed Flexural Reinforcement in Beams”, *ACI Structural Journal*, V. 87, No. 4, 1990, pp. 488-498.
- Wood, S. L., “Minimum Tensile Reinforcement Requirements in Walls”, *ACI Structural Journal*, V. 86, No. 4, 1989, pp. 582-591.
- Xian, Z. X., Park, R., and Tanaka, H., “Behaviour of Reinforced Concrete Interior Beam-Column Joints Designed Using High Strength Concrete and Steel”, *Report No. 92-3, Department of Civil Engineering, The University of Canterbury, Christchurch, New Zealand*, 1992, pp.121.
- Yamamoto, Y. S., Nagai, O., and Maruta, M., “Structure Performance of Hinge Relocated RC Slab-Wall Frame”, *Proceedings of the Japan Concrete Institute*, V. 30, No. 3, 2008, pp. 397-402. (in Japanese)
- Yoshino, M., Takeda, S., and Kamimura, T., “Behavior of Interior RC Beam-Column Connections after Yielding of Flexural Beam Reinforcement (in Japanese)”, *Proceedings of the Japan Concrete Institute*, V. 19, No. 2, 1997, pp. 987-992.

## **Appendix A: Joint Shear Strength and Deformation Capacity Matlab Code**

```
clear all
close all
format compact
format long

cycle=0; %(1st cylc: 1, over 2nd cycle 0)

trans=0; %(with cross-beam: 1, w/o cross-beam: 0)

%% Specimen configuration
hb= 508;          % Beam depth [mm]
bb= 406.4;        % Beam width [mm]
ln1= 1600.2;      % Left beam length [mm]
ln2= 1600.2;      % Right beam length [mm]
hc= 457.2;        % Column depth [mm]
bc= 406.4;        % Column width [mm]
h1= 812.8;        % Bottom column length [mm]
h2= 812.8;        % Top column length [mm]
L= ln1+ln2+hc;
H= h1+h2+hb;

fck= 38.433;      % Concrete strength [MPa]

%% Steel properties
Es=200000;        % Modulus of Elasticity [MPa]
fy= 527.85;       % Bottom re-bar yield strength [MPa]
Nfy= 527.85;      % Top re-bar yield strength [MPa]
ey=fy/Es;         % Yield strain [mm/mm]
Ney=Nfy/Es;       % Top re-bar yield strain [mm/mm]
fyw=fy;           % Yield strength [MPa] (web re-bars)
eyw=fyw/Es;       % Yield strain [mm/mm] (reference)
SHF=0.01;         % Strain Hardening Ratio

%% Section properties
sa(1)=1334.707;    % Area of re-bar 1
sa(2)=667.3535;    % Area of re-bar 2
sa(3)=1334.707;    % Area of web re-bar
sa(4)=0; sa(5)=0; sa(6)=0; sa(7)=0; sa(8)=0;
co(1)=62;          % Cover of re-bar 1
co(2)=110;         % Cover of re-bar 2
co(3)=446;         % Cover of web re-bar from 1 end
co(4)=446; co(5)=0; co(6)=0;
co(7)=0;
co(8)=co(4);

%% Bond-slip
```

```
db= 20.6; % Bottom re-bar diameter (mm)
Ndb= 20.6; % Top re-bar diameter (mm)

%% Axial load
Nc= 0.089698; % Axial load ratio

%% Joint hoop
Ash= 0; % Joint hoop area (mm2)
Fh= 674.928; % Joint hoop yield strength (MPa)

%% Beam and column section
As=0; NAs=0; % separation of top and bottom re-bar area
dp=0; dn=0; % effective d for pos and negative moment

for i=1:8
    if co(i)> hb/2
        As= As+sa(i);
        dp= dp+co(i)*sa(i);
    else
        NAs= NAs+sa(i);
        dn= dn+co(i)*sa(i);
    end
end

dp= dp/As; dn= hb-dn/NAs;

cb1= As*fy/0.85/fck/bb; % comp. length for pos. moment
cb2= NAs*Nfy/0.85/fck/bb; % comp. length for neg. moment
jd=((dp-cb1/2)+(dn-cb2/2))/2;

Mp= As*fy*(dp-cb1/2)/1000; % pos. moment (kN.mm)
Mn= NAs*Nfy*(dn-cb2/2)/1000; % neg. moment (kN.mm)

if fck>28 && fck<=55
    beta= 0.85-(0.85-0.65)/(55-28)*(fck-28);
else if fck>55
    beta= 0.65;
else
    beta= 0.85;
end
end

cp= cb1/beta; cn= cb2/beta; %centroid

cc= (0.25+0.85*Nc)*hc; % comp. length of col. for strut
```

```

%% Bond strength
Vu= (As*fy+NAs*Nfy)/1000-(Mn+Mp)/ln1*L/2/H;

c0= 0.08*Ash*Fh/1000/Vu+0.08;

if c0> 0.08*1.02+0.08;
    c0= 0.08*1.02+0.08;
end

tauu= c0*fck^0.5;

if cycle==1
    tauu= c0*fck^0.5*3;
end

taue= 1.8*fck^0.5;
tauc= 2.2*fck^0.5;

%% Bottom re-bar elongation due to bond-slip
et= ey:ey/10:50*ey;

Esh= SHF*Es;           % Fictitious hardening modulus

for i=1:length(et)
    lu(i)= (et(i)-ey)*Esh*db/4/tauu;    % ultimate length
    le(i)= ey*Es*db/4/taue;           % yield state length
    lc(i)= hc-2*lu(i)-le(i); % compression state length
    if le(i)> hc-2*lu(i)
        le(i)= hc-2*lu(i);
    end
    if le(i)<0
        le(i)= 0;
    end
    if lc(i)<0
        lc(i)= 0;
    end

    % Negative
    Nlu(i)= (et(i)-Ney)*Esh*Ndb/4/tauu;    % ult. length
    Nle(i)= Ney*Es*Ndb/4/taue;           % yield state length
    Nlc(i)= hc-2*Nlu(i)-Nle(i); % compression state length
    if Nle(i)> hc-2*Nlu(i)
        Nle(i)= hc-2*Nlu(i);
    end
    if Nle(i)<0
        Nle(i)= 0;
    end
end

```

```

end
if Nlc(i)<0
    Nlc(i)= 0;
end
%

e00(i)= ey-4*taue/Es/db*le(i);
if e00(i) <0
    e00(i)=0;
end

if lu(i)<= 0.5*hc
    e0(i)= e00(i)-4*tauu/Es/db*lu(i);
else if lu(i)>0.5*hc && lu(i)<=hc
    e0(i)= ey-4*tauu/Es/db*(hc-lu(i));
    es2=i;
else
    e0(i)= et(i)-4*tauu/Esh/db*hc;
end
end
if e0(i) <0
    e0(i)= 0;
    es1=i;
end
end

lx=3*db; % elongation location at the joint interface

for i=1:length(et)
    if le(i)<hc-2*lu(i)
        eb(i)= ey*le(i)/2+(et(i)+ey)*lu(i)/2;
        st1=i;
        if lx>= le(i)+lu(i)
            ebo(i)= ey*le(i)/2+(et(i)+ey)*lu(i)/2; %
related to s
        else
            ebo(i)= (et(i)+ey)*lu(i)/2+ ey*le(i)/2*(1-
((le(i)+lu(i)-lx)/le(i))^2);
        end
        if lx<= lu(i)
            ebo(i)= (2*et(i)-(et(i)-ey)*lx/lu(i))*lx/2;
        end
    else if le(i)==hc-2*lu(i) && le(i)>0
        eb(i)= (e00(i)+e0(i))*lu(i)/2+
(e00(i)+ey)*le(i)/2+ (et(i)+ey)*lu(i)/2;
        st2=i;
        if lx>= lu(i)

```



```

            ebo(i) = (et(i)+ey)*lu(i)/2+ (2*ey-(ey-
e00(i))*(lx-lu(i))/le(i))*(lx-lu(i))/2+
0*(2*e0(i)+(e00(i)-e0(i))*lx/lu(i))*lx/2;
        else
            ebo(i) = (2*et(i)-(et(i)-ey)*lx/lu(i))*lx/2+
0*(2*e0(i)+(e00(i)-e0(i))*lx/lu(i))*lx/2; % related to s
        end
    else
        eb(i) = (e0(i)+ey)*(hc-lu(i))/2+
(et(i)+ey)*lu(i)/2;
        if lu(i) >= hc
            ebo(i) = (2*et(i)-(et(i)-ey)*lx/lu(i))*lx/2+
0*(2*e0(i)+(et(i)-e0(i))*lx/hc)*lx/2; % related to s
        else
            ebo(i) = (2*et(i)-(et(i)-ey)*lx/lu(i))*lx/2+
0*(2*e0(i)+(ey-e0(i))*lx/(hc-lu(i)))*lx/2; % related to s
        end
    end
end
if e0(i) >= ey
    e0(i) = ey;
end
end

%% Truss mechanism

Vt1(1:length(eb)) = Ash*Fh/1000;

for i=1:length(eb)
    if le(i) < hc-2*lu(i)
        Vt2(i) =
(lc(i)*tauc+le(i)*taue+2*lu(i)*tauu)*(4*As/db)/1000; %%%%%%
    else if lu(i) >= 0.5*hc
        Vt2(i) = (hc*tauu)*(4*As/db)/1000;
    else
        Vt2(i) =
(le(i)*taue+2*lu(i)*tauu)*(4*As/db)/1000;
    end
end
end

for i=1:length(eb)
    if Nle(i) < hc-2*Nlu(i)
        Vtn(i) =
(Nlc(i)*tauc+Nle(i)*taue+2*Nlu(i)*tauu)*(4*NAs/Ndb)/1000;
    else if Nlu(i) >= 0.5*hc
        Vtn(i) = (hc*tauu)*(4*NAs/Ndb)/1000;
    end
end
end

```

```

        else
            Vtn(i)=
(Nle(i)*taue+2*Nlu(i)*tauu)*(4*NAs/Ndb)/1000;
        end
    end
end

%% Compressive depth

cb1= (As*fy+NAs*Nfy-Vtn*1000)/0.85/fck/bb; % compression
length for positive moment
cb2= (NAs*Nfy+As*fy-Vt2*1000)/0.85/fck/bb; % compression
length for negative moment

for i=1:length(eb)
    if cb1(i)< As*fy/0.85/fck/bb
        cb1(i)= As*fy/0.85/fck/bb;
    end
    if cb2(i)< NAs*Nfy/0.85/fck/bb
        cb2(i)= NAs*Nfy/0.85/fck/bb;
    end
end

cp= cb1/beta;   cn= cb2/beta;   %centroid

%% Compressive stress by truss mech.

theta=atan((hb-cb1/2-cb2/2)/(hc-cc))*180/pi(); % Inclined
angle of diagonal strut

lt=cc+(hb-dp)*cot(theta*pi()/180); % bond length in strut

for i=1:length(eb)
    if lt(i)>= lu(i) && lt(i)<= lu(i)+lc(i)
        Fb1(i)= (lu(i)*tauu+(lt(i)-
lu(i))*tauc)*(4*As/db)/1000;
    end
    if lt(i)>= lu(i)+lc(i) && lt(i)<= lu(i)+lc(i)+le(i)
        Fb1(i)= (lu(i)*tauu+lc(i)*tauc+(lt(i)-lu(i)-
lc(i))*taue)*(4*As/db)/1000;%%
    end
    if lt(i)>= lu(i)+lc(i)+le(i)
        Fb1(i)= ((lt(i)-lc(i)-
le(i))*tauu+lc(i)*tauc+le(i)*taue)*(4*As/db)/1000;
    end
    if lt(i)<= lu(i)

```

```

        Fb1(i)= lt(i)*tauu*(4*As/db)/1000;
    end
end

Fb2=Vt2-Fb1;    %Fbt

d= ( cc*sin(theta*pi()/180)+cb1.*cos(theta*pi()/180) ...
    + cc*sin(theta*pi()/180)+cb2.*cos(theta*pi()/180) )/2;
% Diagonal strut depth

t= min((bb+bc)/2, bb+0.5*hc);    % Strut width

%% gamma vs. slip ratio
ec00=-(0.002 + 0.001*(fck-20)/80);    % Strain at the
compressive strength [mm/mm]

for i=1:length(eb)
    if Vt1(i)<Fb2(i)
        Fb2(i)=Vt1(i);
    end
end

% compressive strain of sturt
ec0=-((As*fy+NAs*Nfy)/1000-
Fb2)./cos(theta*pi()/180))./(d*t/1000)/(4700*fck^0.5);

% compressive strain of compression field
ec0f= -Fb2./cos(theta*pi()/180)./(hc-
lt).*sin(theta*pi()/180)*t/1000)/(4700*fck^0.5);

alpha= (eb-ebo)./eb;

ex= alpha.*eb/(hc-lx);

s= (1-alpha).*eb;

%eyc= -Nc*fck*bc*hc/(4700*fck^0.5)/hc/bc;
eyc= 0;
gamma=2*( (ex-ec0).*(eyc-ec0) ).^.5;

%% Strut-tie model for joint
e1= ex+eyc-ec0;
elf= ex+eyc-ec0f;

if trans==1

```

```

    fce= fck;      % Compressive force of diagonal strut
    fcef= fck;
else
    fce= fck./(0.8+170*e1);      % Compressive force of
    diagonal strut
    fcef= fck./(0.8+170*e1f);      % Compressive force of
    compression field
end

for i=1:length(fce)
    if fce(i)> fck
        fce(i)= fck;
    end
    if fcef(i)> fck
        fcef(i)= fck;
    end
end

Vc= fce.*d*t.*cos(theta*pi()/180)/1000 ;      % Shear
strength due to diagonal strut

Vt3= fcef.*(hc-
lt).*sin(theta*pi()/180)*t/1000.*cos(theta*pi()/180);      %
compression field

Vt=min(Fb2,min(Vt1,Vt3));

%% Deformation
Dri_y= 0.5*ey*L/hb; % beam yield and column drift

cuv_y= 1.7*(fy/Es)/hb;
Ncuv_y= 1.7*(Nfy/Es)/hb;

lp= 0.08*ln1+0.022*db*fy;

for i=1:length(cp)
    if cp(i)>dp
        cp(i)=cp(i-1);
    end
end

cuv= et./(dp-cp);      % pos. curvature

Dri_p= (cuv-cuv_y)*lp*(ln2-lp/2)*2/L;      % beam plastic
drift

```

```

for i=1:length(Dri_p)
    if Dri_p(i)<0
        Dri_p(i)=0;
    end
end

r_s= s./(dp-cp);    % Rotation by slip
r_s2=r_s;
Dri_br= (r_s*ln1+r_s2*ln2)/L; % Drift by beam rotation

Dri_jt= gamma*(1-hc/2/L-hb/2/H);    % Drift by joint

Tot_dri= Dri_y+Dri_p+Dri_br+Dri_jt;    % Total drift

Ncuv= et./(dn-cn);    % neg. curvature
NDri_p= (Ncuv-Ncuv_y)*lp*(ln1-lp/2)*2/L;    % beam plastic
drift

for i=1:length(NDri_p)
    if NDri_p(i)<0
        NDri_p(i)=0;
    end
end

Nr_s= s./(dn-cn);    % Rotation by slip
NDri_br= (Nr_s*ln1)*2/L; % Drift by beam rotation
NTot_dri= Dri_y+NDri_p+NDri_br+Dri_jt;    % Total drift

%% Load-deflection relationship
Mp= As*fy*(dp-cb1/2)/1000;    % pos. moment (kN.mm)
Mn= NAs*Nfy*(dn-cb2/2)/1000; % neg. moment (kN.mm)

Pd= (Mn'/ln1+Mp'/ln2)*L/2/H;

%% Definition of capacity
Dem= (As*fy+NAs*Nfy)/1000-Pd;    % Axial force is excluded
Cap= Vc+Vt;

Pn= Pd.*(Cap'./Dem);
plot(Tot_dri,Pd)
hold on
plot(Tot_dri, Pn,'r-');    % Shear capacity
axis([0 0.08 0 Pd(1)*2])
Tot_dri=Tot_dri';
gamma=gamma';

```

```

jd=((dp-cb1/2)+(dn-cb2/2))/2;
Pn2= Cap.*jd/H./(1-hc/L-jd/H);
plot(Tot_dri, Pn2,'g--'); % Shear capacity
Pn2=Pn2';
Pnt= Vt.*jd/H./(1-hc/L-jd/H);
plot(Tot_dri, Pnt,'r-'); % Shear capacity by truss mech.

i=1;
while Pn2(i)> Pd(i)*1
    i=i+1;
end
cross= 100*Tot_dri(i) %4.0%

censlip=alpha'.*eb';
et=et';
eb=eb';

i=1;
while et(i)<0.04
    i=i+1;
end
fracture= Tot_dri(i)*100

i=1;
while (cp(i)-(hb-max(co)))/(dp-cp(i))*et(i)<0.004
    i=i+1;
end
crushing= NTot_dri(i)*100

if cross>= fracture
    'BF'
else
    'JF'
end

```

## **Appendix B: Nonlinear Time History Analysis OpenSees Code**

```
#####
# Test for PINCHING MODEL #
# Description: uniaxial material with user defined
# envelope (softening type used here) and damage
# parameters #
# Date: August 08 2013 #
## Model subjected to reverse Cyclic Loading #
## File Name: RCyclicPinch.tcl #
#####

wipe
#create the ModelBuilder object

model BasicBuilder -ndm 2 -ndf 3

# 2nd order effect (option: "Y", "N")
set PMeff "Y"

# mode type (option: "single", "multi")
set mode "multi"

# pinching type (option: "pinch", "normal")
set pinching "pinch"

# analysis type (option: "ela", "inela")
set analy "inela"

# add nodes - command: node nodeId xCrd yCrd
source node.tcl

## please keep the follwoing procedures on the same
path
source procUniaxialPinching.tcl
source procRCycDAns.tcl

set bb 400
set hb 600
set hc 500
set bc 500

##### Positive/Negative envelope Roation/Moment
set ppload [expr 250*1000*1000]
set pnload [expr 400*1000*1000]
```



```

if {$analy=="ela"} {
set ppload [expr $ppload*100]
set pnload [expr $pnload*100]
}

set pload1 [expr 0.63*4.899*$bb*$hb*$hb/6]
set pload2 [expr 1.0*$ppload]
set pload3 [expr 1.25*$ppload]
set pload4 [expr 0.2*$ppload]

set nload1 [expr -0.63*4.899*$bb*$hb*$hb/6]
set nload2 [expr -1.0*$pnload]
set nload3 [expr -1.25*$pnload]
set nload4 [expr -0.2*$pnload]

set pEnvelopeStress [list $pload1 $pload2 $pload3
$pload4]
set nEnvelopeStress [list $nload1 $nload2 $nload3
$nload4]

# rotation
set value 1
set pEnvelopeStrain [list [expr 0.0002/$value] [expr
0.002/$value]\
                        [expr 0.035/$value] [expr
0.07/$value]]
set nEnvelopeStrain [list [expr -0.0002/$value] [expr
-0.002/$value]\
                        [expr -0.035/$value] [expr -
0.07/$value]]

if {$pinching=="pinch"} {
##### Ratio of maximum deformation at which reloading
begins
### Pos_env. Neg_env.
set kap 0.2
set rDisp [list [expr -0.95*$kap+0.5] [expr -
0.95*$kap+0.5]]

##### Ratio of envelope force (corresponding to
maximum deformation) at which reloading begins
### Pos_env. Neg_env.
set rForce [list [expr 1.5*$kap-0.12] [expr 1.5*$kap-
0.12]]

```

```

##### Ratio of monotonic strength developed upon
unloading
### Pos_env. Neg_env.
set uForce [list 0.0 0.0]
} else {
    set rDisp [list 0.0 0.0]
    set rForce [list 0.8 0.8]
    set uForce [list 0.0 0.0]
}

##### Coefficients for Unloading Stiffness degradation
### gammaK1 gammaK2 gammaK3 gammaK4 gammaKLimit
set gammaK [list 0.0 0.21 0.0 0.5 0.9]

##### Coefficients for Reloading Stiffness degradation
### gammaD1 gammaD2 gammaD3 gammaD4 gammaDLimit
set gammaD [list 0.0 0.1 0.0 0.2 0.5]

##### Coefficients for Strength degradation
### gammaF1 gammaF2 gammaF3 gammaF4 gammaFLimit
set gammaF [list 0.0 0.0 0.0 0.0 0.0]

set gammaE 10

# material ID
set matID 1

# damage type (option: "energy", "cycle")
set dam "cycle"

# add the material to domain through the use of a
procedure
procUniaxialPinching $matID $pEnvelopeStress
$nEnvelopeStress $pEnvelopeStrain $nEnvelopeStrain
$rDisp $rForce $uForce $gammaK $gammaD $gammaF $gammaE
$dam

#-----#
#----column plastic hinge
##### Positive/Negative envelope Roation/Moment
set ppload [expr 440*1000*1000]
set pnload [expr 440*1000*1000]

if {$analy=="ela"} {

```

```

set ppload [expr $ppload*100]
set pnload [expr $pnload*100]
}

set pload1 [expr 0.63*4.899*$bc*$hc*$hc/6]
set pload2 [expr 1.0*$ppload]
set pload3 [expr 1.25*$ppload]
set pload4 [expr 0.2*$ppload]

set nload1 [expr -0.63*4.899*$bc*$hc*$hc/6]
set nload2 [expr -1.0*$pnload]
set nload3 [expr -1.25*$pnload]
set nload4 [expr -0.2*$pnload]

set pEnvelopeStress [list $pload1 $pload2 $pload3
$pload4]
set nEnvelopeStress [list $nload1 $nload2 $nload3
$nload4]

set value 1.0

set pEnvelopeStrain [list [expr 0.0002/$value] [expr
0.002/$value]\
                        [expr 0.035/$value] [expr
0.07/$value]]
set nEnvelopeStrain [list [expr -0.0002/$value] [expr
-0.002/$value]\
                        [expr -0.035/$value] [expr -
0.07/$value]]

set kap 0.4
set rDisp [list [expr -0.95*$kap+0.5] [expr -
0.95*$kap+0.5]]
set rForce [list [expr 1.5*$kap-0.12] [expr 1.5*$kap-
0.12]]
set uForce [list 0.0 0.0]

##### Coefficients for Unloading Stiffness degradation
set gammaK [list 0.0 0.21 0.0 0.5 0.9]
set gammaD [list 0.0 0.1 0.0 0.2 0.5]
set gammaF [list 0.0 0.0 0.0 0.0 0.0]

set gammaE 10
set matID 2
set dam "cycle"

```

```

procUniaxialPinching $matID $pEnvelopeStress
$nEnvelopeStress $pEnvelopeStrain $nEnvelopeStrain
$rDisp $rForce $uForce $gammaK $gammaD $gammaF $gammaE
$dam

#-----
#section Uniaxial $secTag $matTag $string
section Uniaxial 1 1 Mz
section Uniaxial 2 2 Mz

if {$PMeff=="Y"} {
    geomTransf PDelta 1
} else {
    geomTransf Linear 1
}
geomTransf Linear 2

#uniaxialMaterial ElasticPP 2 23978.0 0.008

set colA [expr $bc*$hc]
set colE 23000
set colI [expr 0.7*$bc/12.*$hc*$hc*$hc/1.0]
# rigid connection
set colAr [expr $colA*$colA]
set colIr [expr $colI*$colI]

set BeamA [expr $bb*$hb]
set BeamE 23000
set BeamI [expr 0.35*$bb/12.*$hb*$hb*$hb/1.0]
# rigid connection
set BeamAr [expr $BeamA*$BeamA]
set BeamIr [expr $BeamI*$BeamI]

source element.tcl

# set the boundary conditions - command: fix nodeID
xResrnt? yRestrnt?
fix 1 1 1 1
fix 2 1 1 1

# nodal masses: ton
set halfb [expr 2.4*$BeamA/1000000*$L/2000]

```

```

set halfc [expr 2.4*$colA/1000000*$H/2000]
mass 11 [expr $halfb+2*$halfc+3*$L/2/9810] 0 0.;
mass 12 [expr $halfb+2*$halfc+3*$L/2/9810] 0 0.;
mass 21 [expr $halfb+2*$halfc+3*$L/2/9810] 0 0.;
mass 22 [expr $halfb+2*$halfc+3*$L/2/9810] 0 0.;
mass 31 [expr $halfb+$halfc+3*$L/2/9810] 0 0.;
mass 32 [expr $halfb+$halfc+3*$L/2/9810] 0 0.;

# define Gravity Load      #FEMA 273
set WzBeam [expr 1.0*$halfb*9810*2/$L+0.25*12.0]

pattern Plain 2 Constant {
    eleLoad -ele 111 -type -beamUniform -$WzBeam;
    eleLoad -ele 121 -type -beamUniform -$WzBeam;
    eleLoad -ele 131 -type -beamUniform -$WzBeam;
}

# -----
apply gravity load
set Tol 1.0e-8;                # convergence tolerance
for test
constraints Plain;              # how it handles
boundary conditions
numberer Plain;                 # renumber dof's to
minimize band-width (optimization), if you want to
system BandGeneral;            # how to store and solve the
system of equations in the analysis
test NormDispIncr $Tol 6 ;      # determine if
convergence has been achieved at the end of an
iteration step
algorithm Newton;               # use Newton's solution
algorithm: updates tangent stiffness at every
iteration
set NstepGravity 10;            # apply gravity in 10
steps
set DGravity [expr 1./$NstepGravity]; # first load
increment;
integrator LoadControl $DGravity; # determine the
next time step for an analysis
analysis Static;                # define type of
analysis static or transient
analyze $NstepGravity;          # apply gravity
# -----
maintain constant gravity loads and reset time to zero
loadConst -time 0.0

```

```

puts "Model Built"

pattern Plain 1 Linear {
load 31 1 0 0
#load 21 0.67 0 0
#load 11 0.33 0 0
}

recorder Node -file disp.out -load -node 12 22 32 -dof
1 disp;
recorder Node -file rot.out -node 113 213 313 121 221
321 -dof 3 disp;
recorder Node -file rot2.out -node 1130 2130 3130 1210
2210 3210 -dof 3 disp;
recorder Element -file colfor.out -ele 11 12 22 32
globalForce;
recorder Node -file rotcol.out -node 10 20 -dof 3 disp;
recorder Element -file beamfor.out -ele 111 121 131
globalForce;
recorder Node -file acc.out -node 12 22 32 -dof 1
accel;

# build the components for the analysis object
system BandGeneral
constraints Plain
test NormDispIncr 1.0e-8 20
algorithm Newton
numberer RCM

## analysis type used in the procedure is Static

set peakpts [list 1.0 108 108 216 216 324 324 432 432
540 540 648 648]
set increments 1
set nodeTag 31
set dofTag 1

## start procedure for feeding in
## Reverse Cyclic loading to the model by Disp.
control

#procRCycDAns $increments $nodeTag $dofTag $peakpts

source 2D.analyze.Dynamic.EQ.tcl

```

```
#####
# Date: August 08 2013 #
## File Name: node.tcl #
#####

#1bay 3floor

set hc 500 ; # Column depth 480*480
set hb 600 ; # Beam depth 350*500
set L 6000 ; # Span
set H 3600 ; # Height

set NStory 3; # number of stories above ground level -
-- you can change this.
set NBay 1; # number of bays (max 9) --- you can
change this.

node 1 0.0 0.0
node 2 [expr $L] 0.0
node 11 0.0 [expr $H]
node 12 [expr $L] [expr $H]
node 21 0.0 [expr 2*$H]
node 22 [expr $L] [expr 2*$H]
node 31 0.0 [expr 3*$H]
node 32 [expr $L] [expr 3*$H]

#Joint
node 113 [expr $hc/2] [expr $H]
node 121 [expr $L-$hc/2] [expr $H]
node 213 [expr $hc/2] [expr 2*$H]
node 221 [expr $L-$hc/2] [expr 2*$H]
node 313 [expr $hc/2] [expr 3*$H]
node 321 [expr $L-$hc/2] [expr 3*$H]

#equalDOF
node 10 0.0 0.0
node 20 [expr $L] 0.0
node 1130 [expr $hc/2] [expr $H]
node 1210 [expr $L-$hc/2] [expr $H]
node 2130 [expr $hc/2] [expr 2*$H]
node 2210 [expr $L-$hc/2] [expr 2*$H]
node 3130 [expr $hc/2] [expr 3*$H]
node 3210 [expr $L-$hc/2] [expr 3*$H]
```

```
equalDOF 1 10 1 2  
equalDOF 2 20 1 2
```

```
equalDOF 113 1130 1 2  
equalDOF 121 1210 1 2  
equalDOF 213 2130 1 2  
equalDOF 221 2210 1 2  
equalDOF 313 3130 1 2  
equalDOF 321 3210 1 2
```



```
#####
# Date: August 08 2013 #
## File Name: element.tcl #
#####

#columns
element elasticBeamColumn 11 10 11 $colA $colE $colI 1
element elasticBeamColumn 12 20 12 $colA $colE $colI 1
element elasticBeamColumn 21 11 21 $colA $colE $colI 1
element elasticBeamColumn 22 12 22 $colA $colE $colI 1
element elasticBeamColumn 31 21 31 $colA $colE $colI 1
element elasticBeamColumn 32 22 32 $colA $colE $colI 1

#column zeroLength
element zeroLengthSection 110 1 10 2
element zeroLengthSection 120 2 20 2

#beam
element elasticBeamColumn 111 1130 1210 $BeamA $BeamE
$BeamI 2
element elasticBeamColumn 121 2130 2210 $BeamA $BeamE
$BeamI 2
element elasticBeamColumn 131 3130 3210 $BeamA $BeamE
$BeamI 2

# rigid beam
element elasticBeamColumn 1111 11 113 $BeamAr $BeamE
$BeamIr 2
element elasticBeamColumn 1112 121 12 $BeamAr $BeamE
$BeamIr 2
element elasticBeamColumn 1211 21 213 $BeamAr $BeamE
$BeamIr 2
element elasticBeamColumn 1212 221 22 $BeamAr $BeamE
$BeamIr 2
element elasticBeamColumn 1311 31 313 $BeamAr $BeamE
$BeamIr 2
element elasticBeamColumn 1312 321 32 $BeamAr $BeamE
$BeamIr 2

#beam zeroLength
element zeroLengthSection 11110 113 1130 1
element zeroLengthSection 11120 1210 121 1
```

```
element zeroLengthSection 12110 213 2130 1
element zeroLengthSection 12120 2210 221 1
element zeroLengthSection 13110 313 3130 1
element zeroLengthSection 13120 3210 321 1
```

```
#####
# Date: August 08 2013 #
## File Name: procUniaxialPinching.tcl #
# procedure for activating the pinching material given
its parameters in the form of list #
#####

proc procUniaxialPinching { materialTag
pEnvelopeStress nEnvelopeStress pEnvelopeStrain
nEnvelopeStrain rDisp
rForce uForce gammaK gammaD gammaF gammaE damage} {

# add material - command: uniaxialMaterial .....
paramaters as shown
#uniaxialMaterial Pinching4 tag
#### stress1P strain1P stress2P strain2P stress3P
strain3P stress4P strain4P
#### stress1N strain1N stress2N strain2N stress3N
strain3N stress4N strain4N
#### rDispP rForceP uForceP rDispN rForceN uForceN
#### gammaK1 gammaK2 gammaK3 gammaK4 gammaKLimit
#### gammaD1 gammaD2 gammaD3 gammaD4 gammaDLimit
#### gammaF1 gammaF2 gammaF3 gammaF4 gammaFLimit
gammaE $damage

uniaxialMaterial Pinching4 $materialTag [lindex
$pEnvelopeStress 0] [lindex $pEnvelopeStrain 0] \
[lindex $pEnvelopeStress 1] [lindex $pEnvelopeStrain 1]
[lindex $pEnvelopeStress 2] \
[lindex $pEnvelopeStrain 2] [lindex $pEnvelopeStress 3]
[lindex $pEnvelopeStrain 3] \
[lindex $nEnvelopeStress 0] [lindex $nEnvelopeStrain 0]
\
[lindex $nEnvelopeStress 1] [lindex $nEnvelopeStrain 1]
[lindex $nEnvelopeStress 2] \
[lindex $nEnvelopeStrain 2] [lindex $nEnvelopeStress 3]
[lindex $nEnvelopeStrain 3] \
[lindex $rDisp 0] [lindex $rForce 0] [lindex $uForce 0]
\
[lindex $rDisp 1] [lindex $rForce 1] [lindex $uForce 1]
\
[lindex $gammaK 0] [lindex $gammaK 1] [lindex $gammaK
2] [lindex $gammaK 3] [lindex $gammaK 4] \
[lindex $gammaD 0] [lindex $gammaD 1] [lindex $gammaD
2] [lindex $gammaD 3] [lindex $gammaD 4] \
```

```
[lindex $gammaF 0] [lindex $gammaF 1] [lindex $gammaF  
2] [lindex $gammaF 3] [lindex $gammaF 4] \  
$gammaE $damage  
}
```

```
#####
# Date: August 08 2013 #
## File Name: procRCycDAns.tcl #
# procedure for reverse cyclic displacement control
# analysis given the peak pts. #
# analysis type used : STATIC #
#####

proc procRCycDAns { incre nodeTag dofTag peakpts} {

set x [lindex $peakpts 0]
set fir [expr $x/$incre]

integrator DisplacementControl $nodeTag $dofTag 0.0 1
$fir $fir

# create the analysis object
analysis Static
# perform the analysis
analyze $incre
integrator DisplacementControl $nodeTag $dofTag 0.0 1
[expr -$fir] [expr -$fir]
analyze [expr 2*$incre]
integrator DisplacementControl $nodeTag $dofTag 0.0 1
$fir $fir
analyze $incre

for {set j 1} {$j < [llength $peakpts]} {incr j 1} {
set tx [lindex $peakpts $j]
set tinc [expr $tx/$fir]
set rt [expr int($tinc)]

integrator DisplacementControl $nodeTag $dofTag 0.0 1
$fir $fir
analyze $rt
integrator DisplacementControl $nodeTag $dofTag 0.0 1
[expr -$fir] [expr -$fir]
analyze [expr 2*$rt]
integrator DisplacementControl $nodeTag $dofTag 0.0 1
$fir $fir
analyze $rt
}

##### end procRCycDAns.tcl
}
```

```
#####
# Date: August 08 2013 #
## File Name: 2D.analyze.Dynamic.EQ.tcl #
#####

# -----
# 2D -- EQ ground motion
# execute this file after you have built the model,
# and after you apply gravity
#
set sec 1.;
# Uniform Earthquake ground motion (uniform
# acceleration input at all support nodes)
set GMdirection 1;          # ground-motion
# direction
set GMfile "elcen.acc" ;    # ground-motion
# filenames
set GMfact [expr 2.0*2.02]; #
# ground-motion scaling factor

# set up ground-motion-analysis parameters
set DtAnalysis [expr 0.001*$sec]; # time-step Dt
# for lateral analysis
set TmaxAnalysis [expr 32.0 *$sec]; # maximum
# duration of ground-motion analysis -- should be
# 50*$sec

#set GMfile "LomaPrieta05.acc" ;
#set DtAnalysis [expr 0.0005*$sec];
#set TmaxAnalysis [expr 40.0 *$sec];

#set GMfile "Northridge.acc" ;

# DYNAMIC ANALYSIS PARAMETERS
# CONSTRAINTS handler -- Determines how the constraint
# equations are enforced in the analysis
# (http://opensees.berkeley.edu/OpenSees/manuals/userman
# ual/617.htm)
# Plain Constraints -- Removes constrained
# degrees of freedom from the system of equations
# Lagrange Multipliers -- Uses the method of
# Lagrange multipliers to enforce constraints
# Penalty Method -- Uses penalty numbers to
# enforce constraints
# Transformation Method -- Performs a
```

```
condensation of constrained degrees of freedom
constraints Transformation ;

# DOF NUMBERER (number the degrees of freedom in the
domain):
(http://opensees.berkeley.edu/OpenSees/manuals/userman
ual/366.htm)
# determines the mapping between equation numbers and
degrees-of-freedom
# Plain -- Uses the numbering provided by the
user
# RCM -- Renumbers the DOF to minimize the
matrix band-width using the Reverse Cuthill-McKee
algorithm
numberer Plain

# SYSTEM
(http://opensees.berkeley.edu/OpenSees/manuals/userman
ual/371.htm)
# Linear Equation Solvers (how to store and solve the
system of equations in the analysis)
# -- provide the solution of the linear system of
equations  $Ku = P$ . Each solver is tailored to a
specific matrix topology.
# ProfileSPD -- Direct profile solver for
symmetric positive definite matrices
# BandGeneral -- Direct solver for banded
unsymmetric matrices
# BandSPD -- Direct solver for banded symmetric
positive definite matrices
# SparseGeneral -- Direct solver for
unsymmetric sparse matrices (-piv option)
# SparseSPD -- Direct solver for symmetric
sparse matrices
# UmfPack -- Direct UmfPack solver for
unsymmetric matrices
system SparseGeneral -piv

# TEST: # convergence test to
# Convergence TEST
(http://opensees.berkeley.edu/OpenSees/manuals/userman
ual/360.htm)
# -- Accept the current state of the domain as being
on the converged solution path
# -- determine if convergence has been achieved at
```

```

the end of an iteration step
#       NormUnbalance -- Specifies a tolerance on the
norm of the unbalanced load at the current iteration
#       NormDispIncr -- Specifies a tolerance on the
norm of the displacement increments at the current
iteration
#       EnergyIncr-- Specifies a tolerance on the
inner product of the unbalanced load and displacement
increments at the current iteration
#       RelativeNormUnbalance --
#       RelativeNormDispIncr --
#       RelativeEnergyIncr --
set Tol 1.e-4;                                # Convergence Test:
tolerance
set maxNumIter 300;                            # Convergence Test:
maximum number of iterations that will be performed
before "failure to converge" is returned
set printFlag 0;                              # Convergence Test: flag
used to print information on convergence (optional)
# 1: print information on each step;
set TestType NormDispIncr;                    # Convergence-test type
test $TestType $Tol $maxNumIter $printFlag;

# Solution ALGORITHM: -- Iterate from the last time
step to the current
(http://opensees.berkeley.edu/OpenSees/manuals/userman
ual/682.htm)
#       Linear -- Uses the solution at the first
iteration and continues
#       Newton -- Uses the tangent at the current
iteration to iterate to convergence
#       ModifiedNewton -- Uses the tangent at the
first iteration to iterate to convergence
#       NewtonLineSearch --
#       KrylovNewton --
#       BFGS --
#       Broyden --
set algorithmType ModifiedNewton
algorithm $algorithmType;

# Static INTEGRATOR: -- determine the next time step
for an analysis
(http://opensees.berkeley.edu/OpenSees/manuals/userman
ual/689.htm)
#       LoadControl -- Specifies the incremental load

```



```

factor to be applied to the loads in the domain
#           DisplacementControl -- Specifies the
incremental displacement at a specified DOF in the
domain
#           Minimum Unbalanced Displacement Norm --
Specifies the incremental load factor such that the
residual displacement norm is minimized
#           Arc Length -- Specifies the incremental arc-
length of the load-displacement path
# Transient INTEGRATOR: -- determine the next time
step for an analysis including inertial effects
#           Newmark -- The two parameter time-stepping
method developed by Newmark
#           HHT -- The three parameter Hilbert-Hughes-
Taylor time-stepping method
#           Central Difference -- Approximates velocity
and acceleration by centered finite differences of
displacement
set NewmarkGamma 0.5;      # Newmark-integrator gamma
parameter (also HHT)
set NewmarkBeta 0.25;     # Newmark-integrator beta
parameter
integrator Newmark $NewmarkGamma $NewmarkBeta

# ANALYSIS -- defines what type of analysis is to be
performed
(http://opensees.berkeley.edu/OpenSees/manuals/userman
ual/324.htm)
#           Static Analysis -- solves the KU=R problem,
without the mass or damping matrices.
#           Transient Analysis -- solves the time-
dependent analysis. The time step in this type of
analysis is constant. The time step in the output is
also constant.
#           variableTransient Analysis -- performs the
same analysis type as the Transient Analysis object.
The time step, however, is variable. This method is
used when
#           there are convergence problems with the
Transient Analysis object at a peak or when the time
step is too small. The time step in the output is also
variable.
analysis Transient

# define DAMPING-----

```

```

-----
# apply Rayleigh DAMPING from $xDamp
# D=$alphaM*M + $betaKcurr*Kcurrent +
$betaKcomm*KlastCommit + $beatKinit*$Kinitial
set xDamp 0.05;                # 5% damping
ratio

set nEigenI 1;                # mode 1
set nEigenJ 3;                # mode 3
set lambdaN [eigen [expr $nEigenJ]]; #
eigenvalue analysis for nEigenJ modes
set lambdaI [lindex $lambdaN [expr $nEigenI-1]]; #
eigenvalue mode i
set lambdaJ [lindex $lambdaN [expr $nEigenJ-1]]; #
eigenvalue mode j

set omegaI [expr pow($lambdaI,0.5)];
set omegaJ [expr pow($lambdaJ,0.5)];
if {$mode=="single"} {
    set omegaJ 0.0
}

set Tperiod [expr 2*3.141592/$omegaI];
puts $Tperiod

set MpropSwitch 1.0;
set KcurrSwitch 0.0;
set KcommSwitch 1.0;
set KinitSwitch 0.0;

set alphaM [expr
$MpropSwitch*$xDamp*(2*$omegaI*$omegaJ)/($omegaI+$omeg
aJ)]; # M-prop. damping; D = alphaM*M
set betaKcurr [expr
$KcurrSwitch*2.*$xDamp/($omegaI+$omegaJ)]; # K-
proportional damping;      +beatKcurr*KCurrent
set betaKcomm [expr
$KcommSwitch*2.*$xDamp/($omegaI+$omegaJ)]; # K-
prop. damping parameter;  +betaKcomm*KlastCommitt
set betaKinit [expr
$KinitSwitch*2.*$xDamp/($omegaI+$omegaJ)]; # initial-
stiffness proportional damping      +beatKinit*Kini

# define damping
rayleigh $alphaM $betaKcurr $betaKinit $betaKcomm;

```

```

# RAYLEIGH damping

# ----- perform Dynamic
Ground-Motion Analysis
# Uniform EXCITATION: acceleration input
set IDloadTag 400;          # load tag
set dt 0.001;              # time step for input
ground motion
set GMfatt [expr 9810*$GMfact]; # data in input file is
in g Units -- mm/s2
set AccelSeries "Series -dt $dt -filePath $GMfile -
factor $GMfatt";          # time series
information
pattern UniformExcitation $IDloadTag $GMDirection -
accel $AccelSeries ;      # create Uniform
excitation

set Nsteps [expr int($TmaxAnalysis/$DtAnalysis)];
set ok [analyze $Nsteps $DtAnalysis];          #
actually perform analysis; returns ok=0 if analysis
was successful

if {$ok != 0} {          ;          # if
analysis was not successful.
    # change some analysis parameters to achieve
convergence
    # performance is slower inside this loop
    # Time-controlled analysis
    set ok 0;
    set controlTime [getTime];
    while {$controlTime < $TmaxAnalysis && $ok == 0}
    {
        set ok [analyze 1 $DtAnalysis]
        set controlTime [getTime]
        set ok [analyze 1 $DtAnalysis]
        if {$ok != 0} {
            puts "Trying Newton with Initial
Tangent .."
            test NormDispIncr $Tol 1000 0
            algorithm Newton -initial
            set ok [analyze 1 $DtAnalysis]
            test $TestType $Tol $maxNumIter 0
            algorithm $algorithmType
        }
        if {$ok != 0} {

```

```
        puts "Trying Broyden .."
        algorithm Broyden 8
        set ok [analyze 1 $DtAnalysis]
        algorithm $algorithmType
    }
    if {$ok != 0} {
        puts "Trying
NewtonWithLineSearch .."
        algorithm NewtonLineSearch .8
        set ok [analyze 1 $DtAnalysis]
        algorithm $algorithmType
    }
};      # end if ok !0

puts "Ground Motion Done. End Time: [getTime]"
```

## 초 록

주기하중이 작용하는 철근콘크리트 모멘트 저항골조의 강성 및 강도 감소, 에너지 소산능력 등의 주기거동은 보-기둥 접합부의 거동에 영향을 받는다. 본 연구에서는 철근콘크리트 구조물의 성능 기반 내진 설계에 적용할 수 있도록 보-기둥 접합부의 주기 거동 및 내진 성능을 평가하기 위한 이론 및 실험 연구가 수행되었다.

보-기둥 접합부의 거동은 주로 보 주근의 부착 미끄러짐 및 조인트 전단변형에 영향을 받는다. 보 주근에 600 MPa 철근 적용시 보-기둥 접합부의 부착성능 및 내진성능을 평가하기 위하여 실제 크기의 내부 접합부 4개와 외부 접합부 3개에 대해서 주기하중 실험을 수행하였다. 실험체는 ACI 318-11의 내진 설계기준에 따라 설계되었으며, 600 MPa D22, D25 철근을 적용한 실험체의 구조성능을 400 MPa D25 철근을 사용한 실험체와 비교하였다. 내부 접합부의 경우 하중 재하능력 및 최대 변형능력은 400 MPa 철근을 사용한 실험체와 유사하였으나 에너지 소산비는 부착미끄러짐으로 인하여 최대 25% 감소하였다. 외부 접합부의 경우 부착길이 부족으로 보 하부 철근에서 부착 미끄러짐이 발생하였으며, 변형능력 및 에너지 소산능력이 감소하였다.

조인트에서 보 주근의 부착미끄러짐을 평가하기 위하여 부착미끄러짐 모델을 개발하였다. 제안모델에서는 단순 부착강도 및 변형률 기반모델을 이용하여 조인트에서 부착미끄러짐을 고려하였으며, 완전 부착파괴가 발생한 기존 보-기둥 접합부의 실험결과로부터 부착강도를 정의하였다. 제안모델은 기존 콘크리트 블록 부착실험 및 보-기둥 접합부에서 철근의 부착강도 저하 및 부착미끄러짐을 잘 예

측하였다.

부착미끄러짐 모델을 바탕으로 보 주근의 부착미끄러짐을 고려한 조인트 전단강도 모델을 개발하였다. 조인트 전단강도 모델은 트러스 메커니즘과 대각 스트럿 메커니즘으로 구성되며, 부착모델을 보 주근에 적용하였다. 조인트 전단강도와 변형능력을 기존 64개의 내부접합부 실험결과와 비교하였으며, 제안한 모델은 조인트 전단강도 감소 및 변형능력을 잘 예측하였다.

기존 내부접합부 69개와 외부접합부 63개의 실험결과로부터 부착미끄러짐 및 조인트 전단강도에 따른 에너지 소산능력을 분석하였다. 분석결과, 에너지 소산비는 조인트 전단강도보다는 철근의 부착미끄러짐과 연관성이 있는 것으로 나타났으며, 보-기둥 접합부의 에너지 소산비를 부착 설계변수의 함수로 정의하였다. 에너지 함수와 OpenSees의 Pinching 4 모델을 이용하여 주기곡선의 면적이 에너지 소산량 예측값과 동일하도록 에너지기반 이력모델을 개발하였다. 제안한 모델은 보-기둥 접합부의 주기거동을 잘 예측하였다.

다양한 에너지 소산비를 갖는 보-기둥 접합부 및 기둥에 에너지기반 모델을 적용하여 세가지 형태의 저층 모멘트 골조에 대해 비선형 동적해석을 수행하였다. 해석결과 조인트의 에너지 소산능력이 감소할수록 구조물의 변형 및 요구연성도가 증가하였다. 특히, 구조물의 고유주기가 짧을수록 변형이 증가하였다. 소성 설계에 의한 항복강도 감소비가 큰 경우, 구조물의 에너지 소산능력은 구조성능에 큰 영향을 미쳤다.

마지막으로, 부착미끄러짐을 억제하고 보-기둥 접합부의 구조성능을 향상시키기 위하여 소성한지 이동법을 제안하였다. 소성한지 이동효과를 검증하기 위하여 45° 굽힘근 및 90° 후크근으로 보강한

보-기둥 접합부의 주기하중 실험을 수행하였다. 실험체의 기둥춤/보 철근 직경비가 기준에서 제시하는 20보다 작음에도 불구하고 보강 방법으로 인하여 철근의 부착미끄러짐 및 조인트 전단강도 저하가 크게 감소하였다. 엔지니어가 설계에 적용할 수 있도록 기존 설계기준을 바탕으로 보강방법 적용시 성능향상을 고려하여 보 주근의 부착저항 및 조인트 전단강도를 새로 정의하였다. 기존 실험결과로부터 보강철근 사용시 보-기둥 접합부의 내진 설계 및 상세에 대해 권장사항을 제시하였다.

주요어 : 성능기반 내진 설계; 철근콘크리트 보-기둥 접합부; 비선형 시간이력 해석; 부착 미끄러짐; 조인트 전단 강도; 고강도 철근; 보강 방법

학 번 : 2010-30175